A NUMERICAL METHOD FOR CONFINED UNSTEADY FLOWS RELATED TO FLUID-STRUCTURE INTERACTIONS

by

FRANÇOIS BELANGER

Department of Mechanical Engineering
McGill University
Montreal, Québec, Canada.

July, 1991

A Thesis submitted to the Faculty of Graduate Studies and Research
in partial fulfillment of the requirements for the degree of
Doctor of Philosophy.

Abstract

This Thesis elaborates three aspects in the field of flow-induced vibrations associated with annular geometries.

A method to find the unsteady fluid forces on a cylinder oscillating in annular turbulent flow is developed by considering the superposition of the turbulent fluctuating quantities on potential flow. The theory is compared with experiments.

Then, the unsteady fluid forces acting on the vibrating cylinder walls of non-uniform annular configurations are computed by a method which performs the accurate time integration of the Navier-Stokes equations. It is the extension for unsteady flows of the method of artificial compressibility used for steady flows. A time-discretization of the momentum equation using a three-point-backward implicit scheme is introduced, and the addition of pseudo-time derivative terms to the semi-discretized equations, including artificial compressibility in the continuity equation, allows to use time-marching solution techniques thereafter.

Finally, the integration method used for the Navier-Stokes equations is combined with the equation governing the dynamical behavior of a structure in order to perform the fluid-structure stability analysis of this system in the time domain.

Résumé

Cette thèse traite de trois sujets originaux des études fluides-structures en écoulements laminaires.

Une méthode détermine d'abord les forces fluide instationnaires sur un cylindre vibrant dans un écoulement annulaire uniforme turbulent. Elle consiste en la superposition des quantités fluctuantes présentes dans les écoulements turbulents, avec un écoulement potentiel. La théorie est comparée avec des résultats expérimentaux.

Les écoulements laminaires dans des géométries annulaires non uniformes font par la suite l'objet de la thèse, et les forces fluide instationnaires sur les parois vibrantes des cylindres sont calculées par une nouvelle méthode. Elle consiste en l'intégration temporelle des équations de Navier-Stokes par la méthode de compressibilité artificielle généralisée pour résoudre les écoulements instationnaires. Un schéma décentré à trois pas de temps est introduit à cette fin dans l'équation de Navier-Stokes, et l'addition de dérivées en "pseudo-temps" aux équations, incluant de la compressibilité artificielle pour l'équation de continuité, permet alors d'utiliser les méthodes de solution temporelles existantes, en pseudo-temps.

En dernier lieu, la méthode de compressibilité artificielle développée pour les équations de Navier-Stokes est combinée avec l'équation déterminant le comportement dynamique d'un système fluide-structure dans le but d'en étudier la stabilité en domaine temporel.

Acknowledgements

I wish to thank my thesis supervisors, Professors Dan Mateescu and Michael P. Paidoussis, for their support. They provided me with a very interesting subject of study, and encouraged my initiatives as to which direction I should pursue. Their past and present contributions in the fields of flow-induced vibrations, system dynamics and stability, and fluid mechanics and aerodynamics, have laid the ground for many novel methods and approaches in those fields; this Thesis is an outgrowth thereof

I also wish to express my gratitude to Mr. François Axisa, head of the "Laboratoire d'Etudes de Vibrations" of the "Commissariat à l'Energie Atomique", in France, for a very instructive and rewarding stay of six months which I made there and which he contributed to making possible. I'm actually thankful to all the staff at the laboratory, in particular the close and fruitful collaboration with Mr Emmanuel de Langre is acknowledged. The support of Mr Fernand Hareux and Mrs. Thérèse Léna also ought to be mentioned.

Contents

Abstract i

Résumé ii

Acknowledgements iii

Contents vii

List of Figures xv

List of Tables xvii

1 INTRODUCTION **1**

1.1 Flow-induced Vibrations 1

1.2 Vibration Induced by Annular Flow 1

1.3 Modelling of Fluid Forces by the Navier-Stokes Equations 4

2 UNSTEADY TURBULENT EFFECTS IN UNIFORM ANNULAR GEOMETRY **9**

2.1 Equations of Motion 9

2.2 Solution of Unsteady Potential Flow 14

2.3 Solution of Unsteady Turbulent Flow 16

2.4 Theoretical Results Compared with Experiments . . . 23

2.4.1 Theoretical solution 23

2.4.2 Experimental apparatus 24
2.4.3 Comparison between theory and experiments 26
2.5 Conclusions 32

3 A TIME INTEGRATION METHOD USING ARTIFICIAL COMPRESSIBILITY FOR UNSTEADY FLOWS 33

3.1 Introduction 33
3.2 Time Discretization of Navier-Stokes Equations 34
3.3 Pseudo-time Iterative Relaxation Technique 37

4 METHOD OF SOLUTION IN CARTESIAN COORDINATES 40

4.1 Differential Form of Equations 40
4.2 Spatial Discretization of Differential Operators 45
4.2.1 Stretched grid and grid stretching functions 45
4.2.2 Differencing of spatial differential operators 46
4.2.3 Differencing of Navier-Stokes equations 48
4.3 The y-Sweep 52
4.3.1 Discretization of x-momentum equation in y-sweep 52
4.3.2 Discretization of y-momentum and continuity equations in y-sweep 54
4.4 The x-Sweep 55

5 VALIDATION TEST PROBLEMS 59

5.1 Validation for Steady Flow Problems 60
5.1.1 Driven cavity flow 62
5.1.2 Flow over a backward-facing step 67
5.2 Validation for Unsteady Flow Problems 74
5.2.1 Unsteady flow between oscillating plates 75

5.2.2 Unsteady driven cavity flow with oscillating lid 83

6 METHOD OF SOLUTION IN CYLINDRICAL COORDINATES 90

6.1 Introduction . . . 90

6.2 Differential Form of Equations 90

6.3 Hybrid Finite-Difference/Fourier-Expansion Method . . 95

6.4 Linearized Forms of Navier-Stokes Equations 101

7 TWO-DIMENSIONAL UNSTEADY ANNULAR FLOW BETWEEN CONCENTRIC CYLINDERS 107

7.1 Two-Dimensional Equations of Motion 107

7.2 Linearized Equations of Motion . . 114

7.3 Two-Harmonic Non-Linear Solution . 116

7.4 Numerical Results . . . 121

7.4.1 The three-point-backward scheme 121

7.4.2 Comparison with the Crank-Nicolson scheme . . 136

8 COMPUTATION OF 3D UNSTEADY FLOWS 138

8.1 Uniform Annular Flow Geometry . 141

8.2 Annular Flow Geometry with Backstep 171

9 FLUID-STRUCTURE INTERACTION AND STABILITY ANALYSIS IN THE TIME DOMAIN 181

9.1 Introduction 181

9.2 Numerical Procedure 183

9.3 Numerical Results 187

9.3.1 Fluid-structure interaction in 2D annular geometry . 187

9.3.2 Fluid-structure interaction in 3D annular geometry 192

9.4 Discussion 198

10 CONCLUSIONS **200**

BIBLIOGRAPHY **204**

A Discretization of 3D Linearized Solution **A-1**

B Discretization of 2D Nonlinear Solution **B-1**

C Discretization of 3D Nonlinear Solution **C-1**

D Linearized Potential Flow Theory **D-1**

E Program Listings **E-1**

List of Figures

1.1 Core of Advanced Gas Cooled Reactor showing the annular flow configuration. 2

2.1 Geometry of the oscillating center-body in the cylindrical duct 10

2.2 Direction, β, of the flow velocity, W, in the annular space, in the plane tangent to the surface of the center-body and along the coordinate X. 19

2.3 Schematic diagram of the experimental apparatus . . 25

2.4 Comparison between theoretical and experimentally measured unsteady pressures (amplitude $\Delta\hat{P}$ and phase ψ) *versus* oscillation frequency, f, showing the influence of the circumferential position, for $\theta = 0°$, $30°$, $45°$, and $60°$, and for $l_0 = 2.59$, $r = 5.60$ Lines: present unsteady turbulent analysis; the theoretical phase does not depend on θ. Experiments: ◯ $\theta = 0°$, ◇ $\theta = 30°$, □ $\theta = 45°$, △ $\theta = 60°$ (a) $U = 52.4$ m/s, (b) $U = 73.0$ m/s. 29

2.5 Theoretical and experimentally measured unsteady pressures (amplitude ΔP and phase ψ) *versus* oscillation frequency, f, showing the effect of circumferential location θ, for $l_0 = 4.73$, $x = 6.23$ and $U = 52.4$ m/s – – present unsteady turbulent analysis, and – – – potential theory of Ref. [5] Experiments: (a) ◯ $\theta = 0°$, ◇ $\theta = 45°$, (b) ◯ $\theta = 30°$, △ $\theta = 60°$. 30

2.6 Theoretical and experimentally measured unsteady pressures (amplitude $\Delta \hat{P}$ and phase ψ) *versus* oscillation frequency, f, showing the effect of annular flow velocity, U, for $l_0 = 2.59$ and $x = 6.23$; (a) $\theta = 0°$, (b) $\theta = 30°$, (c) $\theta = 45°$ —— present unsteady turbulent analysis, and – – – potential theory of Ref. [5] Experiments: ◯ $U = 52.4$ m/s, ◇ $U = 73.0$ m/s 31

4.1 Mesh generated for the study of fluid flow over backsteps. 45

4.2 Portion of a one dimensional stretched grid. 47

4.3 Schematic representation of the staggered grid used in the spatial differentiation 49

4.4 Evaluation of viscous derivatives near solid walls, where the quantities $u_{t,w}$ and $v_{w,j}$ are defined. 51

5.1 Geometry of the driven cavity flow problem. 62

5.2 Variation of x-component of velocity, u, at cavity center-line, $x = 0.5$, for various Reynolds numbers Re and types of grids. 65

5.3 Convergence history of the rms residuals of the momentum and continuity equations as a function of the iteration count, n. The computations are for the driven cavity flow problem at a Reynolds number $Re = 1\,000$, on a stretched grid. 66

5.4 Geometry of backward-facing step problem. 67

5.5 Pressure profiles along the upper wall and the lower wall of the channel. 72
5.6 Shear stress profiles along the upper wall and the lower wall of the channel. 73
5.7 Variation with y of the x-component of velocity, u. The computations are for $s = 1\,000$, $J = 25$, and three instants within the harmonic cycle have been represented. Comparison is made for (a) $N_t = 9$, and (b) $N_t = 19$. 79
5.8 Variation with y in the x-component of velocity, u. The computations are for $s = 10\,000$, $J = 25$, $N_t = 19$, and three instants within the harmonic cycle have been represented. Comparison is made for (a) $\Delta y_{min} = 0.014$, and (b) $\Delta y_{min} = 0.007$. 80
5.9 Variation with y in the x-component of velocity, u. The computations are for $s = 10\,000$, $J = 51$, $N_t = 19$, and three instants within the harmonic cycle have been represented; Δy_{min} is equal to 0.0063. 81
5.10 Plot of the drag force as a function of time on the oscillating lid 86
5.11 Streamline contours inside the cavity after periodicity has been attained in the flow solution. The times are (a) $t = 8T$, and (b) $t = 8T + 20T/40$. 87
5.12 Streamline contours inside the cavity after periodicity has been attained in the flow solution. The times are (a) $t = 8T + 16T/40$, and (b) $t = 8T + 36T/40$. 88

7.1 Geometry of two-dimensional unsteady annular flow problem. 108
7.2 One-dimensional staggered mesh used to solve the two-dimensional unsteady annular flow problem with the one- and two-harmonic solutions. 115

7.3 Radial profiles of circumferential velocity component w at $\theta = 45°$, for (a) $s = 300$, and (b) $s = 3\,000$. Comparison between the three solutions is made for 5 instants t^n within the harmonic cycle. — full non-linear solution, - - - 2-harmonic solution, and -·- 1-harmonic solution. 128

7.4 Radial profiles of pressure p at $\theta = 3.75°$ for (a) $s = 300$, and (b) $s = 3\,000$. Comparison between the three solutions is made for 5 instants t^n within the harmonic cycle. — full non-linear solution, - - - 2-harmonic solution, and -·- 1-harmonic solution. 129

7.5 Circumferential profiles of circumferential velocity component w at $r = 9.75$, for (a) $s = 300$, and (b) $s = 3\,000$. Comparison between the three solutions is made for 5 instants t^n within the harmonic cycle — full non-linear solution, - - - 2-harmonic solution, and -·- 1-harmonic solution. 130

7.6 Circumferential profiles of pressure p at $r = 9.75$, for (a) $s = 300$, and (b) $s = 3\,000$ Comparison between the three solutions is made for 5 instants t^n within the harmonic cycle. — full non-linear solution, - - - 2-harmonic solution, and -·- 1-harmonic solution. 131

7.7 Comparison of coarse mesh and fine mesh results using the full non-linear solution. Radial profiles of circumferential velocity component w at $\theta = 45°$ are presented for (a) $s = 300$, and (b) $s = 3\,000$, at 5 instants t^n within the harmonic cycle. — fine mesh results, and - - - coarse mesh results. 132

7.8 Comparison of coarse mesh and fine mesh results using the full non-linear solution. Circumferential profiles of circumferential velocity component w at $r = 9.80$ are presented for (a) $s = 300$, and (b) $s = 3000$, at 5 instants t^n within the harmonic cycle. fine mesh results, and - - - coarse mesh results. 133

7.9 Comparison of the fluid force per unit length exerted on the oscillating outer cylinder at (a) $s = 300$, and (b) $s = 3000$ The three solutions are compared and plotted as a function of time full non-linear solution, - - - 2-harmonic solution, and · · 1-harmonic solution. 134

7.10 Comparison of three-point-backward and Crank-Nicolson time-differencing schemes for the time evolution of (a) the circumferential velocity component w, and (b) the pressure p. The Stokes number s is 300. 137

8.1 Three-dimensional annular geometry used for the unsteady flow computations. 139

8.2 Axial variation in the amplitude and phase of pressure, taken at $r = 9.93$, $\theta = 7.5°$, for $Re = 100$ and $s = 10$. 150

8.3 Axial variation in the amplitude and phase of pressure, taken at $r = 9.93$, $\theta = 7.5°$, for $Re = 100$ and $s = 5$. 151

8.4 Axial variation in the amplitude and phase of pressure, taken at $r = 9.93$, $\theta = 7.5°$, for $Re = 100$ and $s = 5$. The mean flow is in the negative axial direction. 152

8.5 Axial variation in the amplitude and phase of pressure, taken at $r = 9.93$, $\theta = 7.5°$, and for $s = 25$. There is no mean axial flow in the annulus. 153

8.6 Axial variation in the amplitude and phase of pressure, taken at $r = 9.93$, $\theta = 7.5°$, and for $s = 300$. There is no mean axial flow in the annulus. 154
8.7 Radial profiles of w taken at $x = 50$, $\theta = 45°$, for $Re = 100$, $s = 5$; amplitude and phase of w are plotted. 155
8.8 Axial variation in the amplitude and phase of pressure, taken at $r = 9.93$, $\theta = 7.5°$, for $Re = 250$, $s = 10$. 156
8.9 Radial profiles of w taken at $x = 50$, $\theta = 45°$, for $Re = 250$, $s = 10$; amplitude and phase of w are plotted. 157
8.10 Axial variation in the amplitude and phase of pressure, taken at $r = 9.93$, $\theta = 7.5°$, for $Re = 250$, $s = 25$. 158
8.11 Radial profiles of w taken at $x = 50$, $\theta = 45°$, for $Re = 250$, $s = 25$; amplitude and phase of w are plotted. 159
8.12 Axial variation in the amplitude and phase of pressure, taken at $r = 9.93$, $\theta = 52.5°$, for $Re = 250$, $s = 25$. 160
8.13 Radial profile of w taken at $x = 1$, $\theta = 45°$, for $Re = 250$, $s = 25$; amplitude and phase of w are plotted. 161
8.14 Comparison of coarse mesh and fine mesh results: axial variation of pressure taken at $r = 9.93$, $\theta = 7.5°$, for $Re = 250$, $s = 25$. 162
8.15 Comparison of coarse mesh and fine mesh results: radial profiles of w taken at $x = 50$, $\theta = 45°$, for $Re = 250$, $s = 25$. 163
8.16 Axial profiles of pressure taken at $r = 9.93$, $\theta = 7.5°$, for $Re = 250$, $s = 25$. Five different instants within the harmonic cycle are represented. 164
8.17 Radial profiles of w taken at $x = 50$, $\theta = 45°$, for $Re = 250$, $s = 25$. Five different instants within the harmonic cycle are represented. . 165

8.18 Axial variation in the amplitude and phase of pressure, taken at $r = 9.93$, $\theta = 7.5°$, for $Re = 100$, $s = 80$. 166
8.19 Radial profiles of w taken at $x = 50$, $\theta = 45°$, for $Re = 100$, $s = 80$, amplitude and phase of w are plotted. 167
8.20 Axial variation of pressure taken at $r = 9.94$, $\theta = 7.5°$, for $Re = 100$, $s = 5$. 174
8.21 Radial profiles of w taken at $x = 23.3$, $\theta = 90°$, for $Re = 100$, $s = 5$. 175
8.22 Axial variation of pressure taken at $r = 9.94$, $\theta = 7.5°$, for $Re = 250$, $s = 10$. 176
8.23 Radial profiles of w taken at $x = 23.3$, $\theta = 90°$, for $Re = 250$, $s = 10$. 177
8.24 Axial variation of pressure taken at $r = 9.94$, $\theta = 7.5°$, for $Re = 250$, $s = 20$. 178
8.25 Radial profiles of w taken at $x = 23.3$, $\theta = 90°$, for $Re = 250$, $s = 20$. 179
8.26 Axial variation of pressure taken on the surface of both the inner and outer cylinders, for $\theta = 7.5°$, $Re = 250$, $s = 20$. . . . 180

9.1 Time evolution of cylinder displacement. (a) Comparison of the potential flow solution with viscous flow solutions computed for three different Reynolds numbers; (b) comparison of numerical and analytical potential flow solutions. 191
9.2 Comparison between potential and viscous flow solutions for the displacement of the oscillating cylinder. (a) $\omega_n = 0.1$, (b) $\omega_n = 1$ 195
9.3 Comparison between potential and viscous flow solutions for the displacement of the oscillating cylinder. (a) $\omega_n = 0.03$, (b) $\omega_n = 0.01$. 196
9.4 Comparison between potential and viscous flow solutions for the displacement of the oscillating cylinder and for $\omega_n = 0.02$. . . . 197

A.1 Schematic representation of the staggered grid used in the spatial discretization of the three-dimensional linearized equations. A-2

A.2 Evaluation of viscous derivatives near solid walls, where $\hat{u}_{i,w}$, $\hat{v}_{w,j}$, $\hat{w}_{i,w}$ and $\hat{w}_{w,j}$ have been defined. A-6

B.1 Schematic representation of the staggered grid used to discretize the two-dimensional non-linear unsteady annular flow equations. B-2

B.2 Evaluation of viscous derivatives near the inner cylinder wall, where the quantity $w_{w,k}$ has been defined. B-5

B.3 Diagram showing the symmetry boundary conditions applied at $\theta = 0$.B-6

List of Tables

5.1 Location, y_{max}, and value, u_{max}, of the maximum recirculating component of velocity, u, for various Reynolds numbers and types of grid. 63

5.2 Rms residual values at convergence for different Reynolds numbers, Re, and types of grids. 64

5.3 Maximum residual values at convergence for different Reynolds numbers, Re, and types of grids. 64

5.4 Cross-channel profiles at $x = 7$ 70

5.5 Cross-channel profiles at $x = 15$ 71

5.6 Values of the parameters used in the computation of the results of Figures 5.7 to 5.9. 77

5.7 Number, k, of pseudo-time steps required to converge at time level t^n, and rms and maximum residual values at convergence. The computations are for the results of Figure 5.9. 82

5.8 Number, k, of pseudo-time steps required to converge at time level t^n and rms and maximum residual values at convergence. The computations are for the results of Figure 5.10 for the unsteady driven cavity flow problem. 89

7.1 Number k of pseudo-time steps required to converge at time level t^n and rms and maximum residual values at convergence. The computations are for the unsteady two-dimensional annular flow at $s = 3.000$, on a 24×24 grid. 135

8.1 Number, k, of pseudo-time steps required to converge at time level t^n, and rms values of residuals at convergence. The computations were performed at $Re = 250$, $s = 25$, with the full non-linear three-dimensional Navier-Stokes equations. 168

8.2 Number, k, of pseudo-time steps required to converge at time level t^n, and rms values of residuals at convergence. The computations were performed at $Re = 250$, $s = 25$, with the linearized three-dimensional Navier-Stokes equations. 169

8.3 Number, k, of pseudo-time steps required to converge at time level t^n, and rms values of residuals at convergence. The computations were performed at $Re = 100$, $s = 80$, with the full non-linear three-dimensional Navier-Stokes equations. 170

9.1 Runge-Kutta scheme applied to the integration of the equation of the structure. 184

Chapter 1

INTRODUCTION

1.1 Flow-induced Vibrations

Vibration problems that have been reported to have occured in different types of industrial installations such as heat exchangers and nuclear reactors have been caused in many cases by fluid flow interacting with the structural components in the equipment concerned. Paidoussis [1] has compiled an interesting account of some of the most frequently encountered problems, and he documented cases in which such problems have occured.

These problems, due to flow-induced vibrations, are the object of ongoing studies, the aim of which is to arrive at a better understanding as to their causes and mechanisms [2].

1.2 Vibration Induced by Annular Flow

One class of problems in which flow-induced vibrations are encountered involves geometries with annular flow, the annular region being delimited by two tubular structures. In the core of the Advanced Gas Cooled Reactor depicted in Figure 1.1

the fuel channels are of this basic geometry.

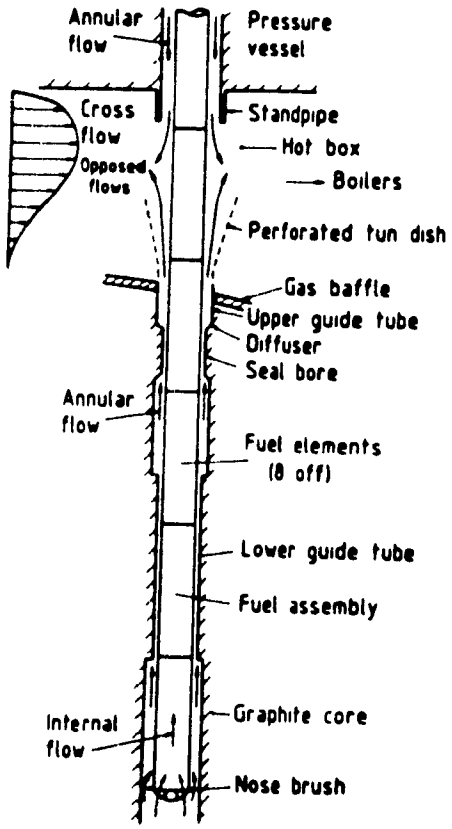

Figure 1.1: Core of Advanced Gas Cooled Reactor showing the annular flow configuration (reprinted from Hobson's [3]).

The inner structure consists in the fuel assembly, whereas the outer body is a graphite core, delimiting a non-uniform annular region in which the coolant flows. Vibrations of the fuel assembly elements caused by the flow of coolant under certain operating conditions (re-fuelling operation) have lowered the performance of the reactor (Hobson [3]). The "control rods", controlling the reaction rates in other types of nuclear reactors, are also annular flow devices, and their problems with regard to flow-induced vibrations have been documented [1].

Studies to explain the mechanisms causing the detrimental vibrations in annular flow configurations have been initiated by Hobson [4], who developed a semi-empirical numerical method in which experimentally determined coefficients supplemented the analytical formulation

An analytical theory that did not require any experimental coefficient was developed by Mateescu & Païdoussis [5]. It was based on potential flow theory and the assumption of smooth variations in the annular flow passage, such that no pronounced viscous flow effects were present (for example no flow separation) They then completed their theory to treat in a simplified manner the unsteady viscous flow effects in the laminar flow regime [6].

Mateescu, Païdoussis & Bélanger [7] then extended this theory by the inclusion of unsteady viscous flow effects in the turbulent regime. The presentation of these results will serve to introduce the topic which is the object of this Thesis, as this work was initiated at the very beginning of the Ph D program Thus, in Chapter 2 the theory [7, 8] used to describe the turbulent phenomenom is presented, along with the experimental tests performed at McGill [9, 10] to validate it. Those experimental tests were carried out on an apparatus which was available at McGill, and the new results thus obtained for the circumferential variation of the unsteady pressure were part of the Ph D work and served to validate the turbulent theory developed concurrently. In this theory, the annular flow passage was supposed to be uniform, and the purpose was to establish theoretical and experimental foundations before tackling more complex configurations The comparison between theory and experiment was good as is shown in Chapter 2

1.3 Modelling of Fluid Forces by the Navier-Stokes Equations

The scope of applicability of the method developed in Refs [7, 8] is limited by the requirement that the annular flow passage is uniform, or that variations in the annular passage width are at least smooth and gradual. The theory expounded in Chapter 2 reduces to the results obtained in Refs [7, 8] for the case of a uniform annular geometry, a different derivation is done in Chapter 2, which permits to envisage the generalization of the method for non-uniform geometries. However, the theory is based on the decomposition of the flow into potential and turbulent parts. In order to generalize the modelling to better take into account geometries in which pronounced diffuser sections or even abrupt discontinuities are present in the annular region, see Figure 1.1, it was decided to model the fluid forces by the direct use of the Navier-Stokes equations, instead of pursuing with the model of Chapter 2. In this case, no assumptions such as flow decomposition are necessary. Indeed, the Navier-Stokes equations can model the viscous effects present in the more general configurations involving flow recirculation.

In order to develop a methodology, the first step undertaken was the treatment of problems in the laminar flow regime, in which case the Navier-Stokes equations can be solved accurately by numerical methods without the need for incorporating a turbulence model in the equations. Thus, the theory of Chapter 2 will be pursued no further in this thesis, and Chapter 2 will conclude the treatment of unsteady turbulent flows. The inclusion of the work of Chapter 2 serves to present the interesting results that have been obtained in the first stage of the Ph.D. program, namely the development of a method determining the unsteady pressure in turbulent flow and its validation on an already existing experimental

apparatus having a uniform annular gap however, in order to develop more general methods dealing with complex geometries a new approach was initiated, namely the solving of the Navier-Stokes equations

The difficulty with that approach is that the fluid forces acting on the structure cannot be determined explicitly in terms of the dynamical parameters describing the structural motion, such as velocity Indeed, the complexity of the Navier-Stokes equations makes it impossible to obtain closed-form expressions for the fluid forces for given boundary conditions and geometry, except in the simplest of cases.

The solution to that difficulty is to treat fluid-structure interaction problems in an interactive manner the equation governing the dynamical behaviour of the structure is integrated simultaneously with the Navier-Stokes equations to obtain the temporal evolution of the structural motion The unsteady fluid forces acting on the structure are determined as a function of the velocity of the structure at the fluid-structure interface Conclusions with regard to stability can thus be reached as it is seen whether the structure has an oscillatory (flutter) instability or one of the divergence type. The study of the stability of a fluid-structure system by this method will serve as a conclusion to the present Thesis, and the results will be presented in Chapter 9.

Before this, however, there is yet a challenging aspect to the problem to consider the accurate time-integration of the unsteady Navier-Stokes equations This problem is central to the present approach, and will be introduced first The integration of the equations is done using a numerical method, specifically the finite difference method is used to discretize the spatial differential operators appearing in the equations However, the equations also have to be integrated in time, and a new method has been developed to accomplish that efficiently, it is presented in Chapters 3 to 8.

The Navier-Stokes equations considered describe the motion of an incompressible fluid, which is the case of practical interest for most problems in flow-induced vibrations. *Steady state* solutions to these equations in the laminar flow regime have been obtained by various methods. Chorin [11] has introduced the method of "artificial compressibility", in which the continuity equation is augmented by a pressure time-derivative term which allows to use time-marching solution techniques to solve the system of equations as a whole. Indeed, the system of incompressible Navier-Stokes equations contains a time derivative of velocity in the momentum equation, but no time derivative term in the continuity equation, and special procedures are needed to implement time-marching solution techniques. Chorin's method is one of them; however, it is applicable only to steady state flow solutions

Another method for solving the incompresible Navier-Stokes equations was originally developed by Harlow & Welch [12]. It is a pressure-correction type method, and variants of which, called projection method and fractional step method, have subsequently been developed [13, 14, 15] It requires the iterative solution of a Poisson equation to obtain corrections to a guessed pressure field. It can be applied to the solution of both the steady and unsteady incompressible flow equations, which is an advantage over Chorin's artificial compressibility method. However, the latter is believed to be more efficient when it comes to obtaining only steady state solutions

Soh & Goodrich [16] have developed a method for solving the *unsteady* flow equations which goes along the lines of the artificial compressibility method. An artificial time-derivative of pressure is added to the continuity equation, after the momentum equation has been time-discretized and put in delta-form. A pseudo-time relaxation procedure is introduced thereafter The formulation was complicated and rendered necessary the introduction of simplifications in the solution

process. Indeed, the way time increments in the flow parameters are defined makes for a cumbersome treatment of the non-linear convective terms. Also, the time-discretization scheme they chose did not resolve well the time-evolution solution for pressure: numerical experiments conducted at McGill by the present author revealed the presence of numerically-induced oscillations.

The present work has remedied these difficulties. The method of artificial compressibility has been extended to solve unsteady incompressible viscous flow problems in straightforward fashion. The equations are put in delta-form *after* performing the time discretization of the momentum equation and introducing the pseudo-time relaxation scheme, not before as in Ref. [16]. This allows to use the already existing time-marching solution techniques in standard manner, in particular, Approximate Factorization and Alternating Direction Implicit methods are implemented along the exact same lines as in the case of the method of artificial compressibility applied to the solution of steady flow problems [17]. Furthermore, the time-discretization of the momentum equation is corrected in order to better resolve the flow quantities and fluid forces, which results in the introduction of the three-point backward implicit time-differencing scheme.

The thesis contents can thus be summarized as follows. In Chapter 2 the simplified theory is first introduced, which takes into account the unsteady viscous effects in the turbulent flow regime; it is applied to the case of a uniform annular geometry. Theory and experiment are compared and the agreement is shown to be good. Then, the extension of the flow theories to generalize their scope of applicabilty to more general configurations is the object of the other chapters, where the treatment is for unsteady viscous laminar flow.

First, the method of artificial compressibility, as extended to also perform the time-accurate integration of the unsteady incompressible Navier-Stokes equations is presented [18]. The time-differencing scheme adopted is introduced in Chapter 3,

and in Chapters 4 and 5 the theory is validated by applying it to some steady and unsteady flow problems in Cartesian coordinates; the finite difference method used to discretize the spatial differential operators is described therein. The remaining chapters apply the theory to the study of unsteady annular flow problems.

In Chapter 6, the solution technique adapted to cylindrical coordinates is described, in particular, linearized forms of the equations are introduced by using the Galerkin method in which the basis functions are Fourier series expressed in terms of the circumferential coordinate This is in fact a hybrid finite difference/ Fourier expansion method which allows to obtain unsteady flow solutions in a very efficient manner, as three-dimensional domains (meshes) become two-dimensional. Chapter 7 gives the particular forms of the equations as well as numerical solutions for a two-dimensional unsteady annular flow problem. There it is demonstrated that the three-point-backward time-differencing scheme which has been introduced in Chapter 3 is superior to the Crank-Nicolson sheme Chapter 8 presents numerical solutions for more general three-dimensional configurations, in particular the unsteady Navier-Stokes equations are resolved on a three-dimensional mesh.

Up to this point in the thesis, the unsteady viscous flow solutions have been obtained by forced-vibration numerical experiments. In Chapter 9, the time-integration scheme developed for the Navier-Stokes equations is combined with the equation governing the dynamical behavior of a structure in order to perform the fluid-structure stability analysis of this system in the time domain.

Finally, Chapter 10 gives the main conclusions arrived at in the Thesis

Chapter 2

UNSTEADY TURBULENT EFFECTS IN UNIFORM ANNULAR GEOMETRY

2.1 Equations of Motion

The geometry for the problem treated in this chapter is shown in Figure 2.1 The present analysis considers the turbulent flow of an incompressible fluid in the narrow annular space formed between a cylindrical duct and a coaxially mounted central cylinder of radius a. The inner radius of the duct is $a+H = a(1+h)$, where the relative annular gap $h = H/a$ is generally small The rigid cylindrical center-body of length $L = al$ is considered to execute angular oscillations about a hinge A situated at a distance $L_o = a\ l_o$ from the upstream end of the cylinder, which is the origin of a cylindrical system of coordinates (X, R, θ) For convenience, the nondimensional cylindrical coordinates $x = X/a$, $r = R/a$ and θ will be used, instead of the dimensional ones, in the formulation of the problem, and the

corresponding unit basis vectors are denoted by $\mathbf{e}_x$, $\mathbf{e}_r$ and $\mathbf{e}_\theta$.

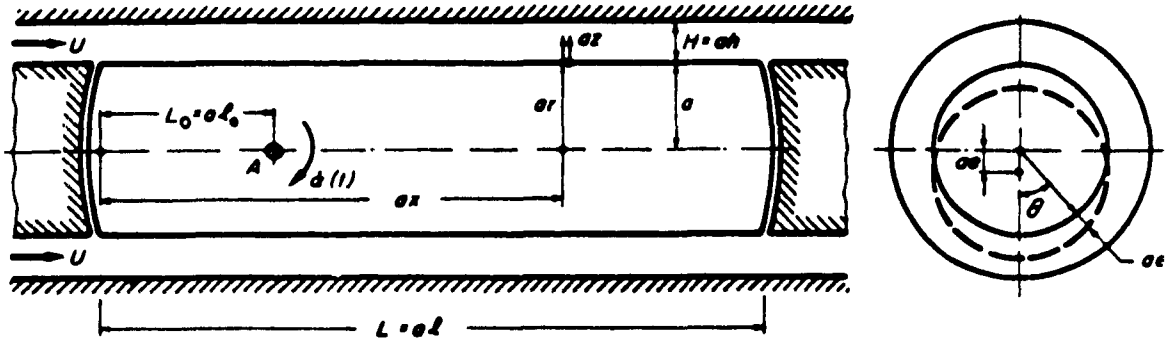

Figure 2.1: Geometry of the oscillating center-body in the cylindrical duct.

We note that the characteristic length used to non-dimensionalize the equations in this chapter is taken to be a, the radius of the inner cylinder; in all subsequent chapters where flow in annular geometry is considered the annular gap width, H, will be chosen instead.

Two long fixed cylinders of the same radius a are situated upstream and downstream of the inner cylinder to regularize the flow in the annulus, and the mean axial flow velocity is denoted by U, see Figure 2.1, where U is used as the characteristic velocity.

Considering a harmonic oscillatory motion of the rigid cylinder, the angular and lateral displacements of the center-body axis can be expressed in the complex form

$$\alpha(t) = \alpha_o e^{i\omega t}, \qquad E(x,t) = a\,e(x,t) = a(x - l_o)\,\alpha_o e^{i\omega t},$$

where ω and t represent the nondimensional frequency and time, which are defined in terms of the dimensional time T and circular frequency Ω ($\Omega = 2\pi f$) as

$$\omega = \Omega\, a/U, \quad t = UT/a.$$

The nondimensional radial displacement, $e_r = E_r/a$, of the center-body surface at any azimuthal position θ (Figure 2.1) is

$$e_r(x,\theta,t) = (x - l_o)\ \alpha_o\ \cos\theta\ e^{i\omega t}.$$

In the present analysis, the flow in the narrow annulus is considered to be a fully developed turbulent flow, and the unsteady turbulent effects on the dynamics of the center-body will be determined. No steady effects of the turbulent flow, such as pressurization (Ref. [19]), are included since these do not affect the dynamics of the rigid center-body (Ref. [20]). We remark in passing that the geometry of Figure 2.1 is aimed at idealizing certain aspects of annular flow configurations and serves in a first approach to gauge the parameters governing annular flow.

The equations governing the motion of an incompressible viscous fluid are the Navier-Stokes equation of momentum and the equation of conservation of mass,

$$\frac{\partial \tilde{\mathbf{V}}}{\partial t} + \boldsymbol{\nabla}\cdot\tilde{\mathbf{V}}\tilde{\mathbf{V}} + \boldsymbol{\nabla}\tilde{p} - \frac{2h}{Re}\nabla^2\tilde{\mathbf{V}} = \mathbf{0}, \tag{2.1}$$

$$\boldsymbol{\nabla}\cdot\tilde{\mathbf{V}} = 0. \tag{2.2}$$

They are in non-dimensional form and $Re = 2HU/\nu$ represents the Reynolds number defined in terms of the hydraulic diameter, $D_h = 2H = 2ah$, and the characteristic velocity, U. ν is the fluid kinematic viscosity, $\tilde{\mathbf{V}}$ the velocity vector and $\tilde{p}$ the pressure. Since we are considering turbulent flows, we make the usual assumption that the term $-(2h/Re)\nabla^2\tilde{\mathbf{V}}$ in the equation of momentum conservation can be dropped.

To solve equations (2.1) and (2.2) and obtain the unsteady turbulent flow effects, we proceed in the following manner. We assume that the flow, including the mean flow and the perturbations induced by the oscillating center-body which are superposed on it, is basically a potential flow, and we denote by $\mathbf{V}$ and p

those potential flow contributions to the flow picture. However, the presence of turbulence in the flow is modelled, as is usually done for turbulent flows, by the introduction of a fluctuating velocity component, $\mathbf{v}'$, and a fluctuating pressure component, p'

At this stage, we have to observe that the unsteady turbulent flow considered is characterized by two distinct scales of time-dependence: (i) a macroscale associated with the oscillatory motion of the center-body, and (ii) a microscale associated with the turbulent fluctuations of the flow parameters. The microscale time-dependence is modelled by $\mathbf{v}'$ and p', which are the usual fluctuating quantities introduced by Reynolds [21] for the study of turbulent flows. The time average of both $\mathbf{v}'$ and p' is zero:

$$\overline{\mathbf{v}'} = \frac{1}{2T}\int_{-T}^{T} \mathbf{v}'(t+\tau)\, d\tau = \mathbf{0}\,, \qquad \frac{1}{2T}\int_{-T}^{T} p'(t+\tau)\, d\tau = 0\,, \tag{2.3}$$

where an overbar here denotes a time-averaged quantity and where the period of time, $2T$, during which time-averaging is performed is of the microscale order; T is necessarily smaller than the macroscale period associated with center-body-induced flow perturbations

Thus, the flow quantities $\tilde{\mathbf{V}}$ and $\tilde{p}$ are separated into the following components:

$$\tilde{\mathbf{V}} = \mathbf{V} + \mathbf{v}'\,, \qquad \tilde{p} = p + \Pi + p'\,, \tag{2.4}$$

where $\mathbf{V}$ and p represent the potential flow contributions, including the oscillation-induced perturbation flow field, $\mathbf{v}'$ and p' are the fluctuating, or "eddy" components which account for turbulence at the microscale level, and Π is a macroscale unsteady turbulent pressure. The particular point about Π is that its time average is not zero; indeed, it accounts in a "time-averaged", macroscale sense for the pres-

ence of turbulence, which is modelled at the microscale by $\mathbf{v}'$ and p'[1]. Thus, we will denote the time-averaged turbulent pressure, $\overline{\Pi}$, by p_t:

$$p_t = \frac{1}{2T}\int_{\tau=-T}^{T} \Pi(t+\tau)\, d\tau \,. \tag{2.5}$$

We note that in the macroscale sense we consider that $\overline{\mathbf{V}} = \mathbf{V}$, $\overline{p} = p$, for the potential flow contributions, such that the pressure on the surface of the oscillating cylinder is given by

$$\overline{\tilde{p}} = p + p_t \,. \tag{2.6}$$

In summary, the quantities $\mathbf{v}'$, Π and p' account for the presence of turbulence in the flow and in this study they are superposed on an inviscid flow field, instead of a "viscous" one.

Thus, equation (2.4) is substituted into (2.1) and (2.2), and the potential flow contribution is extracted to obtain the following two sets of equations:

$$\frac{\partial \mathbf{V}}{\partial t} + \mathbf{V}\cdot\boldsymbol{\nabla}\mathbf{V} + \boldsymbol{\nabla}p = \mathbf{0} \,, \tag{2.7}$$

$$\boldsymbol{\nabla}\cdot\mathbf{V} = 0 \,, \tag{2.8}$$

$$\frac{\partial \mathbf{v}'}{\partial t} + \boldsymbol{\nabla}\cdot\{\mathbf{v}'(\mathbf{V}+\mathbf{v}') + \mathbf{V}\mathbf{v}'\} + \boldsymbol{\nabla}(\Pi + p') = \mathbf{0} \,, \tag{2.9}$$

$$\boldsymbol{\nabla}\cdot\mathbf{v}' = 0 \,. \tag{2.10}$$

[1] In the original presentation of this work [7], a viscous contribution, namely $\mathbf{v}_v$, had also been included in the decomposition of the velocity vector, i.e. we had $\tilde{\mathbf{V}} = \mathbf{V} + \mathbf{v}_v + \mathbf{v}'$, instead of (2.4). A discussion of the implications of this decomposition is made in the conclusion of this chapter, Section 2.5.

As pointed out earlier, the term $-(2h/Re)\nabla^2\tilde{\mathbf{V}}$ has been dropped from the equations. Also, in equation (2.7) the writing of the convective term in that form comes from identity $\boldsymbol{\nabla}\cdot\mathbf{VV} = (\boldsymbol{\nabla}\cdot\mathbf{V})\mathbf{V} + \mathbf{V}\cdot\boldsymbol{\nabla}\mathbf{V}$, combined with (2.8). The solution to equations (2.7) and (2.8) for the potential flow contribution is given in Section 2.2, whereas the turbulent flow solution of equations (2.9) and (2.10) is detailed in Section 2.3. Then, Section 2.4 shows how to combine the potential flow and turbulent flow contributions in order to obtain the unsteady pressure; it also gives the comparison of the theoretical results thus obtained with experimental results.

2.2 Solution of Unsteady Potential Flow

The potential flow solution has previously been obtained in Refs [7, 20], and we summarize here the results that are used in the present approach, namely the solution as applied to a uniform annular gap geometry. We obtain the inviscid contribution, p, to the unsteady pressure by linearized potential flow theory. It is thus assumed that there is a steady mean flow in the annulus, which in the present case is uniform and of magnitude U (or 1 in non-dimensional form), and the perturbations in the mean flow introduced by the oscillations of the center-body are small.

Then, in the case of potential flow, the fluid velocity derives from a velocity potential, $\Phi = Ua(\phi + x)$, where ϕ is the perturbation potential which satisfies $|\boldsymbol{\nabla}\phi| \ll 1$, in view of the small perturbation assumption. The dimensionless velocity vector $\mathbf{V}$ in (2.4) is consequently given by

$$\mathbf{V} = 1\cdot\mathbf{e}_x + \boldsymbol{\nabla}\phi = \left(1 + \frac{\partial\phi}{\partial x}\right)\mathbf{e}_x + \frac{\partial\phi}{\partial r}\,\mathbf{e}_r + \frac{1}{r}\frac{\partial\phi}{\partial\theta}\,\mathbf{e}_\theta\,, \tag{2.11}$$

and upon substituting (2.11) into (2.8), we obtain a Laplace equation in ϕ:

$$\nabla^2\phi = \frac{\partial^2\phi}{\partial x^2} + \frac{\partial^2\phi}{\partial r^2} + \frac{1}{r}\frac{\partial\phi}{\partial r} + \frac{1}{r^2}\frac{\partial^2\phi}{\partial\theta^2} = 0\ . \tag{2.12}$$

Equation (2.7), which is Euler's equation of motion, is then integrated to obtain the perturbation form of the Bernoulli-Lagrange equation, namely

$$p = -\left[\frac{\partial\phi}{\partial t} + \frac{\partial\phi}{\partial x} + \frac{1}{2}(\nabla\phi)^2\right]\ ,$$

where p is the unsteady pressure perturbation corresponding to the potential (inviscid) annular flow.

The solution to Laplace equation (2.12) has been obtained in Ref [5] for the general case of an axially variable annular passage by considering a convenient Fourier expansion of the boundary condition on the oscillating center-body, in the form

$$\begin{aligned}\left.\frac{\partial\phi}{\partial r}\right|_{r=1} &= \frac{\partial e_r}{\partial t} + \frac{\partial e_r}{\partial x} = \left[(x - l_0)\frac{d\alpha}{dt} + \alpha(t)\right]\cos\theta \\ &= \left\{\frac{d\alpha}{dt}\left[\sum_{k=0}^{N} D_k \cos c_k x + \sum_{k=1}^{N} E_k \sin c_k x\right] + \alpha(t)\right\}\cos\theta,\end{aligned}$$

where D_k and E_k are the Fourier coefficients of the expansion and $c_k = 2\pi k/l$. Introducing a new nondimensional coordinate, z, across the annular passage,

$$z = \frac{R - a}{a} = r - 1, \tag{2.13}$$

the solutions for ϕ and p on the cylinder surface ($z = 0$) in the case of a narrow uniform annulus are obtained as

$$\begin{aligned}\phi(x, 0, \theta, t) &= \alpha(t)\ \{(1 + i\omega D_0)\, G_0(h) \\ &+ i\omega \sum_{k=1}^{N} G_k(h)\,[D_k \cos c_k x + E_k \sin c_k x]\Big\}\ \cos\theta,\end{aligned}$$

$$\begin{aligned} \phi(r,0,\theta,t) &= \alpha(t)\left\{\left(\omega^2 D_0 - i\omega\right)\, G_0(h) + \sum_{k=1}^{N} G_k(h)\left[\omega^2\left(D_k\cos c_k x + E_k \sin c_k x\right)\right.\right. \\ &+ \left.\left. i\omega c_k\left(D_k \sin c_k x - E_k \cos c_k x\right)\right]\right\}\cos\theta\,, \end{aligned} \tag{2.14}$$

where

$$G_k(h) = -\frac{4q_k}{q_k^2-1}\,\frac{1}{e^{q_k h}-1} - \frac{2}{q_k+1}, \quad q_k = \sqrt{5+4c_k^2}. \tag{2.15}$$

A simplified unsteady potential solution was also obtained in Ref. [5], which is based on the slender body assumption, and the solutions for ϕ and p are obtained in the following closed forms:

$$\begin{aligned} \phi(x,z,\theta,t) &= -\frac{g(h-z)}{g'(h)}\left[(x-l_0)\frac{d\alpha}{dt} + \alpha(t)\right]\cos\theta\,, \\ p(x,0,\theta,t) &= \frac{g(h)}{g'(h)}\left[(x-l_0)\frac{d^2\alpha}{dt^2} + 2\,\frac{d\alpha}{dt}\right]\cos\theta\,, \end{aligned} \tag{2.16}$$

where

$$g(h-z) = \frac{2}{q+1}e^{\frac{1}{2}(q+1)(h-z)} + \frac{2}{q-1}\,e^{-\frac{1}{2}(q-1)(h-z)}\,, \quad q=\sqrt{5}\,, \tag{2.17}$$

$$g'(h) = e^{\frac{1}{2}(q+1)h} - e^{-\frac{1}{2}(q-1)h}. \tag{2.18}$$

This solution will be used in the next section in the derivation of the turbulent perturbation solution.

2.3 Solution of Unsteady Turbulent Flow

The procedure used to solve equations (2.9) and (2.10) is the one usually used for turbulent flows, in which the microscale fluctuations are averaged out. Thus, we time-average (2.9) and (2.10) as

$$\frac{1}{2T}\int_{\tau=-T}^{T}\left[\left\{\frac{\partial \mathbf{v}'}{\partial t}+\boldsymbol{\nabla}\cdot\{\mathbf{v}'(\mathbf{V}+\mathbf{v}')+\mathbf{V}\mathbf{v}'\}+\boldsymbol{\nabla}(\Pi+p')\right\}(t+\tau)\right]d\tau = \mathbf{0}\,,$$

$$\frac{1}{2T}\int_{\tau=-T}^{T}[\boldsymbol{\nabla}\cdot\mathbf{v}'(t+\tau)]\,d\tau = 0\,,$$

where all the vectors are functions of $(t+\tau)$. Now, by making use of (2.3) and (2.5) these last two equations can be rewritten as

$$\boldsymbol{\nabla}\cdot\overline{(\mathbf{v}'\mathbf{V}+\mathbf{v}'\mathbf{v}'+\mathbf{V}\mathbf{v}')}+\boldsymbol{\nabla}p_t = \mathbf{0}\,. \tag{2.19}$$

$$\boldsymbol{\nabla}\cdot\overline{\mathbf{v}'} = 0 \tag{2.20}$$

We note from (2.3) that the continuity equation (2.20) is automatically satisfied. Also, if we assume that the velocity components $\mathbf{V}$ and $\mathbf{v}'$ are uncorrelated, which is reasonable, we obtain $\overline{\mathbf{V}\mathbf{v}'}=\overline{\mathbf{V}}\,\overline{\mathbf{v}'}=\mathbf{0}$. Then (2.19) reduces to

$$\boldsymbol{\nabla}p_t = -\boldsymbol{\nabla}\cdot\left(\overline{\mathbf{v}'\mathbf{v}'}\right) \tag{2.21}$$

Here, we have that the term $-\overline{\mathbf{v}'\mathbf{v}'}$ represents the turbulent Reynolds stresses [21], equation (2.21) is written, in component form, as

$$\begin{aligned}\boldsymbol{\nabla}p_t &= \hat{\mathbf{e}}_x\left[\frac{\partial(-\overline{u'^2})}{\partial x}+\frac{\partial(-\overline{u'v'})}{\partial r}+\frac{\partial(-\overline{u'w'})}{r\,\partial\theta}+\frac{-\overline{u'v'}}{r}\right]\\ &+ \hat{\mathbf{e}}_r\left[\frac{\partial(-\overline{u'v'})}{\partial x}+\frac{\partial(-\overline{v'^2})}{\partial r}+\frac{\partial(-\overline{v'w'})}{r\,\partial\theta}+\frac{-\overline{v'^2}+\overline{w'^2}}{r}\right]\\ &+ \hat{\mathbf{e}}_\theta\left[\frac{\partial(-\overline{u'w'})}{\partial x}+\frac{\partial(-\overline{v'w'})}{\partial r}+\frac{\partial(-\overline{w'^2})}{r\,\partial\theta}+2\,\frac{-\overline{v'w'}}{r}\right],\end{aligned} \tag{2.22}$$

where u', v' and w' are the components of the turbulent velocity fluctuations in the x-, r- and θ-directions. The different terms in the Reynolds stresses $-\overline{\mathbf{v}'\mathbf{v}'}$ in (2.22) are known to be all of the same order of magnitude [21].

Since the gap is small, $h \ll r$, we have $\partial/\partial x \ll \partial/\partial r$, $\partial/r\,\partial\theta \ll \partial/\partial r$, and we retain only the partial derivatives with respect to r in (2.22); also, we are interested in the pressure on the surface of the inner cylinder where the Reynolds stresses are zero. Equation (2.22) thus reduces to

$$\boldsymbol{\nabla} p_t = \mathbf{e}_r \frac{\partial(-\overline{u'v'})}{\partial z} + \hat{\mathbf{e}}_\theta \frac{\partial(-\overline{v'w'})}{\partial z} = \frac{1}{\rho U^2} \frac{\partial \boldsymbol{\tau}_w}{\partial z}, \tag{2.23}$$

where $z = r - 1$ is the nondimensional coordinate across the annular gap introduced in (2.13), and we have denoted $\boldsymbol{\tau}_w = -\rho U^2(\mathbf{e}_x\,\overline{u'v'} + \mathbf{e}_\theta\,\overline{v'w'})$ as the dimensional turbulent stress vector in the plane tangent to the surface of the cylinder. Hence we note that the radial component of the pressure gradient is omitted from the equation since, as we will see below, we are only interested in $\boldsymbol{\nabla} p_t$ in the plane tangent to the surface of the oscillating center-body, as the unsteady turbulent pressure, p_t, will be obtained by integrating the circumferential component of $\boldsymbol{\nabla} p_t$ over the perimeter of the cylinder.

For this channel-type flow, the turbulent stress vector $\boldsymbol{\tau}_w$ can be expressed, using an eddy viscosity model for the Reynolds stresses [21], in the form

$$\frac{\boldsymbol{\tau}_w}{\rho} = U^2\left[\hat{\mathbf{e}}_x(-\overline{u'v'}) + \hat{\mathbf{e}}_\theta(-\overline{v'w'})\right] = \hat{\mathbf{e}}_x\,\varepsilon\frac{\partial(Uu)}{\partial(az)} + \hat{\mathbf{e}}_\theta\,\varepsilon\frac{\partial(Uw)}{\partial(az)} = \varepsilon\frac{\partial(U\mathbf{W})}{\partial(az)}, \tag{2.24}$$

where ε is the turbulent eddy viscosity, and $\mathbf{W} = \hat{\mathbf{e}}_x\,u + \hat{\mathbf{e}}_\theta\,w$; u and w are the velocity components in the axial and circumferential directions which, in the general case of equation (2.24), are the macroscale, time-averaged "viscous" components. However, in this study we now show how the potential flow solution comes into play to supplement the information supplied by the u and v velocity profiles.

Proceeding in a similar manner as Ref. [6] for the case of unsteady laminar flow, let us consider the average values across the annular gap of the nondimensional axial and circumferential velocity components, u and w, defined as

$$\bar{u}(x,\theta,t) = \frac{1}{h}\int_0^h u(x,z,\theta,t)dz,$$
$$\bar{w}(x,\theta,t) = \frac{1}{h}\int_0^h w(x,z,\theta,t)dz, \qquad (2\ 25)$$

and let us denote by $\overline{\mathbf{W}} = \hat{\mathbf{e}}_x\,\bar{u} + \hat{\mathbf{e}}_\theta\,\bar{w}$ the average velocity of the fluid across the gap, where the radial component is omitted.

One should note that $\overline{W} \simeq 1$ (or, dimensionally, $U\overline{W} \simeq U$) in the assumption of small amplitude oscillations of the cylinder; at the same time one can consider that the velocity profiles across the gap are similar for the velocity components u and w, in which case

$$\frac{w}{W} = \frac{\bar{w}}{\overline{W}} = \sin\beta \simeq \bar{w}\ , \qquad (2\ 26)$$

where $\beta(x,\theta,t)$ is the angle made by the average velocity across the gap, $\overline{\mathbf{W}}$, with the x-axis, see Figure 2.2.

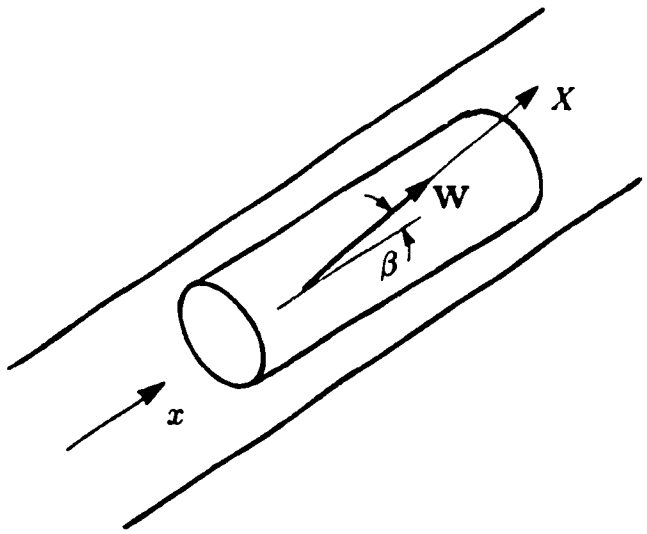

Figure 2.2: Direction, β, of the flow velocity, W, in the annular space, in the plane tangent to the surface of the center-body and along the coordinate X.

Hence, the average velocity of the fluid across the gap, $\overline{\mathbf{W}}$, remains practically constant in magnitude ($\overline{W} \approx 1$), while its direction, defined by the angle $\beta(x,\theta,t)$, oscillates in time with the frequency of the center-body oscillation. In this treatment of unsteady turbulent effects, the quantity $\sin\beta$ is precisely determined using the unsteady potential flow solution of Section 2.2. Upon considering equations (2.11), (2.25) and (2.26), we thus obtain

$$\sin\beta \simeq \bar{w}(x,\theta,t) = \frac{1}{h}\int_0^h \frac{1}{1+z}\frac{\partial\phi}{\partial\theta}\,dz. \tag{2.27}$$

Using the slender-body solution of the potential given by (2.16), $\sin\beta$ is obtained by integrating (2.27):

$$\sin\,\beta = B(x,t)\sin\,\theta, \tag{2.28}$$

where

$$\begin{aligned} B(x,t) &= \frac{1}{h}\frac{g_1(h)}{g'(h)}\left[\frac{d\alpha}{dt}(x-l_0)+\alpha(t)\right], \qquad (2.29)\\ g_1(h) &= \frac{4}{(q+1)^2}\,e^{\frac{1}{2}(q+1)h} - \frac{4}{(q-1)^2}\,e^{-\frac{1}{2}(q-1)h} + \frac{16q}{(q^2-1)^2}\;; \end{aligned}$$

$g'(h)$ and q are defined in (2.17) and (2.18) and we have considered that $h \ll 1$.

Hence, denoting by X the nondimensional coordinate instantaneously aligned with the direction of the gap-average velocity $\overline{\mathbf{W}}$, where $\overline{\mathbf{W}}$ makes an angle β with repect to the x-axis (Figure 2.2), equation (2.23) can be written in the scalar form

$$\frac{\partial p_t}{\partial X} = \frac{1}{\rho U^2}\frac{\partial \tau_w}{\partial z}.$$

Observing that the angle β is small ($\cos\beta \simeq 1$, $\tan\beta \simeq \sin\beta$) in the case of small amplitude oscillations of the cylinder, the scalar projection of (2.23) in the cylindrical system of coordinates leads to

$$\frac{\partial p_t}{\partial x} = \frac{1}{\rho U^2}\frac{\partial \tau_w}{\partial z}\cos\beta \simeq \frac{\partial p_t}{\partial X},$$
$$\frac{\partial p_t}{\partial \theta} = \frac{1}{\rho U^2}\frac{\partial \tau_w}{\partial z}\sin\beta \simeq \frac{\partial p_t}{\partial X}B(x,t)\sin\theta\,, \qquad (2.30)$$

where the expression for $\sin\beta$ from (2.28) has been used.

Now, in order to complete the solution, the value of $\partial p/\partial X \simeq \partial p/\partial r$ has to be found. One can use simplified models of turbulence for channel flows, such as Prandtl's mixing length theory, von Karman's similarity rule, or the simple $(1/n)$th-power law rule describing the turbulent velocity profile. Comparable results were obtained using either methods, and the power law rule has been preferred here since the results can be expressed in simpler form, similar to that obtained for laminar unsteady flows (Ref. [6]).

For the narrow channel-type flow under consideration, the power law for the velocity distribution in a half-height channel is expressed as

$$\frac{UW}{u_\tau} = C\left(\frac{u_\tau}{\nu}az\right)^{1/n}, \qquad (2.31)$$

where $u_\tau = \sqrt{\tau_w/\rho}$ is the wall friction velocity, $\nu = \mu/\rho$ is the kinematic viscosity, and where the constant C and exponent n depend on the Reynolds number of the flow. The coordinate z has been introduced in (2.13) and is measured from the oscillating center-body surface. Equation (2.31) is valid from between $z = 0$ to $z = h/2$. The gap-averaged velocity $U\overline{W}$ calculated from (2.31) is

$$\frac{U\overline{W}}{u_\tau} = \frac{2}{h}\int_0^{h/2} C\left(\frac{u_\tau}{\nu}az\right)^{1/n} dz = \frac{n}{n+1}C\left(\frac{u_\tau a}{\nu}\frac{h}{2}\right)^{1/n}. \qquad (2.32)$$

Applying now the momentum equation to an infinitesimal volume of the annular gap, corresponding to an elemental angle $d\theta$ and length $d(aX)$, defined over the whole height of the gap, one obtains

$$\rho U^2 \frac{\partial p_t}{\partial X} = -\frac{2}{h}\,\tau_w = -\frac{2}{h}\,\rho\,u_\tau^2. \tag{2.33}$$

Combining (2.32) and (2.33) and observing that $U\overline{W} \simeq U$, as discussed above, one obtains

$$\frac{\partial p_t}{\partial X} = -\frac{K}{h}\,Re^{-2/(n+1)}, \quad \text{where } K = 2\left[4^{1/n}\,\frac{n+1}{n}\,\frac{1}{C}\right]^{2n/(n+1)}. \tag{2.34}$$

Considering $n = 7$ and $C = 8.56$ (specified by Blasius), which provides good results for turbulent flows with $Re \leq 10^5$ as shown in Ref [21], the resultant value of the above constant is $K = 0.084$

The turbulent pressure perturbation can now be obtained by substituting (2.34) into (2.30) and integrating with respect to θ, leading to

$$p_t = p_{t_0}(x) + \frac{K}{h} Re^{-2/(n+1)}\,B(x,t)\cos\theta, \tag{2.35}$$

where

$$\frac{dp_{t_0}}{dx} = -\frac{K}{h}\,Re^{-2/(n+1)}.$$

This is the turbulent pressure, p_t, on the surface of the oscillating centerbody, which now has to be combined with the potential flow pressure, p, in order to obtain the total pressure as per equation (2.6). This is done in the next section where the theoretical method is also compared with experiments.

We note in passing that the formalism adopted here permits to envisage the generalization of the method to treat problems with more complex geometries, not limited to uniform annular gaps Indeed, the equation obtained, equation (2.21), is valid even when non-uniform, smooth geometries are considered. Then, it is realized that potential flow theory comes into play

to determine the perturbations in the steady mean flow; once the wall shear stress associated with the steady mean flow is known, it is projected on the wall according to the instanteneous mean velocity vector in the annulus, which is expressed by (2.30), and the unsteady turbulent pressure contribution p_t can be obtained. In the present problem, the wall shear stress was determined by means of equations (2.31)-(2.34), using results particular to channel flows. In the general case, it could be calculated numerically.

2.4 Theoretical Results Compared with Experiments

2.4.1 Theoretical solution

In order to compare the theoretical results with experiments, we need the pressure difference between two points diametrically situated with respect to the plane of oscillation, at the same cross-sectional plane of constant x. Applying (2.6), this pressure difference is defined in terms of the potential and turbulent pressure contributions as

$$\Delta P(x,\theta,t) = \rho U^2 \left[p(x,\theta,t) + p_t(x,\theta,t) - p(x,\pi-\theta,t) - p_t(x,\pi-\theta,t)\right] .$$

Considering (2.14) and (2.35), the dimensional differential pressure ΔP can be expressed in the form

$$\Delta P(x,\theta,t) = 2\rho U^2 \alpha_0 \left[\hat{P}_R(x) + \imath\omega\hat{P}_I(x)\right] \cos\theta \, e^{\imath\omega t} , \qquad (2.36)$$

where

$$\hat{P}_R(x) = \omega^2 D_0 G_0(h) + \omega^2 \sum_{k=1}^{N} G_k(h)\ [D_k \cos c_k x + E_k \sin c_k x] + \frac{K}{h^2}\ \frac{g_1(h)}{g'(h)}\ Re^{-2/(n+1)}, \tag{2.37}$$

$$\hat{P}_I(x) = -G_0(h) + \sum_{k=1}^{N} c_k G_k(h)\ [D_k \sin c_k x - E_k \cos c_k x] + \frac{K}{h^2}\ \frac{g_1(h)}{g'(h)}\ (x - l_0)\ Re^{-2/(n+1)}. \tag{2.38}$$

The Fourier coefficients D_k and E_k have been computed using Fast Fourier Transform [20].

In order to facilitate the comparison with the experimental results obtained in terms of the measured amplitude and phase of the differential pressure ΔP, equation (2.36) will also be expressed in the form

$$\Delta P(x, \theta, t) = \Delta \hat{P}(x, \theta)\ e^{i[\omega t + \psi(x)]},$$

where the amplitude $\Delta \hat{P}(x, \theta)$ and phase angle $\psi(x)$ are calculated as

$$\Delta \hat{P}(x, \theta) = 2\rho U^2\, \alpha_0 \sqrt{\left[\hat{P}_R(x)\right]^2 + \left[\omega \hat{P}_I(x)\right]^2}\, \cos\theta, \tag{2.39}$$

$$\psi(x) = \tan^{-1} \frac{\omega \hat{P}_I(x)}{\hat{P}_R(x)}. \tag{2.40}$$

2.4.2 Experimental apparatus

A schematic representation of the experimental apparatus is shown in Figure 2.3. It consists of a rigid cylindrical center-body of length L = 421 mm and diameter $2a$ = 88.9 mm (3.5 in.), pendularly supported by a hinge inside a coaxial cylindrical

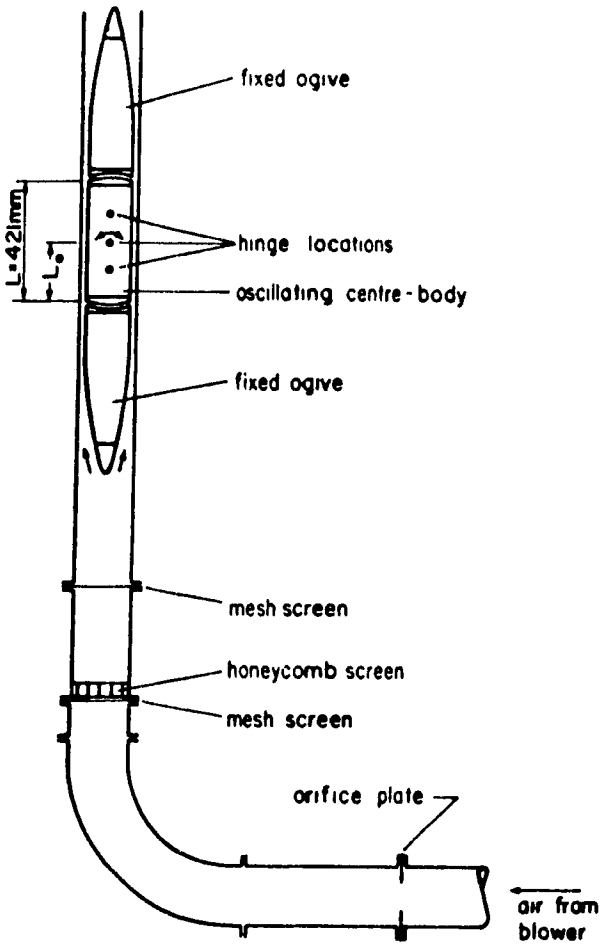

Figure 2.3. Schematic diagram of the experimental apparatus.

duct of 98.6 mm diameter. The annular gap is 4.85 mm, so that $h = 0.109$ Two elongated ogives, shown to scale in Figure 2.3, are rigidly mounted on either side of the center-body, so as to render the flow about the central part of the apparatus as uniform and axisymmetric as possible.

The center-body is forced to execute harmonic angular oscillations about the hinge via a motion-transmission mechanism connected to a shaker (not shown). The hinge could be located at one of three different positions: $L_0 = 115$, 210 or 306 mm.

The air flow is upwards and is provided by a blower through a fairly long, flexible hose system, and is controlled by a valve (not shown). The flow rate is measured by an orifice plate, with appropriate length of piping upstream and downstream for accurate measurements. To further improve flow uniformity and reduce flow fluctuations, a honeycomb screen and several wire meshes were placed upstream of the test-section. The flow was further regularized and smoothed by the contraction provided by the upstream ogive.

The unsteady pressure in the annular flow is measured differentially at two diametrally opposed points on the fixed outer pipe, in the plane of oscillation and at various circumferential locations, namely at $\theta = 0°$, $30°$, $45°$ and $60°$. More details on the experimental procedure can be found in References [7, 9, 20].

The following, main parameters characterized the experiments performed:

Relative annular clearance:	$h = 0.109$.
Mean flow velocity range:	$U = 52.4$ - 73 m/s.
Frequency of oscillations:	$f = \Omega/2\pi = 15$ - 75 Hz.
Reynolds number range:	$Re = (3.3$ - $4.8) \times 10^4$.
Centre-body relative length:	$l = L/a = 9.46$.

2.4.3 Comparison between theory and experiments

The theoretical amplitude $\Delta\hat{P}(x, \theta)$ and phase $\psi(x)$ of the differential pressure, calculated from (2.39) and (2.40), are compared in the following with the experimentally measured ones for various frequencies of oscillation. (No significance should be attached to the form of variation of $\Delta\hat{P}$ with frequency, f, of oscillations; this is related to the amplitude-frequency limitations of the shaker [9]).

In Figure 2.4, the comparison is made with the differential pressure measurements taken at a nondimensional distance $x = 5.60$ from the upstream extremity

of the center-body and at four circumferential locations: $\theta = 0°$, 30°, 45° and 60° In this case, the center-body was forced to oscillate harmonically about a hinge situated at $l_0 = 2.59$ from the upstream end of the cylinder, with frequencies from 15 to 75 Hz. Figure 2.4(a) shows the results obtained with a mean flow velocity $U = 52.4$ m/s, and Figure 2.4(b) corresponds to another magnitude of the mean flow velocity, $U = 73$ m/s.

A very good agreement is observed in Figure 2.4 between the theoretical turbulent solution derived in Section 2.3 and the experimental results, for both the amplitude $\Delta\hat{P}$ and phase angle ψ. With regard to the phase angle, the theoretical solution (2.40) does not depend on θ, while the experimentally measured phase slightly varies with θ; however, the differences are small, specially for the upper range of frequencies tested.

This generally good agreement between the theoretical predictions and the experimental results is observed for all tests, except when the pressure measurements are taken close to one of the center-body extremities; in this case, the experimental results are strongly influenced by the peculiarities of the experimental apparatus, which are discussed in more detail in Refs [9, 20]

Figure 2.5 shows a comparison between theory and experiments for another axial location, $x = 6.23$, and another hinge position, $l_0 = 4.73$. In this case, the unsteady turbulent solution and the experimental results are also compared with the inviscid-only solution, obtained by introducing $K = 0$ in (2.37) and (2.38). One can notice that the unsteady turbulent solution is in much better agreement with the experimental results than the potential solution, especially with regard to the phase angle.

The influence of the mean flow velocity in the annulus, for various circumferential positions, is shown in Figure 2.6 for $x = 6.23$ and $l_0 = 2.59$. The agreement between theory and experiments appears to be slightly better for the lower flow ve-

locity. One can notice that the unsteady turbulent solution is in better agreement with the experiments than the potential (inviscid) solution; this is most markedly so for the phase angle results, which are expected to be more sensitive to turbulence effects. More detailed experimental testing is reported in Ref. [9].

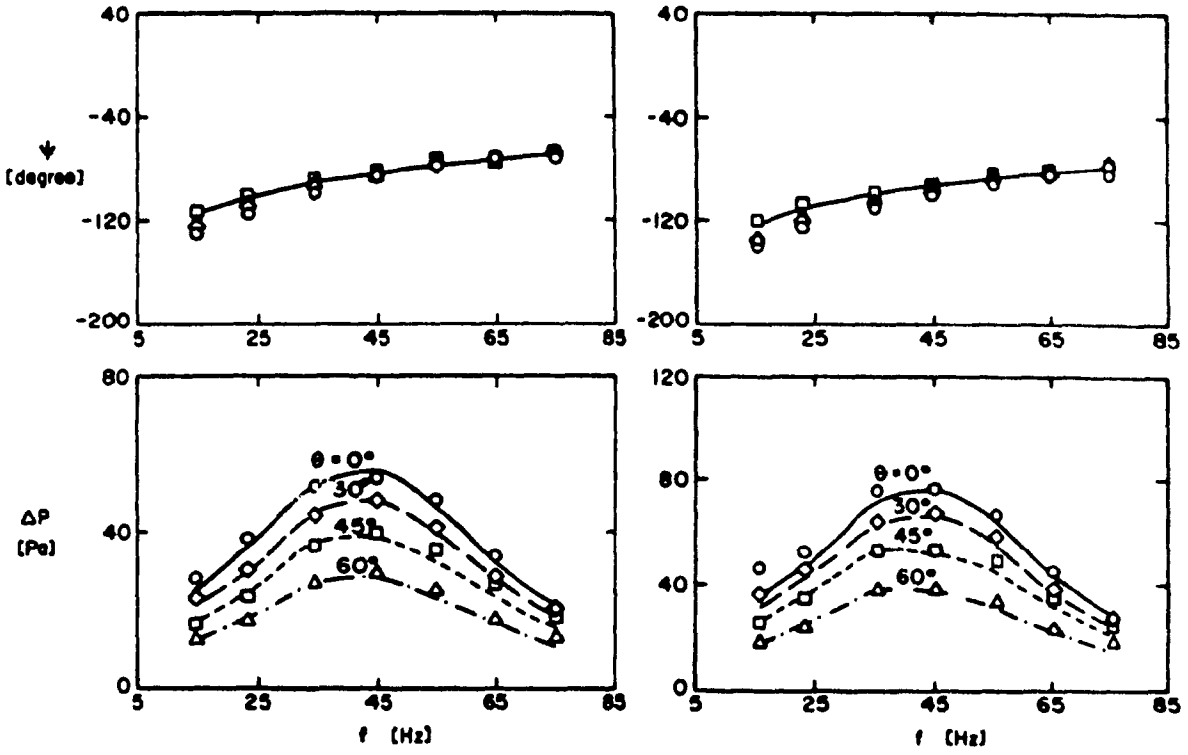

Figure 2.4: Comparison between theoretical and experimentally measured unsteady pressures (amplitude $\Delta\hat{P}$ and phase ψ) *versus* oscillation frequency, f, showing the influence of the circumferential position, for $\theta = 0°$, $30°$, $45°$, and $60°$, and for $l_0 = 2.59$, $x = 5.60$. Lines: present unsteady turbulent analysis; the theoretical phase does not depend on θ Experiments: ◯ $\theta = 0°$, ◇ $\theta = 30°$, □ $\theta = 45°$, △ $\theta = 60°$. (a) $U = 52.4$ m/s, (b) $U = 73.0$ m/s.

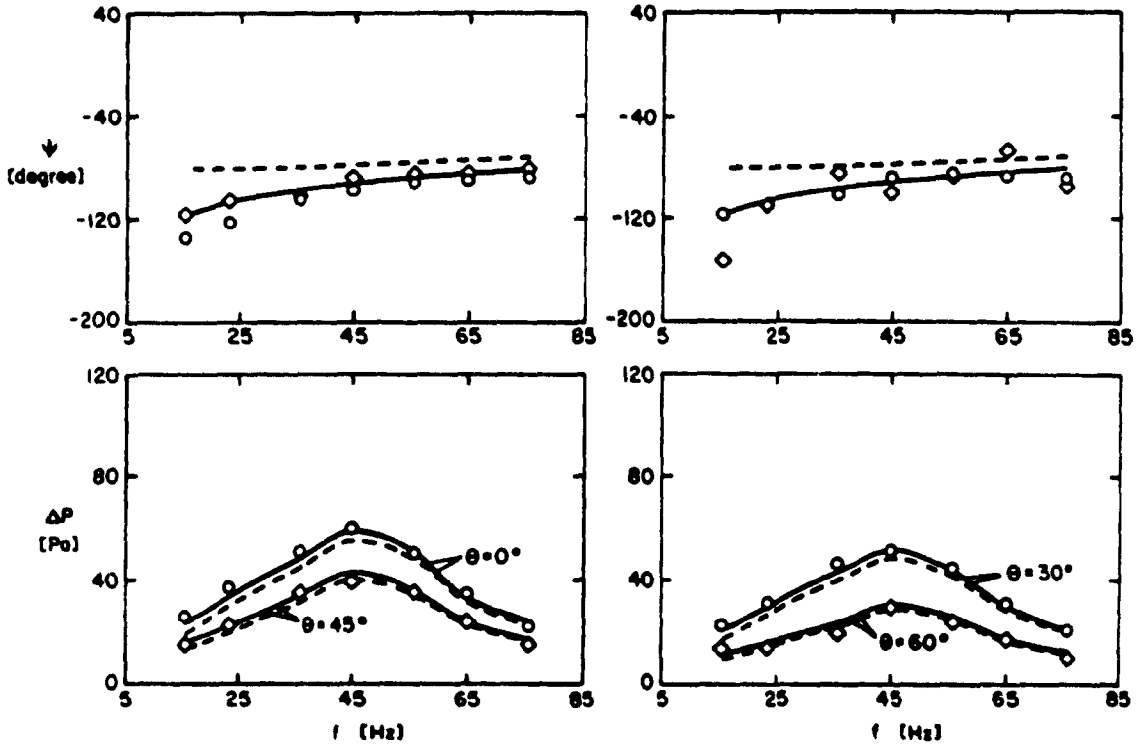

Figure 2.5: Theoretical and experimentally measured unsteady pressures (amplitude $\Delta\hat{P}$ and phase ψ) *versus* oscillation frequency, f, showing the effect of circumferential location θ, for $l_0 = 4.73$, $x = 6.23$ and $U = 52.4$ m/s. —— present unsteady turbulent analysis, and – – – potential theory of Ref. [5]. Experiments: (a) ◯ $\theta = 0°$, ◇ $\theta = 45°$, (b) ◯ $\theta = 30°$, △ $\theta = 60°$.

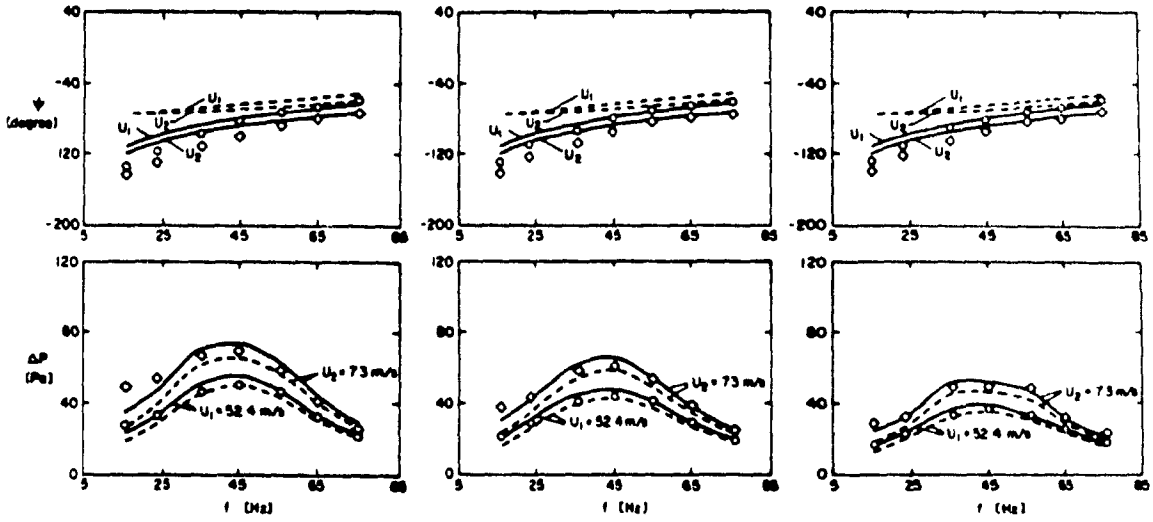

Figure 2.6: Theoretical and experimentally measured unsteady pressures (amplitude $\Delta\hat{P}$ and phase ψ) *versus* oscillation frequency, f, showing the effect of annular flow velocity, U, for $l_0 = 2.59$ and $x = 6.23$; (a) $\theta = 0°$, (b) $\theta = 30°$, (c) $\theta = 45°$. —— present unsteady turbulent analysis, and – – – potential theory of Ref [5] Experiments: ◯ $U = 52.4$ m/s, ◇ $U = 73.0$ m/s.

2.5 Conclusions

In this chapter, an expression for the unsteady turbulent pressure acting on a center-body oscillating in annular flow has been obtained (the results can be used for the stability analysis of the fluid-structure system by using the approach developed in Ref [6]) We considered a uniform cross-section annular region, and an approximate method has been designed in which the fluctuating small-scale turbulent quantities are superposed on a potential flow, instead of a "viscous" one. We remarked at one point that the formulation adopted here is slightly different from that developed in Ref. [7], although the same results obtain for the particular case of a uniform annular configuration. In Ref. [7], the decomposition of the velocity vetor in (2.4) included a "viscous" contribution, $\mathbf{v}_v$, which rendered necessary the introduction of simplifications in the solution process. However, the addition of this "viscous term" might contribute to making the description of the flow phenomenom more complete, and more study is required in that direction. The present formulation leads to a theory which is more straightforward in its development, and furthermore it can be generalized, as was mentioned earlier, although this remains to be done.

At this point, instead of generalizing the results for turbulent flow to more complex configurations, we will do so for laminar flow; this chapter thus concludes the treatment of unsteady turbulent flows. The rest of this thesis is devoted to the computation of unsteady laminar flows using the incompressible Navier-Stokes equations Unsteadiness in the flow patterns comes from interaction with structural walls which undergo oscillations, and this leads to the development of a methodology to study fluid-structure interaction problems.

Chapter 3

A TIME INTEGRATION METHOD USING ARTIFICIAL COMPRESSIBILITY FOR UNSTEADY FLOWS

3.1 Introduction

The study of fluid-structure interaction problems requires mathematical modelling of the physics at two levels. First of all, one is concerned with the mathematical representation of the dynamical behaviour of a structure which is submitted to a set of externally applied forces. In flow-induced vibrations, the externally applied forces are fluid forces and these cannot be treated independently of the response of the structure. Indeed, as the structure responds to the fluid forces, the latter are precisely determined as functions of the dynamical parameters describing the structural motion.

Hence, at the second level of physical modelling the fluid forces must be determined as functions, for example, of the velocity of the structure at the fluid-structure interface. The approach that we adopt here is one in which the fluid forces are calculated from the incompressible Navier-Stokes equations – or linearized forms thereof. The boundary conditions required to solve the Navier-Stokes equations are the velocity of the walls bounding the fluid domain, namely the velocity of the structural parts in contact with the fluid. The solving of these equations then allows for computing the fluid forces at the fluid-structure interface.

We delay until Chapter 9 how the interactive response of both the fluid and structure is effectively treated, as the problem that we first tackle is of the forced-vibration type. Indeed, an important aspect of fluid-structure interaction problems is the accurate determination of the fluid forces acting on the structure, and a method for doing so is developed and tested in Chapters 3 to 8. Thus, we are first concerned with the determination of the unsteady fluid forces which result from a time-accurate integration of the unsteady incompressible Navier-Stokes equations. The boundary conditions will be assumed to be known for all time, for example the structure will be imposed a harmonic vibration, and the fluid forces acting on it will be determined therefrom. This chapter presents the time integration method used for solving the Navier-Stokes equations, which is the method of artificial compressibility for unsteady flows.

3.2 Time Discretization of Navier-Stokes Equations

The equations governing the motion of an incompressible viscous fluid are the momentum and continuity equations,

$$\frac{\partial \mathbf{V}}{\partial t} + \mathbf{G}\,(\mathbf{V},\, p) \;=\; \mathbf{0}\,, \tag{3.1}$$

$$\boldsymbol{\nabla} \cdot \mathbf{V} \;=\; 0\,, \tag{3.2}$$

where we have

$$\mathbf{G}\,(\mathbf{V},\, p) = \boldsymbol{\nabla} \cdot \mathbf{V}\mathbf{V} + \boldsymbol{\nabla} p - \frac{1}{Re}\nabla^2 \mathbf{V}\,. \tag{3.3}$$

The equations are in non-dimensional form and Re represents the Reynolds number defined for each specific problem in terms of a characteristic length and velocity, $\mathbf{V}$ is the velocity vector and p the pressure. These equations must be integrated in both time and space. This chapter details the time integration scheme developed as part of the present work, where the method of artificial compressibility is used in straightforward fashion to solve unsteady flow problems.

We remark first that a time derivative appears only in the momentum equation (3.1). The discretization of that time derivative is accomplished as follows, introducing the three-point-backward implicit time-differencing scheme,

$$\frac{3\,\mathbf{V}^{n+1} - 4\,\mathbf{V}^{n} + \mathbf{V}^{n-1}}{2\,\Delta t} + \mathbf{G}^{n+1} = \mathbf{0}\,, \tag{3.4}$$

where Δt is the time step and $\mathbf{G}^{n+1} = \mathbf{G}\,(\mathbf{V}^{n+1},\, p^{n+1})$

This second order time-accurate scheme is used to advance the solution to time level $t^{n+1} = (n+1)\,\Delta t$, and requires that the solution be known at the two previous time levels t^n and t^{n-1}. We also experimented with another time-differencing scheme, namely the Crank-Nicolson one,

$$\frac{\mathbf{V}^{n+1} - \mathbf{V}^{n}}{\Delta t} + \frac{1}{2}(\mathbf{G}^{n+1} + \mathbf{G}^{n}) = \mathbf{0}\,, \tag{3.5}$$

which has been used by Soh & Goodrich [16]. We found problems with the time solution of the pressure variable; these will be reported in Section 7.4. The scheme (3.4) has thus been introduced to correct these difficulties and we can rewrite it, together with the continuity equation which must be satisfied for all time, as

$$\mathbf{V}^{n+1} + \alpha\, \mathbf{G}^{n+1} = \mathbf{F}^n \,, \tag{3.6}$$

$$\boldsymbol{\nabla} \cdot \mathbf{V}^{n+1} = 0 \,, \tag{3.7}$$

where

$$\alpha = \frac{2}{3}\,\Delta t \,, \quad \mathbf{F}^n = \frac{1}{3}\,(4\,\mathbf{V}^n - \mathbf{V}^{n-1}) \,.$$

In order to initiate the time integration procedure, initial conditions must be specified for $\mathbf{V}^1$ and p^1 throughout the fluid domain, which implies that the solution is known at only one previous time level, namely t^1. In order to advance the solution to t^2, a simple implicit Euler scheme can be used instead of the three-point-backward scheme (3.4), which can also be put in equation form (3.6), with

$$\alpha = \Delta t \,, \qquad \mathbf{F}^n = \mathbf{V}^n \,.$$

Equations (3.6) and (3.7) represent the semi-discretized form of the Navier-Stokes equations. They are solved for the flow quantities $\mathbf{V}^{n+1}$ and p^{n+1} by imposing no-slip boundary conditions for the velocity components, namely the velocity of the fluid is equal to the velocity of the wall at the fluid-structure interface. Hence, if we know the velocity, $\mathbf{V}_w^{n+1}$, of the walls bounding the fluid domain at time level t^{n+1}, then (3.6) and (3.7), which are a non-homogeneous system of non-linear equations, can be solved for $\mathbf{V}^{n+1}$ and p^{n+1}. In most problems, boundary conditions also need to be imposed on the velocity and/or pressure at any inflow

or outflow portion to the fluid domain, and their treatment will be discussed in the next chapters when the finite difference method used to discretize the spatial differential operators is introduced.

3.3 Pseudo-time Iterative Relaxation Technique

In order to solve equations (3.6) and (3.7), we resort to a pseudo-time iterative relaxation procedure, whereby the continuity equation and the momentum equation are augmented by pseudo-time derivative terms involving pressure and velocity, respectively $\delta\,(\partial\check{p}/\partial\tau)$ and $\partial\check{\mathbf{V}}/\partial\tau$, in which δ is the artificial compressibility. Thus, introducing the pseudo-time τ and denoting by $\check{\mathbf{V}}$ and $\check{p}$ the pseudo-functions corresponding to the iterated velocity and pressure variables during the relaxation procedure between time levels t^n and t^{n+1}, equations (3.6) and (3.7) are replaced by

$$\frac{\partial\check{\mathbf{V}}}{\partial\tau} + \check{\mathbf{V}} + \alpha\,\check{\mathbf{G}} \;=\; \mathbf{F}^n\,. \tag{3.8}$$

$$\delta\,\frac{\partial\check{p}}{\partial\tau} + \boldsymbol{\nabla}\cdot\check{\mathbf{V}} \;=\; 0\,. \tag{3.9}$$

These equations are integrated in pseudo-time until a steady state is reached. An implicit Euler scheme is used for the pseudo-time semi-discretization,

$$\frac{\check{\mathbf{V}}^{\nu+1}-\check{\mathbf{V}}^{\nu}}{\Delta\tau} + \check{\mathbf{V}}^{\nu+1} + \alpha\check{\mathbf{G}}^{\nu+1} \;=\; \mathbf{F}^n\,. \tag{3.10}$$

$$\frac{\check{p}^{\nu+1}-\check{p}^{\nu}}{\Delta\tau} + \frac{1}{\delta}\,\boldsymbol{\nabla}\cdot\check{\mathbf{V}}^{\nu+1} \;=\; 0\,, \tag{3.11}$$

where $\Delta\tau$ is the pseudo-time step and the superscript ν indicates the solution at the pseudo-time level $\tau^{\nu} = \nu\,\Delta\tau$. Also, we have $\check{\mathbf{G}}^{\nu+1} = \mathbf{G}(\check{\mathbf{V}}^{\nu+1}, \check{p}^{\nu+1})$. The

initial conditions required to start the pseudo-time integration are taken to be $\mathbf{V}^n$ and p^n inside the fluid domain, namely

$$\check{\mathbf{V}}^\nu \Big|_{\nu=1} = \mathbf{V}^n \,, \qquad \check{p}^\nu \Big|_{\nu=1} = p^n \,,$$

whereas on the boundary of the fluid domain the known velocity $\mathbf{V}_w^{n+1}$ of the walls at the advanced time level t^{n+1} are set as boundary conditions and kept unchanged until steady state has been reached in pseudo-time. $\mathbf{V}_w^{n+1}$ serves as a driving term to advance the solution to time level $(n+1)\Delta t$, along with the non-homogeneous term $\mathbf{F}^n$, which is also calculated at the beginning of pseudo-time relaxation and kept constant throughout.

When steady state is reached in pseudo-time, at $\nu = k$, the pseudo-time derivatives become zero ($\check{\mathbf{V}}^{k+1} = \check{\mathbf{V}}^k$ and $\check{p}^{k+1} = \check{p}^k$), and equations (3.10) and (3.11) reduce to (3.6) and (3.7), at which point

$$\check{\mathbf{V}}^{k+1} \equiv \mathbf{V}^{n+1} \,, \qquad \check{p}^{k+1} \equiv p^{n+1} \,.$$

Introducing the pseudo-time variations

$$\begin{aligned} \Delta\mathbf{V} &= \check{\mathbf{V}}^{\nu+1} - \check{\mathbf{V}}^\nu \,, \qquad \Delta p = \check{p}^{\nu+1} - \check{p}^\nu \,, \\ \Delta\mathbf{G} &= \check{\mathbf{G}}^{\nu+1} - \check{\mathbf{G}}^\nu \,, \end{aligned}$$

equations (3.10) and (3.11) can be recast in delta form

$$(1+\Delta\tau)\,\Delta\mathbf{V} + \alpha\,\Delta\tau\,\Delta\mathbf{G} = \Delta\tau\,(\mathbf{F}^n - \check{\mathbf{V}}^\nu - \alpha\,\check{\mathbf{G}}^\nu)\,, \tag{3.12}$$

$$\Delta p + \frac{\Delta\tau}{\delta}\,\boldsymbol{\nabla}\cdot(\Delta\mathbf{V}) = -\frac{\Delta\tau}{\delta}\,\boldsymbol{\nabla}\cdot\check{\mathbf{V}}^\nu \,. \tag{3.13}$$

Equations (3.12) and (3.13) are an implicit system of equations, nonlinearly coupled by the term $\Delta\mathbf{G}$. In summary, their solution proceeds as follows. The flow variables are known everywhere in the fluid domain at the time levels t^n and t^{n-1}. The term $\mathbf{F}^n$ is calculated and the known velocity, $\mathbf{V}_w^{n+1}$, of the walls bounding the fluid domain is imposed as a boundary condition. $\mathbf{V}^n$ and p^n then serve as initial conditions inside the fluid domain to iterate (3.12) and (3.13) in pseudo-time until a steady state is reached, at which point Δp and $\Delta\mathbf{V}$ are equal to zero and $\mathbf{V}^{n+1}$ and p^{n+1} are obtained. This solution process in conjunction with the spatial discretization will be detailed in the following chapters as specific problems are treated.

Chapter 4

METHOD OF SOLUTION IN CARTESIAN COORDINATES

The time integration method used to solve the unsteady incompressible Navier-Stokes equations was developed in the previous chapter. To proceed further and obtain a numerical solution to these equations, we must introduce a discretization of the spatial differential operators, which we do here in two-dimensional Cartesian coordinates using finite differences. The implicit nonlinear system (3.12) and (3.13) must then be appropriately linearized in order to facilitate the pseudo-time iterative process. Furthermore, the effort required to invert the linearized equations can be reduced by the use of the Approximate Factorization and Alternating Direction Implicit (ADI) methods. These are the subjects of this chapter.

4.1 Differential Form of Equations

In Cartesian coordinates, the nondimensional fluid velocity vector $\mathbf{V}$, the convective, pressure and viscous terms included in $\mathbf{G}(\mathbf{V}, p)$, and the velocity divergence $\nabla \cdot \mathbf{V}$ (see equations (3.1-3.3)) are given by

$$\mathbf{V} = \begin{bmatrix} u \\ v \end{bmatrix}, \qquad \mathbf{G}(\mathbf{V}, p) = \begin{bmatrix} G_u(u, v, p) \\ G_v(u, v, p) \end{bmatrix},$$

$$G_u(u, v, p) = \frac{\partial(uu)}{\partial x} + \frac{\partial(vu)}{\partial y} + \frac{\partial p}{\partial x} - \frac{1}{Re}\left(\frac{\partial^2 u}{\partial x^2} + \frac{\partial^2 u}{\partial y^2}\right), \tag{4.1}$$

$$G_v(u, v, p) = \frac{\partial(uv)}{\partial x} + \frac{\partial(vv)}{\partial y} + \frac{\partial p}{\partial y} - \frac{1}{Re}\left(\frac{\partial^2 v}{\partial x^2} + \frac{\partial^2 v}{\partial y^2}\right), \tag{4.2}$$

$$\nabla \cdot \mathbf{V} = \frac{\partial u}{\partial x} + \frac{\partial v}{\partial y}. \tag{4.3}$$

Now, linearization of the term $\Delta\mathbf{G}$ which enforces implicit coupling in (3.12) is done by simply lagging the velocity components [22], which in the pseudo-time variation form is expressed as

$$\Delta\mathbf{V} = \begin{bmatrix} \Delta u \\ \Delta v \end{bmatrix} = \begin{bmatrix} \breve{u}^{\nu+1} - \breve{u}^{\nu} \\ \breve{v}^{\nu+1} - \breve{v}^{\nu} \end{bmatrix},$$

$$\Delta\mathbf{G} = \begin{bmatrix} \Delta G_u \\ \Delta G_v \end{bmatrix} = \begin{bmatrix} \breve{G}_u^{\nu+1} - \breve{G}_u^{\nu} \\ \breve{G}_v^{\nu+1} - \breve{G}_v^{\nu} \end{bmatrix},$$

with

$$\Delta G_u \equiv \frac{\partial(\breve{u}^{\nu}\Delta u)}{\partial x} + \frac{\partial(\breve{v}^{\nu}\Delta u)}{\partial y} + \frac{\partial(\Delta p)}{\partial x} - \frac{1}{Re}\left[\frac{\partial^2(\Delta u)}{\partial x^2} + \frac{\partial^2(\Delta u)}{\partial y^2}\right],$$

$$\Delta G_v \equiv \frac{\partial(\breve{u}^{\nu}\Delta v)}{\partial x} + \frac{\partial(\breve{v}^{\nu}\Delta v)}{\partial y} + \frac{\partial(\Delta p)}{\partial y} - \frac{1}{Re}\left[\frac{\partial^2(\Delta v)}{\partial x^2} + \frac{\partial^2(\Delta v)}{\partial y^2}\right]$$

This approximation is first-order accurate, which is consistent with the order of accuracy of the Euler pseudo-time semi-discretization in (3.10) and (3.11). We

also note that $\check{G}_u^\nu = G_u(\check{u}^\nu, \check{v}^\nu, \check{p}^\nu)$, $\check{G}_v^\nu = G_v(\check{u}^\nu, \check{v}^\nu, \check{p}^\nu)$. We can now rewrite (3.12) and (3.13) in global matrix form as

$$[\mathbf{I} + \alpha\, \Delta\tau\, (\mathbf{D}_x + \mathbf{D}_y)]\ \Delta\boldsymbol{\Phi} = \Delta\tau\, \mathbf{R}, \tag{4.4}$$

where the matrices $\mathbf{D}_x$ and $\mathbf{D}_y$, which respectively contain the spatial derivatives with respect to x and y of the variable $\Delta\boldsymbol{\Phi} = [\Delta u\ \Delta v\ \Delta p]^T$, take the form

$$\mathbf{D}_x = \begin{bmatrix} M + 1/\alpha & 0 & \partial/\partial x \\ 0 & M & 0 \\ (1/\alpha\delta)\partial/\partial x & 0 & 0 \end{bmatrix}, \quad \mathbf{D}_y = \begin{bmatrix} N & 0 & 0 \\ 0 & N + 1/\alpha & \partial/\partial y \\ 0 & (1/\alpha\delta)\partial/\partial y & 0 \end{bmatrix}, \tag{4.5}$$

and where

$$M v = \frac{\partial(\check{u}^\nu v)}{\partial x} - \frac{1}{Re}\frac{\partial^2 v}{\partial x^2}, \qquad N v = \frac{\partial(\check{v}^\nu v)}{\partial y} - \frac{1}{Re}\frac{\partial^2 v}{\partial y^2}.$$

$$\mathbf{R} = \begin{bmatrix} \mathbf{F}^n - \check{\mathbf{V}}^\nu - \alpha\, \check{\mathbf{G}}^\nu \\ -(1/\delta)\, \boldsymbol{\nabla} \cdot \check{\mathbf{V}}^\nu \end{bmatrix}.$$

The vector $\mathbf{R}$ is expressed in terms of its scalar components as

$$\mathbf{R} = \begin{bmatrix} R_u \\ R_v \\ R_p \end{bmatrix} = \begin{bmatrix} F_u^n - \check{u}^\nu - \alpha\, \check{G}_u^\nu \\ F_v^n - \check{v}^\nu - \alpha\, \check{G}_v^\nu \\ -(1/\delta)\, \boldsymbol{\nabla} \cdot \check{\mathbf{V}}^\nu \end{bmatrix},$$

in which

$$F_u^n = \frac{1}{3}\left(4\, u^n - u^{n-1}\right), \qquad F_v^n = \frac{1}{3}\left(4\, v^n - v^{n-1}\right).$$

Note that $\Delta\tau\, \Delta u$ and $\Delta\tau\, \Delta v$, arising from the vector term $\Delta\tau\, \Delta\mathbf{V}$ which appears undifferentiated in (3.12), have been conveniently (but arbitrarily) included

in the matrices $\mathbf{D}_x$ and $\mathbf{D}_y$, respectively. Now, we apply an Approximate Factorization to (4.4), thereby rewriting its implicit left-hand side as

$$[\mathbf{I} + \alpha\, \Delta\tau\, (\mathbf{D}_x + \mathbf{D}_y)]\ \Delta\boldsymbol{\Phi} = (\mathbf{I} + \alpha\, \Delta\tau\, \mathbf{D}_y)(\mathbf{I} + \alpha\, \Delta\tau\, \mathbf{D}_x)\, \Delta\boldsymbol{\Phi}\ .$$

Equation (4.4) is thus rewritten

$$(\mathbf{I} + \alpha\, \Delta\tau\, \mathbf{D}_y)(\mathbf{I} + \alpha\, \Delta\tau\, \mathbf{D}_x)\, \Delta\boldsymbol{\Phi} = \Delta\tau\, \mathbf{R}$$

This last linear implicit system of equations can now be solved with the Alternating Direction Implicit (ADI) method, whereby upon introducing the intermediate variable

$$\overline{\Delta\boldsymbol{\Phi}} = (\mathbf{I} + \alpha\, \Delta\tau\, \mathbf{D}_x)\, \Delta\boldsymbol{\Phi}\ ,$$

the solution proceeds with the sequence of a y-sweep and a x-sweep [22, 23, 24] The y-sweep is thus

$$(\mathbf{I} + \alpha\, \Delta\tau\, \mathbf{D}_y)\, \overline{\Delta\boldsymbol{\Phi}} = \Delta\tau\, \mathbf{R}\ , \tag{4.6}$$

whereas the x-sweep is defined by

$$(\mathbf{I} + \alpha\, \Delta\tau\, \mathbf{D}_x)\, \Delta\boldsymbol{\Phi} = \overline{\Delta\boldsymbol{\Phi}}\ . \tag{4.7}$$

Since, as we show shortly, we are using central differences to discretize the spatial differential operators, only tridiagonal systems of equations need to be solved, which is computationally efficient We can now write the y-sweep and x-sweep matrix equations (4.6) and (4.7) into their scalar form, namely we obtain for the y-sweep

$$\overline{\Delta u} + \alpha\,\Delta\tau\left[\frac{\partial(\check{v}^{\nu}\overline{\Delta u})}{\partial y} - \frac{1}{Re}\frac{\partial^2(\overline{\Delta u})}{\partial y^2}\right] = \Delta\tau\,(F_u^n - \check{u}^{\nu} - \alpha\,\check{G}_u^{\nu})\,, \tag{4.8}$$

$$(1+\Delta\tau)\,\overline{\Delta v} + \alpha\,\Delta\tau\left[\frac{\partial(\check{v}^{\nu}\overline{\Delta v})}{\partial y} + \frac{\partial(\overline{\Delta p})}{\partial y} - \frac{1}{Re}\frac{\partial^2(\overline{\Delta v})}{\partial y^2}\right] = \Delta\tau\,(F_v^n - \check{v}^{\nu} - \alpha\,\check{G}_v^{\nu})\,, \tag{4.9}$$

$$\overline{\Delta p} + \frac{\Delta\tau}{\delta}\frac{\partial(\overline{\Delta v})}{\partial y} = -\frac{\Delta\tau}{\delta}\,\nabla\cdot\check{\mathbf{V}}^{\nu}\,, \tag{4.10}$$

whereas Δu, Δv and Δp are solved subsequently in the x-sweep defined by the equations

$$(1+\Delta\tau)\,\Delta u + \alpha\,\Delta\tau\left[\frac{\partial(\check{u}^{\nu}\Delta u)}{\partial x} + \frac{\partial(\Delta p)}{\partial x} - \frac{1}{Re}\frac{\partial^2(\Delta u)}{\partial x^2}\right] = \overline{\Delta u}\,, \tag{4.11}$$

$$\Delta v + \alpha\,\Delta\tau\left[\frac{\partial(\check{u}^{\nu}\Delta v)}{\partial x} - \frac{1}{Re}\frac{\partial^2(\Delta v)}{\partial x^2}\right] = \overline{\Delta v}\,, \tag{4.12}$$

$$\Delta p + \frac{\Delta\tau}{\delta}\frac{\partial(\Delta u)}{\partial x} = \overline{\Delta p}\,. \tag{4.13}$$

The variables $\check{u}^{\nu+1} = \check{u}^{\nu} + \Delta u$, $\check{v}^{\nu+1} = \check{v}^{\nu} + \Delta v$, and $\check{p}^{\nu+1} = \check{p}^{\nu} + \Delta p$, are thus obtained by solving (4.8-4.13) and the solution can proceed to another pseudo-time iteration step, until convergence when Δu, Δv and Δp are equal to zero. Note that Δu and Δv are equal to zero on solid walls, as the values u^{n+1} and v^{n+1} are imposed before pseudo-time iteration is started and kept constant.

4.2 Spatial Discretization of Differential Operators

4.2.1 Stretched grid and grid stretching functions

The finite difference method was used to discretize the spatial differential operators, which were centrally differenced on a staggered grid. In order to obtain a good spatial resolution, stretched grids were used to concentrate more points in regions of higher velocity gradients, for example near solid walls.

Hyperbolic tangent and hyperbolic sine stretching functions were used as they provide best accuracy for the difference representation of differential operators [25]. The hyperbolic tangent was used to concentrate grid points normal to solid walls, and the hyperbolic sine was used in flow problems involving a preferred flow direction, to distribute the points in that direction. Figure 4.1 gives an example of the type of grid that was generated for a problem involving either a Cartesian or an annular backstep.

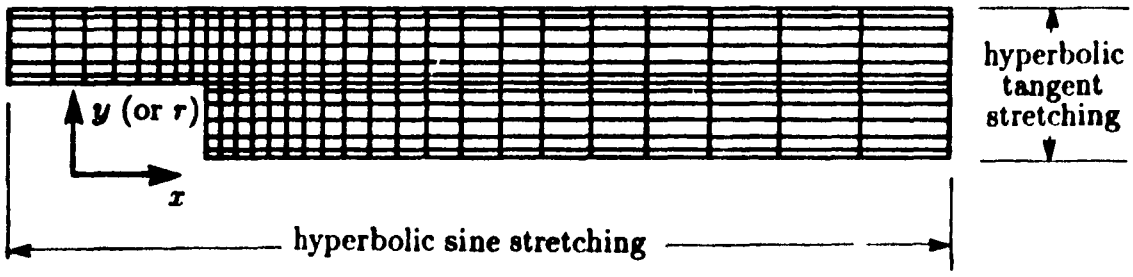

Figure 4.1: Mesh generated for the study of fluid flow over backsteps.

Given two walls parallel to each other and $(J+1)$ points spanning the region between them, the hyperbolic-tangent stretching function gives the coordinates y_j, $j = 0, \ldots, J$, of the grid points between the two walls by the relation

$$y_j = y_0 + (y_J - y_0)\left[\frac{1}{2} + \frac{\tanh\left(\gamma\frac{2j-J}{2J}\right)}{2\tanh\gamma/2}\right] . \tag{4.14}$$

The parameter γ controls the amount of stretching, and the larger it is, the more the points are concentrated near the walls. If, on the other hand, we want to stretch the grid in the x-direction, which in Figure 4.1 corresponds to the mean flow direction, we can use the hyperbolic-sine stretching function. Denoting by x_0 the coordinate of the point where the mesh is the finest, and by x_I the coordinate at the coarsest mesh location, the locations x_i of the $(I+1)$ points between x_0 and x_I are given by

$$x_i = x_0 + (x_I - x_0)\frac{\sinh\left(\gamma\frac{i}{I}\right)}{\sinh\gamma} . \tag{4.15}$$

Other uses of the hyperbolic tangent and hyperbolic sine stretching functions are described in Vinokur [25].

Equations (4.14) and (4.15) define coordinate transformations and introduce a computational space. Indeed, the fluid equations are now considered to be solved on a normalized domain with coordinates $\xi = i/I$, $0 \le \xi \le 1$, $\eta = j/J$, $0 \le \eta \le 1$, instead of on the original physical domain with coordinates x, $x_0 \le x \le x_I$, and y, $y_0 \le y \le y_J$. This has to be taken into account when solving the equations.

4.2.2 Differencing of spatial differential operators

In all of the present work the stretched meshes used were rectangular ones. In that case the coordinate transformation that defines the point spacing in physical space along one coordinate direction is a function of one transformed, computational

coordinate. The mesh is stretched along one coordinate direction independently of the other coordinate directions. The functional dependence of the coordinate transformation along, say, the x-coordinate is of the form $x \equiv x(\xi)$, as for example in (4.15). In order to evaluate the derivative with respect to x of a function $f(x)$ we thus have, in computational space and as a function of the transformed coordinate ξ,

$$\frac{df}{dx} = \frac{df/d\xi}{dx/d\xi} .$$

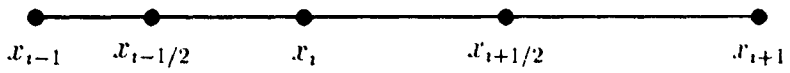

Figure 4.2: Portion of a one-dimensional stretched grid.

The term $dx/d\xi$ in the denominator of the above expression is called the metric term of the transformation. Referring to Figure 4.2 where the stretched portion of a one-dimensional mesh is shown, and denoting by $x_i \equiv x(\xi_i)$ the coordinate of a mesh point and by $f_i \equiv f(x_i)$ the function value at that point, the numerical evaluation at the point x_i of the first derivative with respect to x of a function $f(x)$ is given by

$$\left.\frac{df}{dx}\right|_{x=x_i} = \frac{f_{i+1} - f_{i-1}}{x_{i+1} - x_{i-1}} \qquad \text{or} \qquad \left.\frac{df}{dx}\right|_{x=x_i} = \frac{f_{i+1/2} - f_{i-1/2}}{x_{i+1/2} - x_{i-1/2}} ,$$

where central differences have been used. Notice the alternative forms. An important aspect in these relations is that although the functional dependence $x(\xi)$ may be known analytically, as for example in (4.15), the metric term derivative $dx/d\xi$ is evaluated numerically, not analytically. This results in a better accuracy of the

differenced approximations [26]. Similarly, the evaluation of the second derivative of the function $f(x)$ is done as

$$\begin{aligned}
\left.\frac{d^2f}{dx^2}\right|_{x=x_i} &= \left[\frac{d}{dx}\left(\frac{df}{dx}\right)\right]_{x=x_i} \\
&= \frac{1}{x_{i+1/2}-x_{i-1/2}}\left[\left(\frac{df}{dx}\right)_{x_{i+1/2}} - \left(\frac{df}{dx}\right)_{x_{i-1/2}}\right] \qquad (4.16) \\
&= \frac{1}{x_{i+1/2}-x_{i-1/2}}\left[\frac{f_{i+1}-f_i}{x_{i+1}-x_i} - \frac{f_i-f_{i-1}}{x_i-x_{i-1}}\right] .
\end{aligned}$$

Notice that differencing at mid-point has been used for each of the first-derivatives.

4.2.3 Differencing of Navier-Stokes equations

The flow equations were centrally differenced on a staggered grid [12], indicated schematically in Figure 4.3. In a staggered grid, the velocity components u and v are defined at different grid points, namely at (x_i^u, y_j^u) and (x_i^v, y_j^v) for $u_{i,j}$ and $v_{i,j}$, which are also different from the grid point where the pressure $p_{i,j}$ is defined, which is (x_i^v, y_j^u). For a cell (i,j) centered at the point (x_i^v, y_j^u) where the pressure $p_{i,j}$ is defined, the four sides correspond to grid points where $u_{i-1,j}$, $u_{i,j}$, $v_{i,j-1}$ and $v_{i,j}$ are defined. Moreover, the x- and y-momentum equations and the continuity one are differenced about the points where $u_{i,j}$, $v_{i,j}$ and $p_{i,j}$ are defined, respectively.

Before performing the spatial discretization of the equations, we first introduce the linear interpolates of the velocity components on the staggered mesh, which are given by

$$u_u^{x+} = \frac{\nabla x_{i+1}^u\, u_{i,j} + \nabla x_{i+1}^v\, u_{i+1,j}}{\Delta x_{i+1}^v} \quad , \qquad u_u^{x-} = \frac{\nabla x_i^u\, u_{i-1,j} + \nabla x_i^v\, u_{i,j}}{\Delta x_i^v}$$

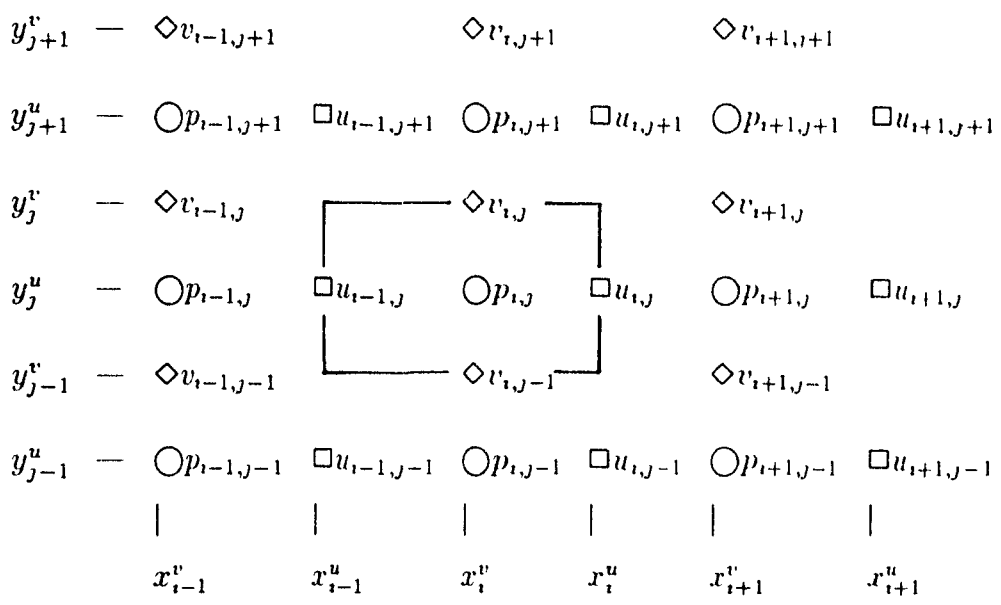

Figure 4.3: Schematic representation of the staggered grid used in the spatial differentiation.

$$u_u^{y+} = \frac{\nabla y^u_{j+1}\, u_{i,j} + \nabla y^v_j\, u_{i,j+1}}{\Delta y^v_j} \quad , \qquad u_u^{y-} = \frac{\nabla y^u_j\, u_{i,j-1} + \nabla y^v_{j-1}\, u_{i,j}}{\Delta y^v_{j-1}}$$

$$v_u^{y+} = \frac{\nabla x^v_{i+1}\, v_{i,j} + \nabla x^u_i\, v_{i+1,j}}{\Delta x^u_i} \quad , \qquad v_u^{y-} = \frac{\nabla x^v_{i+1}\, v_{i,j-1} + \nabla x^u_i\, v_{i+1,j-1}}{\Delta x^u_i}$$

$$v_v^{x+} = \frac{\nabla x^v_{i+1}\, v_{i,j} + \nabla x^u_i\, v_{i+1,j}}{\Delta x^u_i} \quad , \qquad v_v^{x-} = \frac{\nabla x^v_i\, v_{i-1,j} + \nabla x^u_{i-1}\, v_{i,j}}{\Delta x^u_{i-1}}$$

$$v_v^{y+} = \frac{\nabla y^v_{j+1}\, v_{i,j} + \nabla y^u_{j+1}\, v_{i,j+1}}{\Delta y^u_{j+1}} \quad , \qquad v_v^{y-} = \frac{\nabla y^v_j\, v_{i,j-1} + \nabla y^u_j\, v_{i,j}}{\Delta y^u_j}$$

$$u_v^{x+} = \frac{\nabla y^u_{j+1}\, u_{i,j} + \nabla y^v_j\, u_{i,j+1}}{\Delta y^v_j} \quad , \qquad u_v^{x-} = \frac{\nabla y^u_{j+1}\, u_{i-1,j} + \nabla y^v_j\, u_{i-1,j+1}}{\Delta y^v_j}$$

where, in these last relations, Δ and ∇, which we will sometimes refer to as the delta's and nabla's of the grid point coordinates, denote the central and backward

difference operators applied to these grid point coordinates. They are defined as

$$\Delta x_i^u = x_{i+1}^v - x_i^v \,, \qquad \Delta x_i^v = x_i^u - x_{i-1}^u \,,$$
$$\Delta y_j^u = y_j^v - y_{j-1}^v \,, \qquad \Delta y_j^v = y_{j+1}^u - y_j^u \,,$$
$$\nabla x_i^u = x_i^u - x_i^v \,, \qquad \nabla x_i^v = x_i^v - x_{i-1}^u \,,$$
$$\nabla y_j^u = y_j^u - y_{j-1}^v \,, \qquad \nabla y_j^v = y_j^v - y_j^u \,.$$

The discretization of equations (4 1-4.3) is thus given by the following relations:

$$\begin{aligned}
(G_u)_{i,j} &= \frac{1}{\Delta x_i^u}\left[(u_u^{x+})^2 - (u_u^{x-})^2 + p_{i+1,j} - p_{i,j}\right. \\
&- \left.\frac{1}{Re}\left(\frac{u_{i+1,j} - u_{i,j}}{\Delta x_{i+1}^v} - \frac{u_{i,j} - u_{i-1,j}}{\Delta x_i^v}\right)\right] \\
&+ \frac{1}{\Delta y_j^u}\left[v_u^{y+}\, u_u^{y+} - v_u^{y-}\, u_u^{y-}\right. \\
&- \left.\frac{1}{Re}\left(\frac{u_{i,j+1} - u_{i,j}}{\Delta y_j^v} - \frac{u_{i,j} - u_{i,j-1}}{\Delta y_{j-1}^v}\right)\right],
\end{aligned} \tag{4.17}$$

$$\begin{aligned}
(G_v)_{i,j} &= \frac{1}{\Delta x_i^v}\left[u_v^{x+}\, v_v^{x+} - u_v^{x-}\, v_v^{x-}\right. \\
&- \left.\frac{1}{Re}\left(\frac{v_{i+1,j} - v_{i,j}}{\Delta x_i^u} - \frac{v_{i,j} - v_{i-1,j}}{\Delta x_{i-1}^u}\right)\right] \\
&+ \frac{1}{\Delta y_j^v}\left[(v_v^{y+})^2 - (v_v^{y-})^2 + p_{i,j+1} - p_{i,j}\right. \\
&- \left.\frac{1}{Re}\left(\frac{v_{i,j+1} - v_{i,j}}{\Delta y_{j+1}^u} - \frac{v_{i,j} - v_{i,j-1}}{\Delta y_j^u}\right)\right],
\end{aligned} \tag{4.18}$$

$$(\nabla \cdot \mathbf{V})_{i,j} = \frac{u_{i,j} - u_{i-1,j}}{\Delta x_i^v} - \frac{v_{i,j} - v_{i,j-1}}{\Delta y_j^u} \,. \tag{4.19}$$

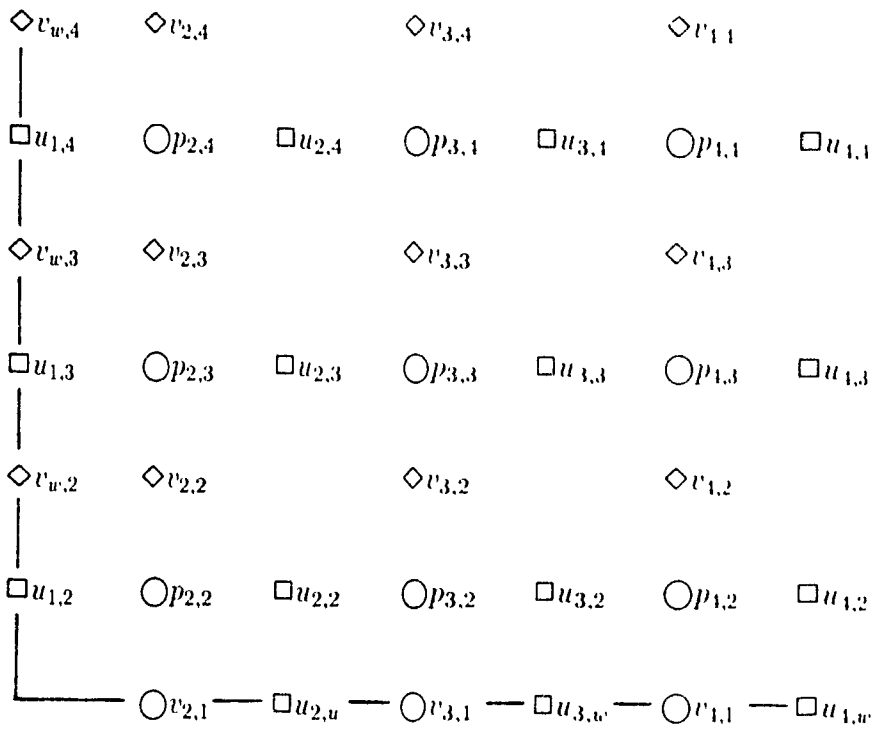

Figure 4 4: Evaluation of viscous derivatives near solid walls, where the quantities $u_{1,w}$ and $v_{w,j}$ are defined.

Now, we remark in passing that the evaluation of the viscous derivatives near a solid wall requires special treatment. Indeed, in the staggered grid a wall parallel with the x-coordinate passes through the points where for example, $v_{i,1}$ are defined, and similarly a wall parallel with the y-coordinate passes through the points where $u_{1,j}$ are defined, see Figure 4 4. Hence the numerical evaluation of $\partial^2 u/\partial y^2$ in the former case and of $\partial^2 v/\partial x^2$ in the latter case would require points defined outside the physical domain To circumvent that difficulty, we use non central differencing to compute the derivative of the term in (4 16) which would otherwise require points outside the domain, and hence we have, for example

$$\left.\frac{\partial^2 u}{\partial y^2}\right|_{y=y_2^u} = \frac{1}{\Delta y_2^u}\left[\frac{u_{i,3}-u_{i,2}}{\Delta y_2^v} - \frac{\frac{8}{3}\,u_{i,w} - 3\,u_{i,2} + \frac{1}{3}\,u_{i,3}}{\frac{8}{3}\,y_1^v - 3\,y_2^u + \frac{1}{3}\,y_3^u}\right] .$$

$$\left.\frac{\partial^2 v}{\partial x^2}\right|_{x=x_2^v} = \frac{1}{\Delta x_2^v}\left[\frac{v_{3,j}-v_{2,j}}{\Delta x_2^u} - \frac{\frac{8}{3}\,v_{w,j} - 3\,v_{2,j} + \frac{1}{3}\,v_{3,j}}{\frac{8}{3}\,x_1^u - 3\,x_2^v + \frac{1}{3}\,x_3^v}\right] .$$

It is remarked in these last two expressions that the second term in the square brackets is precisely the one-sided evaluation of the first derivative at the solid wall, and $u_{i,w}$ and $v_{w,j}$ are the wall velocity components which are given as boundary conditions.

4.3 The y-Sweep

It is seen in the y-sweep, equations (4.8-4.10), that $\overline{\Delta u}$ as obtained from solving the x-momentum equation (4.8) is uncoupled from $\overline{\Delta v}$ and $\overline{\Delta p}$. Hence (4.8) can be solved for $\overline{\Delta u}$ independently of (4.9) and (4.10). However, these last two equations, the y-momentum and continuity ones, couple $\overline{\Delta v}$ and $\overline{\Delta p}$. It is nevertheless possible to uncouple $\overline{\Delta v}$ from $\overline{\Delta p}$ by elimination of $\overline{\Delta p}$ from the equations after differencing on the staggered grid has been performed.

4.3.1 Discretization of x-momentum equation in y-sweep

The x-momentum equation (4.8) is written in differenced form as

$$\overline{\Delta u}_{i,j} + \frac{\alpha\,\Delta\tau}{\Delta y_j^u}\left[(\breve{v}^{\nu})_u^{y+}(\overline{\Delta u})_u^{y+} - (\breve{v}^{\nu})_u^{y-}(\overline{\Delta u})_u^{y-} - \frac{1}{Re}\left(\frac{\overline{\Delta u}_{i,j+1}-\overline{\Delta u}_{i,j}}{\Delta y_j^v} - \frac{\overline{\Delta u}_{i,j}-\overline{\Delta u}_{i,j-1}}{\Delta y_{j-1}^v}\right)\right]$$

$$= \Delta\tau\,(F_u^n - \check{u}^\nu - \alpha\,\check{G}_u^\nu)_{i,j}$$

When expressions for the interpolates of overbarred quantity $\overline{\Delta u}$ similar to those found in Section 4.2.3 are introduced into this last equation, we obtain, after regrouping terms,

$$\left[\frac{\alpha\,\Delta\tau}{\Delta y_j^u}\left\{-(\check{v}^\nu)_u^{y-}\frac{\nabla y_j^u}{\Delta y_{j-1}^v} - \frac{1}{Re\,\Delta y_{j-1}^v}\right\}\right]\overline{\Delta u}_{i,j-1}$$

$$+\left[1+\frac{\alpha\,\Delta\tau}{\Delta y_j^u}\left\{(\check{v}^\nu)_u^{y+}\frac{\nabla y_{j+1}^u}{\Delta y_j^v} - (\check{v}^\nu)_u^{y-}\frac{\nabla y_{j-1}^v}{\Delta y_{j-1}^v} + \frac{1}{Re\,\Delta y_j^v} + \frac{1}{Re\,\Delta y_{j-1}^v}\right\}\right]\overline{\Delta u}_{i,j}$$

$$+\left[\frac{\alpha\,\Delta\tau}{\Delta y_j^u}\left\{(\check{v}^\nu)_u^{y+}\frac{\nabla y_j^v}{\Delta y_j^v} - \frac{1}{Re\Delta y_j^v}\right\}\right]\overline{\Delta u}_{i,j+1} = \Delta\tau\,(R_u)_{i,j} \qquad (4.20)$$

where $(R_u)_{i,j} = (F_u^n - \check{u}^\nu - \alpha\,\check{G}_u^\nu)_{i,j}$, in which $(\check{G}_u^\nu)_{i,j}$ is obtained from (4.17) and $(F_u^n)_{i,j} = (4u_{i,j}^n - u_{i,j}^n)/3$. For a given x-coordinate location, x_I, the setting up of (4.20) for each j, $2 \le j \le J-1$, where J is the number of grid points in the y-direction, gives a tridiagonal system of equations which has to be solved for $\overline{\Delta u}_{I,j}$. This is done at each $x_\mathcal{I}$, $2 \le \mathcal{I} \le I-1$, where I is the number of grid points in the x-direction, in order to obtain $\overline{\Delta u}_{i,j}$, for all i,j. The flow quantities at $x_\mathcal{I}$, $\mathcal{I}=1$ and $\mathcal{I}=I$, are specified as boundary conditions and this is why the tridiagonal systems are set up only for $x_\mathcal{I}$, $2 \le \mathcal{I} \le I-1$.

Note that the implicit left-hand side of (4.20) comes from using central differences for the viscous derivatives. Near a solid wall, the use of non-central differencing as explained in Section 4.2.3 will result in a slightly modified equation [24]. Also, $\overline{\Delta u}$ is zero on a solid wall even when the wall has non-zero velocity. We recall that this is because the velocity, $u_{i,w}^{n+1}$, of the wall at t^{n+1} is imposed as a boundary condition and remains fixed during the pseudo-time relaxation.

4.3.2 Discretization of y-momentum and continuity equations in y-sweep

Proceeding as with the x-momentum equation, we can write down the y-momentum and continuity equations (4.9) and (4.10) in differenced form, after using expressions like those of Section 4.2.3 for the interpolates of $\overline{\Delta v}$, and regrouping terms.

$$\frac{\alpha\,\Delta\tau}{\Delta y_j^v}\left(\overline{\Delta p}_{i,j+1}-\overline{\Delta p}_{i,j}\right)+\left[\frac{\alpha\,\Delta\tau}{\Delta y_j^v}\left\{-(\check{v}^\nu)_v^{y-}\frac{\nabla y_j^v}{\Delta y_j^u}-\frac{1}{Re\,\Delta y_j^u}\right\}\right]\overline{\Delta v}_{i,j-1}$$

$$+\left[1+\Delta\tau+\frac{\alpha\,\Delta\tau}{\Delta y_j^v}\left\{(\check{v}^\nu)_v^{y+}\frac{\nabla y_{j+1}^v}{\Delta y_{j+1}^u}-(\check{v}^\nu)_v^{y-}\frac{\nabla y_j^u}{\Delta y_j^u}+\frac{1}{Re\,\Delta y_{j+1}^u}+\frac{1}{Re\,\Delta y_j^u}\right\}\right]\overline{\Delta v}_{i,j}$$

$$+\left[\frac{\alpha\,\Delta\tau}{\Delta y_j^v}\left\{(\check{v}^\nu)_v^{y+}\frac{\nabla y_{j+1}^u}{\Delta y_{j+1}^u}-\frac{1}{Re\Delta y_{j+1}^u}\right\}\right]\overline{\Delta v}_{i,j+1}=\Delta\tau(R_v)_{i,j}\,. \tag{4.21}$$

$$\overline{\Delta p}_{i,j}+\frac{\Delta\tau}{\delta}\frac{1}{\Delta y_j^u}(\overline{\Delta v}_{i,j}-\overline{\Delta v}_{i,j-1})=-\frac{\Delta\tau}{\delta}(\boldsymbol{\nabla}\cdot\check{\mathbf{V}})_{i,j}^\nu \tag{4.22}$$

As before, we have $(R_v)_{i,j}=(F_v^n-\check{v}^\nu-\alpha\,\check{G}_v^\nu)_{i,j}$, where $(\check{G}_v^\nu)_{i,j}$ and $(\boldsymbol{\nabla}\cdot\check{\mathbf{V}})_{i,j}^\nu$ are obtained from (4.18) and (4.19), repectively, and $(F_v^n)_{i,j}=(4v_{i,j}^n-v_{i,j}^n)/3$. It is seen that (4.21) requires the expression $\overline{\Delta p}_{i,j+1}-\overline{\Delta p}_{i,j}$, which can be obtained from (4.22), namely

$$\overline{\Delta p}_{i,j+1}-\overline{\Delta p}_{i,j}=-\frac{\Delta\tau}{\delta}\left[(\boldsymbol{\nabla}\cdot\check{\mathbf{V}})_{i,j+1}^\nu-(\boldsymbol{\nabla}\cdot\check{\mathbf{V}})_{i,j}^\nu\right]$$

$$-\frac{\Delta\tau}{\delta}\frac{\overline{\Delta v}_{i,j+1}}{\Delta y_{j+1}^u}+\frac{\Delta\tau}{\delta}\left(\frac{1}{\Delta y_{j+1}^u}+\frac{1}{\Delta y_j^u}\right)\overline{\Delta v}_{i,j}-\frac{\Delta\tau}{\delta}\frac{\overline{\Delta v}_{i,j-1}}{\Delta y_j^u}.$$

Upon substituting this last expression in (4.21), we thus obtain for the latter

$$\left[\frac{\alpha\,\Delta\tau}{\Delta y_j^v}\left\{-(\check{v}^\nu)_v^{y-}\frac{\nabla y_j^v}{\Delta y_j^u}-\frac{1}{Re\,\Delta y_j^u}-\frac{\Delta\tau}{\delta}\frac{1}{\Delta y_j^u}\right\}\right]\overline{\Delta v}_{i,j-1}$$

$$+\left[1+\Delta\tau+\frac{\alpha\,\Delta\tau}{\Delta y_j^v}\left\{(\check{v}^\nu)_v^{y+}\frac{\nabla y_{j+1}^v}{\Delta y_{j+1}^u}-(\check{v}^\nu)_v^{y-}\frac{\nabla y_j^u}{\Delta y_j^u}\right.\right.$$

$$\left.\left.+\frac{1}{Re\,\Delta y_{j+1}^u}+\frac{1}{Re\,\Delta y_j^u}+\frac{\Delta\tau}{\delta}\frac{1}{\Delta y_j^u}+\frac{\Delta\tau}{\delta}\frac{1}{\Delta y_{j+1}^u}\right\}\right]\overline{\Delta v}_{i,j}$$

$$+\left[\frac{\alpha\,\Delta\tau}{\Delta y_j^v}\left\{(\check{v}^\nu)_v^{y+}\frac{\nabla y_{j+1}^u}{\Delta y_{j+1}^u}-\frac{1}{Re\,\Delta y_{j+1}^u}-\frac{\Delta\tau}{\delta}\frac{1}{\Delta y_{j+1}^u}\right\}\right]\overline{\Delta v}_{i,j+1}$$

$$=\Delta\tau\,(R_v)_{i,j}+\frac{\alpha\,\Delta\tau}{\Delta y_j^v}\frac{\Delta\tau}{\delta}\left[(\boldsymbol{\nabla}\quad\check{\mathbf{V}})_{i,j+1}^v-(\boldsymbol{\nabla}\quad\check{\mathbf{V}})_{i,j}^v\right]\qquad(4.23)$$

This is the tridiagonal system of equations which has to be solved to obtain $(\overline{\Delta v})_{i,j}$, which has been uncoupled from $(\overline{\Delta p})_{i,j}$. A similar procedure as in the case of the y-sweep for $\overline{\Delta u}_{i,j}$ is used, namely equation (4.23) is set up for each j, $2 \le j \le J-2$ ($j = J-1$ corresponds, for example, to a solid wall [17]), to obtain tridiagonal systems of equations which are solved for $\overline{\Delta v}_{I,j}$, where $2 \le I \le I-1$. $\overline{\Delta p}_{i,j}$ is obtained from (4.22) after solving for $\overline{\Delta v}_{i,j}$.

4.4 The x-Sweep

The solution in the x-sweep proceeds in similar manner as in the y-sweep, namely Δv which is uncoupled from Δu and Δp is first solved for through the difference form of equation (4.12), and Δp is eliminated from (4.11) with the aid of (4.13) to obtain Δu. Here we will thus only give the scalar tridiagonal systems of equations that one sets up from the differenced forms of equations (4.11-4.13). First, we have the equation for Δv.

$$\left[\frac{\alpha\,\Delta\tau}{\Delta x_i^v}\left\{-(\breve{u}^\nu)_v^{x-}\frac{\nabla x_i^v}{\Delta x_{i-1}^u}-\frac{1}{Re\,\Delta x_{i-1}^u}\right\}\right]\Delta v_{i-1,j}$$

$$+\left[1+\frac{\alpha\,\Delta\tau}{\Delta x_i^v}\left\{(\breve{u}^\nu)_i^{x+}\frac{\nabla x_{i+1}^v}{\Delta x_i^u}-(\breve{u}^\nu)_v^{x-}\frac{\nabla x_{i-1}^u}{\Delta x_{i-1}^u}+\frac{1}{Re\,\Delta x_i^u}+\frac{1}{Re\,\Delta x_{i-1}^u}\right\}\right]\Delta v_{i,j}$$

$$+\left[\frac{\alpha\,\Delta\tau}{\Delta x_i^v}\left\{(\breve{u}^\nu)_v^{x+}\frac{\nabla x_i^u}{\Delta x_i^u}-\frac{1}{Re\,\Delta x_i^u}\right\}\right]\Delta v_{i+1,j}=\overline{\Delta v}_{i,j} \tag{4.24}$$

and then the equation for Δu

$$\left[\frac{\alpha\,\Delta\tau}{\Delta x_i^u}\left\{-(\breve{u}^\nu)_u^{x-}\frac{\nabla x_i^u}{\Delta x_i^v}-\frac{1}{Re\,\Delta x_i^v}-\frac{\Delta\tau}{\delta}\frac{1}{\Delta x_i^v}\right\}\right]\Delta u_{i-1,j}$$

$$+\left[1+\Delta\tau+\frac{\alpha\,\Delta\tau}{\Delta x_i^u}\left\{(\breve{u}^\nu)_u^{x+}\frac{\nabla x_{i+1}^u}{\Delta x_{i+1}^v}-(\breve{u}^\nu)_u^{x-}\frac{\nabla x_i^v}{\Delta x_i^v}\right.\right.$$
$$\left.\left.+\frac{1}{Re\,\Delta x_i^v}+\frac{1}{Re\,\Delta x_{i+1}^v}+\frac{\Delta\tau}{\delta}\frac{1}{\Delta x_i^v}+\frac{\Delta\tau}{\delta}\frac{1}{\Delta x_{i+1}^v}\right\}\right]\Delta u_{i,j}$$

$$+\left[\frac{\alpha\,\Delta\tau}{\Delta x_i^u}\left\{(\breve{u}^\nu)_u^{x+}\frac{\nabla x_{i+1}^v}{\Delta x_{i+1}^v}-\frac{1}{Re\,\Delta x_{i+1}^v}-\frac{\Delta\tau}{\delta}\frac{1}{\Delta x_{i+1}^v}\right\}\right]\Delta u_{i+1,j}$$

$$=\overline{\Delta u}_{i,j}-\frac{\alpha\,\Delta\tau}{\Delta x_i^u}(\overline{\Delta p}_{i+1,j}-\overline{\Delta p}_{i,j})\,. \tag{4.25}$$

The solving of (4.24) and (4.25) is done as follows. The setting up of (4.24) (or (4.25)) for each i, $2\le i\le I-1$, gives a tridiagonal system of equations which is solved for $\Delta u_{i,J}$ (or $\Delta v_{i,\mathcal{J}}$), and this is done at each $y_\mathcal{J}$, $2\le\mathcal{J}\le J-1$ for $\Delta u_{i,j}$, and $2\le\mathcal{J}\le J-2$ for $\Delta v_{i,j}$. Finally, the pressure variation Δp is recovered by the relation

$$\Delta p_{i,j}+\frac{\Delta\tau}{\delta}\frac{1}{\Delta x_i^t}\left[\Delta u_{i,j}-\Delta u_{i-1,j}\right]=\overline{\Delta p}_{i,j}\,.$$

At this point, details will be given concerning the treatment of inflow or outflow boundary conditions, where we suppose that we have the inflow and outflow at x_1, $i = 1$ and $i = I$, respectively, or at x_1 and x_I. Fluid is entering the domain at the inlet, such that we impose the velocity profile there; the velocity components u and v will thus be set to known values at x_1, for example in the form of developed velocity profiles for laminar flow (see Sections 5.1.2 and 8.1). Since the velocity components u and v are imposed at the inflow, we thus have that $\Delta u_{1,j}$ and $\Delta v_{1,j}$ are equal to zero there. Also, since we are using a staggered mesh there is no need to impose boundary conditions for pressure at the inflow. This can be seen from (4.17), where we only need the quantities $p_{i,j}$ and $p_{i+1,j}$, and not $p_{i-1,j}$ which represents the inlet pressure when (4.20) is set up for $i = 2$.

Now, at the outlet, $x = x_I$, the fluid leaves the domain and the velocity components are thus extrapolated from inside the fluid domain, using the following formulas,

$$u_{I,j} = \left(1 + \frac{\Delta x_I^v}{\Delta x_{I-1}^v}\right) u_{I-1,j} - \frac{\Delta x_I^v}{\Delta x_{I-1}^v} u_{I-2,j} , \tag{4.26}$$

$$v_{I,j} = \left(1 + \frac{\Delta x_{I-1}^u}{\Delta x_{I-2}^u}\right) v_{I-1,j} - \frac{\Delta x_{I-1}^u}{\Delta x_{I-2}^u} v_{I-2,j} , \tag{4.27}$$

which are second-order accurate. Thus, after each pseudo-time step the velocity components $\breve{u}_{I,j}$ and $\breve{v}_{I,j}$ are found from (4.26) and (4.27), which allows to compute (4.17) and (4.18) when equations (4.20) and (4.23) are set up for $i = I - 1$, at $x = x_{I-1}$. The values of $\Delta u_{I,j}$ and $\Delta v_{I,j}$ can be set equal to zero, which introduces an error which is of the same order as the Euler pseudo-time scheme chosen [27], or formulas (4.26) and (4.27) can be incorporated in the implicit left-hand sides of (4.24) and (4.25) [24]. As far as the pressure at the outlet is concerned, $p_{I,j}$, we see that it is needed when writing (4.17) at x_{I-1}, and it can either be set equal

to zero or calculated from the momentum equation normal to a wall at the outlet, using the following formula.

$$p_{I,J} - p_{I,2} = -\int_{y_2^v}^{y_J^v} \left[\frac{\partial(uv)}{\partial x} + \frac{\partial(vv)}{\partial y} - \frac{1}{Re} \left(\frac{\partial^2 v}{\partial x^2} + \frac{\partial^2 v}{\partial y^2} \right) \right]_{x=x_I^v} dy \,. \qquad (4.28)$$

The pressure point $p_{I,2}$ would be for example that the nearest to the bottom wall, and in the examples treated in this Thesis, it is set equal to zero in order to fix the pressure level in the domain.

Chapter 5

VALIDATION TEST PROBLEMS

Two benchmark problems will first be solved by considering steady flow problems, the purpose of which is to test the accuracy of the difference representation of the differential operators and the effectiveness of the pseudo-time iteration technique. Indeed, whether the artificial compressibility method is used to solve the steady or unsteady flow equations, the procedure is exactly the same regarding the spatial discretization and pseudo-time relaxation. Thus, the flow inside a square cavity with a lid moving at constant velocity is calculated and comparison of the present results with those published by Soh (Ref. [17]) is done. The flow over a backward-facing step is then computed and comparison with Gartling's calculations (Ref. [28]) is made.

The validation of the method as applied to actual unsteady flow problems proceeds as described in Section 5.2. First, the numerical results obtained with the present artificial compressibility method for the unsteady flow between two oscillating plates are compared with the analytical solution derived for that par-

ticular problem. Finally, the unsteady flow inside a cavity with an oscillating lid is computed and the results compared with Soh and Goodrich [16].

5.1 Validation for Steady Flow Problems

In the case of a steady flow problem, the term $\partial \mathbf{V}/\partial t$ disappears from (3.1) and the equations to be solved are thus

$$\mathbf{G}(\mathbf{V}, p) = \mathbf{0}, \tag{5.1}$$

$$\boldsymbol{\nabla} \cdot \mathbf{V} = 0. \tag{5.2}$$

The term $\mathbf{G}(\mathbf{V}, p)$ is given by (3.3), as before. The pseudo-time iteration is introduced at this point (see also equations (3.8-3.9)),

$$\frac{\partial \check{\mathbf{V}}}{\partial \tau} + \check{\mathbf{G}} = \mathbf{0}, \tag{5.3}$$

$$\delta \frac{\partial \check{p}}{\partial \tau} + \boldsymbol{\nabla} \cdot \check{\mathbf{V}} = 0, \tag{5.4}$$

and application of the implicit Euler scheme to semi-discretize (5.3) and (5.4) in pseudo-time gives

$$\frac{\check{\mathbf{V}}^{\nu+1} - \check{\mathbf{V}}^{\nu}}{\Delta\tau} + \check{\mathbf{G}}^{\nu+1} = \mathbf{0}, \tag{5.5}$$

$$\frac{\check{p}^{\nu+1} - \check{p}^{\nu}}{\Delta\tau} + \frac{1}{\delta} \boldsymbol{\nabla} \cdot \check{\mathbf{V}}^{\nu+1} = 0. \tag{5.6}$$

These last equations are finally arranged, after putting them in Delta form, as

$$\Delta \mathbf{V} + \Delta\tau\, \Delta \mathbf{G} = -\Delta\tau\, \check{\mathbf{G}}^{\nu} , \tag{5.7}$$

$$\Delta p + \frac{\Delta\tau}{\delta} \boldsymbol{\nabla} \cdot (\Delta \mathbf{V}) = -\frac{\Delta\tau}{\delta} \boldsymbol{\nabla} \cdot \check{\mathbf{V}}^{\nu} \tag{5.8}$$

Equations (5.7) and (5.8) are thus obtained when the method of artificial compressibility is applied to the solution of steady flow problems [11, 17, 29]. Notice their great similarity with equations (3.12) and (3.13), the method of solution thus proceeds in exactly the same manner. Hence (5.7) and (5.8) are also put in the matrix form (4.4), with the difference here that (i) $\alpha = 1$, (ii) the term $1/\alpha$ is dropped from both matrices $\mathbf{A}_x$ and $\mathbf{A}_y$ in (4.5), and (iii) $\mathbf{R}$ is given by

$$\mathbf{R} = \begin{bmatrix} R_u \\ R_v \\ R_p \end{bmatrix} = \begin{bmatrix} -\check{G}_u^{\nu} \\ -\check{G}_v^{\nu} \\ -(1/\delta)\, \boldsymbol{\nabla} \cdot \check{\mathbf{V}}^{\nu} \end{bmatrix}$$

The rest of the method is as described in Chapter 4. The selection of the pseudo-time step $\Delta\tau$ and artificial compressibility δ is done as explained in Ref. [17][1], namely we have

$$\delta = \frac{1}{3\, q^2} , \quad \Delta\tau = \frac{Cr\, \Delta x}{\lambda} ,$$

where $q = \sqrt{u^2 + v^2}$ is a representative flow speed, $\lambda = q + \sqrt{q^2 + 1/\delta}$ is a characteristic propagation speed introduced by the artificial compressibility, and Δx is a typical mesh spacing. The Courant number Cr is chosen to be approximately 20 in order to select $\Delta\tau$, and then both δ and $\Delta\tau$ are optimized by numerical experimentation.

[1] See also Section 5.2 where the procedure is outlined for unsteady flow problems.

5.1.1 Driven cavity flow

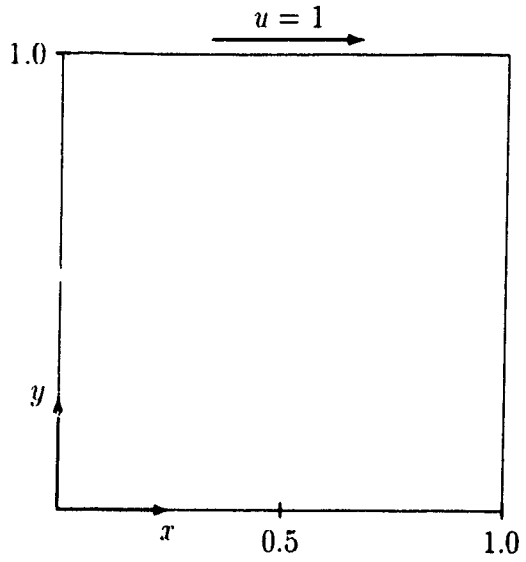

Figure 5.1: Geometry of the driven cavity flow problem.

We consider a square cavity the upper wall of which is moving at constant velocity and compute the steady flow pattern inside the cavity for three Reynolds numbers, $Re = 400,\ 1\,000,\ 5\,000$, where Re is based on the length of the cavity sides and the lid velocity, see Figure 5.1. Hence in non-dimensional units the cavity sides are of length 1 and the lid velocity is 1 as well. The initial conditions required to start the pseudo-time iteration procedure were taken to be zero velocity and pressure inside the cavity whereas a lid velocity of $u = 1$ was imposed on the upper wall. Velocity components were zero on the other walls and no boundary conditions for pressure or for the velocity components at the upper two corners are required because a staggered mesh is used [17]. Equations (5.7) and (5.8) were then iterated in pseudo-time until $\Delta \mathbf{V}$ and Δp were equal to zero, at which point the steady state solution was obtained.

Typical variations, with y (the axis of coordinate normal to the lid) of the x-component of velocity, u, at the cavity centerline, $x = 0.5$, are shown in Figure 5.2, for three Reynolds numbers and for uniform or stretched grids; in all cases the grid was defined by 40×40 points. The value, u_{max}, of the maximum recirculating velocity at $x = 0.5$, and the corresponding location, y_{max}, are shown in Table 5.1 and are seen to be in good agreement with Soh [17], as expected, although a different treatment was used for the boundary conditions, namely that described in Section 4.2.2. We note that the stretched grids used were such that the minimum mesh spacing near the walls was 0.0125 at $Re = 1\,000$, and 0.0083 at $Re = 5\,000$, in non-dimensional units.

Grid	Reynolds number	δ	$\Delta\tau$	no. time steps	y_{max}		u_{max}	
					Present solution	Ref [17]	Present solution	Ref [17]
Uniform	400	4.0	0.4	152	0.288	0.288	-0.312	-0.312
Uniform	1 000	4.0	0.4	224	0.183	0.181	- 0.347	- 0.348
Stretched	1 000	2.2	0.2	314	0.175	0.185	- 0.371	- 0.372
Stretched	5 000	2.2	0.05	2206	0.076	0.081	- 0.396	-0.415

Table 5.1: Location, y_{max}, and value, u_{max}, of the maximum recirculating component of velocity, u, for various Reynolds numbers and types of grid.

Convergence was reached and the iterations stopped in pseudo-time when the rms values of the numerical residuals of the momentum and continuity equations were all less than 10^{-4}. The residuals are the numerical evaluation of the right-hand sides of (5.7) and (5.8), at the grid points – actually, (5.7) must be divided

by $\Delta\tau$ and (5.8) by $\Delta\tau/\delta$. Figure 5.3 shows the convergence history of the rms residuals as a function of the iteration count for the computations performed at $Re = 1000$ with a stretched grid. Tables 5.2 and 5.3 list the values of the rms residuals and maximum residuals at convergence

Grid	Re	rms(R_u)	rms(R_v)	rms(R_p)
Uniform	400	6.6×10^{-5}	9.4×10^{-5}	8.0×10^{-5}
Uniform	1000	6.0×10^{-5}	9.9×10^{-5}	9.5×10^{-5}
Stretched	1000	7.4×10^{-5}	1.0×10^{-4}	7.1×10^{-5}
Stretched	5000	2.7×10^{-4}	3.0×10^{-4}	1.6×10^{-4}

Table 5.2: Rms residual values at convergence for different Reynolds numbers, Re, and types of grids

Grid	Re	max(R_u)	max(R_v)	max(R_p)
Uniform	400	9.7×10^{-4}	1.9×10^{-3}	1.3×10^{-3}
Uniform	1000	1.5×10^{-4}	3.7×10^{-4}	3.9×10^{-4}
Stretched	1000	2.0×10^{-4}	3.4×10^{-4}	2.8×10^{-4}
Stretched	5000	9.1×10^{-4}	1.9×10^{-3}	5.3×10^{-4}

Table 5.3: Maximum residual values at convergence for different Reynolds numbers, Re, and types of grids.

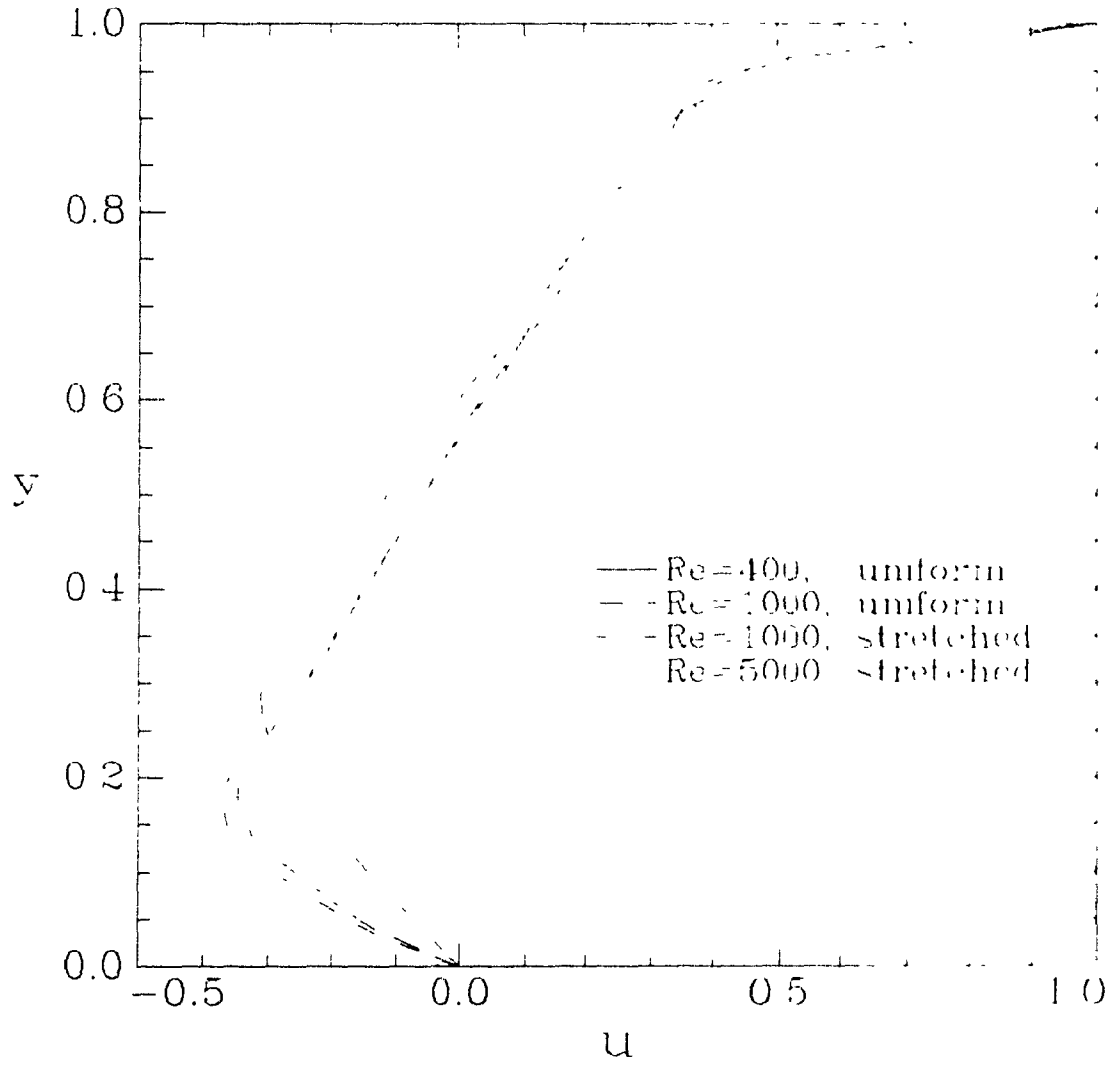

Figure 5.2: Variation of x-component of velocity, u, at cavity center-line, $x = 0.5$, for various Reynolds numbers Re and types of grids

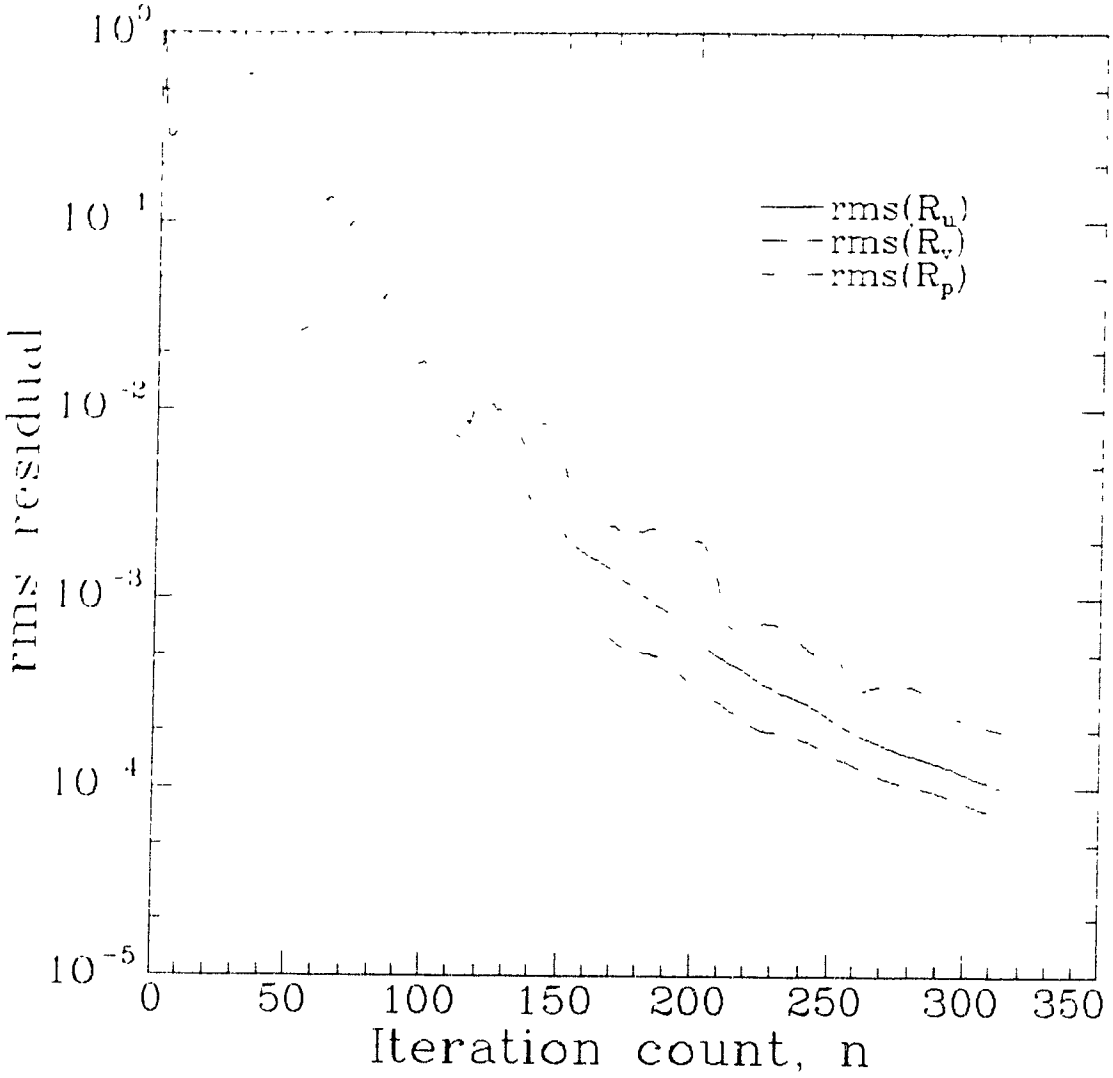

Figure 5.3: Convergence history of the rms residuals of the momentum and continuity equations as a function of the iteration count, n. The computations are for the driven cavity flow problem at a Reynolds number $Re = 1\,000$, on a stretched grid.

5.1.2 Flow over a backward-facing step

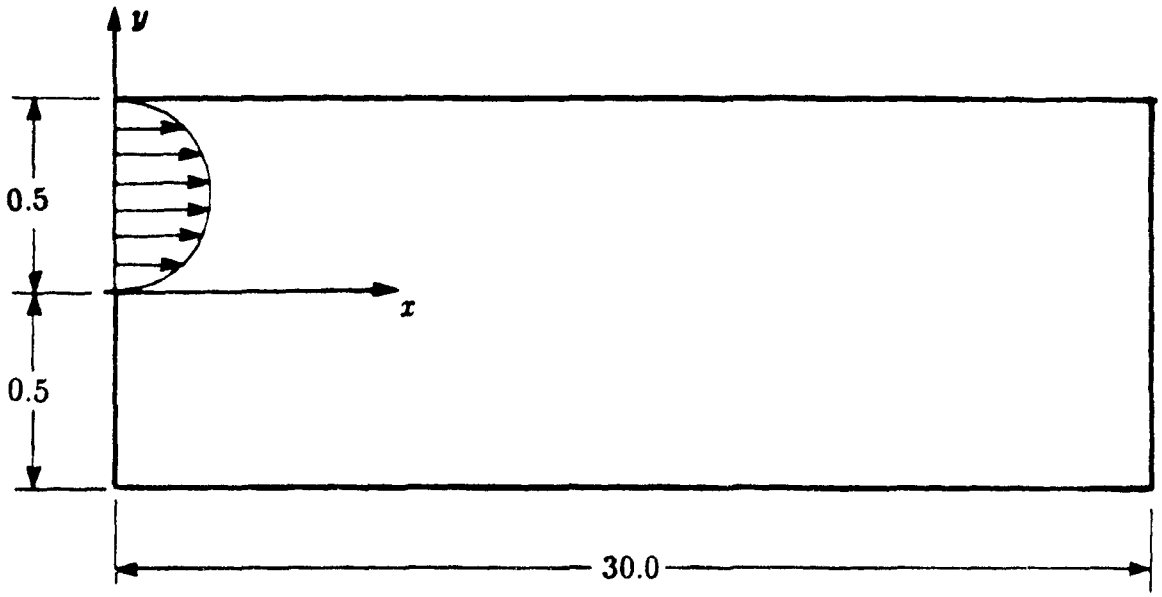

Figure 5.4. Geometry of backward-facing step problem

A detailed benchmark solution for the flow over a backward-facing step in two-dimensional Cartesian coordinates has been published by Gartling [28]. The non-dimensional geometry is shown in Figure 5.4. The downstream channel has a height of 1 whereas both the upstream channel region and the step height are equal to 1/2. The channel portion upstream of the step is excluded in this benchmark solution, and the system of coordinates is centered at the step corner. (We remark that the present method was also compared with the results of Benocci et al. [29] for the backward-facing step problem, in which the channel geometry included a portion upstream of the step. Good results were also obtained [18], for example the reattachment length at $Re = 67$ was found to be 2.1, compared to values in the range of 2.0-2.2 reported in Ref. [29]. Here, we only present a detailed

comparison of our results with those of Gartling's, as he provided more data in his presentation.)

The boundary conditions associated with the geometry of Figure 5.4 are a developed parabolic velocity profile at the inlet, $x = 0$, $0 \leq y \leq 0.5$, which gives a x-component of velocity $u(0, y) = 24y(1/2 - y)$, and a y-component of velocity $v(0, y) = 0$. As was discussed in Chapter 4, no boundary conditions for pressure are required at the inlet because of the use of the staggered mesh. The average non-dimensional x-component of velocity at the inlet is thus equal to 1. No-slip boundary conditions apply on the walls, whereas at the outlet the velocity components are extrapolated to second-order accuracy from inside the flow domain, using the formulas (4.26) and (4.27). The pressure at the outlet is determined by integrating the normal momentum equation from the bottom wall [17], using equation (4.28) in which the trapezoidal rule was employed for the integration. The pressure at (x_I^n, y_2^n), which is $p_{I,2}$, was set equal to zero during the computations, after the computations were completed, the pressure data was normalized by taking the point at which the pressure was zero to be at the step corner, as done by Gartling.

The mesh was stretched by concentrating the grid points near the walls and near the step region, and the resulting grid was much like that shown in Figure 4.1, page 45, except that the mesh portion upstream of the step was omitted, as per Figure 5.4. The hyperbolic-tangent stretching function was used normal to the upper and lower walls, and the hyperbolic-sine function was employed along the streamwise, x-direction. The domain had a non-dimensional length of 30, with 560 grid points spanning the streamwise direction; this gave a minimum mesh spacing of 0.08 at the step and maximum mesh spacing of 0.21 at the outlet, in non-dimensional units. In the cross-stream direction (y-direction), 50 points were included and the minimum mesh spacing was 0.015 at the walls.

The computations were performed at a Reynolds number of 800, based on downstream channel height and average inlet velocity. The initial conditions were $v = p = 0$ throughout the whole domain, whereas $u(x, y) = 24y(1/2 - y)$, $0 \leq x \leq 30$, $0 \leq y \leq 1/2$, and $u = 0$ for $0 \leq x \leq 30$, $-1/2 \leq y \leq 0$. The artificial compressibility, δ, and pseudo-time step, $\Delta\tau$, were set equal to 0.8 and 0.2, respectively. The convergence criteria was when the rms values of the numerical residuals of the momentum and continuity equations were all less than 3×10^{-5}, which took 2006 iterations.

Tables 5.4 and 5.5 present cross-channel profiles of the velocity components u and v, and of pressure p, at two different streamwise locations, $x = 7$ and $x = 15$. Comparison is made with the tabulated results of Gartling [28].

This problem has two recirculating eddies, one on the bottom wall, $y = -1/2$, and one on the upper wall, $y = 1/2$. The length of the lower wall eddy was found to be 6.0 in the present calculations, compared to 6.1 in Ref. [28], whereas the point of separation, point of reattachment and length of the upper wall eddy were computed to be 4.80, 10.30 and 5.50, respectively, compared to 4.85, 10.48 and 5.63 in Ref. [28].

Finally, the pressure and shear stress profiles along the upper wall and the lower wall of the channel are plotted in Figures 5.5 and 5.6, respectively.

All these results show good agreement with Gartling's results [28], which allows us to proceed further and consider unsteady flow problems. This is done in the next section.

	u		100 v		p	
y	present	Ref [28]	present	Ref [28]	present	Ref.[28]
0 50	0 000	0.000	0 000	0.000	0.1523	0.1562
0 45	-0 041	-0 038	-0.035	-0.027	0.1523	0.1562
0 40	-0 054	-0.049	-0.107	-0 086	0.1523	0.1562
0 35	-0 037	-0 032	-0.172	-0.147	0 1523	0 1562
0.30	0 009	0.015	-0 198	-0 193	0.1523	0.1562
0 25	0 089	0.092	-0 181	-0.225	0.1523	0 1562
0 20	0 202	0 204	-0 140	-0.268	0.1524	0.1563
0 15	0.353	0 349	-0 128	-0.362	0.1528	0 1567
0.10	0.532	0.522	-0.200	-0.544	0.1536	0.1574
0.05	0 723	0 709	-0.378	-0 823	0.1551	0.1590
0.00	0 899	0 885	-0.624	-1.165	0.1575	0.1615
-0 05	1 034	1 024	-0.886	-1.507	0 1610	0 1652
-0 10	1 109	1.105	-1.110	-1.778	0.1652	0 1697
-0.15	1.116	1 118	-1.250	-1.925	0.1697	0.1746
-0 20	1.058	1.062	-1.274	-1.917	0 1738	0.1792
-0.25	0.938	0.948	-1.182	-1.748	0 1773	0.1831
-0.30	0.784	0 792	-0.961	-1.423	0.1798	0.1859
-0.35	0.609	0.613	-0.650	-1.000	0.1813	0.1876
-0.40	0.427	0 428	-0.296	-0.504	0 1821	0.1885
-0.45	0.231	0 232	-0 053	-0.118	0 1824	0.1888
-0 50	0.000	0.000	0.000	0.000	0.1824	0.1889

Table 5.4: Cross-channel profiles at $x = 7$

	u		$100\,v$		p	
y	present	Ref [28]	present	Ref [28]	present	Ref [28]
0.50	0.000	0 000	0 000	0 000	0 2450	0 2460
0.45	0 104	0 101	0 020	0 021	0 2450	0 2460
0.40	0.207	0 202	0.069	0 072	0 2450	0 2459
0.35	0.311	0.304	0.132	0 140	0 2450	0 2459
0 30	0.416	0 408	0.193	0 207	0.2450	0 2459
0.25	0 521	0 512	0 240	0 260	0 2450	0 2459
0 20	0 622	0 613	0 259	0 288	0 2450	0 2459
0 15	0 712	0 704	0 248	0 283	0 2450	0 2459
0 10	0.785	0 779	0 205	0 245	0 2450	0 2459
0.05	0.834	0 831	0 135	0 180	0 2450	0 2459
0 00	0.853	0.853	0 049	0 095	0 2450	0 2459
-0.05	0 841	0 844	-0 041	0 003	0 2450	0 2459
-0.10	0 798	0.804	-0.121	-0 081	0 2450	0 2459
-0.15	0.729	0.737	-0 181	-0 147	0.2450	0.2459
-0.20	0.640	0.649	-0 211	-0 185	0 2450	0 2459
-0.25	0.538	0.547	-0.211	-0 191	0.2450	0 2459
-0.30	0.431	0.438	-0.178	-0.166	0.2450	0 2459
-0.35	0.322	0.328	-0.126	-0 119	0.2450	0.2459
-0.40	0.214	0.218	-0.067	-0.065	0 2451	0 2459
-0.45	0.107	0.109	-0.020	-0.019	0.2451	0.2459
-0.50	0.000	0.000	0.000	0.000	0.2451	0 2459

Table 5.5. Cross-channel profiles at $r = 15$

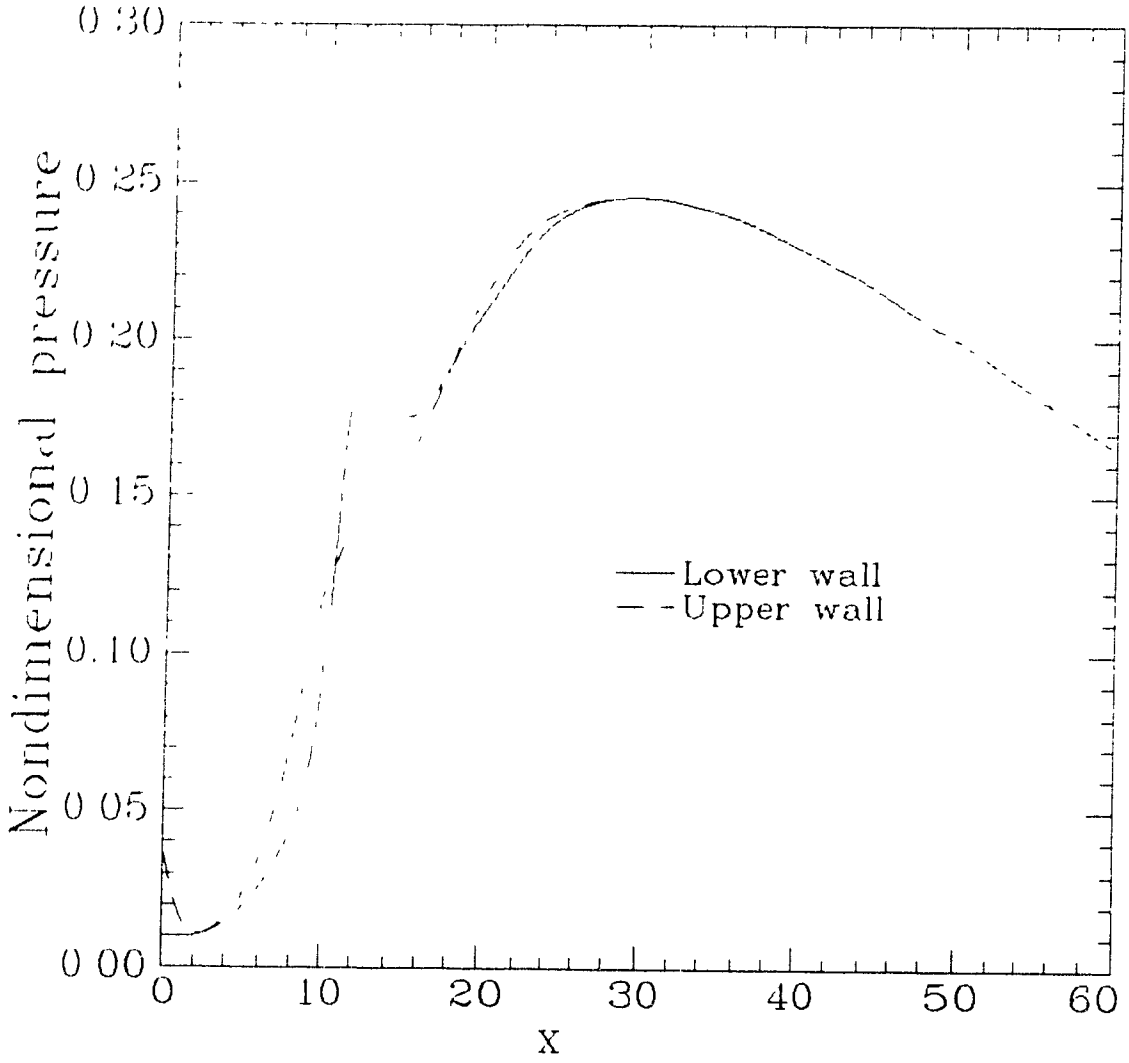

Figure 5.5: Pressure profiles along the upper wall and the lower wall of the channel.

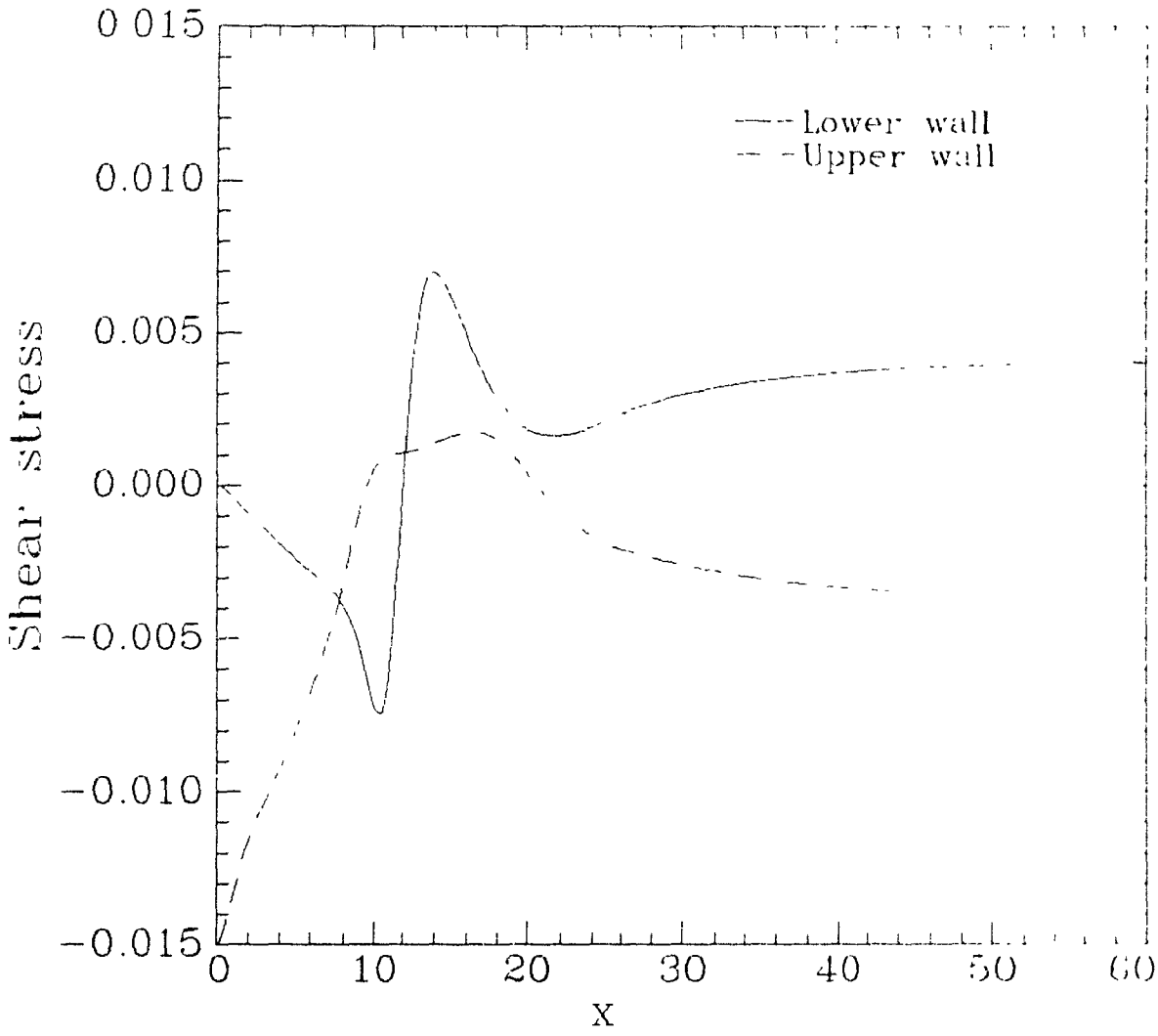

Figure 5.6: Shear stress profiles along the upper wall and the lower wall of the channel.

5.2 Validation for Unsteady Flow Problems

The equations have been developed in Chapter 4. We first need to determine the artificial compressibility, δ, and the pseudo-time step, $\Delta\tau$. To that end, we consider the one-dimensional inviscid model problem from equations (3.8) and (3.9), dropping the undifferentiated and non-homogeneous terms; it is put in matrix form as

$$\frac{\partial}{\partial\tau}\begin{Bmatrix}\check{u}\\ \check{p}\end{Bmatrix}+\begin{bmatrix}2\alpha\check{u} & \alpha\\ 1/\delta & 0\end{bmatrix}\frac{\partial}{\partial x}\begin{Bmatrix}\check{u}\\ \check{p}\end{Bmatrix}=0 \tag{5.9}$$

The eigenvalues, $\lambda_{\pm}$, of the square matrix in (5.9) are

$$\lambda_{\pm}=\alpha\check{u}\pm\sqrt{(\alpha\check{u})^2+\alpha/\delta} \tag{5.10}$$

Equations (5.9) and (5.10) are identical to those obtained by Soh and Goodrich [16], and the same conclusions apply in the present formulation, namely the system with artificial compressibility is hyperbolic in pseudo-time, since the eigenvalues are real, and it is "subsonic", since they are of opposite signs. The flow model defined by (5.9) is thus similar to a subsonic compressible flow characterized by an artificial Mach number $M_a=q\sqrt{\alpha\delta}=q\sqrt{2\delta\Delta t/3}$, in which q represents a characteristic flow speed, i.e. $q=\sqrt{u^2+v^2}$, also $\alpha=2\Delta t/3$. The artificial compressibility can be determined from (5.10) by considering $M_a\approx\sqrt{1/3}$, which provides good computing efficiency, and we thus obtain

$$\delta=\frac{1}{2q^2\,\Delta t}\,. \tag{5.11}$$

where Δt is the real, physical time step. Now, an estimate of the pseudo-time step $\Delta\tau$ is made on the basis of the formula

$$\Delta\tau = \frac{Cr\,\Delta x}{\lambda_+}\,, \tag{5.12}$$

where Δx is a characteristic mesh spacing, and a Courant number Cr of approximately 30 to 40 is chosen to evaluate $\Delta\tau$. Numerical experimentation is required to optimize both δ and $\Delta\tau$

5.2.1 Unsteady flow between oscillating plates

This problem has an analytical solution. We consider two infinite plates, parallel with each other and aligned with the $\bar{x}$-coordinate[2]. They are separated by a distance H. The top plate is fixed while the bottom one has a harmonic oscillatory motion of frequency Ω:

$$\begin{aligned} \bar{u}(\bar{y},\bar{t})\,|_{y=0} &= \Omega H \sin\Omega\bar{t}\,, \\ \bar{u}(\bar{y},\bar{t})\,|_{y=H} &= 0\,. \end{aligned} \tag{5.13}$$

H and ΩH serve as characteristic length and velocity to non-dimensionalize the equations and a dimensionless parameter, s, called the Stokes number is introduced, namely

$$s = \frac{\Omega H^2}{\nu}\,, \tag{5.14}$$

where ν is the fluid kinematic viscosity. We then have to solve the equation

$$\frac{\partial u}{\partial t} - \frac{1}{s}\frac{\partial^2 u}{\partial y^2} = 0\,,$$

subject to boundary conditions (5.13) Notice that the problem shows no dependence on the x-direction and that the y-component of velocity is zero, laminar flow is considered. The solution is

[2]In this section, barred quantities are dimensional, non-barred ones non-dimensional.

$$u(y,t) = \Im\left\{F(y)\,e^{\imath t}\right\} ,$$

where $\Im$ denotes the imaginary part and where

$$F(y) = \frac{\sinh\, \beta(1-y)}{\sinh\, \beta} ,$$

with $\imath = \sqrt{-1}$ and $\beta = \sqrt{\imath s}$.

Now, in the numerical solution to that problem, 10 grid points were chosen in the x-direction by applying periodic boundary conditions [24, 33]. Thus, even though no dependence on the x-coordinate is actually present in the problem the numerical grid was two-dimensional. In view of the choice of characteristic length and velocity made to non-dimensionalize the equations, the term $1/Re$ in (3.3) has to be replaced by $1/s$, where s is the Stokes number given by (5.14).

To obtain numerically a harmonic solution, the equations were integrated in time until a periodic solution was obtained, which was achieved after 8 harmonic cycles. Convergence in pseudo-time was reached when the rms values of the residuals of the continuity and momentum equations (calculated from the right-hand sides of (4.20), (4.21) and (4.22)) all fell below 10^{-4}, which took around 15 pseudo-time iterations (see also Table 5.7 below).

In Figures 5.7 to 5.9, the analytical results (full lines) are compared with the numerical results, plotted with markers. Table 5.6 summarizes the data that apply to each of the figures. The grid was stretched in the y-direction and the entry Δy_{min} in Table 5.6 is the minimum mesh spacing at the walls. J grid points span the y-direction; s is the Stokes number, N_t the number of time steps per harmonic cycle, and δ and $\Delta\tau$ are the artificial compressibility and pseudo-time step, respectively.

Figure 5.7 compares, for $s = 1\,000$ and $J = 25$, the influence of N_t on the solution. In Figure 5.7(a), each harmonic cycle has been divided up into 9 time

Figure	s	J	Δy_{min}	N_t	δ	$\Delta\tau$
5.7(a)	1 000	25	0.0140	9	5.7	0.6
5.7(b)	1 000	25	0.0140	19	12	1.2
5.8(a)	10 000	25	0.0140	19	12	1.2
5.8(b)	10 000	25	0.0070	19	12	1.2
5.9	10 000	51	0.0063	19	12	1.2

Table 5.6: Values of the parameters used in the computation of the results of Figures 5.7 to 5.9.

steps, whereas in Figure 5.7(b) there are 19 time steps per cycle, which effectively corresponds to a smaller time increment. As expected, this leads to a better accuracy, which is seen by comparing Figures 5.7(a) and 5.7(b). The results of Figures 5.8 and 5.9 have thus been computed with $N_t = 19$. Note that each analytical and numerical curve in Figures 5.7(b), 5.8 and 5.9, corresponds to one given instant, t^n, within the harmonic cycle, namely to

$$t^n = \frac{n}{19}\frac{2\pi}{\omega}, \qquad n = 0, 2, 4,$$

starting with the left-most curve, whereas in Figure 5.7(a) we have $t^n = (n/9)(2\pi/\omega)$, $n = 0, 1, 2$. The motion is mostly confined to near the bottom plate, which is why the results are plotted only for $0 \leq y \leq 0.2$. Figures 5.8 and 5.9 present results from between $y = 0$ to $y = 0.1$, for $s = 10\,000$.

Figure 5.8 compares, for $J = 25$, the influence of the mesh stretching on the solution. It is seen that the results are better in Figure 5.8(b), compared to Figure 5.8(a), after decreasing the spacing near the wall. The agreement between analytical and numerical results is similar to that obtained after doubling the number of mesh points, as is shown in Figure 5.9, where $J = 51$ grid points have

been included in the y-direction.

Table 5.7 shows results obtained with respect to the computations of Figure 5.9. At each n, corresponding to time step t^n, the number k of pseudo-time steps required to converge and obtain the solution at t^{n+1} is shown, along with the rms values of the residuals of the momentum and continuity equations, rms(R_u), rms(R_v), rms(R_p), and along with the maximum values of the residuals, max(R_u), max(R_v), max(R_p), at convergence. Results are for integration during the first harmonic cycle. It is seen that convergence in pseudo-time is very quick for that problem.

The method shows good performance for this simple test problem, both in terms of the number of pseudo-time steps required between two real-time levels and in terms of the accuracy obtained as compared to the analytical solution

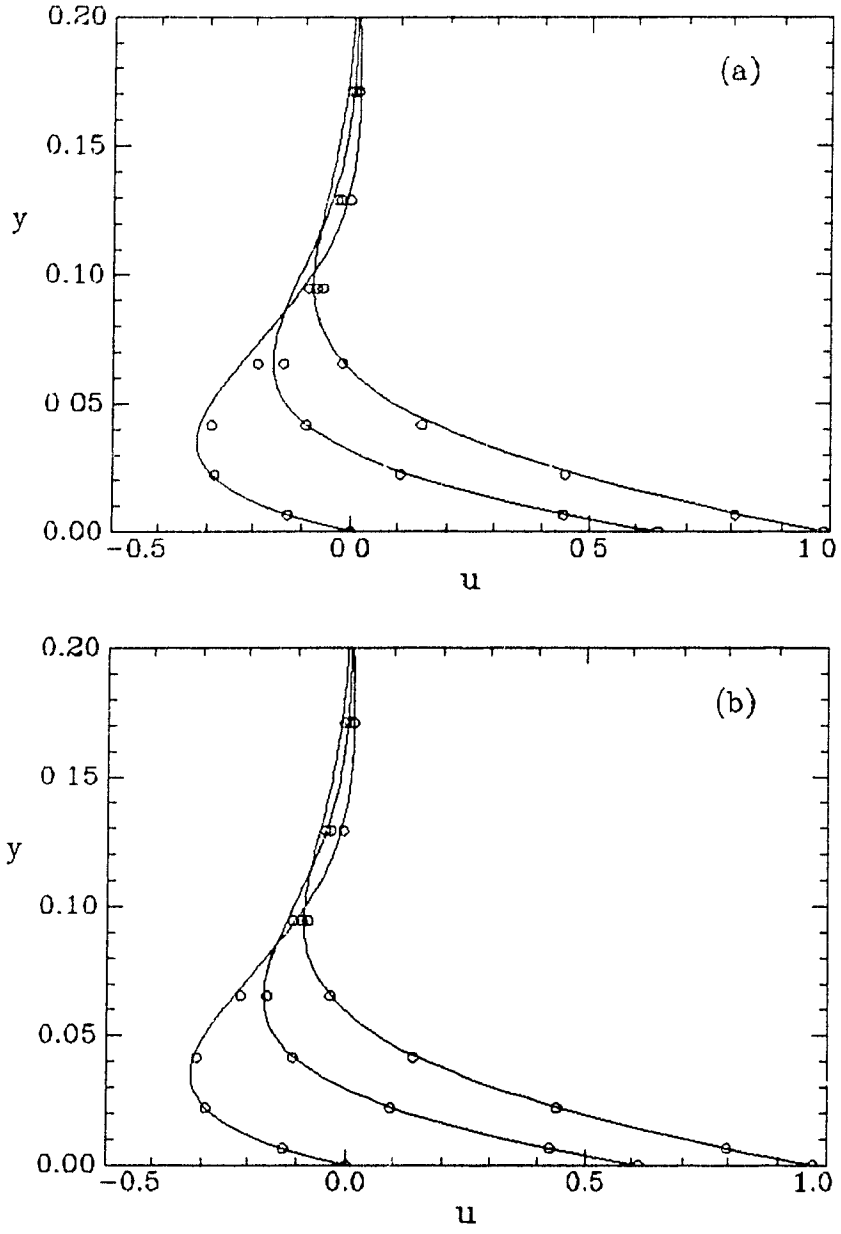

Figure 5.7: Variation with y of the x-component of velocity, u. The computations are for $s = 1\,000$, $J = 25$, and three instants within the harmonic cycle have been represented. Comparison is made for (a) $N_t = 9$, and (b) $N_t = 19$.

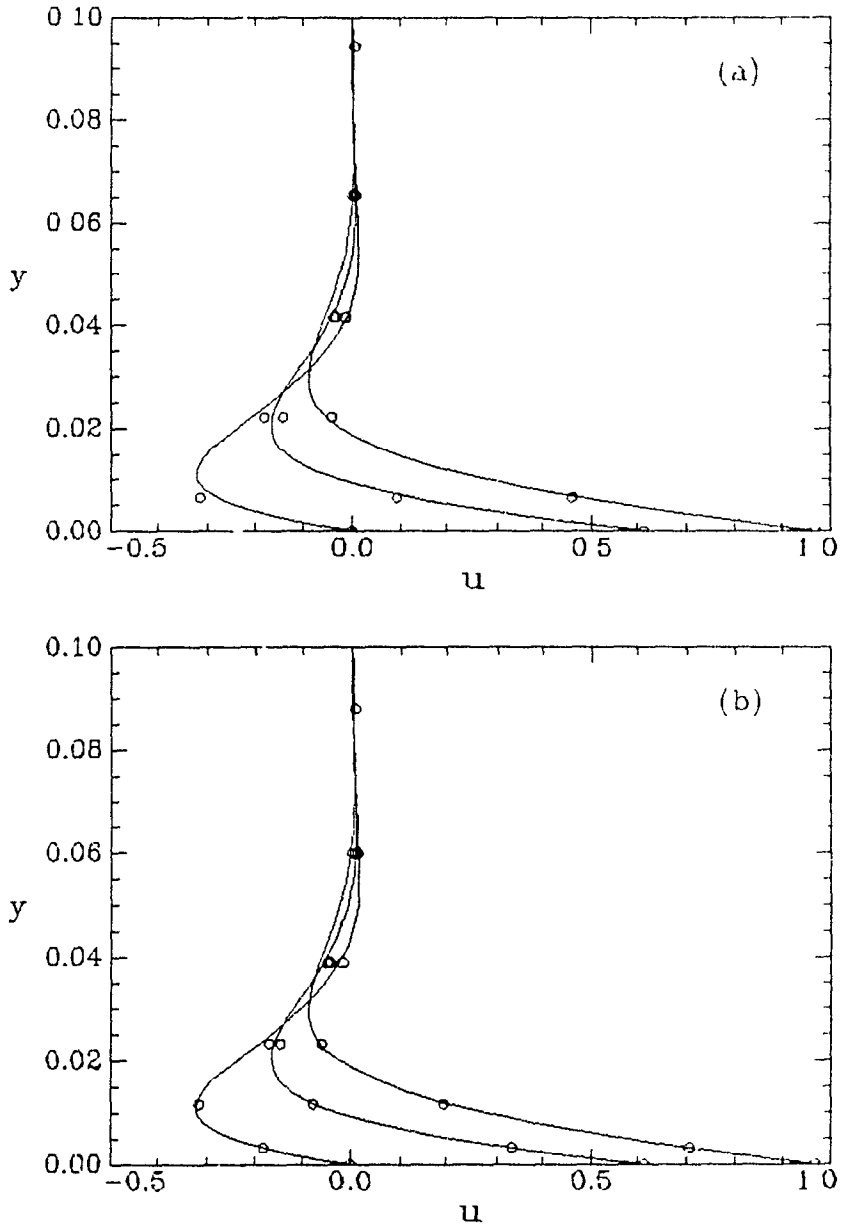

Figure 5.8: Variation with y in the x-component of velocity, u. The computations are for $s = 10000$, $J = 25$, $N_t = 19$, and three instants within the harmonic cycle have been represented. Comparison is made for (a) $\Delta y_{min} = 0.014$, and (b) $\Delta y_{min} = 0.007$.

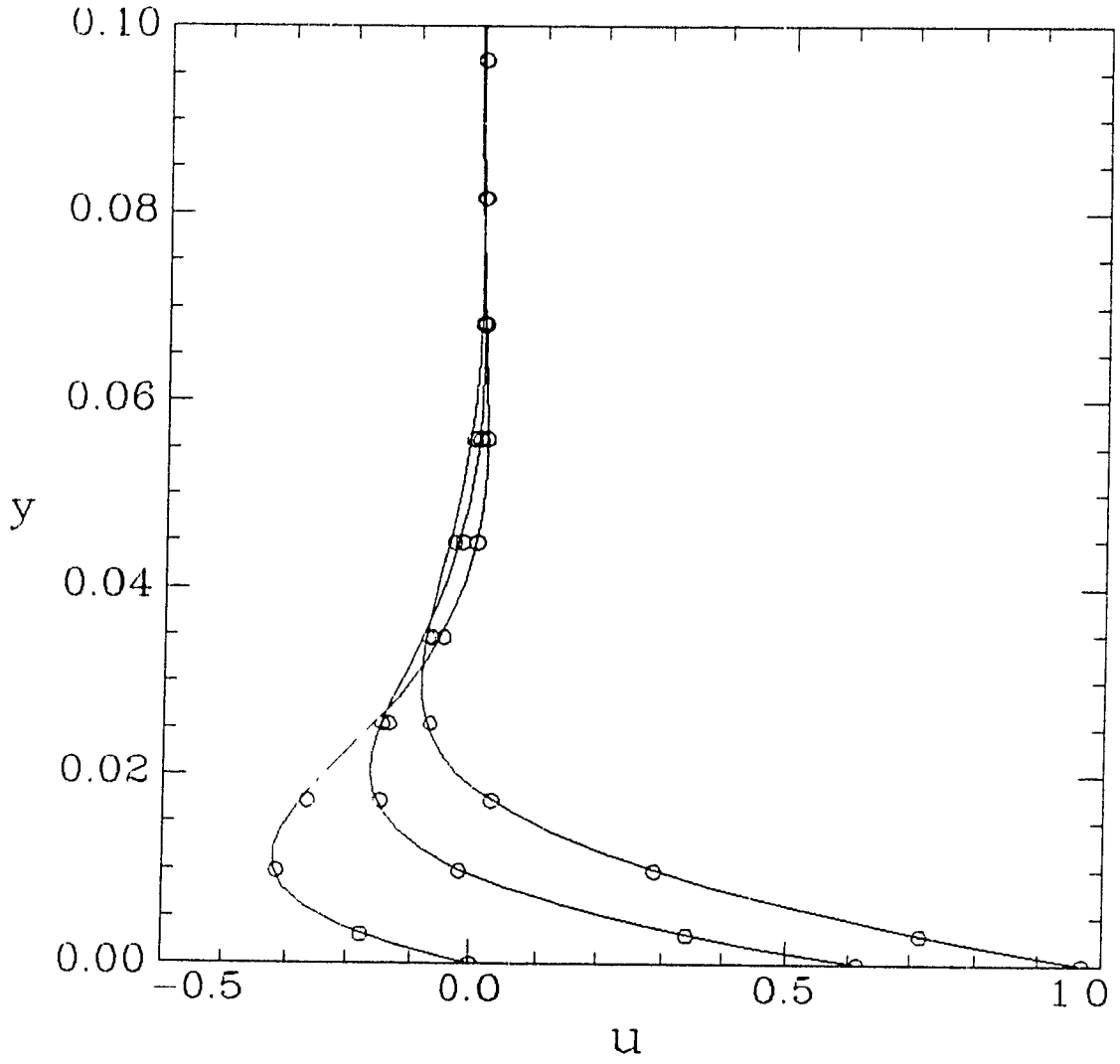

Figure 5.9: Variation with y in the x-component of velocity, u. The computations are for $s = 10\,000$, $J = 51$, $N_t = 19$, and three instants within the harmonic cycle have been represented; Δy_{min} is equal to 0.0063.

n	k	rms(R_u)	rms(R_v)	rms(R_p)	max(R_u)	max(R_v)	max(R_p)
2	15	0.658E-04	0.155E-08	0.272E-09	0.322E-03	0 154E-07	0.185E-08
3	15	0.892E-04	0.146E-06	0.202E-07	0.443E-03	0 201E-05	0 260E-06
4	15	0.926E-04	0.956E-07	0.153E-07	0.439E-03	0 105E-05	0 179E-06
5	15	0.827E-04	0.187E-06	0.414E-07	0.357E-03	0 274E-05	0 407E-06
6	15	0.636E-04	0.314E-06	0.643E-07	0.282E-03	0.285E-05	0 722E-06
7	14	0.686E-04	0.216E-06	0.559E-07	0.300E-03	0 160E-05	0 459E-06
8	14	0.607E-04	0.178E-06	0.235E-07	0 245E-03	0 160E-05	0 237E-06
9	14	0.948E-04	0.120E-06	0 131E-07	0 477E-03	0 862E-06	0 123E-06
10	15	0.794E-04	0.126E-06	0.249E-07	0.412E-03	0 117E-05	0 251E-06
11	16	0.592E-04	0.564E-07	0.202E-07	0 295E-03	0 504E-06	0 164E-06
12	16	0 674E-04	0.958E-07	0.230E-07	0 321E-03	0 876E-06	0 229E-06
13	16	0 694E-04	0 192E-06	0 721E-07	0 313E-03	0.195E-05	0 751E-06
14	16	0 649E-04	0.118E-06	0.311E-07	0 281E-03	0 146E-05	0 312E-06
15	15	0.902E-04	0.559E-07	0 984E-08	0.39\ E-03	0.473E-06	0 738E-07
16	15	0.662E-04	0.622E-07	0 814E-08	0.287E-03	0.701E-06	0 599E-07
17	14	0 740E-04	0.754E-07	0.422E-07	0 335E-03	0 602E-06	0 579E-06
18	14	0.754E-04	0.104E-06	0.341E-07	0.306E-03	0.108E-05	0 313E-06
19	15	0 627E-04	0.738E-07	0.131E-07	0.324E-03	0 729E-06	0 115E-06
20	15	0.861E-04	0.412E-07	0.582E-08	0 445E-03	0 356E-06	0 632E-07

Table 5.7: Number, k, of pseudo-time steps required to converge at time level t^n, and rms and maximum residual values at convergence. The computations are for the results of Figure 5.9.

5.2.2 Unsteady driven cavity flow with oscillating lid

The second test case that we consider is the unsteady driven cavity flow problem the geometry of which has been described in Section 5.1. However, in the present case the lid has a harmonic oscillatory motion, instead of constant velocity. Unsteady periodic solutions will thus be obtained after the equations have been integrated for a sufficient number of harmonic cycles — 8 cycles.

The lid velocity $U_w(t)$ is assumed to be of the non-dimensional form

$$U_w(t) = u(1,t) = \cos \omega t \ , \tag{5.15}$$

where ω is the non-dimensional frequency of oscillation. Soh and Goodrich [16] have performed calculations on a uniform 40×40 grid, at $Re = 400$ and for $\omega = 1$, using $N_t = 40$ time steps per harmonic cycle. The Reynolds number Re is based on the maximum lid velocity and the length of the cavity sides.

We will present results for the same values of Re, ω, N_t, and on a uniform 40×40 grid as well. As initial conditions, the converged steady state solution obtained in Section 5.1 at $Re = 400$ has been used.

The drag coefficient, C_D, on the oscillating lid as a function of time is first computed. At a given instant of time t^n, the drag D is given by integrating the wall shear stress, τ_w, on the lid, i.e. in non-dimensional form,

$$D = \int_0^1 \tau_w \, dx \ , \qquad \text{where} \qquad \tau_w = \left. \frac{\partial u}{\partial y} \right|_{y=1} \ .$$

The non-dimensional drag coefficient is defined to be

$$C_D = \frac{D}{Re} \ ,$$

and it is the latter which will be presented shortly. Now, Simpson's rule was used to perform the integration in the previous equation, and the numerical evaluation of $\partial u / \partial y$ was done as

$$\left.\frac{\partial u}{\partial y}\right|_{y=1} = \frac{\frac{8}{3}u_{i,n} - 3\,u_{i,J} + \frac{1}{3}u_{i,J-1}}{\frac{8}{3}y_J^n - 3\,y_J^n + \frac{1}{3}y_{J-1}^n},$$

where $y_J^n = 1$ here is the y-coordinate of the lid and $u_{i,n} = U_w(t)$ is the lid velocity given by (5.15).

The plot of the drag coefficient, C_D, as a function of time is presented in Figure 5.10, for the first 8 harmonic cycles. It is seen that it quickly reaches a periodic state. The maximum value of C_D is 0.0671 and it has a phase angle of -20.9 degrees with respect to the lid velocity. Soh & Goodrich [16] found a value of drag coefficient, $C_D = 0.0785$, and a phase angle value of -31.5 degrees. Their results differ sensibly from ours. One reason to explain this difference may be related to the different treatment of the boundary conditions that was employed in the present formulation, see Section 4.2.3, compared to Soh & Goodrich [16]. Also, we imposed here that the wall shear stress was equal to zero in the upper two corners, and we do not know the procedure adopted by Soh & Goodrich, which may be different. In any case, those calculations were not the primary objectives of this thesis and a thorough investigation was not pursued to clarify these details.

Next, streamline contours are plotted for different instants of time within the harmonic cycle, after the solution has reached a periodic state. Remembering that each cycle, of period T, was divided into 40 time steps, we thus have in Figure 5.11(a) streamlines for the time $t = 8T$, compared to $t = 8T + 20T/40$ in Figure 5.11(b). Similarly, in Figures 5.12(a) and 5.12(b) the times chosen are $t = 8T + 16T/40$ and $t = 8T + 36T/40$, respectively. We remark that the parts (b) in these figures are mirror images of the parts (a). The results of Figures 5.11 and 5.12 are this time very much similar to those presented by Soh & Goodrich [16] as well as other results plotted for different times, not presented here.

The values of artificial compressibility, δ, and pseudo-time step, $\Delta\tau$, chosen

were 15.3 and 1.9 respectively, compared to 50 and 20 by Soh and Goodrich [16]. As for the previous problem in Section 5.2.1, convergence in pseudo-time was reached when the rms values of the numerical residuals of the momentum and continuity equations all fell below 10^{-4}, which took around 40 pseudo-time iterations per real-time step. Table 5.8 shows, for integration during the first-half of the first harmonic cycle, the number, k, of pseudo-time steps required to converge as well as the values of rms(R_u), rms(R_v), rms(R_p), and max(R_u), max(R_v), max(R_p), at convergence.

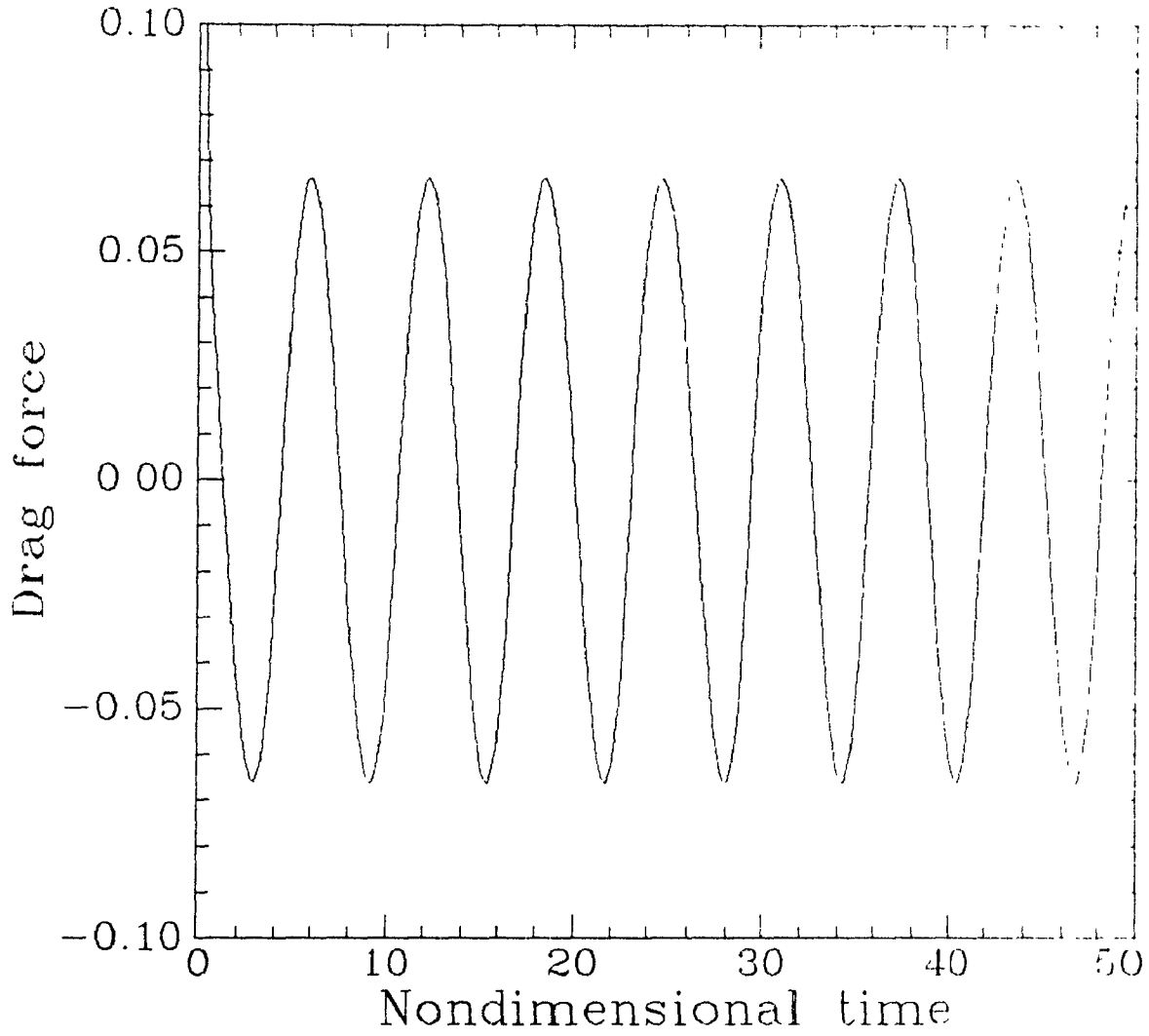

Figure 5.10: Plot of the drag force as a function of time on the oscillating lid.

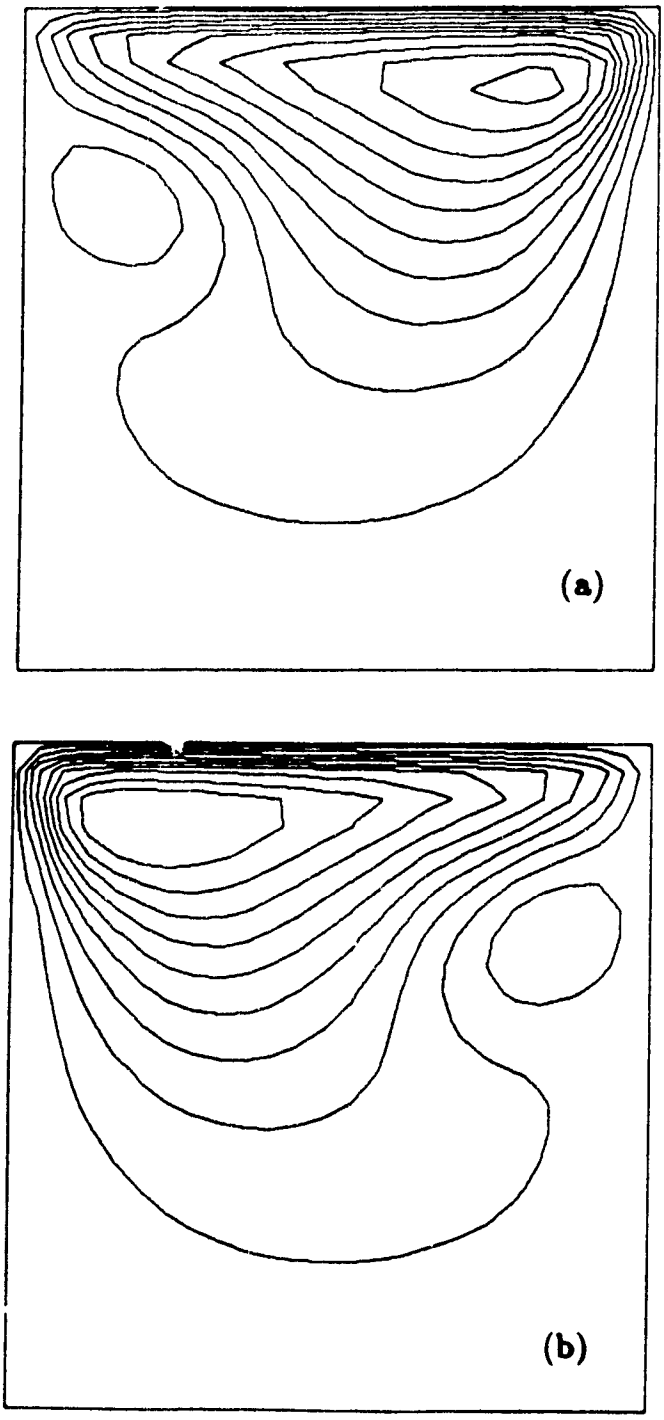

Figure 5.11: Streamline contours inside the cavity after periodicity has been attained in the flow solution. The times are (a) $t = 8T$, and (b) $t = 8T + 20T/40$.

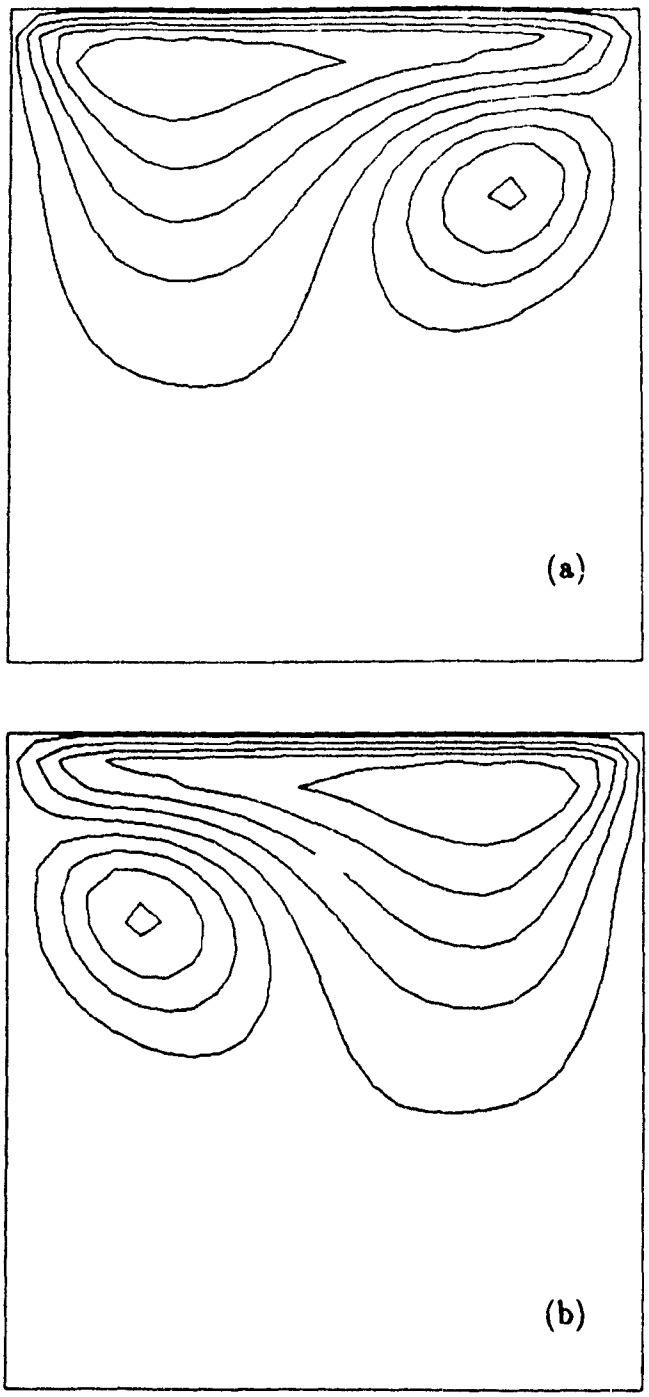

Figure 5.12: Streamline contours inside the cavity after periodicity has been attained in the flow solution. The times are (a) $t = 8T + 16T/40$, and (b) $t = 8T + 36T/40$.

n	k	rms(R_u)	rms(R_v)	rms(R_p)	max(R_u)	max(R_v)	max(R_p)
2	57	0 315E-04	0.836E-04	0 977E-04	0.393E-03	0.201E-02	0.758E-03
3	50	0 277E-04	0 544E-04	0 945E-04	0.372E-03	0.109E-02	0.513E-03
4	43	0 304E-04	0 698E-04	0.944E-04	0 465E-03	0 144E-02	0.608E-03
5	42	0 340E-04	0.951E-04	0 651E-04	0.637E-03	0.245E-02	0.924E-03
6	45	0 306E-04	0.887E-04	0.439E-04	0.635E-03	0.227E-02	0.633E-03
7	43	0.325E-04	0.999E-04	0.482E-04	0 653E-03	0.267E-02	0.654E-03
8	41	0 316E-04	0 981E-04	0.564E-04	0 613E-03	0.263E-02	0 939E-03
9	40	0 288E-04	0 879E-04	0.619E-04	0.516E-03	0 206E-02	0.112E-02
10	39	0 279E-04	0.868E-04	0 708E-04	0.424E-03	0.166E-02	0.126E-02
11	38	0.279E-04	0 941E-04	0.832E-04	0.504E-03	0.198E-02	0.154E-02
12	38	0 250E-04	0 930E-04	0.835E-04	0.426E-03	0.206E-02	0.153E-02
13	38	0 254E-04	0 966E-04	0.832E-04	0.462E-03	0 207E-02	0.147E-02
14	39	0.253E-04	0 897E-04	0.700E-04	0.523E-03	0.181E-02	0.142E-02
15	40	0.275E-04	0.882E-04	0.601E-04	0.516E-03	0.179E-02	0.118E-02
16	41	0.288E-04	0.879E-04	0.522E-04	0.506E-03	0.189E-02	0.890E-03
17	41	0 304E-04	0 925E-04	0 498E-04	0.622E-03	0.248E-02	0.749E-03
18	40	0.292E-04	0.919E-04	0.483E-04	0.563E-03	0 247E-02	0.709E-03
19	38	0.267E-04	0.898E-04	0 531E-04	0 482E-03	0.189E-02	0.108E-02
20	38	0.282E-04	0.955E-04	0.677E-04	0.580E-03	0 234E-02	0.157E-02
21	40	0.179E-04	0.951E-04	0 786E-04	0 329E-03	0.191E-02	0.103E-02

Table 5.8: Number, k, of pseudo-time steps required to converge at time level t^n and rms and maximum residual values at convergence. The computations are for the results of Figure 5.10 for the unsteady driven cavity flow problem.

Chapter 6

METHOD OF SOLUTION IN CYLINDRICAL COORDINATES

6.1 Introduction

The time-integration method using artificial compressibility, which has been developed in the previous chapters for the incompressible Navier-Stokes equations, is implemented in cylindrical coordinates in this Chapter. The scalar form of the equations is different than in Cartesian coordinates, and we expose the details for implementing the method in three-dimensional cylindrical coordinates.

6.2 Differential Form of Equations

In three-dimensional cylindrical coordinates, if we denote by u, v and w, the velocity components along the axial, radial and circumferential coordinates, x, r and θ,

then the nondimensional fluid velocity vector $\mathbf{V}$ and the terms $\mathbf{G}(\mathbf{V},p)$ and $\boldsymbol{\nabla}\cdot\mathbf{V}$ from equations (3.1-3.3) are given by

$$\mathbf{V} = \begin{bmatrix} u \\ v \\ w \end{bmatrix}, \qquad \mathbf{G}(\mathbf{V},p) = \begin{bmatrix} G_u\,(u,v,w,p) \\ G_v\,(u,v,w,p) \\ G_w\,(u,v,w,p) \end{bmatrix},$$

$$\begin{aligned} G_u(u,v,w,p) &= \frac{\partial(uu)}{\partial x} + \frac{1}{r}\frac{\partial(rvu)}{\partial r} + \frac{1}{r}\frac{\partial(wu)}{\partial\theta} + \frac{\partial p}{\partial x} \\ &- \frac{1}{Re}\left[\frac{\partial^2 u}{\partial x^2} + \frac{1}{r}\frac{\partial}{\partial r}\left(r\frac{\partial u}{\partial r}\right) + \frac{1}{r^2}\frac{\partial^2 u}{\partial\theta^2}\right], \end{aligned} \tag{6.1}$$

$$\begin{aligned} G_v(u,v,w,p) &= \frac{\partial(uv)}{\partial x} + \frac{1}{r}\frac{\partial(rvv)}{\partial r} + \frac{1}{r}\frac{\partial(wv)}{\partial\theta} - \frac{w^2}{r} + \frac{\partial p}{\partial r} \\ &- \frac{1}{Re}\left[\frac{\partial^2 v}{\partial x^2} + \frac{1}{r}\frac{\partial}{\partial r}\left(r\frac{\partial v}{\partial r}\right) + \frac{1}{r^2}\frac{\partial^2 v}{\partial\theta^2} - \frac{2}{r^2}\frac{\partial w}{\partial\theta} - \frac{v}{r^2}\right], \end{aligned} \tag{6.2}$$

$$\begin{aligned} G_w(u,v,w,p) &= \frac{\partial(uw)}{\partial x} + \frac{1}{r}\frac{\partial(rvw)}{\partial r} + \frac{1}{r}\frac{\partial(ww)}{\partial\theta} + \frac{vw}{r} + \frac{1}{r}\frac{\partial p}{\partial\theta} \\ &- \frac{1}{Re}\left[\frac{\partial^2 w}{\partial x^2} + \frac{1}{r}\frac{\partial}{\partial r}\left(r\frac{\partial w}{\partial r}\right) + \frac{1}{r^2}\frac{\partial^2 w}{\partial\theta^2} + \frac{2}{r^2}\frac{\partial v}{\partial\theta} - \frac{w}{r^2}\right], \end{aligned} \tag{6.3}$$

$$\boldsymbol{\nabla}\cdot\mathbf{V} = \frac{\partial u}{\partial x} + \frac{1}{r}\frac{\partial(rv)}{\partial r} + \frac{1}{r}\frac{\partial w}{\partial\theta}. \tag{6.4}$$

Now, equation (3.12) is again linearized by lagging the velocity components in the term $\Delta\mathbf{G}$ which is derived from (6.1-6.3), and equations (3.12) and (3.13) can be put in the global matrix form

$$[\mathbf{I} + \alpha\,\Delta\tau(\mathbf{D}_x + \mathbf{D}_r + \mathbf{D}_\theta)]\;\Delta\boldsymbol{\Phi} = \Delta\tau\,\mathbf{R}, \tag{6.5}$$

where the matrices $\mathbf{D}_x$, $\mathbf{D}_r$ and $\mathbf{D}_\theta$ contain, respectively, the spatial derivatives

with respect to x, r and θ of the variable $\Delta\mathbf{\Phi} = [\Delta u \ \Delta v \ \Delta w \ \Delta p]^T$. They take the form

$$\mathbf{D}_x = \begin{bmatrix} L + 1/\alpha & 0 & 0 & \partial/\partial x \\ 0 & L & 0 & 0 \\ 0 & 0 & L & 0 \\ (1/\alpha\delta)\partial/\partial x & 0 & 0 & 0 \end{bmatrix},$$

$$\mathbf{D}_r = \begin{bmatrix} M & 0 & 0 & 0 \\ 0 & M + 1/\alpha + 1/(Re\, r^2) & 0 & \partial/\partial r \\ 0 & 0 & M & 0 \\ 0 & (1/\alpha\delta\, r)(\partial/\partial r)(r) & 0 & 0 \end{bmatrix},$$

$$\mathbf{D}_\theta = \begin{bmatrix} N & 0 & 0 & 0 \\ 0 & N & -\breve{w}^\nu/r + (2/Re\, r^2)\partial/\partial\theta & 0 \\ 0 & -(2/Re\, r^2)\partial/\partial\theta & N + 1/\alpha + \breve{v}^\nu/r + 1/(Re\, r^2) & (1/r)\partial/\partial\theta \\ 0 & 0 & (1/\alpha\delta\, r)\partial/\partial\theta & 0 \end{bmatrix},$$

where

$$L\psi = \frac{\partial(\breve{u}^\nu\psi)}{\partial x} - \frac{1}{Re}\frac{\partial^2\psi}{\partial x^2},$$

$$M\psi = \frac{\partial(r\breve{v}^\nu\psi)}{r\,\partial r} - \frac{1}{Re}\frac{\partial}{r\,\partial r}\left(r\frac{\partial\psi}{\partial r}\right),$$

$$N\psi = \frac{\partial(\breve{w}^\nu\psi)}{r\,\partial\theta} - \frac{1}{Re}\frac{\partial^2\psi}{r^2\,\partial\theta^2},$$

$$\mathbf{R} = \begin{bmatrix} \mathbf{F}^n - \breve{\mathbf{V}}^\nu - \alpha\,\acute{\mathbf{G}}^\nu \\ -(1/\delta)\,\boldsymbol{\nabla}\cdot\breve{\mathbf{V}}^\nu \end{bmatrix}.$$

As for Cartesian coordinates, the undifferentiated terms arising from $\Delta\tau\,\Delta\mathbf{V}$ have been included within $\mathbf{D}_x$, $\mathbf{D}_r$ or $\mathbf{D}_\theta$, as well as other undifferentiated terms which arise in cylindrical coordinates, namely $-\breve{w}^\nu\,\Delta w/r$ and $\Delta v/(Re\,r^2)$ in the r-momentum equation and $\breve{v}^\nu\,\Delta w/r$ and $\Delta w/(Re\,r^2)$ in the θ-momentum equation. Also, the off-diagonal terms $[-\breve{w}^\nu/r + (2/Re\,r^2)\partial/\partial\theta]$ and $[-(2/Re\,r^2)\partial/\partial\theta]$ in the $\mathbf{D}_\theta$ matrix will contribute coupling between the velocity components Δv and Δw in the r- and θ-momentum equations. This means that scalar tridiagonal systems of equations will not be obtained anymore when using the factored ADI scheme and eliminating the pressure with the aid of the continuity equation. This inconvenience is avoided by simply dropping those terms from the $\mathbf{D}_\theta$ matrix, which does not affect significantly the overall implicit coupling and convergence rate of the method as the numerical examples presented in the next chapters show.

Thus, introducing the factored ADI solution scheme, we rewrite (6.5) in factored form as

$$(\mathbf{I} + \alpha\,\Delta\tau\mathbf{D}_x)(\mathbf{I} + \alpha\,\Delta\tau\mathbf{D}_r)(\mathbf{I} + \alpha\,\Delta\tau\mathbf{D}_\theta)\Delta\boldsymbol{\Phi} = \Delta\tau\,\mathbf{R}.$$

This last linear system of equations is now solved by the succession of the x-, r- and θ-sweeps.

$$(\mathbf{I} + \alpha\,\Delta\tau\mathbf{D}_x)\,\widetilde{\Delta\boldsymbol{\Phi}} = \Delta\tau\,\mathbf{R} \tag{6.6}$$

$$(\mathbf{I} + \alpha\,\Delta\tau\mathbf{D}_r)\,\overline{\Delta\boldsymbol{\Phi}} = \widetilde{\Delta\boldsymbol{\Phi}} \tag{6.7}$$

$$(\mathbf{I} + \alpha\,\Delta\tau\mathbf{D}_\theta)\,\Delta\boldsymbol{\Phi} = \overline{\Delta\boldsymbol{\Phi}}\,. \tag{6.8}$$

At this point we are ready to write down the actual scalar equations that result from the matrix equations (6.6-6.8). Hence, we will have for the x-, r- and θ-sweeps the following equations, first for the x-sweep,

$$(1+\Delta\tau)\,\widetilde{\Delta u} \;+\; \alpha\,\Delta\tau\left[\frac{\partial(\check{u}^{\nu}\widetilde{\Delta u})}{\partial x}+\frac{\partial(\widetilde{\Delta p})}{\partial x}-\frac{1}{Re}\frac{\partial^2(\widetilde{\Delta u})}{\partial x^2}\right]$$
$$= \Delta\tau\,(F_u^n-\check{u}^{\nu}-\alpha\,\check{G}_u^{\nu}) \qquad (6.9)$$

$$\widetilde{\Delta v} \;+\; \alpha\,\Delta\tau\left[\frac{\partial(\check{u}^{\nu}\widetilde{\Delta v})}{\partial x}-\frac{1}{Re}\frac{\partial^2(\widetilde{\Delta v})}{\partial x^2}\right]$$
$$= \Delta\tau\,(F_v^n-\check{v}^{\nu}-\alpha\,\check{G}_v^{\nu})\,, \qquad (6.10)$$

$$\widetilde{\Delta w} \;+\; \alpha\,\Delta\tau\left[\frac{\partial(\check{u}^{\nu}\widetilde{\Delta w})}{\partial x}-\frac{1}{Re}\frac{\partial^2(\widetilde{\Delta w})}{\partial x^2}\right]$$
$$= \Delta\tau\,(F_w^n-\check{w}^{\nu}-\alpha\,\check{G}_w^{\nu})\,, \qquad (6.11)$$

$$\widetilde{\Delta p}+\frac{\Delta\tau}{\delta}\frac{\partial(\widetilde{\Delta u})}{\partial x}=-\frac{\Delta\tau}{\delta}\,\nabla\cdot\check{\mathbf{V}}^{\nu}\,, \qquad (6.12)$$

then for the r-sweep,

$$\overline{\Delta u} \;+\; \alpha\,\Delta\tau\left[\frac{\partial(r\,\check{v}^{\nu}\overline{\Delta u})}{r\,\partial r}-\frac{1}{Re}\frac{\partial}{r\,\partial r}\left(r\,\frac{\partial(\overline{\Delta u})}{\partial r}\right)\right]=\widetilde{\Delta u} \qquad (6.13)$$

$$(1+\Delta\tau)\,\overline{\Delta v} \;+\; \alpha\,\Delta\tau\left[\frac{\partial(r\,\check{v}^{\nu}\,\overline{\Delta v})}{r\,\partial r}+\frac{\partial(\overline{\Delta p})}{\partial r}\right.$$
$$\left.-\;\frac{1}{Re}\left\{\frac{\partial}{r\,\partial r}\left(r\,\frac{\partial(\overline{\Delta v})}{\partial r}\right)-\frac{\overline{\Delta v}}{r^2}\right\}\right]=\widetilde{\Delta v} \qquad (6.14)$$

$$\overline{\Delta w} \;+\; \alpha\,\Delta\tau\left[\frac{\partial(r\,\check{v}^{\nu}\,\overline{\Delta w})}{r\,\partial r}-\frac{1}{Re}\frac{\partial}{r\,\partial r}\left(r\,\frac{\partial(\overline{\Delta w})}{\partial r}\right)\right]=\widetilde{\Delta w} \qquad (6.15)$$

$$\overline{\Delta p}+\frac{\Delta\tau}{\delta}\frac{\partial(r\,\overline{\Delta v})}{r\,\partial r}=\widetilde{\Delta p}\,, \qquad (6.16)$$

and finally, for the θ-sweep,

$$\Delta u \;+\; \alpha\,\Delta\tau\left[\frac{\partial(\check{w}^{\nu}\Delta u)}{r\,\partial\theta} - \frac{1}{Re}\frac{\partial^2(\Delta u)}{r^2\,\partial\theta^2}\right] = \overline{\Delta u} \tag{6.17}$$

$$\Delta v \;+\; \alpha\,\Delta\tau\left[\frac{\partial(\check{w}^{\nu}\Delta v)}{r\,\partial\theta} - \frac{1}{Re}\frac{\partial^2(\Delta v)}{r^2\,\partial\theta^2}\right] = \overline{\Delta v} \tag{6.18}$$

$$\begin{aligned}(1+\Delta\tau)\,\Delta w \;+\; \alpha\,\Delta\tau\Bigg[&\frac{\partial(\check{w}^{\nu}\Delta w)}{r\,\partial\theta} + \frac{\check{v}^{\nu}\Delta w}{r} + \frac{\partial(\Delta p)}{r\,\partial\theta} \\ &- \frac{1}{Re}\left\{\frac{\partial^2(\Delta w)}{r^2\,\partial\theta^2} - \frac{\Delta w}{r^2}\right\}\Bigg] = \overline{\Delta w}\end{aligned} \tag{6.19}$$

$$\Delta p + \frac{\Delta\tau}{\delta}\frac{\partial(\Delta w)}{r\,\partial\theta} = \overline{\Delta p}\,. \tag{6.20}$$

As usual, in the above equations the superscript ν means that the quantity is evaluated at pseudo-time level t^{ν}, and

$$\begin{aligned} F_u^n &= \frac{1}{3}(4\,u^n - u^{n-1})\,, \\ F_v^n &= \frac{1}{3}(4\,v^n - v^{n-1})\,, \\ F_w^n &= \frac{1}{3}(4\,w^n - w^{n-1})\,. \end{aligned}$$

6.3 Hybrid Finite-Difference/Fourier-Expansion Method

The equations developed in last section must be solved on a three-dimensional mesh, which is a costly undertaking. Here we derive simplified forms, whereby

expansions of the flow variables $\mathbf{V}$ and p in terms of the circumferential coordinate θ are made. Complex Fourier series are thus assumed for the flow quantities,

$$u(x,r,\theta,t) = \sum_{\rho=-N}^{N} \hat{u}_\rho(x,r,t)e^{\imath\rho\theta} , \tag{6.21}$$

$$v(x,r,\theta,t) = \sum_{\rho=-N}^{N} \hat{v}_\rho(x,r,t)e^{\imath\rho\theta} , \tag{6.22}$$

$$w(x,r,\theta,t) = \imath \sum_{\rho=-N}^{N} \hat{w}_\rho(x,r,t)e^{\imath\rho\theta} , \tag{6.23}$$

$$p(x,r,\theta,t) = \sum_{\rho=-N}^{N} \hat{p}_\rho(x,r,t)e^{\imath\rho\theta} . \tag{6.24}$$

The quantities $\hat{u}_\rho$, $\hat{v}_\rho$, $\hat{w}_\rho$ and $\hat{p}_\rho$ are the Fourier coefficients. The reason why the factor $\imath = \sqrt{-1}$ has been included in (6.23) for w will be made clear in the next sections. The number of circumferential harmonics chosen in the expansions is N and we thus note that the Fourier series are truncated; they serve as basis functions for a Galerkin solution in which equations (6.21-6.24) are substituted in (6.9-6.20), the latter then being each in turn multiplied by $(1/2\pi)\exp(-\imath\mu\theta)$ and integrated over θ between 0 and 2π. This is equivalent to taking the Fourier transform of the governing equations and getting them written down in terms of the Fourier coefficients of the variables involved (the domain is periodic in θ). The following orthogonality relation is used in applying the Galerkin method.

$$\frac{1}{2\pi}\int_0^{2\pi} \exp^{\imath(\rho-\mu)\theta}\, d\theta = \delta_{\rho\mu} .$$

where $\delta_{\rho\mu}$ denotes the Kronecker Delta. Thus, denoting by a circle, $\circ$, the convolution products, defined shortly, and noting that $\partial/\partial\theta \equiv \imath\mu$, and $\partial^2/\partial\theta^2 \equiv -\mu^2$, after taking the Fourier transform, we have the following equations for the x-, r- and θ-sweeps, first for the x-sweep,

$$(1+\Delta\tau)\,\widetilde{\Delta\hat{u}}_\mu \;+\; \alpha\,\Delta\tau\left[\frac{\partial(\hat{u}^\nu \circ \widetilde{\Delta\hat{u}})_\mu}{\partial x} + \frac{\partial(\widetilde{\Delta\hat{p}}_\mu)}{\partial x} - \frac{1}{Re}\frac{\partial^2(\widetilde{\Delta\hat{u}}_\mu)}{\partial x^2}\right]$$
$$= \Delta\tau\left[(\hat{F}_u^n)_\mu - \hat{u}_\mu^\nu - \alpha\,(\hat{G}_u^\nu)_\mu\right] \tag{6.25}$$

$$\widetilde{\Delta\hat{v}}_\mu \;+\; \alpha\,\Delta\tau\left[\frac{\partial(\hat{u}^\nu \circ \widetilde{\Delta\hat{v}})_\mu}{\partial x} - \frac{1}{Re}\frac{\partial^2(\widetilde{\Delta\hat{v}}_\mu)}{\partial x^2}\right]$$
$$= \Delta\tau\left[(\hat{F}_v^n)_\mu - \hat{v}_\mu^\nu - \alpha\,(\hat{G}_v^\nu)_\mu\right] \tag{6.26}$$

$$\widetilde{\Delta\hat{w}}_\mu \;+\; \alpha\,\Delta\tau\left[\frac{\partial(\hat{u}^\nu \circ \widetilde{\Delta\hat{w}})_\mu}{\partial x} - \frac{1}{Re}\frac{\partial^2(\widetilde{\Delta\hat{w}}_\mu)}{\partial x^2}\right]$$
$$= \Delta\tau\left[(\hat{F}_w^n)_\mu - \hat{w}_\mu^\nu - \alpha\,(\hat{G}_w^\nu)_\mu\right] \tag{6.27}$$

$$\widetilde{\Delta\hat{p}}_\mu \;+\; \frac{\Delta\tau}{\delta}\frac{\partial(\widetilde{\Delta\hat{u}}_\mu)}{\partial x} = -\frac{\Delta\tau}{\delta}\,(\boldsymbol{\nabla}\cdot\hat{\mathbf{V}})_\mu^\nu\,, \tag{6.28}$$

then for the r-sweep,

$$\overline{\Delta\hat{u}}_\mu \;+\; \alpha\,\Delta\tau\left[\frac{\partial\, r(\hat{v}^\nu \circ \overline{\Delta\hat{u}})_\mu}{r\,\partial r}\right.$$
$$\left. -\;\frac{1}{Re}\frac{\partial}{r\,\partial r}\left(r\,\frac{\partial(\overline{\Delta\hat{u}}_\mu)}{\partial r}\right)\right] = \widetilde{\Delta\hat{u}}_\mu \tag{6.29}$$

$$(1+\Delta\tau)\,\overline{\Delta\hat{v}}_\mu \;+\; \alpha\,\Delta\tau\left[\frac{\partial\, r(\hat{v}^\nu \circ \overline{\Delta\hat{v}})_\mu}{r\,\partial r} + \frac{\partial(\overline{\Delta\hat{p}}_\mu)}{\partial r}\right.$$
$$\left. -\;\frac{1}{Re}\left\{\frac{\partial}{r\,\partial r}\left(r\,\frac{\partial(\overline{\Delta\hat{v}}_\mu)}{\partial r}\right) - \frac{\overline{\Delta\hat{v}}_\mu}{r^2}\right\}\right] = \widetilde{\Delta\hat{v}}_\mu \tag{6.30}$$

$$\overline{\Delta\hat{w}}_\mu + \alpha\,\Delta\tau\left[\frac{\partial\, r(\hat{v}^\nu \circ \overline{\Delta\hat{w}})_\mu}{r\,\partial r} - \frac{1}{Re}\frac{\partial}{r\,\partial r}\left(r\,\frac{\partial(\overline{\Delta\hat{w}}_\mu)}{\partial r}\right)\right] = \widetilde{\Delta\hat{w}}_\mu \tag{6.31}$$

$$\overline{\Delta\hat{p}}_\mu + \frac{\Delta\tau}{\delta}\frac{\partial(r\,\overline{\Delta\hat{v}}_\mu)}{r\,\partial r} = \widetilde{\Delta\hat{p}}_\mu\ , \tag{6.32}$$

and finally for the θ-sweep,

$$\Delta\hat{u}_\mu + \alpha\,\Delta\tau\left[\frac{-\mu}{r}(\hat{w}^\nu \circ \Delta\hat{u})_\mu + \frac{\mu^2}{r^2}\frac{\Delta\hat{u}_\mu}{Re}\right] = \overline{\Delta\hat{u}}_\mu \tag{6.33}$$

$$\Delta\hat{v}_\mu + \alpha\,\Delta\tau\left[\frac{-\mu}{r}(\hat{w}^\nu \circ \Delta\hat{v})_\mu + \frac{\mu^2}{r^2}\frac{\Delta\hat{v}_\mu}{Re}\right] = \overline{\Delta\hat{v}}_\mu \tag{6.34}$$

$$(1+\Delta\tau)\,\Delta\hat{w}_\mu + \alpha\,\Delta\tau\left[\frac{-\mu}{r}(\hat{w}^\nu \circ \Delta\hat{w})_\mu + \frac{(\hat{v}^\nu \circ \Delta\hat{w})_\mu}{r} + \frac{\mu}{r}\,\Delta p_\mu + \frac{\mu^2+1}{r^2}\frac{\Delta\hat{w}_\mu}{Re}\right] = \overline{\Delta\hat{w}}_\mu \tag{6.35}$$

$$\Delta\hat{p}_\mu - \frac{\Delta\tau}{\delta}\frac{\mu}{r}\Delta\hat{w}_\mu = \overline{\Delta\hat{p}}_\mu \tag{6.36}$$

In equations (6.25-6.36) we have the following relations

$$\begin{aligned}(\hat{F}_u^n)_\mu &= \frac{1}{3}(4\,\hat{u}_\mu^n - \hat{u}_\mu^{n-1})\\ (\hat{F}_v^n)_\mu &= \frac{1}{3}(4\,\hat{v}_\mu^n - \hat{v}_\mu^{n-1})\\ (\hat{F}_w^n)_\mu &= \frac{1}{3}(4\,\hat{w}_\mu^n - \hat{w}_\mu^{n-1})\ ,\end{aligned}$$

$$
\begin{aligned}
(\hat{G}_u^\nu)_\mu &= \frac{\partial(\hat{u}^\nu \circ \hat{u}^\nu)_\mu}{\partial x} + \frac{\partial\, r(\hat{v}^\nu \circ \hat{u}^\nu)_\mu}{r\,\partial r} - \frac{\mu}{r}(\hat{w}^\nu \circ \hat{u}^\nu)_\mu + \frac{\partial \hat{p}_\mu^\nu}{\partial x} \\
&- \frac{1}{Re}\left[\frac{\partial^2 \hat{u}_\mu^\nu}{\partial x^2} + \frac{1}{r}\frac{\partial}{\partial r}\left(r\,\frac{\partial \hat{u}_\mu^\nu}{\partial r}\right) - \frac{\mu^2}{r^2}\,\hat{u}_\mu^\nu\right]
\end{aligned}
$$

$$
\begin{aligned}
(\hat{G}_v^\nu)_\mu &= \frac{\partial(\hat{u}^\nu \circ \hat{v}^\nu)_\mu}{\partial x} + \frac{\partial\, r(\hat{v}^\nu \circ \hat{v}^\nu)_\mu}{r\,\partial r} - \frac{\mu}{r}(\hat{w}^\nu \circ \hat{v}^\nu)_\mu + \frac{(\hat{w}^\nu \circ \hat{w}^\nu)_\mu}{r} + \frac{\partial \hat{p}_\mu^\nu}{\partial r} \\
&- \frac{1}{Re}\left[\frac{\partial^2 \hat{v}_\mu^\nu}{\partial x^2} + \frac{1}{r}\frac{\partial}{\partial r}\left(r\frac{\partial \hat{v}_\mu^\nu}{\partial r}\right) - \frac{(\mu^2+1)}{r^2}\,\hat{v}_\mu^\nu + \frac{2\mu}{r^2}\,\hat{w}_\mu^\nu\right]
\end{aligned}
$$

$$
\begin{aligned}
(\hat{G}_w^\nu)_\mu &= \frac{\partial(\hat{u}^\nu \circ \hat{w}^\nu)_\mu}{\partial x} + \frac{\partial\, r(\hat{v}^\nu \circ \hat{w}^\nu)_\mu}{r\,\partial r} - \frac{\mu}{r}(\hat{w}^\nu \circ \hat{w}^\nu)_\mu + \frac{(\hat{v}^\nu \circ \hat{w}^\nu)_\mu}{r} + \frac{\mu}{r}\,\hat{p}_\mu^\nu \\
&- \frac{1}{Re}\left[\frac{\partial^2 \hat{w}_\mu^\nu}{\partial x^2} + \frac{1}{r}\frac{\partial}{\partial r}\left(r\,\frac{\partial \hat{w}_\mu^\nu}{\partial r}\right) - \frac{(\mu^2+1)}{r^2}\hat{w}_\mu^\nu + \frac{2\mu}{r^2}\,\hat{v}_\mu^\nu\right]
\end{aligned}
$$

$$
(\boldsymbol{\nabla}\cdot\hat{\mathbf{V}})_\mu^\nu = \frac{\partial \hat{u}_\mu^\nu}{\partial x} + \frac{\partial(r\,\hat{v}_\mu^\nu)}{r\,\partial r} - \frac{\mu}{r}\,\hat{w}_\mu^\nu\,.
$$

We note that a factor $\imath$ has disappeared from all the θ-momentum equations, and we recall that superscript ν in the above equations denotes quantities evaluated at pseudo-time level t^ν; for ease of notation, the breve symbol $\breve{}$ denoting the pseudo-functions $\breve{\mathbf{V}}$ and $\breve{p}$ during pseudo-time integration has been omitted, and the superscript ν alone is taken to represent these pseudo-functions during the pseudo-time relaxation. Now, it is to be noticed that nonlinearities present in the Navier-Stokes equations appear in the Fourier-transformed equations in the form of convolution products, which are defined as

$$
(\hat{u}^\nu \circ \hat{v}^\nu)_\mu = \sum_{\rho+\lambda=\mu} \hat{u}_\rho^\nu \hat{v}_\lambda^\nu\,.
$$

For example, if N is equal to 2 in (6.21-6.24) we then have

$$
\begin{aligned}
(\hat{u}^{\nu} \circ \hat{v}^{\nu})_2 &= \hat{u}_0^{\nu}\hat{v}_2^{\nu} + \hat{u}_1^{\nu}\hat{v}_1^{\nu} + \hat{u}_2^{\nu}\hat{v}_0^{\nu} \\
(\hat{u}^{\nu} \circ \hat{v}^{\nu})_1 &= \hat{u}_{-1}^{\nu}\hat{v}_2^{\nu} + \hat{u}_0^{\nu}\hat{v}_1^{\nu} + \hat{u}_1^{\nu}\hat{v}_0^{\nu} + \hat{u}_2^{\nu}\hat{v}_{-1}^{\nu} \\
(\hat{u}^{\nu} \circ \hat{v}^{\nu})_0 &= \hat{u}_{-2}^{\nu}\hat{v}_2^{\nu} + \hat{u}_{-1}^{\nu}\hat{v}_1^{\nu} + \hat{u}_0^{\nu}\hat{v}_0^{\nu} + \hat{u}_1^{\nu}\hat{v}_{-1}^{\nu} + \hat{u}_2^{\nu}\hat{v}_{-2}^{\nu} \\
(\hat{u}^{\nu} \circ \hat{v}^{\nu})_{-1} &= \hat{u}_{-2}^{\nu}\hat{v}_1^{\nu} + \hat{u}_{-1}^{\nu}\hat{v}_0^{\nu} + \hat{u}_0^{\nu}\hat{v}_{-1}^{\nu} + \hat{u}_1^{\nu}\hat{v}_{-2}^{\nu} \\
(\hat{u}^{\nu} \circ \hat{v}^{\nu})_{-2} &= \hat{u}_{-2}^{\nu}\hat{v}_0^{\nu} + \hat{u}_{-1}^{\nu}\hat{v}_{-1}^{\nu} + \hat{u}_0^{\nu}\hat{v}_{-2}^{\nu}
\end{aligned}
$$

The convolution products provide the non-linear coupling between the different circumferential harmonics and between the equations themselves, as it is to be realized that equations (6.25-6.36) have to be written down $(2N+1)$ times, since there will be one such set of equations for each positive and negative harmonic μ, $\mu = -N, \ldots, N$. The equations between the different sets are coupled by the convolution products. The actual equations will be given for $N = 1$ harmonic in three-dimensional cylindrical coordinates in the next section, and for $N = 2$ harmonics for a special two-dimensional annular flow problem, in the next chapter.

Originally, the system of incompressible Navier-Stokes equations contained four equations and now, after using the Galerkin procedure, we in fact have four times $(2N+1)$ equations to solve. The Galerkin procedure seems unjustified. However, in the process the number of independent variables has gone from three to two, in other words the coordinate θ has been eliminated and the equations need to be solved on a two-dimensional domain in the variables x and r, which is a major advantage. As we will see, the more the number of harmonics N we choose, the more the equations become complicated, such that the method is in fact mostly useful for deriving linearized forms of Navier-Stokes equations and for investigating the importance of nonlinear effects in particular types of flow problems. These are detailed in the next section and chapter.

6.4 Linearized Forms of Navier-Stokes Equations

The annular flow geometries that will be considered throughout are composed of two bodies of revolution which are concentric with each other and delimit the annular space. Furthermore, the vibration of either body is considered to take place in one plane, the plane of oscillation, such that if the circumferential coordinate is measured from the plane of oscillation, then the flow variables u, v and p are even functions of θ and w is an odd function of θ. This last constraint simplifies the solution process because of symmetry with respect to the plane of oscillation. Indeed, it is known [30] that the negative and positive Fourier coefficients, $\hat{f}_{-\mu}$ and $\hat{f}_{\mu}$, of a *real* function $f(\theta)$ are related to each other by the relation $\hat{f}_{-\mu} = \hat{f}_{\mu}^{*}$, where the star denotes complex conjugate. Furthermore, if $f(\theta)$ is an even function of θ then all its Fourier coefficients are also real and even, whereas if $f(\theta)$ is odd then its Fourier coefficients are pure imaginary and odd. In other words we have

$$\begin{aligned} \hat{f}_{-\mu} &= \hat{f}_{\mu}\,, \quad \text{if } f(\theta) \text{ is real and even} \\ \imath\,\hat{f}_{-\mu} &= -\imath\,\hat{f}_{\mu}\,, \quad \text{if } f(\theta) \text{ is real and odd}\,, \end{aligned} \tag{6.37}$$

where $\hat{f}_{\mu}$ is real in both of the above relations. This means that the set of equations (6.25-6.36) will have to be set up only for $\mu = 0, 1, \ldots, N$, in order to obtain the positive harmonics, and then (6.37) can be used to obtain the negative ones. We note that this explains the factor $\imath$ in the series form (6.23) for w, and we conclude in equations (6.21-6.24) that $\hat{u}_{\rho}$, $\hat{v}_{\rho}$ and $\hat{p}_{\rho}$ are real and even, and $\hat{w}_{\rho}$ is real and odd.

Now, since one of the objectives of fluid-structure interaction study is to determine the stability of structures under the effect of fluid flow, we consider that there is a mean fluid flow in the annular space, and the mean flow is axisymmetric because the two bodies delimiting the annular region are concentric. We will be

considering small amplitude oscillations of either the inner or outer body delimiting the annular space, and the perturbations in the flow variables that are thus produced are small with respect to the mean flow quantities. The latter are described exclusively by the quantities $\hat{u}_0$, $\hat{v}_0$ and $\hat{p}_0$ when the inner and outer bodies are fixed (steady flow), and any departure from axisymmetry brought about by unsteady motion is reflected by the higher order harmonics (note that $\hat{w}_0$ is zero whether the flow is steady or unsteady, because the $\hat{w}_\rho$ are odd).

As a first step toward obtaining a linearized solution to the Navier-Stokes equations, we take only $N = 1$ circumferential harmonic in (6.21-6.24), which is justified for small departures from axisymmetry in the case of small perturbations. Thus for the simple case $N = 1$, we write down two times equations (6.25-6.36), for $\mu = 0$ and $\mu = 1$, and these two sets of equations must in principle be simultaneously integrated in time to reflect the nonlinear interaction between the zeroth-order quantities ($\mu = 0$) and the first-order ones ($\mu = 1$). However, the linearization is precisely accomplished by computing the mean flow first, as a steady flow and in the absence of vibration, and the quantities $\hat{u}_0$, $\hat{v}_0$ and $\hat{p}_0$ thus obtained are kept constant and not simultaneously integrated with the second set of equations for the quantities $\hat{u}_1$, $\hat{v}_1$, $\hat{w}_1$ and $\hat{p}_1$. The latter only are considered to be time dependent and reflect the unsteady nature of the flow problem. It is to be noted that this method is only valid for concentric geometries as any excentricity of the outer body with respect to the inner one causes the steady flow not to be axisymmetric and require infinite series in (6.21-6.24).

Thus, the mean flow is obtained first by solving the axisymmetric steady flow equations, namely

$$\frac{\partial(\hat{u}_0\hat{u}_0)}{\partial x} + \frac{\partial\,(r\,\hat{v}_0\hat{u}_0)}{r\,\partial r} + \frac{\partial\hat{p}_0}{\partial x} - \frac{1}{Re}\left[\frac{\partial^2\hat{u}_0}{\partial x^2} + \frac{1}{r}\frac{\partial}{\partial r}\left(r\,\frac{\partial\hat{u}_0}{\partial r}\right)\right] \;=\; 0 \qquad (6.38)$$

$$\frac{\partial(\hat{u}_0\hat{v}_0)}{\partial x} + \frac{\partial\,(r\,\hat{v}_0\hat{v}_0)}{r\,\partial r} + \frac{\partial\hat{p}_0}{\partial r} - \frac{1}{Re}\left[\frac{\partial^2\hat{v}_0}{\partial x^2} + \frac{1}{r}\frac{\partial}{\partial r}\left(r\,\frac{\partial\hat{v}_0}{\partial r}\right) - \frac{\hat{v}_0}{r^2}\right] = 0 \quad (6.39)$$

$$\frac{\partial\hat{u}_0}{\partial x} + \frac{\partial(r\,\hat{v}_0)}{r\,\partial r} = 0 \quad (6.40)$$

and the quantities $\hat{u}_0$, $\hat{v}_0$ and $\hat{p}_0$ are kept constant while solving the following equations for $\hat{u}_1$, $\hat{v}_1$, $\hat{w}_1$ and p_1. They are obtained from (6.25-6.36) by writing them for $N = 1$ harmonic, with $\mu = 1$. Noting that $\hat{w}_0 = 0$, because the $\hat{w}_\mu$ are odd, and $\Delta\hat{u}_0 = \Delta\hat{v}_0 = 0$, because they are kept constant in the linearization, we then have, first for the x- sweep,

$$[1 + \Delta\tau\,\widetilde{\Delta\hat{u}_1}] + \alpha\,\Delta\tau\left[\frac{\partial(\hat{u}_0^\nu\,\widetilde{\Delta\hat{u}_1})}{\partial x} + \frac{\partial(\widetilde{\Delta\hat{p}_1})}{\partial x} - \frac{1}{Re}\frac{\partial^2(\widetilde{\Delta\hat{u}_1})}{\partial x^2}\right] = \Delta\tau\left[(\hat{F}_u^n)_1 - \hat{u}_1^\nu - \alpha\,(\hat{G}_u^\nu)_1\right] \quad (6.41)$$

$$\widetilde{\Delta\hat{v}_1} + \alpha\,\Delta\tau\left[\frac{\partial(\hat{u}_0^\nu\,\widetilde{\Delta\hat{v}_1})}{\partial x} - \frac{1}{Re}\frac{\partial^2(\widetilde{\Delta\hat{v}_1})}{\partial x^2}\right] = \Delta\tau\left[(\hat{F}_v^n)_1 - \hat{v}_1^\nu - \alpha\,(\hat{G}_v^\nu)_1\right] \quad (6.42)$$

$$\widetilde{\Delta\hat{w}_1} + \alpha\,\Delta\tau\left[\frac{\partial(\hat{u}_0^\nu\,\widetilde{\Delta\hat{w}_1})}{\partial x} - \frac{1}{Re}\frac{\partial^2(\widetilde{\Delta\hat{w}_1})}{\partial x^2}\right] = \Delta\tau\left[(\hat{F}_w^n)_1 - \hat{w}_1^\nu - \alpha\,(\hat{G}_w^\nu)_1\right] \quad (6.43)$$

$$\widetilde{\Delta\hat{p}_1} + \frac{\Delta\tau}{\delta}\frac{\partial(\widetilde{\Delta\hat{u}_1})}{\partial x} = -\frac{\Delta\tau}{\delta}\,(\boldsymbol{\nabla}\cdot\hat{\mathbf{V}})_1^\nu, \quad (6.44)$$

then for the z-sweep,

$$\overline{\Delta\hat{u}_1} + \alpha\,\Delta\tau\left[\frac{\partial\, r(\hat{v}_0^{\nu}\,\overline{\Delta\hat{u}_1})}{r\,\partial r} - \frac{1}{Re\, r}\frac{\partial}{\partial r}\left(r\,\frac{\partial(\overline{\Delta\hat{u}_1})}{\partial r}\right)\right] = \widetilde{\Delta\hat{u}_1} \tag{6.45}$$

$$(1+\Delta\tau)\,\overline{\Delta\hat{v}_1} + \alpha\,\Delta\tau\left[\frac{\partial\, r(\hat{v}_0^{\nu}\overline{\Delta\hat{v}_1})}{r\,\partial r} + \frac{\partial(\overline{\Delta\hat{p}_1})}{\partial r} - \frac{1}{Re}\left\{\frac{\partial}{r\,\partial r}\left(r\,\frac{\partial(\overline{\Delta\hat{v}_1})}{\partial r}\right) - \frac{\overline{\Delta\hat{v}_1}}{r^2}\right\}\right] = \widetilde{\Delta\hat{v}_1} \tag{6.46}$$

$$\overline{\Delta\hat{w}_1} + \alpha\,\Delta\tau\left[\frac{\partial\, r(\hat{v}_0^{\nu}\,\overline{\Delta\hat{w}_1})}{r\,\partial r} - \frac{1}{Re\, r}\frac{\partial}{\partial r}\left(r\,\frac{\partial(\overline{\Delta\hat{w}_1})}{\partial r}\right)\right] = \widetilde{\Delta\hat{w}_1} \tag{6.47}$$

$$\overline{\Delta\hat{p}_1} + \frac{\Delta\tau}{\delta}\frac{\partial(r\,\overline{\Delta\hat{v}_1})}{r\,\partial r} = \widetilde{\Delta\hat{p}_1}\,, \tag{6.48}$$

and finally for the θ-sweep,

$$\Delta\hat{u}_1 + \frac{\alpha\,\Delta\tau}{Re}\frac{\Delta\hat{u}_1}{r^2} = \overline{\Delta\hat{u}_1} \tag{6.49}$$

$$\Delta\hat{v}_1 + \frac{\alpha\,\Delta\tau}{Re}\frac{\Delta\hat{v}_1}{r^2} = \overline{\Delta\hat{v}_1} \tag{6.50}$$

$$(1+\Delta\tau)\Delta\hat{w}_1 + \alpha\,\Delta\tau\left[\frac{\hat{v}_0^{\nu}\,\Delta\hat{w}_1}{r} + \frac{\Delta\hat{p}_1}{r} + \frac{2}{r}\cdot\frac{\Delta\hat{w}_1}{Re}\right] = \overline{\Delta w_1} \tag{6.51}$$

$$\Delta\hat{p}_1 - \frac{\Delta\tau}{\delta}\frac{\Delta\hat{w}_1}{r} = \overline{\Delta\hat{p}_1}\,. \tag{6.52}$$

As usual, in (6.41-6.52) we have the following relations:

$$(\hat{F}_u^n)_1 = \frac{1}{3}(4\,\hat{u}_1^n - \hat{u}_1^{n-1}) \tag{6.53}$$

$$(\hat{F}_v^n)_1 = \frac{1}{3}(4\,\hat{v}_1^n - \hat{v}_1^{n-1}) \tag{6.54}$$

$$(\hat{F}_w^n)_1 = \frac{1}{3}(4\,\hat{w}_1^n - \hat{w}_1^{n-1})\,, \tag{6.55}$$

$$\begin{aligned}(\hat{G}_u^\nu)_1 &= 2\,\frac{\partial(\hat{u}_0^\nu\,\hat{u}_1^\nu)}{\partial x} + \frac{1}{r}\frac{\partial}{\partial r}\left[\,r(\hat{v}_0^\nu\,\hat{u}_1^\nu + \hat{v}_1^\nu\,\hat{u}_0^\nu)\right] - \frac{\hat{w}_1^\nu\,\hat{u}_0^\nu}{r} + \frac{\partial\hat{p}_1^\nu}{\partial x} \\ &- \frac{1}{Re}\left[\frac{\partial^2\hat{u}_1^\nu}{\partial x^2} + \frac{1}{r}\frac{\partial}{\partial r}\left(r\,\frac{\partial\hat{u}_1^\nu}{\partial r}\right) - \frac{\hat{u}_1^\nu}{r^2}\right]\end{aligned} \tag{6.56}$$

$$\begin{aligned}(\hat{G}_v^\nu)_1 &= \frac{\partial}{\partial x}(\hat{u}_0^\nu\hat{v}_1^\nu + \hat{u}_1^\nu\hat{v}_0^\nu) + \frac{2}{r}\frac{\partial}{\partial r}(r\,\hat{v}_0^\nu\hat{v}_1^\nu) - \frac{\hat{w}_1^\nu\hat{v}_0^\nu}{r} + \frac{\partial\hat{p}_1^\nu}{\partial r} \\ &- \frac{1}{Re}\left[\frac{\partial^2\hat{v}_1^\nu}{\partial x^2} + \frac{1}{r}\frac{\partial}{\partial r}\left(r\,\frac{\partial\hat{v}_1^\nu}{\partial r}\right) - \frac{2\,\hat{v}_1^\nu}{r^2} + \frac{2\,\hat{w}_1^\nu}{r^2}\right]\end{aligned} \tag{6.57}$$

$$\begin{aligned}(\hat{G}_w^\nu)_1 &= \frac{\partial(\hat{u}_0^\nu\hat{w}_1^\nu)}{\partial x} + \frac{\partial(r\,\hat{v}_0^\nu\hat{w}_1^\nu)}{r\,\partial r} + \frac{\hat{v}_0^\nu\hat{w}_1^\nu}{r} + \frac{\hat{p}_1^\nu}{r} \\ &- \frac{1}{Re}\left[\frac{\partial^2\hat{w}_1^\nu}{\partial x^2} + \frac{1}{r}\frac{\partial}{\partial r}\left(r\,\frac{\partial\hat{w}_1^\nu}{\partial r}\right) - \frac{2\,\hat{w}_1^\nu}{r^2} + \frac{2\,\hat{v}_1^\nu}{r^2}\right]\end{aligned} \tag{6.58}$$

$$(\boldsymbol{\nabla}\cdot\hat{\mathbf{V}})_1^\nu = \frac{\partial\hat{u}_1^\nu}{\partial x} + \frac{\partial(r\,\hat{v}_1^\nu)}{r\,\partial r} - \frac{\hat{w}_1^\nu}{r}\,. \tag{6.59}$$

Now, as was mentioned in last section the mesh on which equations (6.41-6.59) are discretized spans the coordinate directions x and r; it is a two-dimensional grid (the independent variable θ has been eliminated). As before, we use a stretched staggered grid which is similar to the two-dimensional grid presented in Chapter 4

for Cartesian coordinates. The details for the solution of these equations are presented in Appendix A.

We note that the linearized equations developed in this section can actually be used without the presence of a steady mean flow in the annular region. Indeed, one then sets $\hat{u}_0 = \hat{v}_0 = 0$ in (6.41–6.59); it is then understood that the perturbations $\hat{u}_1$, $\hat{v}_1$, $\hat{w}_1$ and $\hat{p}_1$ are small, and no important non-linear effects, such as would arise if the solving of the full non-linear equations were envisaged, are present.

Chapter 7

TWO-DIMENSIONAL UNSTEADY ANNULAR FLOW BETWEEN CONCENTRIC CYLINDERS

7.1 Two-Dimensional Equations of Motion

In this chapter, we derive simplified forms of the equations for the two-dimensional unsteady annular flow problem in which two concentric cylinders of infinite length delimit a uniform annular region, see Figure 7.1. The inner cylinder is fixed while the outer cylinder is assumed to undergo transverse oscillations, its axis always remaining parallel with the axis of the inner cylinder. In that case, there are no axial variations in the flow parameters such that in the equation of motion (6.5) all derivatives with respect to x are equal to zero. Furthermore, it is then realized that the equation of axial momentum does not need to be solved either; this means

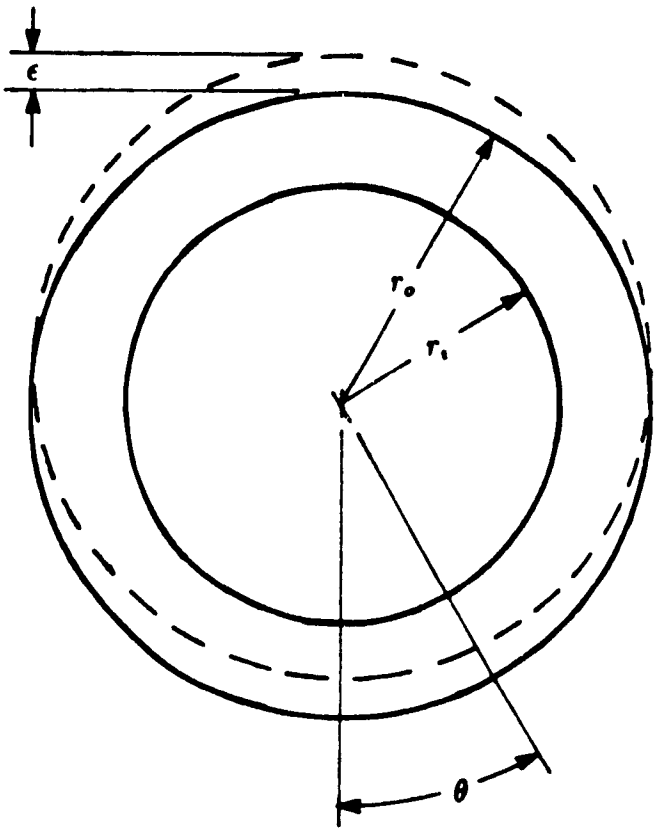

Figure 7.1: Geometry of two-dimensional unsteady annular flow problem.

that the dynamics of fluid flow induced by the oscillation of the outer cylinder does not depend on the presence or absence of axial flow in the annulus. Thus, there only remains the radial and circumferential momentum equations and the continuity one, and we can particularize the more general solution (6.9-6.20) to obtain the following r-sweep and θ-sweep equations (there is no x-sweep because the derivatives with respect to x are zero). The r-sweep is

$$(1+\Delta\tau)\,\overline{\Delta v}+\alpha\,\Delta\tau\,\left[\frac{\partial(r\,\check{v}^{\nu}\,\overline{\Delta v})}{r\,\partial r}+\frac{\partial(\overline{\Delta p})}{\partial r}\right.$$

$$\left.-\frac{1}{Re}\left\{\frac{\partial}{r\,\partial r}\left(r\,\frac{\partial(\overline{\Delta v})}{\partial r}\right)-\frac{\overline{\Delta v}}{r^2}\right\}\right]=\Delta\tau\,(F_v^n-\check{v}^{\nu}-\alpha\,\check{G}_v^{\nu})\,, \qquad (7.1)$$

$$\overline{\Delta w}+\alpha\,\Delta\tau\,\left[\frac{\partial(r\,\check{v}^{\nu}\,\overline{\Delta w})}{r\,\partial r}-\frac{1}{Re}\frac{\partial}{r\,\partial r}\left(r\,\frac{\partial(\overline{\Delta w})}{\partial r}\right)\right]$$

$$=\Delta\tau\,(F_w^n-\check{w}^{\nu}-\alpha\,\check{G}_w^{\nu})\,, \qquad (7.2)$$

$$\overline{\Delta p}+\frac{\Delta\tau}{\delta}\frac{\partial(r\,\overline{\Delta v})}{r\,\partial r}=-\frac{\Delta\tau}{\delta}\,\nabla\cdot\check{\mathbf{V}}^{\nu}\,, \qquad (7.3)$$

whereas the θ-sweep is

$$\Delta v \;+\; \alpha\,\Delta\tau\,\left[\frac{\partial(\check{w}^{\nu}\Delta v)}{r\,\partial\theta}-\frac{1}{Re}\frac{\partial^2(\Delta v)}{r^2\,\partial\theta^2}\right]=\overline{\Delta v}\,, \qquad (7.4)$$

$$(1+\Delta\tau)\,\Delta w \;+\; \alpha\,\Delta\tau\,\left[\frac{\partial(\check{w}^{\nu}\Delta w)}{r\,\partial\theta}+\frac{\check{v}\Delta w}{r}+\frac{\partial(\Delta p)}{r\,\partial\theta}\right.$$

$$\left.-\;\frac{1}{Re}\left\{\frac{\partial^2(\Delta w)}{r^2\,\partial\theta^2}-\frac{\Delta w}{r^2}\right\}\right]=\overline{\Delta w}\,, \qquad (7.5)$$

$$\Delta p \;+\; \frac{\Delta\tau}{\delta}\frac{\partial(\Delta w)}{r\,\partial\theta}=\overline{\Delta p}\,. \qquad (7.6)$$

As usual, in the above equations we have the following terms:

$$F_v^n=\frac{1}{3}(4\,v^n-v^{n-1})\,, \qquad F_w^n=\frac{1}{3}(4\,w^n-w^{n-1})\,,$$

$$G_v(v,w,p) = \frac{\partial(rvv)}{r\,\partial r} + \frac{\partial(wv)}{r\,\partial\theta} - \frac{w^2}{r} + \frac{\partial p}{\partial r} - \frac{1}{Re}\left[\frac{1}{r}\frac{\partial}{\partial r}\left(r\frac{\partial v}{\partial r}\right) + \frac{1}{r^2}\frac{\partial^2 v}{\partial\theta^2} - \frac{2}{r^2}\frac{\partial w}{\partial\theta} - \frac{v}{r^2}\right], \tag{7.7}$$

$$G_w(v,w,p) = \frac{\partial(rvw)}{r\,\partial r} + \frac{\partial(ww)}{r\,\partial\theta} + \frac{vw}{r} + \frac{1}{r}\frac{\partial p}{\partial\theta} - \frac{1}{Re}\left[\frac{1}{r}\frac{\partial}{\partial r}\left(r\frac{\partial w}{\partial r}\right) + \frac{1}{r^2}\frac{\partial^2 w}{\partial\theta^2} + \frac{2}{r^2}\frac{\partial v}{\partial\theta} - \frac{w}{r^2}\right], \tag{7.8}$$

$$\nabla\cdot\mathbf{V} = \frac{1}{r}\frac{\partial(rv)}{\partial r} + \frac{1}{r}\frac{\partial w}{\partial\theta}. \tag{7.9}$$

and we have $\check{G}_v^\nu = G_v(\check{v}^\nu, \check{w}^\nu, \check{p}^\nu)$, $\check{G}_w^\nu = G_w(\check{v}^\nu, \check{w}^\nu, \check{p}^\nu)$. These equations are solved on a two-dimensional mesh spanning the radial and circumferential coordinate directions. The details for the discretization of (7.1–7.9) are given in Appendix B

The boundary conditions on the velocity components must now be specified to solve the problem. Here, contrary to what we had in Cartesian coordinates in Chapter 5, the geometry of the fluid domain is deforming with time as the outer cylinder undergoes oscillation. This requires the use of a time-dependent nonsteady coordinate transformation [26, 31, 32], which maps the physical domain with moving boundaries into a computational domain with fixed boundaries Thus, if the position vector in computational space is denoted by $\hat{\mathbf{r}}$, and that in physical space by $\mathbf{r}$, we have a time-dependent transformation between physical and computational space which is of the form

$$\mathbf{r} = \mathbf{r}(\hat{\mathbf{r}}, t). \tag{7.10}$$

This transformation is defined throughout the whole fluid domain and prescribes uniquely the motion of moving boundaries in physical space as a function

of fixed boundaries in computational space. For example, in the present two-dimensional unsteady annular flow problem, the computational space may be taken as a cylindrical coordinate system whose origin corresponds with the axis of the fixed inner cylinder, of radius r_i; the radius of the outer cylinder is r_o. In that case, we denote by $\hat{r}_i$ the radial coordinate of the inner cylinder, and by $\hat{r}_o$ that of the outer cylinder in the equilibrium, concentric configuration in which $\epsilon(t) = 0$, see Figure 7.1. This concentric configuration defines the computational space in which the equations are resolved, namely the Navier-Stokes equations are solved on the computational domain

$$\hat{r}_i \leq \hat{r} \leq \hat{r}_o \,, \qquad 0 \leq \hat{\theta} \leq 2\,\pi \,.$$

However, as the outer cylinder undergoes oscillation the actual physical domain in which the Navier-Stokes equations are defined no longer corresponds with the original, concentric configuration. Instead, the physical space is defined between radial coordinates

$$r = \hat{r}_i$$

and

$$r = \sqrt{\left\{\epsilon(t) + \hat{r}_o \cos\hat{\theta}\right\}^2 + \left(\hat{r}_o \sin\hat{\theta}\right)^2} \,, \tag{7.11}$$

which correspond with the inner and outer cylinder, respectively. Hence, for our problem the coordinate transformation (7.10) may take the form

$$r(\hat{r},\hat{\theta},t) = \sqrt{\left\{\bar{\epsilon}(\hat{r},t) + \hat{r}\cos\hat{\theta}\right\}^2 + \left(\hat{r}\sin\hat{\theta}\right)^2} \tag{7.12}$$

$$\theta(\hat{r},\hat{\theta},t) = \arctan\left(\frac{\hat{r}\sin\hat{\theta}}{\bar{\epsilon}(\hat{r},t) + \hat{r}\cos\hat{\theta}}\right) \,, \tag{7.13}$$

where

$$\bar{\epsilon}(\hat{r},t) = \left(\frac{\hat{r}-\hat{r}_i}{\hat{r}_o-\hat{r}_i}\right)\epsilon(t)\,.$$

We remark that $\bar{\epsilon}$ is zero on the inner cylinder and equal to $\epsilon(t)$ on the outer cylinder. Also, the coordinate transformation (7.10) is defined uniquely only at the boundaries of the fluid domain, where the displacement of a moving wall must be precisely prescribed. Inside the fluid domain, the transformation is arbitrary and $\bar{\epsilon}$ could also have been defined as

$$\bar{\epsilon}(\hat{r},t) = \left(\frac{\hat{r}-\hat{r}_i}{\hat{r}_o-\hat{r}_i}\right)^2\epsilon(t)\,,$$

which still satisfies (7.11) for the time-dependent outer cylinder radial coordinate in the physical domain.

Now, in the equations of motion every derivative with respect to r or θ must be replaced by derivatives with respect to $\hat{r}$ and $\hat{\theta}$, namely by the chain rule we have

$$\frac{\partial}{\partial r} = \frac{\partial \hat{r}}{\partial r}\frac{\partial}{\partial \hat{r}} + \frac{\partial \hat{\theta}}{\partial r}\frac{\partial}{\partial \hat{\theta}}\,, \qquad \frac{\partial}{\partial \theta} = \frac{\partial \hat{r}}{\partial \theta}\frac{\partial}{\partial \hat{r}} + \frac{\partial \hat{\theta}}{\partial \theta}\frac{\partial}{\partial \hat{\theta}} \tag{7.14}$$

According to equations (7.12) and (7.13), we see that the physical coordinates r and θ differ from their computational counterparts $\hat{r}$ and $\hat{\theta}$ by terms of order ϵ, and hence it easily follows by inversion of the transformation (7.12) and (7.13), and evaluation of (7.14) [22] that the partial derivatives in the physical and computational domains also differ by terms of order ϵ

It is also to be noticed that the partial derivative with respect to time that appears in the equations of motion and which is evaluated at constant physical space location has to be replaced [31] in the computational space by

$$\left.\frac{\partial}{\partial t}\right|_{\mathbf{r}} \equiv \left.\frac{\partial}{\partial t}\right|_{\hat{\mathbf{r}}} - \dot{\mathbf{r}}\cdot\nabla\,, \tag{7.15}$$

where $\mathbf{r}$ is the time derivative of the physical space position vector at constant computational space position The coordinates of $\mathbf{r}$ are given by (7.12–7.13).

From (7.15) and the previous remarks we conclude that if the displacement $\epsilon(t)$ is sufficiently small, then the error incurred by neglecting to use the non-steady coordinate transformation is of order ϵ. Since we are precisely considering small displacements of the outer cylinder in the present work we will thus identify throughout

$$\frac{\partial}{\partial r} \equiv \frac{\partial}{\partial \hat{r}}, \qquad \frac{\partial}{\partial \theta} \equiv \frac{\partial}{\partial \hat{\theta}}, \qquad \left.\frac{\partial}{\partial t}\right|_{\mathbf{r}} \equiv \left.\frac{\partial}{\partial t}\right|_{\hat{\mathbf{r}}}.$$

The boundary conditions associated with equations (7.1–7.9) are thus the following ones. Since the motion of the outer cylinder is in one plane, the plane of oscillation, we measure the circumferential coordinate with respect to the plane of oscillation, Figure 7.1, and the velocity components, v_w and w_w, of the inner cylinder and outer cylinder are given by

$$\left.\begin{aligned} v_w(r_i,\theta,t) &= 0 \\ w_w(r_i,\theta,t) &= 0 \end{aligned}\right\} \text{ on the inner cylinder}, \tag{7.16}$$

$$\left.\begin{aligned} v_w(r_o,\theta,t) &= \dot{\epsilon}(t)\cos\theta \\ w_w(r_o,\theta,t) &= -\epsilon(t)\sin\theta \end{aligned}\right\} \text{ on the outer cylinder}. \tag{7.17}$$

Equations (7.16) and (7.17) represent the velocity components on the inner and outer cylinder walls as a function of time. In a forced vibration numerical experiment, the function $\epsilon(t)$ is a known function of time and hence $\mathbf{V}_w^{n+1} = [v_w^{n+1}\ w_w^{n+1}]^T$ can be imposed as a boundary condition to solve the flow problem, as explained in Chapter 3.

7.2 Linearized Equations of Motion

The linearized one-harmonic solution presented in section 6.4 for the Navier-Stokes equations can be particularized for the present two-dimensional problem. First, we note that $\hat{v}_0$ is zero in the present case because the annular passage is uniform. Also, we will take $\hat{u}_0$ equal to zero – we recall that $\hat{w}_0$ is equal to zero because w is an odd function of θ. We thus obtain the following r- and θ-sweep equations for the perturbation quantities $\hat{v}_1, \hat{w}_1$ and $\hat{p}_1$. From (6.46-6.48), the r-sweep is then

$$\begin{aligned}(1+\Delta\tau)\,\overline{\Delta\hat{v}_1} \;+\; \alpha\,\Delta\tau\left[\frac{\partial(\overline{\Delta\hat{p}_1})}{\partial r}-\frac{1}{Re}\left\{\frac{\partial}{r\,\partial r}\left(r\,\frac{\partial(\overline{\Delta\hat{v}_1})}{\partial r}\right)-\frac{\overline{\Delta\hat{v}_1}}{r^2}\right\}\right] \\ = \Delta\tau\left[(\hat{F}_v^n)_1-\hat{v}_1^\nu-\alpha\,(\hat{G}_v^\nu)_1\right] \qquad (7.18)\end{aligned}$$

$$\begin{aligned}\overline{\Delta\hat{w}_1} \;-\; \frac{\alpha\,\Delta\tau}{Re}\frac{\partial}{r\,\partial r}\left(r\,\frac{\partial(\overline{\Delta\hat{w}_1})}{\partial r}\right) \\ = \Delta\tau\left[(\hat{F}_w^n)_1-\hat{w}_1^\nu-\alpha\,(\hat{G}_w^\nu)_1\right] \qquad (7.19)\end{aligned}$$

$$\overline{\Delta\hat{p}_1} \;+\; \frac{\Delta\tau}{\delta}\frac{\partial(r\,\overline{\Delta\hat{v}_1})}{r\,\partial r}=-\frac{\Delta\tau}{\delta}\,(\nabla\cdot\hat{\mathbf{V}})_1^\nu\,, \qquad (7.20)$$

and the θ-sweep is derived from equations (6.50-6.52),

$$\Delta\hat{v}_1 \;+\; \frac{\alpha\,\Delta\tau}{Re}\frac{\Delta\hat{v}_1}{r^2}=\overline{\Delta\hat{v}_1} \qquad (7.21)$$

$$(1+\Delta\tau)\,\Delta\hat{w}_1 \;+\; \alpha\,\Delta\tau\left[\frac{\Delta\hat{p}_1}{r}+\frac{2}{r^2}\frac{\Delta\hat{w}_1}{Re}\right]=\overline{\Delta w_1} \qquad (7.22)$$

$$\Delta\hat{p}_1 \;-\; \frac{\Delta\tau}{\delta}\frac{\Delta\hat{w}_1}{r}=\overline{\Delta\hat{p}_1} \qquad (7.23)$$

As usual, in equations (7.18-7.20) we have the following relations:

$$(\hat{F}_v^n)_1 = \frac{1}{3}(4\,\hat{v}_1^n - \hat{v}_1^{n-1})$$
$$(\hat{F}_w^n)_1 = \frac{1}{3}(4\,\hat{w}_1^n - \hat{w}_1^{n-1})\,,$$

$$(\hat{G}_v^\nu)_1 = \frac{\partial \hat{p}_1^\nu}{\partial r} - \frac{1}{Re}\left[\frac{1}{r}\frac{\partial}{\partial r}\left(r\,\frac{\partial \hat{v}_1^\nu}{\partial r}\right) - \frac{2\,\hat{v}_1^\nu}{r^2} + \frac{2\,\hat{w}_1^\nu}{r^2}\right] \tag{7.24}$$

$$(\hat{G}_w^\nu)_1 = \frac{\hat{p}_1^\nu}{r} - \frac{1}{Re}\left[\frac{1}{r}\frac{\partial}{\partial r}\left(r\,\frac{\partial \hat{w}_1^\nu}{\partial r}\right) - \frac{2\,\hat{w}_1^\nu}{r^2} + \frac{2\,\hat{v}_1^\nu}{r^2}\right] \tag{7.25}$$

$$(\nabla\cdot\hat{\mathbf{V}})_1^\nu = \frac{\partial(r\,\hat{v}_1^\nu)}{r\,\partial r} - \frac{\hat{w}_1^\nu}{r}\,. \tag{7.26}$$

The method for solving (7.18–7.26) is a particular case of the more general method presented in Appendix A for the three-dimensional linearized equations. The mesh is then a one-dimensional staggered grid, Figure 7.2, where the velocity component $\hat{v}_{1(j)}$ is defined at radial coordinate r_j^v, and both velocity component $\hat{w}_{1(j)}$ and pressure $\hat{p}_{1(j)}$ are defined at radial coordinate r_j^w. The procedure is thus a particularization of that described in Appendix A for the three-dimensional equations and will not be repeated here.

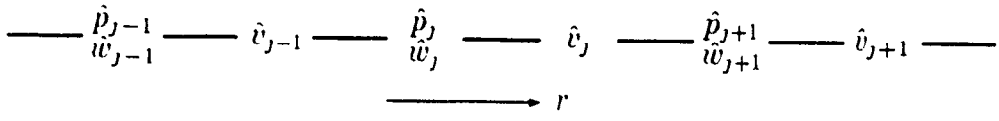

Figure 7.2: One-dimensional staggered mesh used to solve the two-dimensional unsteady annular flow problem with the one- and two-harmonic solutions.

The boundary conditions associated with those equations are derived by applying the Galerkin procedure to (7.16) and (7.17), and we readily find

$$\left.\begin{aligned} \hat{v}_{1(w)} &= 0 \\ \hat{w}_{1(w)} &= 0 \end{aligned}\right\} \text{ on the inner cylinder,} \tag{7.27}$$

$$\left.\begin{aligned} \hat{v}_{1(w)} &= \epsilon(t)/2 \\ \hat{w}_{1(w)} &= \epsilon(t)/2 \end{aligned}\right\} \text{ on the outer cylinder} \tag{7.28}$$

7.3 Two-Harmonic Non-Linear Solution

Now, we consider $N = 2$ harmonics in (6.21–6.24) for the series expansions of the flow variables, such that we can derive the following two sets of equations from (6.25–6.36), under the following assumptions, the usual ones for the problem at hand. First, all derivatives with respect to r are equal to zero, and there is no need to solve the axial momentum equation; also $\hat{v}_0$ is equal to zero and we take u_0 equal to zero as well. Then (6.25-6.36) reduce to the following two sets of equations, one for $\mu = 1$ and one for $\mu = 2$, where we make use of relations (6.37) in writing them down. The first set of equations for $\mu = 1$ is thus, with (7.29–7.31) being the r-sweep and (7.32–7.34) being the θ-sweep,

$$(1+\Delta\tau)\,\overline{\Delta\hat{v}}_1 + \alpha\,\Delta\tau\left[\frac{1}{r}\frac{\partial}{\partial r}\left\{r\left(\hat{v}_2^{\nu}\overline{\Delta\hat{v}}_1 + \hat{v}_1^{\nu}\overline{\Delta\hat{v}}_2\right)\right\} + \frac{\partial(\overline{\Delta\hat{p}}_1)}{\partial r}\right.$$

$$\left. - \frac{1}{Re}\left\{\frac{\partial}{r\,\partial r}\left(r\,\frac{\partial(\overline{\Delta\hat{v}}_1)}{\partial r}\right) - \frac{\overline{\Delta\hat{v}}_1}{r^2}\right\}\right] = \Delta\tau\left[(\hat{F}_r^n)_1 - \hat{v}_1^{\nu} - \alpha\,(G_r^{\nu})_1\right] \tag{7.29}$$

$$\overline{\Delta\hat{w}}_1 + \alpha\,\Delta\tau\left[\frac{1}{r}\frac{\partial}{\partial r}\left\{r\left(-\hat{v}_2^{\nu}\overline{\Delta\hat{w}}_1 + \hat{v}_1^{\nu}\overline{\Delta\hat{w}}_2\right)\right\}\right.$$

$$\left. - \frac{1}{Re\,r}\frac{\partial}{\partial r}\left(r\,\frac{\partial(\overline{\Delta\hat{w}}_1)}{\partial r}\right)\right] = \Delta\tau\left[(\hat{F}_w^n)_1 - \hat{w}_1^{\nu} - \alpha\,(\hat{G}_w^{\nu})_1\right] \qquad (7.30)$$

$$\overline{\Delta\hat{p}}_1 + \frac{\Delta\tau}{\delta}\frac{\partial(r\,\overline{\Delta\hat{v}}_1)}{r\,\partial r} = -\frac{\Delta\tau}{\delta}\,(\nabla\cdot\hat{\mathbf{V}})_1^{\nu}\,, \qquad (7.31)$$

$$\Delta\hat{v}_1 \;+\; \alpha\,\Delta\tau\left[\frac{1}{r}\,(\hat{w}_1^{\nu}\Delta\hat{v}_2 - \hat{w}_2^{\nu}\Delta\hat{v}_1) + \frac{\Delta\hat{v}_1}{Re\,r^2}\right] = \overline{\Delta\hat{v}}_1 \qquad (7.32)$$

$$(1+\Delta\tau)\,\Delta\hat{w}_1 \;+\; \alpha\,\Delta\tau\left[\frac{\hat{w}_2^{\nu}\Delta\hat{w}_1 + \hat{w}_1^{\nu}\Delta\hat{w}_2}{r} + \frac{\hat{v}_1^{\nu}\Delta\hat{w}_2 - \hat{v}_2^{\nu}\Delta\hat{w}_1}{r}\right.$$

$$\left. +\; \frac{\Delta\hat{p}_1}{r} + \frac{2\,\Delta\hat{w}_1}{Re\,r^2}\right] = \overline{\Delta\hat{w}}_1 \qquad (7.33)$$

$$\Delta\hat{p}_1 \;-\; \frac{\Delta\tau}{\delta}\frac{\Delta\hat{w}_1}{r} = \overline{\Delta\hat{p}}_1\,. \qquad (7.34)$$

Then, we have the set of equations for $\mu = 2$, in which (7.35–7.37) represent the r-sweep and (7.38–7.40) the θ-sweep:

$$(1+\Delta\tau)\,\overline{\Delta\hat{v}}_2 + \alpha\,\Delta\tau\left[\frac{1}{r}\frac{\partial}{\partial r}\left(r\,\hat{v}_1^{\nu}\overline{\Delta\hat{v}}_1\right) + \frac{\partial(\overline{\Delta\hat{p}}_2)}{\partial r}\right.$$

$$\left. - \frac{1}{Re}\left\{\frac{\partial}{r\,\partial r}\left(r\,\frac{\partial(\overline{\Delta\hat{v}}_2)}{\partial r}\right) - \frac{\overline{\Delta\hat{v}}_2}{r^2}\right\}\right] = \Delta\tau\left[(\hat{F}_v^n)_2 - \hat{v}_2^{\nu} - \alpha\,(\hat{G}_v^{\nu})_2\right] \qquad (7.35)$$

$$\overline{\Delta\hat{w}_2} + \alpha\,\Delta\tau\left[\frac{1}{r}\frac{\partial}{\partial r}\left(r\,\hat{v}_1^{\nu}\overline{\Delta\hat{w}_1}\right)\right.$$

$$\left. - \frac{1}{Re\,r}\frac{\partial}{\partial r}\left(r\,\frac{\partial(\overline{\Delta\hat{w}_2})}{\partial r}\right)\right] = \Delta\tau\,\left[(\hat{F}_w^n)_2 - \hat{w}_2^{\nu} - \alpha\,(\hat{G}_w^{\nu})_2\right] \tag{7.36}$$

$$\overline{\Delta\hat{p}_2} + \frac{\Delta\tau}{\delta}\frac{\partial(r\,\overline{\Delta\hat{v}_2})}{r\,\partial r} = -\frac{\Delta\tau}{\delta}\,(\nabla\cdot\hat{\mathbf{V}})_2^{\nu}\,, \tag{7.37}$$

$$\Delta\hat{v}_2 \;+\; \alpha\,\Delta\tau\left[\frac{-2\,\hat{w}_1^{\nu}\Delta\hat{v}_1}{r} + \frac{4\,\Delta\hat{v}_2}{Re\,r^2}\right] = \overline{\Delta\hat{v}_2}\,, \tag{7.38}$$

$$(1+\Delta\tau)\,\Delta\hat{w}_2 \;+\; \alpha\,\Delta\tau\left[\frac{-2\,\hat{w}_1^{\nu}\Delta\hat{w}_1}{r} + \frac{\hat{v}_1^{\nu}\Delta\hat{w}_1}{r}\right.$$

$$\left. +\; \frac{2\,\Delta\hat{p}_2}{r} + \frac{5\,\Delta\hat{w}_2}{Re\,r^2}\right] = \overline{\Delta\hat{w}_2}\,, \tag{7.39}$$

$$\Delta\hat{p}_2 \;-\; 2\,\frac{\Delta\tau}{\delta}\frac{\Delta\hat{w}_2}{r} = \overline{\Delta\hat{p}_2}\,. \tag{7.40}$$

As usual in the last equations we have

$$\begin{aligned}
(\hat{F}_v^n)_1 &= \tfrac{1}{3}(4\,\hat{v}_1^n - \hat{v}_1^{n-1}) \qquad & (\hat{F}_w^n)_1 &= \tfrac{1}{3}(4\,\hat{w}_1^n - \hat{w}_1^{n-1}) \\
(\hat{F}_v^n)_2 &= \tfrac{1}{3}(4\,\hat{v}_2^n - \hat{v}_2^{n-1}) \qquad & (\hat{F}_w^n)_2 &= \tfrac{1}{3}(4\,\hat{w}_2^n - \hat{w}_2^{n-1})\,,
\end{aligned} \tag{7.41}$$

$$\begin{aligned}
(\hat{G}_v^{\nu})_1 &= \frac{2}{r}\frac{\partial}{\partial r}(r\,\hat{v}_2^{\nu}\hat{v}_1^{\nu}) \\
&- \frac{1}{r}(\hat{w}_2^{\nu}\hat{v}_1^{\nu} - \hat{w}_1^{\nu}\hat{v}_2^{\nu}) - \frac{2}{r}\hat{w}_2^{\nu}\hat{w}_1^{\nu} \\
&+ \frac{\partial\hat{p}_1^{\nu}}{\partial r} - \frac{1}{Re}\left[\frac{\partial}{r\,\partial r}\left(r\,\frac{\partial\hat{v}_1^{\nu}}{\partial r}\right) + \frac{2}{r^2}(\hat{w}_1^{\nu} - \hat{v}_1^{\nu})\right]
\end{aligned}$$

$$
\begin{aligned}
(\hat{G}_v^\nu)_1 &= \frac{1}{r}\frac{\partial}{\partial r}\left\{r\left(-\hat{v}_2^\nu \hat{w}_1^\nu + \hat{v}_1^\nu \hat{w}_2^\nu\right)\right\} \\
&+ \frac{2}{r}\hat{w}_2^\nu \hat{w}_1^\nu + \frac{1}{r}\left(\hat{v}_1^\nu \hat{w}_2^\nu - \hat{v}_2^\nu \hat{w}_1^\nu\right) \\
&+ \frac{\hat{p}_1^\nu}{r} - \frac{1}{Re}\left[\frac{\partial}{r\,\partial r}\left(r\,\frac{\partial \hat{w}_1^\nu}{\partial r}\right) + \frac{2}{r^2}\left(\hat{v}_1^\nu - \hat{w}_1^\nu\right)\right]
\end{aligned}
$$

$$
(\nabla \cdot \hat{\mathbf{V}})_1^\nu = \frac{\partial(r\,\hat{v}_1^\nu)}{r\,\partial r} - \frac{\hat{w}_1^\nu}{r}\,,
$$

$$
\begin{aligned}
(\hat{G}_v^\nu)_2 &= \frac{\partial\left(r\,\hat{v}_1^\nu \hat{v}_1^\nu\right)}{r\,\partial r} - \frac{2}{r}\hat{w}_1^\nu \hat{v}_1^\nu + \frac{\hat{w}_1^\nu \hat{w}_1^\nu}{r} + \frac{\partial \hat{p}_2^\nu}{\partial r} \\
&- \frac{1}{Re}\left[\frac{\partial}{r\,\partial r}\left(r\,\frac{\partial \hat{v}_2^\nu}{\partial r}\right) + \frac{1}{r^2}\left(4\,\hat{w}_2^\nu - 5\,\hat{v}_2^\nu\right)\right]
\end{aligned}
$$

$$
\begin{aligned}
(\hat{G}_w^\nu)_2 &= \frac{\partial\left(r\,\hat{v}_1^\nu \hat{w}_1^\nu\right)}{r\,\partial r} - \frac{2}{r}\hat{w}_1^\nu \hat{w}_1^\nu + \frac{\hat{v}_1^\nu \hat{w}_1^\nu}{r} + \frac{2}{r}\hat{p}_2^\nu \\
&- \frac{1}{Re}\left[\frac{\partial}{r\,\partial r}\left(r\,\frac{\partial \hat{w}_2^\nu}{\partial r}\right) + \frac{1}{r^2}\left(4\,\hat{v}_2^\nu - 5\,\hat{w}_2^\nu\right)\right]
\end{aligned}
$$

$$
(\nabla \cdot \hat{\mathbf{V}})_2^\nu = \frac{\partial(r\,\hat{v}_2^\nu)}{r\,\partial r} - \frac{2}{r}\hat{w}_2^\nu\,.
$$

The boundary conditions for the first-harmonic variables are exactly the same as in the previous section, namely equations (7.27) and (7.28), whereas the second-harmonic variables are solved by imposing $\hat{v}_2 = \hat{w}_2 = 0$ on both the inner and outer cylinders, which is also derived by applying the Galerkin procedure to (7.16) and (7.17).

The mesh used to solve these equations is the same as that presented in the previous section, Figure 7.2, for the $N = 1$ harmonic solution. The interpolates of the variables $\hat{v}_2$ and $\hat{w}_2$ are defined as those for $\hat{v}_1$ and $\hat{w}_1$. However, here

we have two sets of equations which are coupled. In order to deal with that difficulty we do the following thing. In equation (7.29) for $\overline{\Delta\hat{v}}_1$, we see that $\overline{\Delta v}_1$ and $\overline{\Delta\hat{v}}_2$ are coupled, hence we drop the term involving $\overline{\Delta\hat{v}}_2$ to uncouple the velocity components. Similarly, in (7.30) the term involving $\overline{\Delta\hat{w}}_2$ is dropped, in (7.32) the term containing $\Delta\hat{v}_2$ is dropped, and in (7.33) the term containing $\Delta\hat{w}_2$ is removed. Also, the terms containing $\overline{\Delta\hat{v}}_1$, $\overline{\Delta\hat{w}}_1$, $\Delta\hat{v}_1$ and Δw_1 are dropped from equations (7.35), (7.36), (7.38) and (7.39), respectively.

Note that the terms that are removed from the equations, which are in delta form, only affect the coupling on the implicit left-hand sides of the equations, which eventually might affect the convergence rate of the pseudo-time iteration procedure only. Indeed, when convergence has been reached in pseudo-time it is to be noted that $\Delta\mathbf{V}$ is zero, and all the terms that have been dropped would then be zero in any case, as are the ones that are kept. The coupling between the equations is ensured by the terms $(\hat{G}_v^\nu)_1, (\hat{G}_w^\nu)_1, (G_v^\nu)_2$ and $(G_w^\nu)_2$, which are on the right-hand sides of equations (7.29), (7.30), (7.35) and (7.36), and which are always calculated in their integrity.

The method of solution is thus the following one, after the implicit left-hand sides of equations (7.29–7.40) have been decoupled. At a given pseudo-time iteration step t^ν, (7.29–7.34) are solved for $\Delta\hat{v}_1, \Delta\hat{w}_1$ and Δp_1, in a manner similar to what is done in the case of the $N = 1$ harmonic solution, and then the variables are updated to obtain $\hat{v}_1^{\nu+1}$, $\hat{w}_1^{\nu+1}$ and $\hat{p}_1^{\nu+1}$; equations (7.35–7.40) are solved thereafter for $\Delta\hat{v}_2, \Delta\hat{w}_2$ and $\Delta\hat{p}_2$ in order to obtain $\hat{v}_2^{\nu+1}$, $\hat{w}_2^{\nu+1}$ and $\hat{p}_2^{\nu+1}$. The procedure is repeated until convergence. Note that a variable is updated as soon as it is obtained, not only at the end of a pseudo-time step.

7.4 Numerical Results

As was the case in Chapter 5, the results presented in Section 7.4.1 have been computed using the three-point-backward implicit time-differencing scheme developed in Chapter 3, equation (3.4). The results obtained with this scheme are compared in Section 7.4.2 with the same method which uses a Crank-Nicolson time-differencing scheme instead, as per equation (3.5). The comparison shows that the present three-point-backward scheme is free of the spurious numerically-induced oscillations present in the results obtained with the Crank-Nicolson scheme.

7.4.1 The three-point-backward scheme

In the geometry of the problem which is shown in Figure 7.1, page 108, the two cylinders delimit an annular region containing a fluid which is initially at rest. Then the outer cylinder, of radius r_o, starts to undergo transverse harmonic oscillations in one plane, its axis remaining parallel with the axis of the fixed inner cylinder, of radius r_i. If the circumferential coordinate θ is measured from the plane of oscillation, then the velocity components $\bar{v}_w(\theta,\bar{t})$ and $\bar{w}_w(\theta,\bar{t})$ of the outer cylinder are given by[1]

$$\begin{aligned} \bar{v}_w(\theta,\bar{t}) &= \bar{v}(\bar{r}_o,\theta,\bar{t}) &= \Omega\bar{\epsilon}_o \sin\Omega\bar{t}\,\cos\theta\,, \\ \bar{w}_w(\theta,\bar{t}) &= \bar{w}(\bar{r}_o,\theta,\bar{t}) &= -\Omega\bar{\epsilon}_o \sin\Omega\bar{t}\,\sin\theta\,, \end{aligned} \tag{7.42}$$

where $\bar{\epsilon}_o$ is the maximum transverse displacement of the cylinder axis and Ω is the angular frequency of oscillation. Now, the Reynolds number appearing in the fluid equations has to be defined for the problem at hand. We elect to chose H, the annular gap width, as characteristic length, and the characteristic velocity is taken to be ΩH. Then the Reynolds number is found to be equal to

[1] Barred quantities are dimensional.

$$Re \equiv s = \frac{\Omega H^2}{\nu} , \tag{7.43}$$

where ν is the fluid kinematic viscosity. We remark that we identify the Reynolds number, Re, with s, the Stokes number, for that particular problem. We will actually use the Stokes number, for notation, in this chapter as it best describes the frequency characteristics of the system. In view of the choice of characteristic length and velocity, the non-dimensional angular frequency of oscillation becomes 1 and the boundary conditions (7.42) take the form

$$\begin{aligned} v_w(\theta, t) &= \frac{\bar{\epsilon}_o}{H} \sin t \cos\theta , \\ w_w(\theta, t) &= -\frac{\bar{\epsilon}_o}{H} \sin t \sin\theta . \end{aligned}$$

Numerical computations have been performed on a non-dimensional geometry of inner radius $r_i = 9$ and outer radius $r_o = 10$, for two Stokes numbers, $s = 300$ and $s = 3\,000$. The presentation of the results is done in Figures 7.3 to 7.9, where the computations are made with the full non-linear solution described in Section 7.1, the one-harmonic solution of Section 7.2 and the two-harmonic solution of Section 7.3. All the quantities in those figures are *dimensionless*.

Initial conditions were zero velocity components and pressure in the fluid domain and the equations were integrated until a periodic state was reached, which took 8 harmonic cycles, where each cycle was divided up into 19 time steps. The hyperbolic tangent function was used to stretch the grid in the radial direction and we will denote by Δr_{min} the minimum mesh spacing near the inner or outer cylinder walls. The one- and two-harmonic solutions require only a one-dimensional mesh spanning the radial direction, and the full non-linear solution requires that the grid be two-dimensional, the circumferential direction being included. In that case the

mesh spans the circumferential direction between $\theta = 0$ and $\theta = \pi$, and is uniform in that direction, see Appendix B. When comparison is made between the three solutions on one given figure, such as in Figures 7.3 to 7.6 and in Figure 7.9, all three solutions have the same stretching and number of grid points in the radial direction.

Figures 7.3 to 7.6 contain 15 curves each, representing the three solutions for each of 5 instants t^n within the harmonic cyle. The five instants are

$$t^n = \frac{2\pi n}{19}, \quad n = 5, 7, 9, 11, 13, \tag{7.44}$$

for the results involving the circumferential velocity component w, and

$$t^n = \frac{2\pi n}{19}, \quad n = 1, 3, 5, 7, 9, \tag{7.45}$$

for the results involving the pressure p. The mesh in Figures 7.3 to 7.6 was composed of 24 × 24 grid points, where Δr_{min} is equal to 0.020 when $s = 300$ and $\Delta r_{min} = 0.0075$ at $s = 3\,000$.

Figure 7.3 presents radial profiles of the circumferential velocity component w, at an azimuth of $\theta = 45°$. Figure 7.3(a) is for $s = 300$ and Figure 7.3(b) for $s = 3\,000$. It is seen that the one-harmonic solution differs from the two-harmonic and non-linear solutions, the latter two being close to each other at $s = 300$ and differing slightly at $s = 3\,000$, probably due to the stronger non-linearities present at this higher Stokes number. In Figure 7.4, the radial profiles of pressure taken at $\theta = 3.75°$ are plotted for $s = 300$ and $s = 3\,000$. All three solutions are seen to be very close to one another for these pressure results.

In Figures 7.5 and 7.6 circumferential profiles of velocity component w and pressure p, taken at $r = 9.75$, are plotted for two Stokes numbers, $s = 300$ and $s = 3\,000$. Same remarks as before apply regarding the agreement between the

three solutions for velocity or pressure.

In each of the previous figures, the number of grid points in both the radial and circumferential directions was 24, even though stretching near cylinder walls was different in solutions at $s = 300$ or $s = 3000$. In Figures 7.7 and 7.8 comparison is made using the non-linear solution between computations performed on coarse and fine meshes. Figures 7.7(a) and 7.7(b) present radial profiles of velocity component w taken at $\theta = 45°$, for $s = 300$ and $s = 3000$, respectively, and Figure 7.8 gives circumferential profiles of w, taken at $r = 9.75$ for $s = 300$ in Figure 7.8(a), and taken at $r = 9.80$ for $s = 3000$ in Figure 7.8(b). The fine mesh contained 24 grid points in both the radial and circumferential directions for the computations performed at $s = 300$, with $\Delta r_{min} = 0.020$, and the coarse mesh had 12 grid points in both these directions with $\Delta r_{min} = 0.045$. For the computations at $s = 3000$, the fine mesh had $J = 38$ grid points in the radial direction, and $K = 36$ grid points in the circumferential direction, with $\Delta r_{min} = 0.0040$, whereas the coarse mesh had both J and K equal to 24, with $\Delta r_{min} = 0.0075$. It is seen from Figures 7.7 and 7.8 that the agreement between the coarse mesh and fine mesh results for w is very good, which was also the case for the pressure results, not presented here.

Finally, Figures 7.9(a) and 7.9(b) are time-evolution curves of the fluid force per unit length exerted on the oscillating outer cylinder, which includes the pressure force and the viscous shearing force. It is derived as follows, where capital bold letters denote second order tensors and where $\hat{\mathbf{e}}_r$ and $\hat{\mathbf{e}}_\theta$ are the unit vectors in the radial and circumferential directions, respectively. The viscous stress tensor, $\boldsymbol{\Sigma}$, in an incompressible viscous fluid is given by [34]

$$\boldsymbol{\Sigma} = -p\,\mathbf{I} + \frac{1}{Re}\left\{(\nabla\mathbf{v}) + (\nabla\mathbf{v})^T\right\}, \tag{7.46}$$

where p is the pressure, $\mathbf{I}$ is the second-order unit tensor and $\nabla\mathbf{v}$ the gradient of the velocity vector, a second order tensor also; $(\nabla\mathbf{v})^T$ is its transpose. To obtain the stress vector on the outer cylinder, we dot (7.46) with the unit vector normal to the cylinder surface, which is $-\hat{\mathbf{e}}_r$, and we obtain

$$-\hat{\mathbf{e}}_r \cdot \boldsymbol{\Sigma} = \sigma_{rr}\hat{\mathbf{e}}_r + \sigma_{r\theta}\hat{\mathbf{e}}_\theta \ ,$$

where

$$\begin{aligned} \sigma_{rr} &= p - \frac{2}{Re}\frac{\partial v}{\partial r} \ , \\ \sigma_{r\theta} &= -\frac{1}{Re}\left[\frac{\partial w}{\partial r} + \frac{1}{r}\left(\frac{\partial v}{\partial \theta} - w\right)\right] \ . \end{aligned} \tag{7.47}$$

The axial component of stress has been omitted for the present problem. The force, f, per unit length on the oscillating cylinder is then given by projecting the stress vector into the plane of oscillation and integrating over θ between 0 and 2π:

$$f = \int_0^{2\pi} (\sigma_{rr}\cos\theta - \sigma_{r\theta}\sin\theta)\ r_o d\theta \ . \tag{7.48}$$

When the one- or two-harmonic solutions are chosen, the integration in (7.48) can be done analytically and we obtain the following expression for the force f^n at time t^n:

$$f^n = 2\pi r_o \left[\hat{p}_1^n - \frac{1}{Re}\left(2\frac{\partial \hat{v}_1^n}{\partial r} + \frac{\partial \hat{w}_1^n}{\partial r}\right)\right]_w \ , \tag{7.49}$$

where the above expression is evaluated at the wall, indicated by the subscript w. We note that the second harmonic variables $\hat{v}_2^n$, $\hat{w}_2^n$ and $\hat{p}_2^n$ do not appear in the expression for the force even when the two-harmonic solution is chosen because of the orthogonality properties of the trigonometric functions. The non-linear

solution requires that the integration in (7.48) be performed numerically; this has been done in the present case using Simpson's rule.

Hence, Figure 7.9(a) is the force on the outer cylinder calculated during the first 6 harmonic cycles at a Stokes number s of 300. It is seen that all three solutions are perfectly superimposed, as is the case in Figure 7.9(b) for the computations performed at Stokes number $s = 3\,000$. This can be explained by noting that in the previous figures the pressure results were all very nearly equal, whether one-harmonic, two-harmonic or non-linear solutions were used, and the pressure is the major contributor to the fluid force. Also, the radial derivative of the circumferential velocity component w at the wall, which is mostly responsible for the shear stress contribution to the fluid force, see equation (7.47), is nearly the same for all three solutions, as is seen from Figure 7.3.

To conclude the present section, we discuss the choice of the artificial compressibility, δ, and pseudo-time step, $\Delta\tau$, made regarding the computations of this problem. The formulas developed in Section 5.2, equations (5.11) and (5.12), were applied in the present case, where the characteristic velocity was chosen to be, in non-dimensional form,

$$q = \frac{\Omega\bar{\epsilon}_o}{\Omega H} = \frac{\bar{\epsilon}_o}{H} . \tag{7.50}$$

Now, we note that correction factors had to be applied to the values of δ predicted by (5.11), namely 0.0001 for both the one- and two-harmonic solutions and 0.005 for the full non-linear solution. The new values of δ are thus orders of magnitude different from their estimates and one is tempted to question the validity of (5.11) in this case. However, it is remarked that (7.50), which is the maximum velocity amplitude at the wall of either v or w, is much smaller than the actual value that the velocity takes inside the fluid domain. Indeed, the value of q determined from

(7.50) is 0.1, whereas we can see from Figure 7.3 that w gets to be of the order of 1 in mid-annulus: the value of δ is thus overestimated. Note that the smaller correction factor of 0.005 in the case of the non-linear solution is likely to come from the fact that after each time step an estimate of the "mean" velocity in the annulus was done, based on the rms value of velocity calculated from the grid point values. This was not done for the one- and two-harmonic solutions.

The optimal Courant number from equation (5.12) was found to be around 2000 for the one-harmonic solution, 1500 for the two-harmonic one and 500 for the full non-linear solution.

We note that the unsteady flow problems treated in Section 5.2 in Cartesian coordinates did not present that difficulty, as the estimates were of the same order of magnitude as the optimal values found from numerical experimentation, as is also the case for the results presented in the next chapter: the Courant numbers also took more reasonable values there, of the order of 40.

To give an indication on how well the method performed, Table 7.1 presents data obtained from computations with the full non-linear solution at $s = 3000$, on the 24×24 grid. The number, k, of pseudo-time steps required to converge as well as the rms and maximum values of the residuals at convergence are tabulated for integration during the first harmonic cycle, at the 19 time steps t^n, $n = 3, 21$. Convergence was reached in pseudo-time when the rms residuals of R_v, R_w and R_p were all less than 10^{-4}. Results for the one- and two-harmonic solutions were better as convergence in pseudo-time was achieved in around 30 steps.

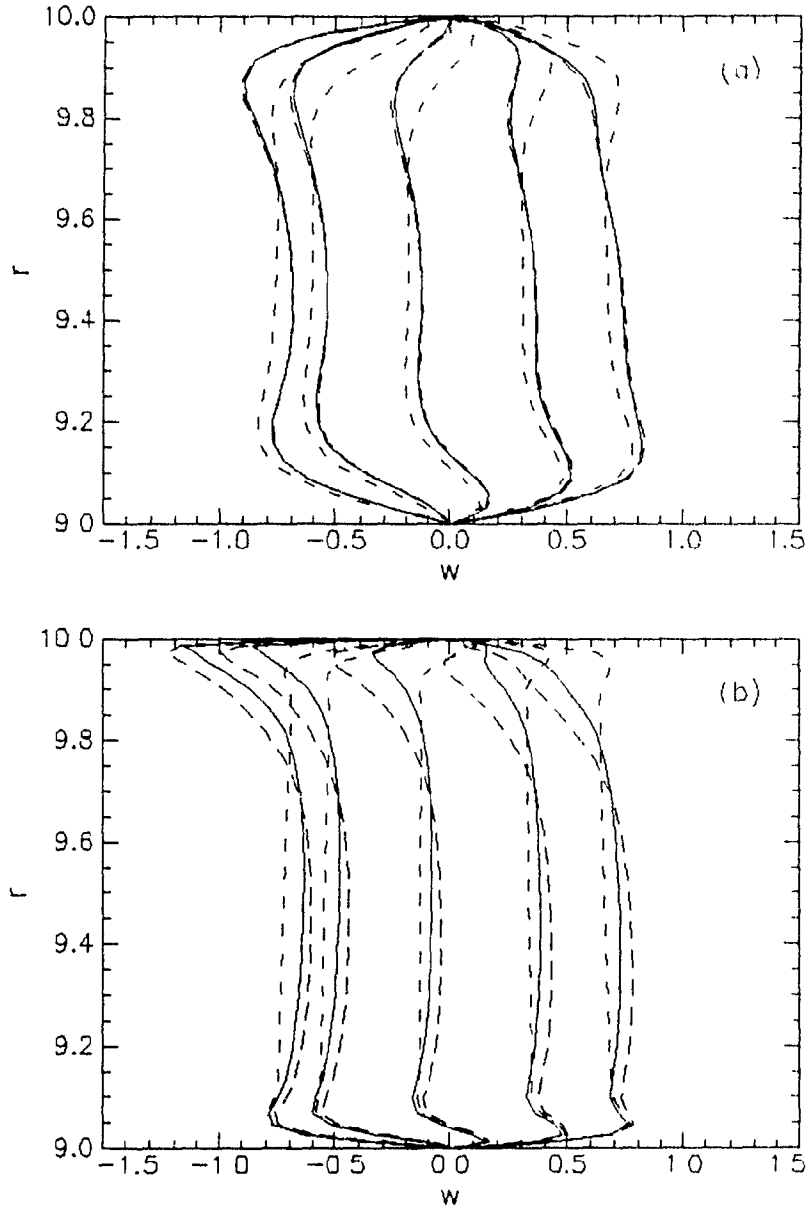

Figure 7.3: Radial profiles of circumferential velocity component w at $\theta = 15°$, for (a) $s = 300$, and (b) $s = 3000$. Comparison between the three solutions is made for 5 instants t^n within the harmonic cycle. – full non-linear solution, – 2-harmonic solution, and –·–· 1-harmonic solution.

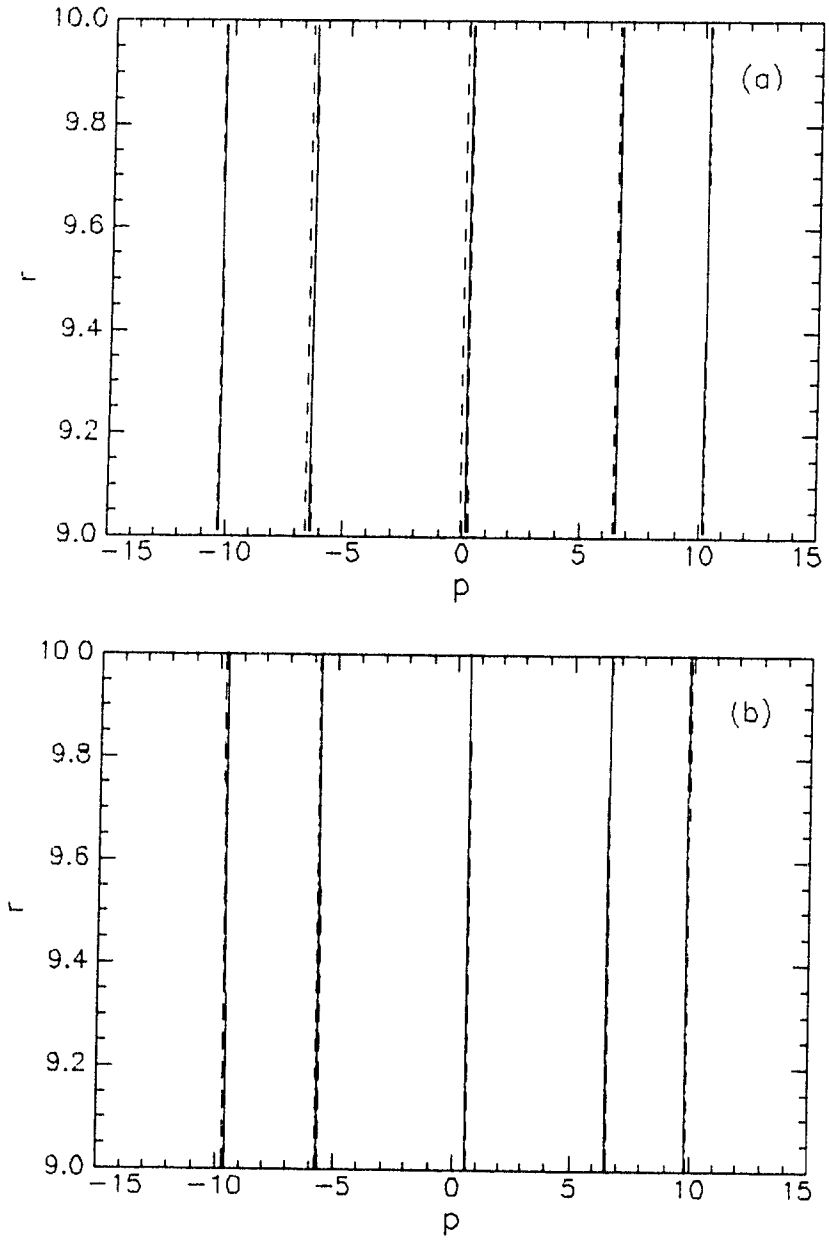

Figure 7.4: Radial profiles of pressure p at $\theta = 3.75°$ for (a) $s = 300.$ and (b) $s = 3000.$ Comparison between the three solutions is made for 5 instants t^n within the harmonic cycle. — full non-linear solution, - - - 2-harmonic solution, and ··· 1-harmonic solution.

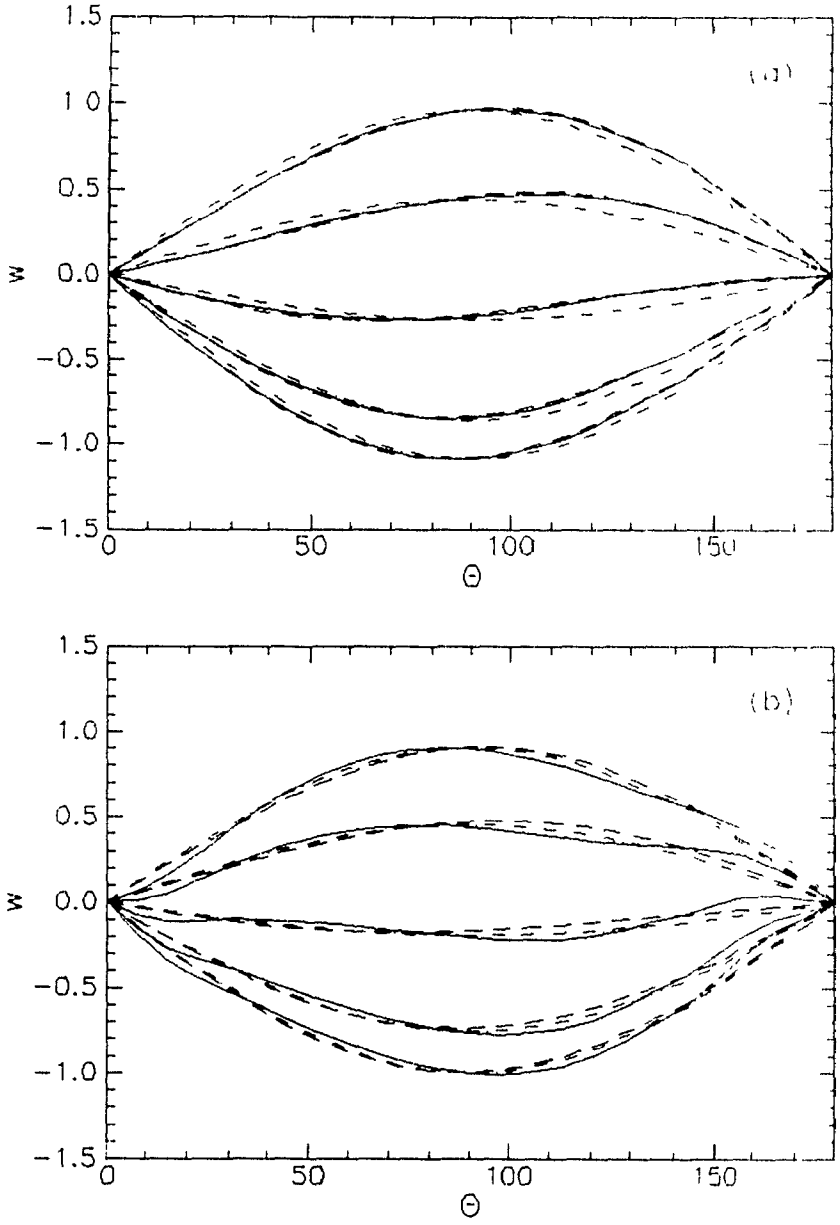

Figure 7.5: Circumferential profiles of circumferential velocity component w at $r = 9.75$, for (a) $s = 300$, and (b) $s = 3000$. Comparison between the three solutions is made for 5 instants t^n within the harmonic cycle. —— full non-linear solution, – – – 2-harmonic solution, and –·– 1-harmonic solution.

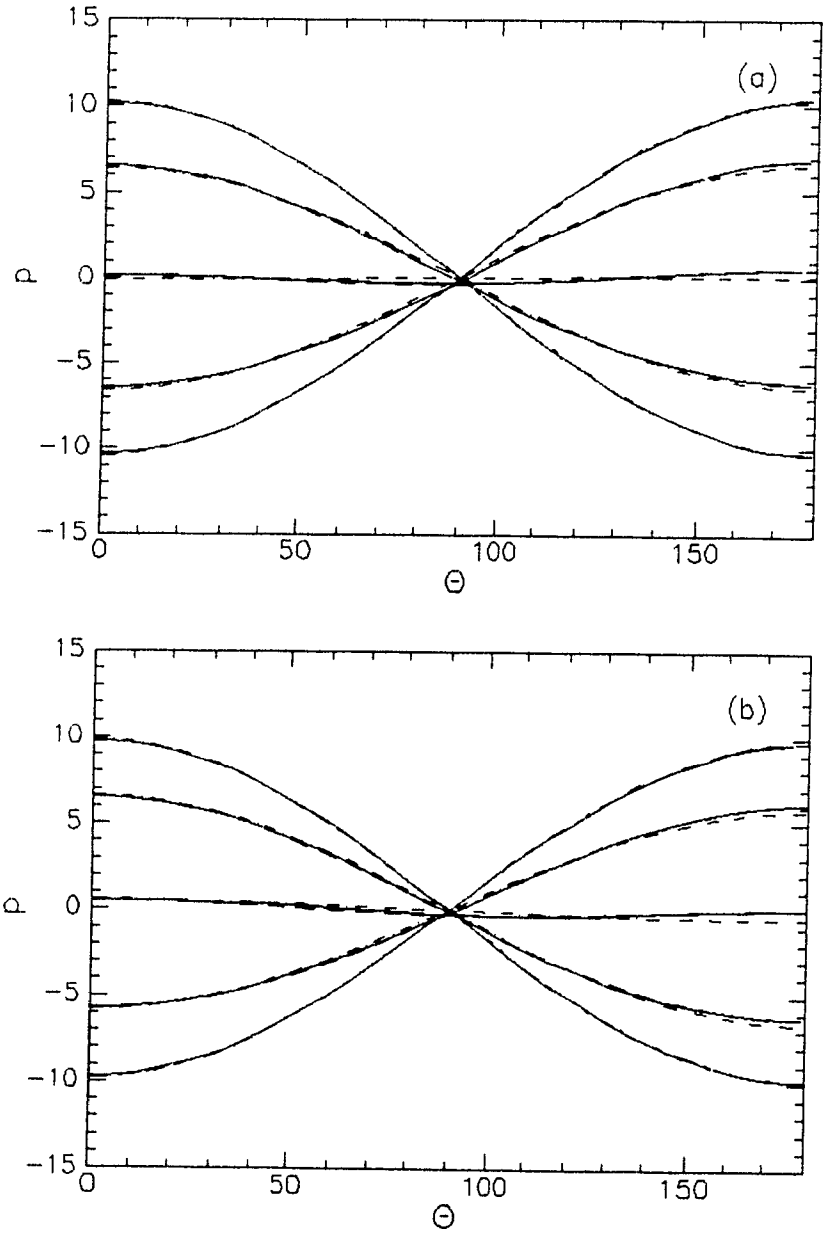

Figure 7.6. Circumferential profiles of pressure p at $r = 9.75$, for (a) $s = 300$, and (b) $s = 3000$. Comparison between the three solutions is made for 5 instants t^n within the harmonic cycle. – full non-linear solution, – – – 2-harmonic solution, and · · 1-harmonic solution.

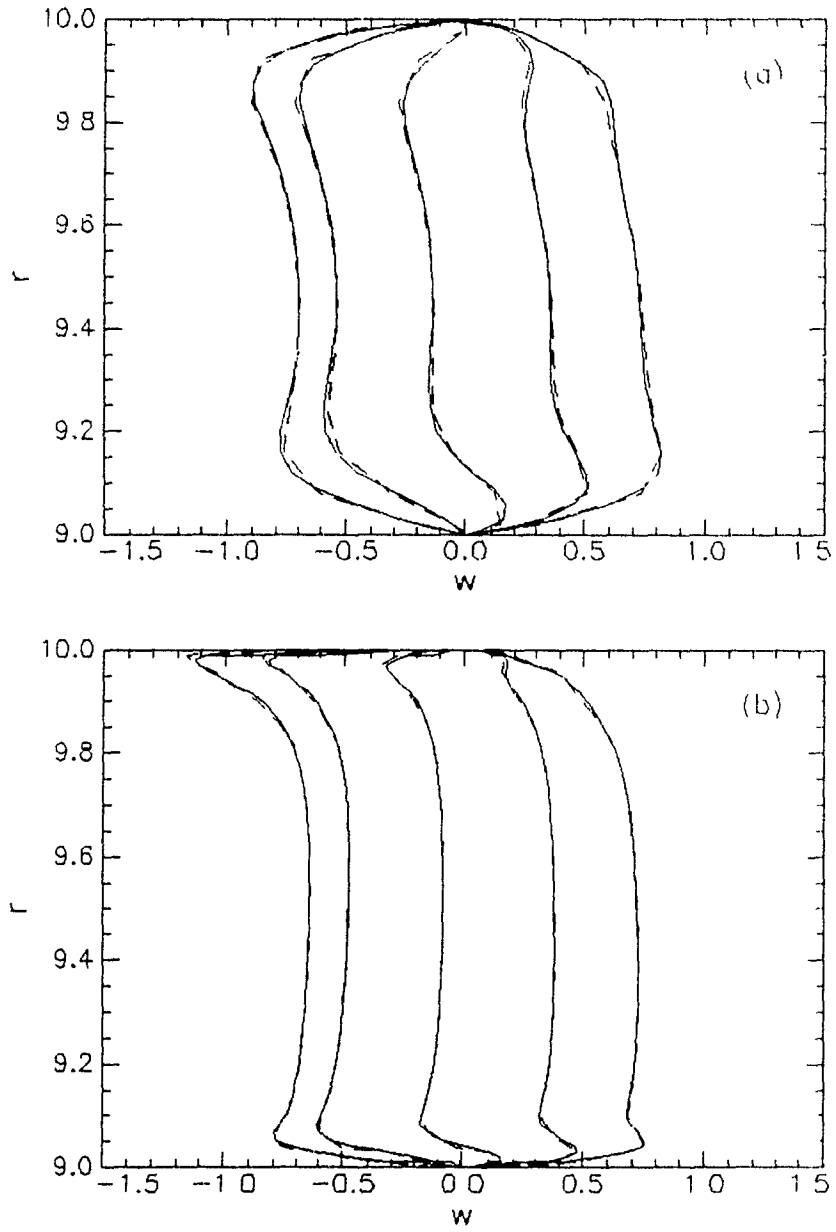

Figure 7.7: Comparison of coarse mesh and fine mesh results using the full nonlinear solution. Radial profiles of circumferential velocity component w at $\theta = 45°$ are presented for (a) $s = 300$, and (b) $s = 3000$, at 5 instants t^n within the harmonic cycle. — fine mesh results, and - - - coarse mesh results.

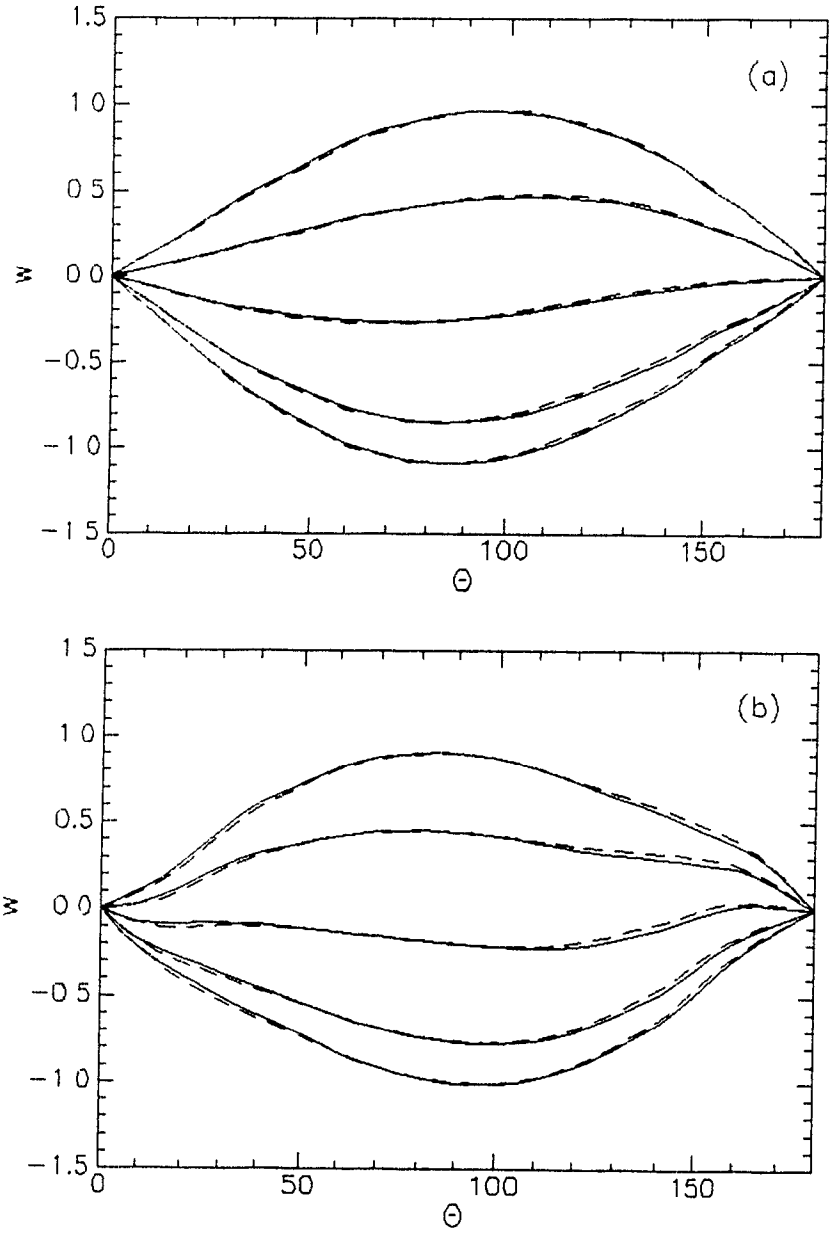

Figure 7.8: Comparison of coarse mesh and fine mesh results using the full non-linear solution. Circumferential profiles of circumferential velocity component w at $r = 9.80$ are presented for (a) $s = 300$, and (b) $s = 3\,000$, at 5 instants t^n within the harmonic cycle — fine mesh results, and - - - coarse mesh results.

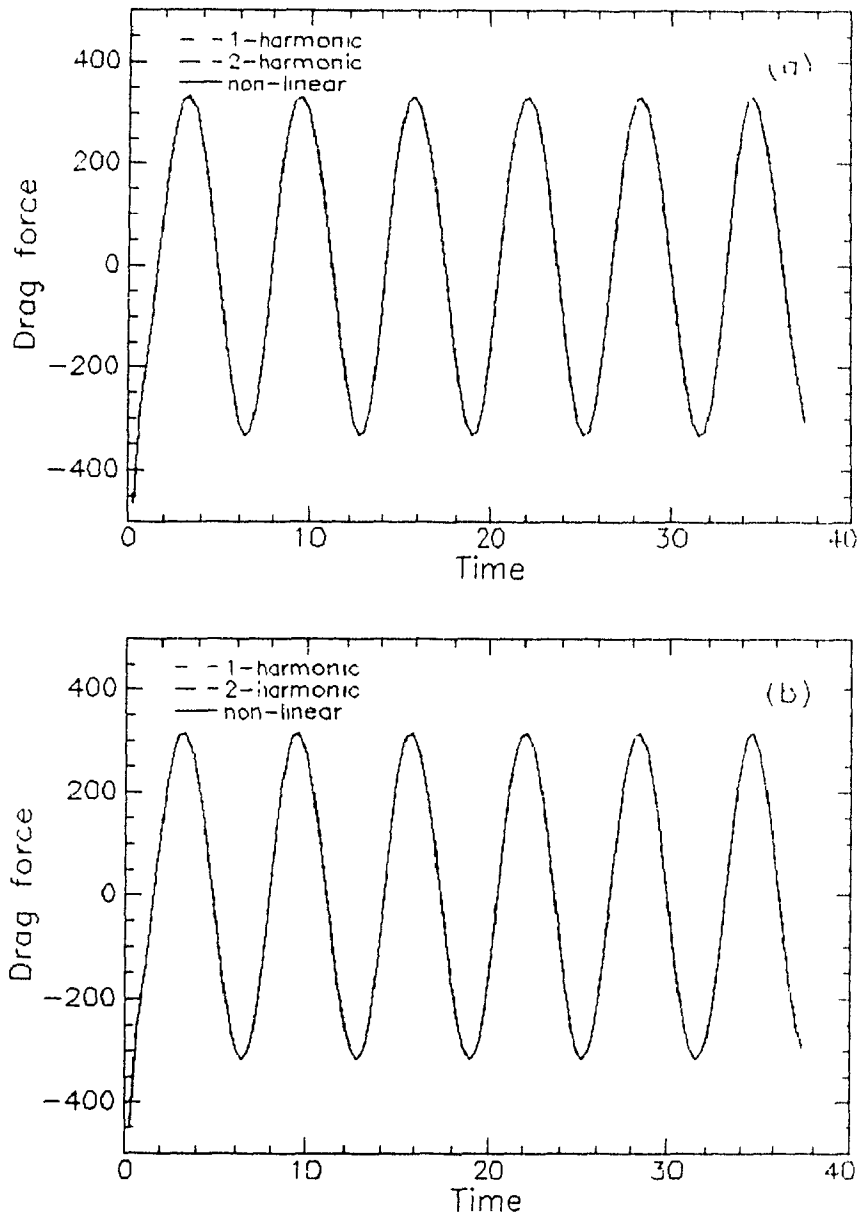

Figure 7.9: Comparison of the fluid force per unit length exerted on the oscillating outer cylinder at (a) $s = 300.$ and (b) $s = 3000$. The three solutions are compared and plotted as a function of time. — full non-linear solution, 2-harmonic solution, and -·- 1-harmonic solution.

n	k	rms(R_v)	rms(R_w)	rms(R_p)	max(R_v)	max(R_w)	max(R_p)
3	136	0.965E-04	0 289E-04	0 401E-05	0.530E-03	0.152E-03	0.643E-05
4	78	0 907E-04	0 783E-05	0.101E-05	0.520E-03	0 415E-04	0.193E-05
5	64	0 967E-04	0.325E-05	0.362E-06	0.609E-03	0.152E-04	0 127E-05
6	81	0 966E-04	0.256E-06	0.115E-06	0.496E-03	0.122E-05	0.913E-06
7	87	0.965E-04	0.227E-06	0.104E-06	0.542E-03	0.134E-05	0 106E-05
8	75	0.999E-04	0.267E-06	0.927E-07	0.543E-03	0.173E-05	0.708E-06
9	62	0 884E-04	0 509E-05	0.637E-06	0 489E-03	0.228E-04	0.108E-05
10	78	0.957E-04	0.133E-04	0.186E-05	0.545E-03	0.668E-04	0.280E-05
11	37	0.990E-04	0.559E-04	0.540E-05	0.776E-03	0.331E-03	0.803E-05
12	116	0 972E-04	0 363E-04	0.510E-05	0 577E-03	0.186E-03	0.781E-05
13	82	0.964E-04	0.101E-04	0.133E-05	0.583E-03	0.524E-04	0.257E-05
14	65	0.932E-04	0 429E-05	0 492E-06	0.453E-03	0.207E-04	0.116E-05
15	78	0.940E-04	0.261E-06	0.106E-06	0.613E-03	0.152E-05	0.724E-06
16	90	0.975E-04	0.263E-06	0.110E-06	0.546E-03	0.213E-05	0.778E-06
17	85	0.996E-04	0.256E-06	0.988E-07	0 453E-03	0.153E-05	0.655E-06
18	67	0.941E-04	0.573E-06	0.897E-07	0.503E-03	0.250E-05	0.563E-06
19	66	0.922E-04	0.738E-05	0.981E-06	0.517E-03	0.348E-04	0.163E-05
20	85	0 961E-04	0 241E-04	0.344E-05	0.555E-03	0.125E-03	0.498E-05
21	126	0 993E-04	0 877E-04	0.124E-04	0.589E-03	0.454E-03	0.182E-04

Table 7 1: Number k of pseudo-time steps required to converge at time level t^n and rms and maximum residual values at convergence. The computations are for the unsteady two-dimensional annular flow at $s = 3\,000$, on a 24 x 24 grid.

7.4.2 Comparison with the Crank-Nicolson scheme

Figure 7.10 presents results computed with the full non-linear solution of Section 7.1, using either the three-point-backward time-differencing scheme (3.4) or the Crank-Nicolson scheme (3.5). The mesh was a fine 24×24 grid with $\Delta t_{min} = 0.02$. Time evolution curves of the circumferential velocity component w at $s = 300$ are plotted in Figure 7.10(a), for the eigth harmonic cycle of time integration, at position in annular space $r = 9.75$ and $\theta = 90°$. Similar time evolution curves at $s = 300$ for the pressure p are plotted in Figure 7.10(b), at position in annular space $r = 9.75$ and $\theta = 3\ 75°$. There were 19 time steps per harmonic cycle for those computations.

It is seen in Figure 7.10(a) that the results for w are nearly completely superimposed, and both methods resolve the non-dimensional velocity component w with the same accuracy. However, the non-dimensional pressure results show great differences, namely the Crank-Nicolson scheme gives rise to numerically-induced oscillations in the time evolution of pressure, which are superposed on the harmonic variation imposed by the oscillating outer cylinder. The three-point-backward scheme gives a smooth solution corresponding to the outer cylinder oscillations. Crank-Nicolson time-differencing thus has to be avoided for the present method of artificial compressibility applied to unsteady viscous flows. We remark that the spurious numerical oscillations observed with the Crank-Nicolson scheme are not related to a time-step limitation of the scheme, since up to one hundred time steps per harmonic cycle were included in some computations (not presented here), and the oscillations were still present at these very small time steps.

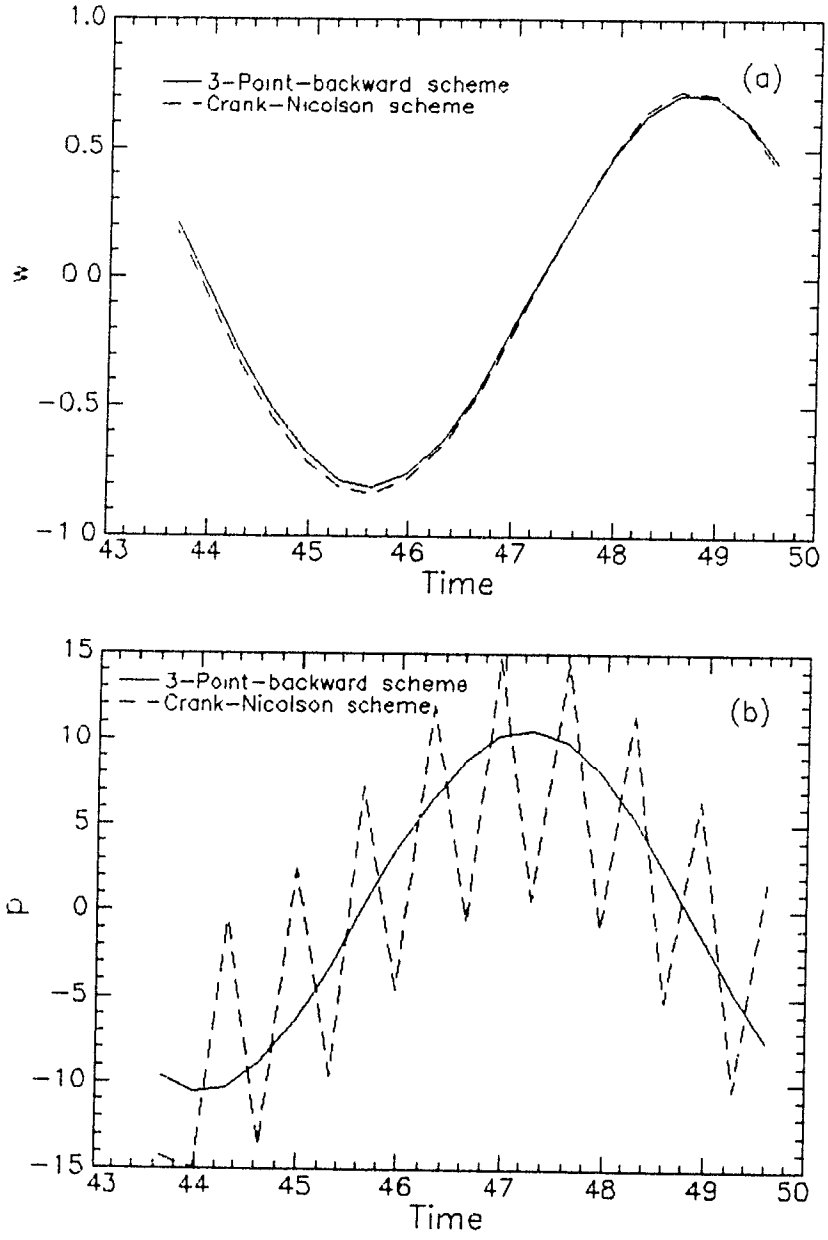

Figure 7.10: Comparison of three-point-backward and Crank-Nicolson time-differencing schemes for the time evolution of (a) the circumferential velocity component w, and (b) the pressure p. The Stokes number s is 300.

Chapter 8

COMPUTATION OF 3D UNSTEADY FLOWS

This chapter presents the results of numerical computations performed on three-dimensional unsteady annular flow configurations which are representative of geometries encountered in engineering applications, and provides a major test for the final validation of the method developed in the previous chapters.

Two annular flow geometries are considered, which are schematically represented in Figure 8.1. The first one has a uniform annular passage, in which case $h_d = 0$ in Figure 8.1, and by choosing $h_d \neq 0$ the second geometry studied had an annular backstep. According to the notation of Chapter 6, the flow is described in a cylindrical coordinate system, in which x, r and θ denote the non-dimensional axial, radial and circumferential coordinate directions, with u, v and w being, respectively, the velocity components in those directions, p is the pressure. The characteristic length and velocity used to nondimensionalize the equations are the annular gap width, H, and the mean flow velocity, U, defined in the upstream

portion of the domain.

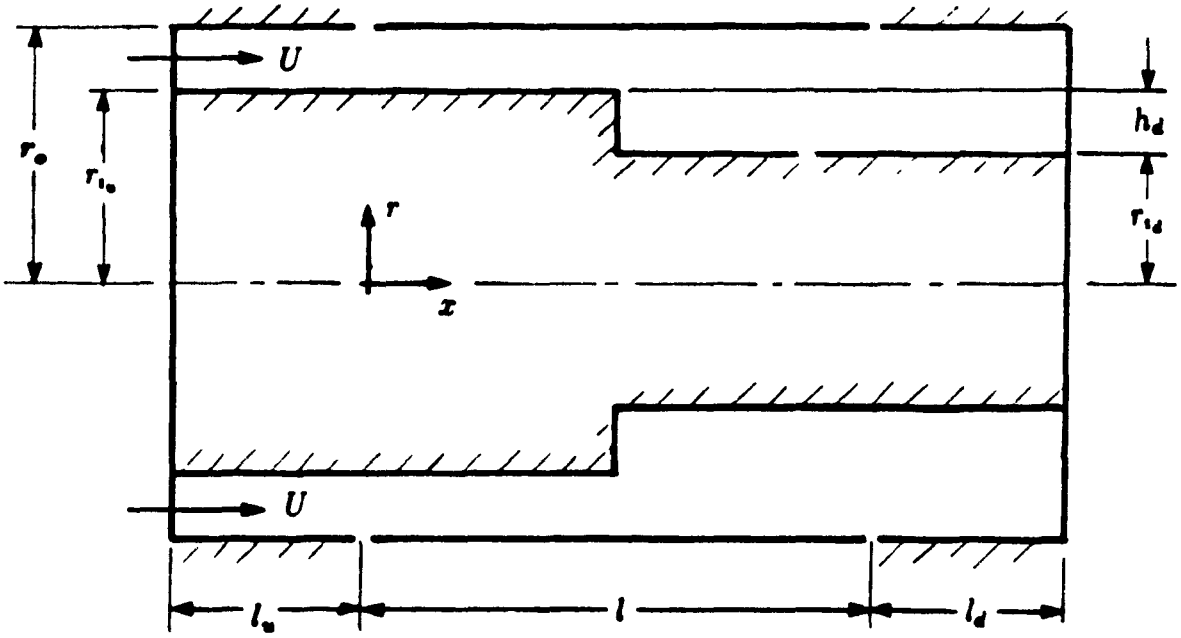

Figure 8.1: Three-dimensional annular geometry used for the unsteady flow computations.

The Reynolds number, Re, is defined in terms of the hydraulic diameter of the annular space at the inlet and is given by

$$Re = \frac{2H\,U}{\nu}\,, \tag{8.1}$$

where ν is the fluid kinematic viscosity. The equations and method of solution for the three-dimensional unsteady annular flow problems have been presented in Chapter 6; Appendix C gives the details for their numerical solution. In view of the present definition of the Reynolds number, we note that Re in (6.1-6.3) has to be replaced by $Re/2$.

In the numerical computations that were performed, the outer cylinder, of

radius r_o, is uniform in cross-section and is composed of three portions; the central portion has length l and is considered to have a harmonic oscillatory motion of frequency Ω, or $\omega = \Omega H/U$ in non-dimensional form. Two fixed portions are situated upstream and downstream of it; they have length l_u and l_d, respectively. In non-dimensional form, the radius of the inner cylinder at the inlet is $r_{i_u} = r_o - 1$, and at the outlet it is $r_{i_d} = r_o - 1 - h_d$. The Stokes number, s, defined by

$$s = \frac{\Omega H^2}{\nu},$$

was used to describe the vibrational characteristics of the system.

The solutions for the unsteady annular flow problems were obtained by three different methods. The first method consists in solving the full three-dimensional unsteady Navier-Stokes equations, as described in Section 6.2, and is the most demanding one in terms of computational time. It requires a three-dimensional mesh, which was stretched in the axial and radial directions and uniform in the circumferential direction. The following boundary conditions were imposed. At the inlet, $x = -l_u$, a developed laminar flow profile is imposed, and by setting $n = r_o/r_{i_u}$, it is given by

$$u = \frac{2[1 - (r/r_{i_u})^2 + (n^2 - 1)\ln(r/r_{i_u})/(\ln n)]}{n^2 + 1 - (n^2 - 1)/(\ln n)}, \qquad v = w = 0$$

There are no boundary conditions required for pressure at the inlet, and in the cross-sectional plane of the domain situated at the outlet, $x = l + l_d$, the pressure is set equal to zero, i.e., $p = 0$, $x = l + l_d$, $r_{i_d} \le r \le r_o$, $0 \le \theta \le 2\pi$, whereas all velocity components are extrapolated to second order accuracy from inside the flow domain. The procedure has been described in Chapter 4. As initial conditions, the steady flow solution, obtained in the absence of vibration of the outer cylinder, was imposed, and then the harmonic oscillation of the cylinder was started, the

equations were integrated for 5 harmonic cycles, until a periodic solution was obtained. The details for the discretization of the equations for the three-dimensional annular geometry are presented in Appendix C.

The second method of solution consisted in solving the linearized set of equations developed in Section 6.4; the solution procedure is described in Appendix A. The two-dimensional grid that the method requires for the axial and radial directions was the same as that used for the full three-dimensional Navier-Stokes solution, in those directions. For this method, the steady annular flow in the geometries considered must be computed first by solving (6.38-6.40), and then the unsteady solution corresponding to the perturbations in the flow quantities is obtained by integrating (6.41-6.52). The boundary conditions imposed to (6.41-6.52) were that all perturbations in the flow quantities are equal to zero at both the inlet and outlet of the domain, including velocity components and pressure. The initial conditions were also to set the perturbations equal to zero: the vibration of the outer cylinder is then started and the equations integrated until periodic state is achieved, which takes 5 harmonic cycles

Finally, an unsteady potential flow solution was also computed and compared with the viscous solutions, in the case of the calculations done on the uniform annular geometry ($h_d = 0$) An outline of unsteady potential flow theory can be found in Appendix D. A finite difference method was used to resolve the flow potential, requiring a two dimensional grid which was the same as that used for the linearized viscous solution

8.1 Uniform Annular Flow Geometry

The first geometry considered is thus of uniform cross-section and consists in two concentric cylinders delimiting the annular space; in this case $h_d = 0$ in Figure 8.1.

The inner cylinder is taken to have radius $r_{i_u} = r_{i_d} = 9$, and is fixed, whereas the central portion of the outer cylinder of length $l = 100$, undergoes a translational vibratory motion, with its axis remaining parallel with the axis of the inner cylinder. The radius of the outer cylinder is $r_o = 10$, and two fixed portions of the same radius r_o are situated upstream and downstream of it. Their lengths are $l_u = l_d = 20$.

Results were obtained on two different grids, one which was coarse and one which was fine. They had the following characteristics, where a subscript c denotes the coarse grid and a subscript f the fine one. In the axial direction, the mesh spacing Δx was uniform over $10 \leq x \leq 90$, and equal to $\Delta x_c = 3.64$ and $\Delta x_f = 2.42$. Then, it was diminished going toward the extremities of the oscillating portion of the outer cylinder, to reach the minimum values of $\Delta x_c = 0.50$ and $\Delta x_f = 0.30$, at $x = 0$ and $x = 100$. Mesh spacing was then increased moving away from either extremity of the oscillating cylinder, toward the inlet and outlet of the flow domain, to reach $\Delta x_c = 3.75$ (or $\Delta x_f = 2.75$) at $x = -20$ and $x = 120$. A total number of 65 grid points thus spanned the axial direction in the case of the coarse mesh, compared to 96 grid points for the fine mesh. Now, the radial direction was spanned by a stretched grid having 11 grid points in the case of the coarse mesh, and 17 grid points for the fine one, and the minimum spacing at the walls of the inner and outer cylinders was $\Delta y_c = 0.066$ and $\Delta y_f = 0.042$. The stretching functions used were the hyperbolic sine in the axial direction and the hyperbolic tangent in the radial direction. The three-dimensional solution also required that the discretization included the circumferential direction, and the coarse mesh had 12 grid points in this direction, compared to 20 for the fine mesh. The grid was uniform in this circumferential direction. Note that in all the computations of this chapter, the time step Δt was equal to $2\pi/19\omega$.

The results of the numerical computations are presented in Figures 8.2–8.19.

where all the quantities are *non-dimensional* ones. The figures in which the amplitude and phase of p or w are presented have been obtained by performing a Discrete Fourier Transform (DFT) on the periodic flow solution in order to extract the first time-harmonic, and it is the amplitude and phase of the latter which are plotted in those figures, the phase being with respect to the displacement of the outer cylinder. For the figures involving the velocity component w, the higher-order time-harmonics were 4 to 5 orders of magnitude smaller than the first harmonic, for both the non-linear and linearized viscous solutions, which was also the case for the pressure results computed with the linearized solution: the pressure results computed with the non-linear solution had higher-order time-harmonics of the order of one hundred times smaller than the first harmonic, and these relatively larger higher-order contributions, which capture the non-linear effects, can be explained by the non-linear terms in the Navier-Stokes equations. However, these are still small and negligible and point out to the essentially linear character of the flow solution when small vibrations of the oscillating cylinder are imposed, which was the case here (an exception is depicted in Figures 8.18 and 8.19).

In the case of small vibrations, we require that the perturbations introduced in the velocity field by the oscillation of the outer cylinder remain small with respect to the mean annular flow velocity, which is expressed in non-dimensional form by

$$\omega\epsilon \ll 1 ,$$

where ϵ is the displacement of the outer cylinder and ω is its frequency of vibration. In other words, the vibration-induced perturbations in the flow field have velocity of order $\omega\epsilon$, which must be smaller than the mean axial flow velocity, $U = 1$, in non-dimensional form. Since we imposed $\epsilon = 0.1$ as boundary condition for all the problems tested, and since

$$\frac{2s}{Re} = \frac{2\Omega H^2}{\nu}\frac{\nu}{2HU} = \frac{\Omega H}{U} = \omega\epsilon .$$

we must then have that

$$\frac{2s}{Re} \ll 10 . \tag{8.2}$$

Linear flow theory is thus valid as long as the Stokes number, s, is much smaller than at least five times the Reynolds number, Re. We remark that the full three-dimensional non-linear Navier-Stokes equations which were also used in this chapter to obtain solutions do not require the assumption (8.2). In this chapter, we will compare the nonlinear and linearized solutions when (8.2) is satisfied, and comparison will also be made for larger values of $\omega\epsilon$, when (8.2) is not satisfied, in order to find out the validity of a linear flow theory, as well as its limits.

Thus, Figures 8.2 and 8.3 present pressure results for $Re = 100$, at $s = 10$ and $s = 5$, respectively, where the axial variation is plotted for $r = 9.93$ and $\theta = 7.5°$. It is seen that there are marked differences between the viscous flow results and the potential ones; however, the viscous and potential solutions get closer when the Stokes number is increased. The pressure amplitude in the case of the potential flow results is symmetric with respect to the mid-section of the oscillating outer cylinder, where the phase, in particular, is zero. For the viscous flow results, it is non-symmetric; at $s = 5$, the pressure amplitude quickly reaches its maximum value at $x = 0$, then remains constant up to $x \approx 80$, before gradually decreasing to zero at the outlet, $x = 120$; the phase is confined to negative values over most of the cylinder length. We recall that the phase is with respect to the displacement of the oscillating cylinder.

In order to make sure that these effects were not attributable to the numerical scheme and staggered mesh, the mean flow direction was inverted and computa-

tions were performed for the same Reynolds number of 100, at $s = 5$. Figure 8.4 shows that the results are now mirror images, with respect to the cylinder mid-section, of the plots obtained in the previous figure. Hence the numerical method shows consistency with regard to the direction of the mean flow velocity.

Computations were also performed without axial mean flow in the annulus, and the results are presented in Figures 8.5 and 8.6. In this case, the Reynolds number, which is defined in terms of the mean flow velocity U, has no signification, since $U = 0$; thus, we choose instead ΩH as characteristic velocity, and the Reynolds number in the equations of motion (6.1–6.3) becomes the Stokes number, or $Re \equiv s = \Omega H^2/\nu$. The procedure is the same as that described in Chapter 7 for the two-dimensional annular flow problem. Hence the results in Figures 8.5 and 8.6 for which $U = 0$ are for $s = 25$ and $s = 300$, respectively. It is seen that the higher the Stokes number, the closer the agreement between the potential and viscous solutions becomes. Moreover, the results are now perfectly symmetric with respect to the cylinder mid-section. The results at $s = 300$ can be compared with Figure 7.4(a), in which computations are also performed at $s = 300$ for the two-dimensional geometry. Actually, in the present three-dimensional flow problem, if we are sufficiently far from the extremities of the vibrating outer cylinder, we find ourselves in the situation of the two-dimensional problem of Figure 7.4(a), the end effects not being felt far from the extremities. Thus, the pressure amplitude should be the same, which it is, at a level of slightly more than 10, in non-dimensional units. An important remark is that in all of the present figures the linearized and non-linear viscous solutions are nearly perfectly superimposed.

Figure 8.7 presents results involving the circumferential velocity component w, at $Re = 100$, $s = 5$, and for $x = 50$, $\theta = 45°$. Again, the agreement between the two viscous solutions is very good, as opposed to the potential flow results which

are different, although they represent relatively well in an average sense the flow properties. We remark in Figure 8.7 that the amplitude of the flow velocity is of order 0.1, which is ten times smaller than the mean axial flow velocity in the annular region ($U = 1$). At $s = 10$ the amplitude of w is of order 0.2, and in both cases we thus see that this is within the ordinarily accepted limits of a linear flow theory. (We note in this chapter, as was the case in the previous one, that the results involving the radial velocity component v are never presented, as the corresponding velocity profiles do not have the same interest as those for w. The radial gradients, for example, are not as pronounced as for w, whose amplitude in mid-annulus is seen to be much greater than its amplitude at the moving wall.)

Figures 8.8 to 8.11 are results for p and w for calculations performed at Reynolds number $Re = 250$, for two Stokes numbers, $s = 10$ and $s = 25$, and for position in annular space $r = 9.93$ and $\theta = 7.5°$, for p, and $r = 50$ and $\theta = 45°$ for w. It is seen that as the Stokes number is increased the viscous solutions and the potential one become closer together, both in terms of the amplitude and the phase results. We see again that the amplitudes of w at $s = 10$ and $s = 25$ are of the order of 0.1 and 0.2, respectively.

Figure 8.12 is a plot of the axial variation of pressure, taken at $r = 9.93$ in the annular space, but at a different circumferential position, namely at $\theta = 52.5°$, and the agreement still goes along the lines of that in the previous figures. Also, Figure 8.13 represents the circumferential velocity component, w, taken at an azimuthal position $\theta = 45°$, as before, but at a different axial position than in

the previous figures, namely at $x = 1$, which is close to the upstream extremity of the oscillating outer pipe. The results in both Figures 8.12 and 8.13 are for $Re = 250$, $s = 25$. It is seen that the agreement between the different methods is qualitatively as before

A comparison between results obtained on coarse and fine meshes is presented in Figures 8.14 and 8.15 for $Re = 250$, $s = 25$, and for computations performed with the non-linear solution. It is seen from those figures that the coarse mesh provided a good resolution of the flow solution as the fine mesh results are almost perfectly superimposed on them, both in terms of the results involving the pressure, p, and the velocity component, w.

Finally, in Figures 8.16 and 8.17 the results are presented in a different manner, namely axial variations in p and radial variations in w are plotted for different instants within the harmonic cycle, after the solution had reached a periodic state. The five instants t^n chosen were

$$t^n = \frac{2\pi n}{\omega}, \qquad n = 3, 5, 7, 9, 11$$

for the pressure results, and

$$t^n = \frac{2\pi n}{\omega}, \qquad n = 5, 7, 9, 11, 13$$

for the results with w. Only the two viscous flow solutions are presented, namely the linearized and non-linear ones, and the values chosen for Re and s were 250 and 25, respectively. It is seen that the agreement is good and consistent with the previous results, which were precisely obtained by taking the DFT of data such as those plotted in Figures 8.16 and 8.17. In those figures, $r = 9.93$, $\theta = 7.5°$ for p, and $r = 50$, $\theta = 45°$ for w.

To conclude the results part of this section, computations were performed at $Re = 100$ and $s = 80$, which corresponds to a case for which linear flow theory

is no longer valid, see (8.2). The results are presented in Figures 8.18 and 8.19, and it is most surprising to see that no deterioration in the agreement between the non-linear and linearized viscous solutions is noted. Furthermore, the potential flow results are in better agreement with the viscous solutions than was the case at $s = 10$ or $s = 5$, the results for which were presented in Figures 8.2 and 8.3, respectively. We note from Figure 8.19 that the amplitude of velocity component w is of the order of 1, in non-dimensional form, which is comparable with the mean annular flow velocity and points out to the fact that we no longer have small perturbations in the flow field. The pressure results from Figure 8.18 are seen not to exibit a dependence on the flow direction, as was the case in the previous figures for lower Stokes numbers.

Now, to give an idea of the performance of the method, Tables 8.1 - 8.3 outline the convergence aspects of the computations. In all the computations of this chapter, each harmonic cycle was divided up into 19 time steps, which gave a time step size of $\Delta t = 2\pi/19\omega$. In Table 8.1, the data are for computations performed with the non-linear viscous solution at $Re = 250$, $s = 25$, and they are compiled for integration of the equations during the first harmonic cycle (periodicity in the solution was obtained after 5 cycles). The number of pseudo-time steps required to converge at each time level is indicated, along with the rms values of the residuals at convergence; convergence in pseudo-time was reached when the rms values of the residuals all fell below 10^{-4}. It is seen that the results are very good as the number of pseudo-time steps is of the order of 40.

Table 8.2 presents the same data pertaining to the same problem, but for computations performed with the linearized Navier-Stokes equations. Again, the performance is observed to be very good regarding the number of pseudo-time steps required to converge and advance to a new time level. Finally, Table 8.3 presents results calculated with the non-linear equations, but this time at $Re = 100$, $s = 80$.

for which case the perturbations induced by the oscillating cylinder are no longer small, see Figure 8.19. It is seen that on the average, three to four times more pseudo-time steps are required for convergence. The same quatitative results are obtained when the computations are performed with the linearized viscous solution.

In all the computations presented in this chapter, the estimates (5.11) and (5.12) for the artificial compressibility δ and the pseudo-time step $\Delta\tau$ proved to be accurate. The Courant number in (5.12) was systematically chosen to be 40, whereas the value predicted for δ in (5.11) had to be corrected by the factor 0.2, except for the computations performed at the higher Stokes number of 80 in Figures 8.18 and 8.19, and for the computations done without mean axial flow velocity, Figures 8.5 and 8.6. In this case the value of δ predicted by (5.11) had to be corrected by factors of order 0.06 or 0.02, instead of 0.2.

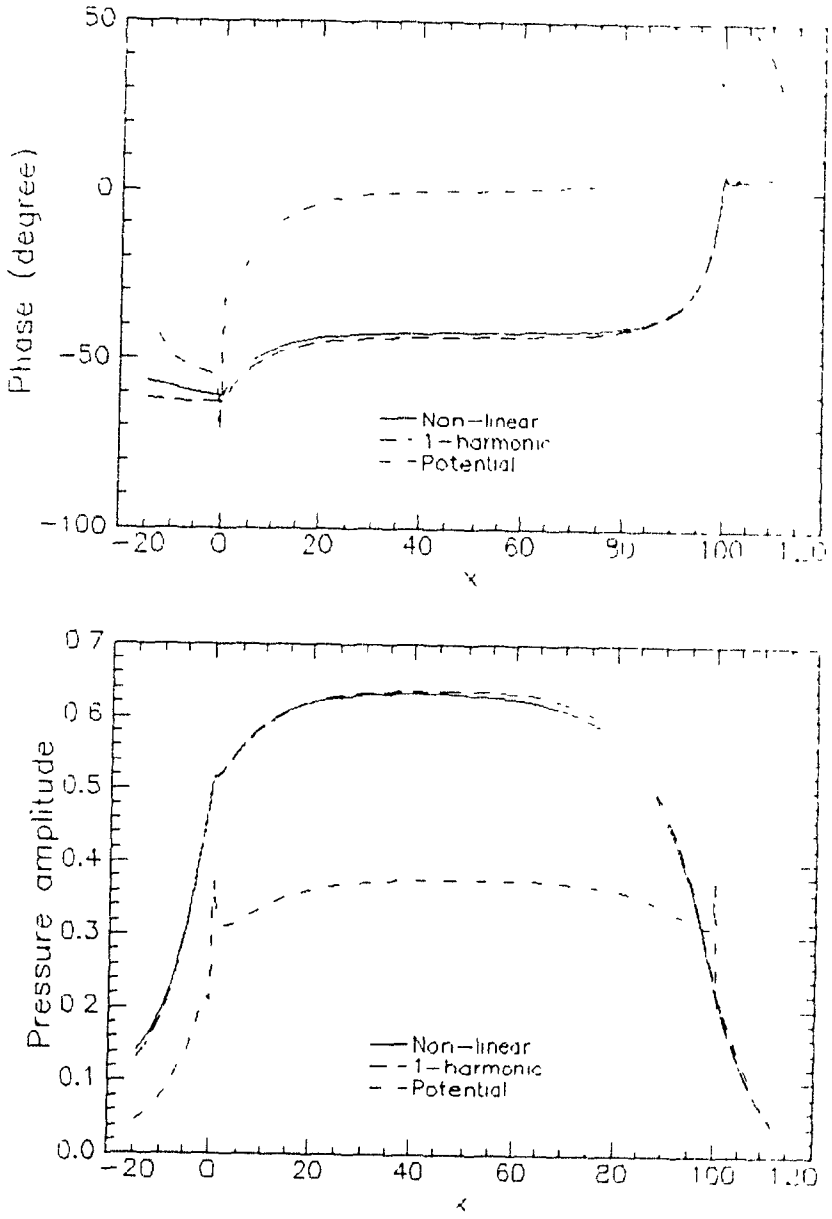

Figure 8.2: Axial variation in the amplitude and phase of pressure, taken at $r = 9.93$, $\theta = 7.5°$, for $Re = 100$ and $s = 10$.

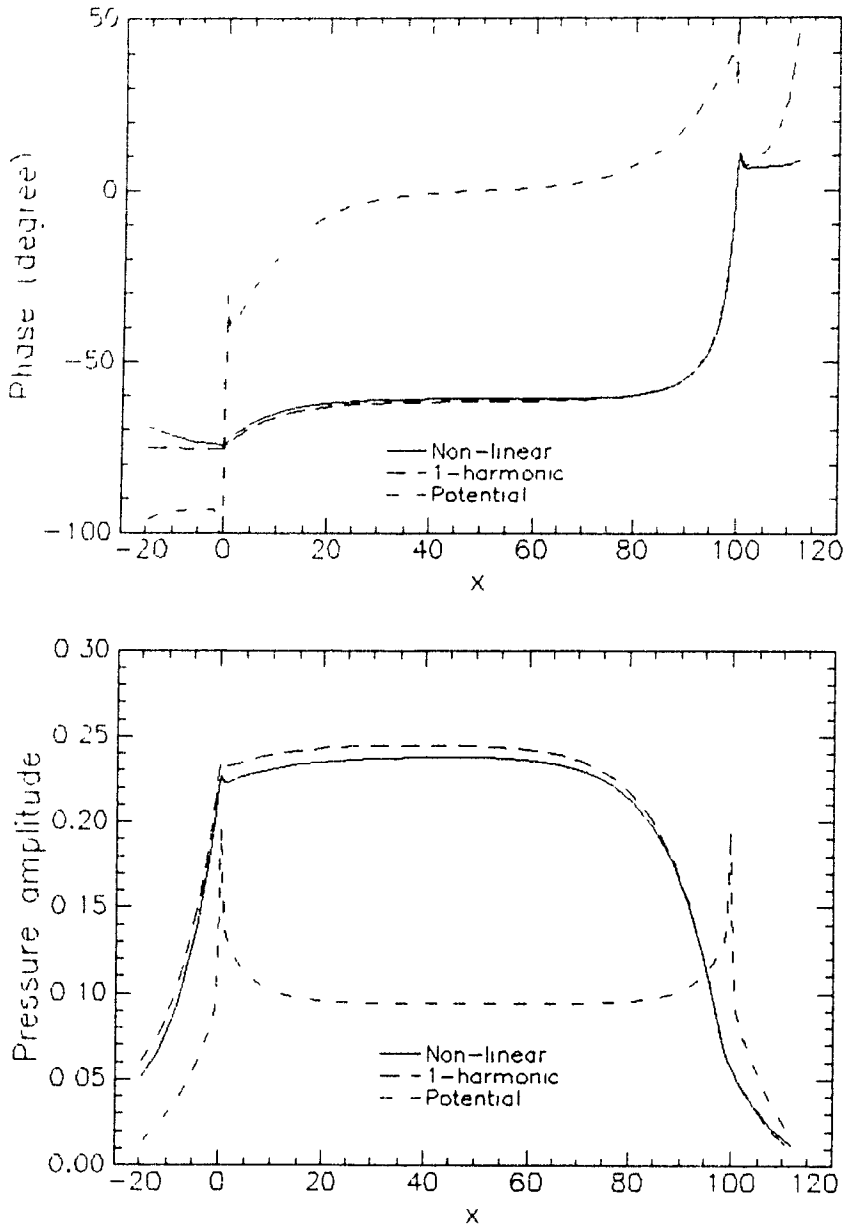

Figure 8.3: Axial variation in the amplitude and phase of pressure, taken at $r = 9.93$, $\theta = 7.5°$, for $Re = 100$ and $s = 5$.

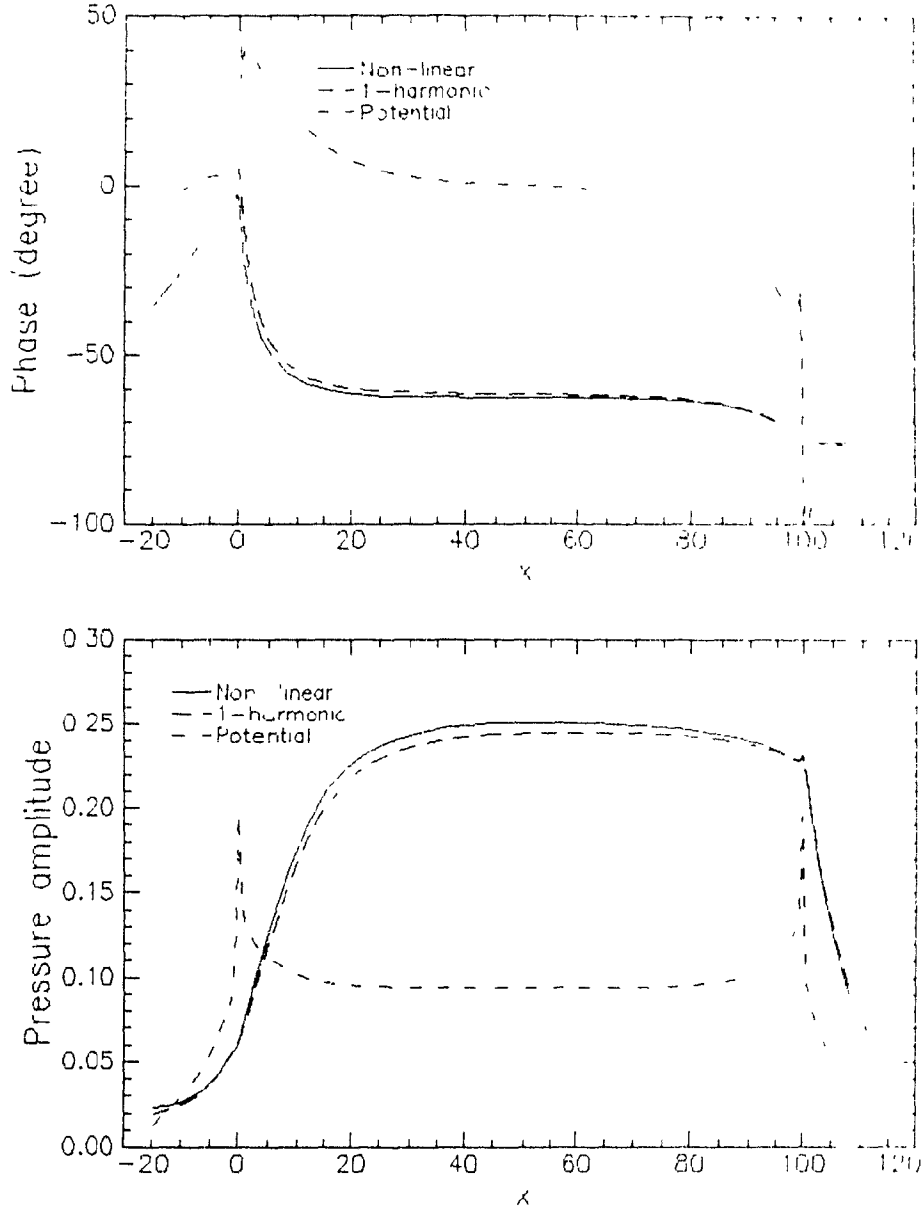

Figure 8.4: Axial variation in the amplitude and phase of pressure, taken at t = 9.93, $\theta = 7.5°$, for $Re = 100$ and $s = 5$. The mean flow is in the negative axial direction.

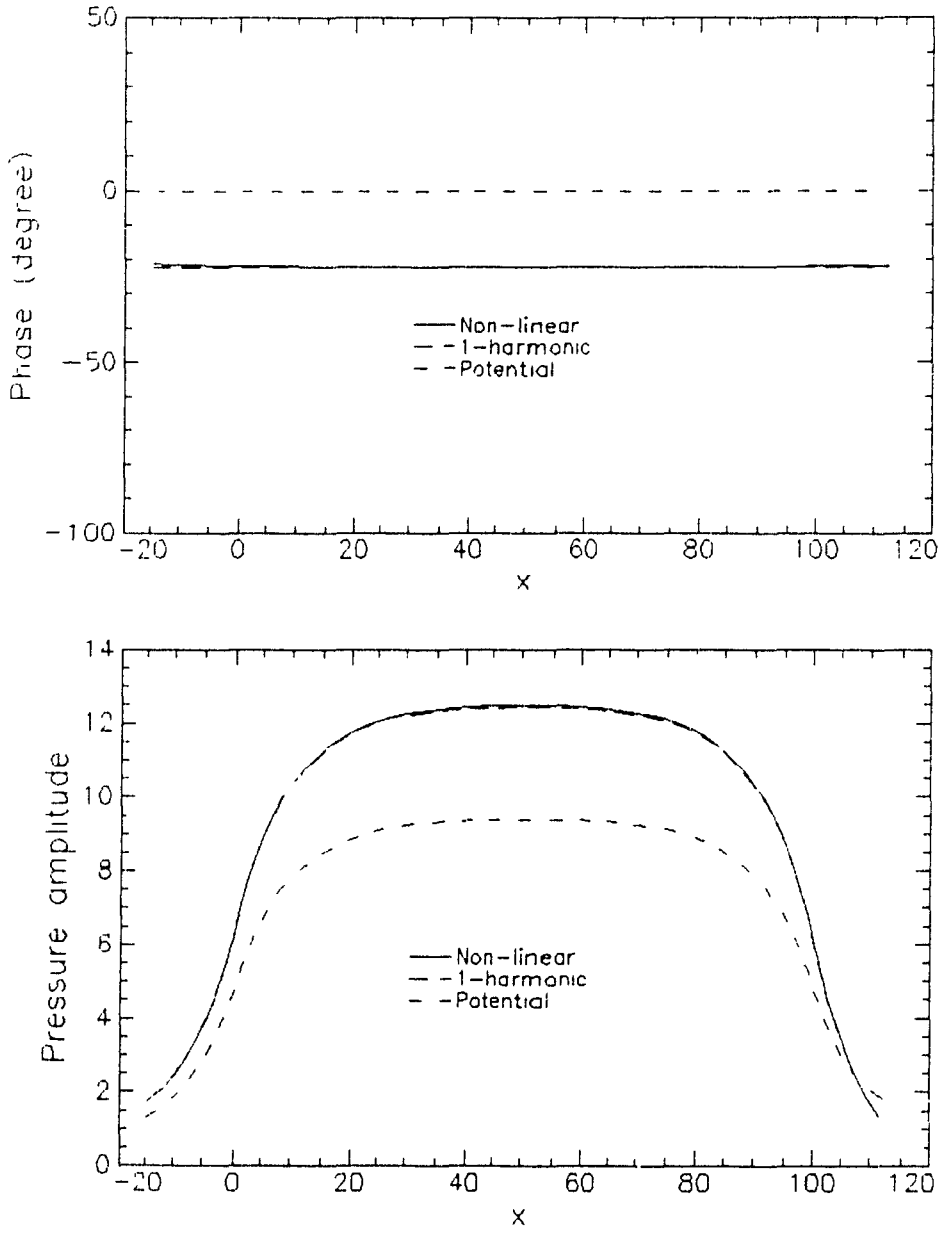

Figure 8.5: Axial variation in the amplitude and phase of pressure, taken at $r = 9.93$, $\theta = 7.5°$, and for $s = 25$. There is no mean axial flow in the annulus.

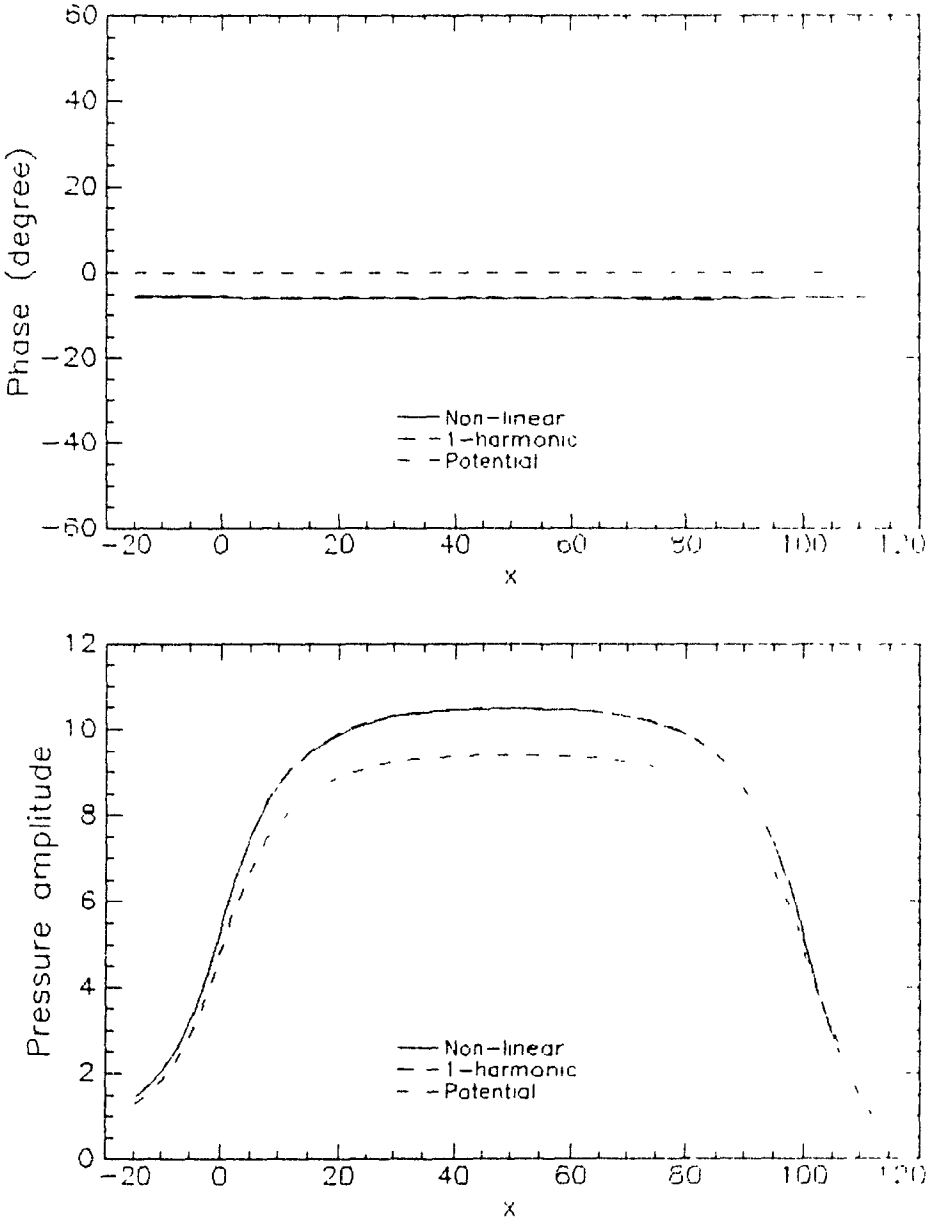

Figure 8.6: Axial variation in the amplitude and phase of pressure, taken at $r = 9.93$, $\theta = 7.5°$, and for $s = 300$. There is no mean axial flow in the annulus

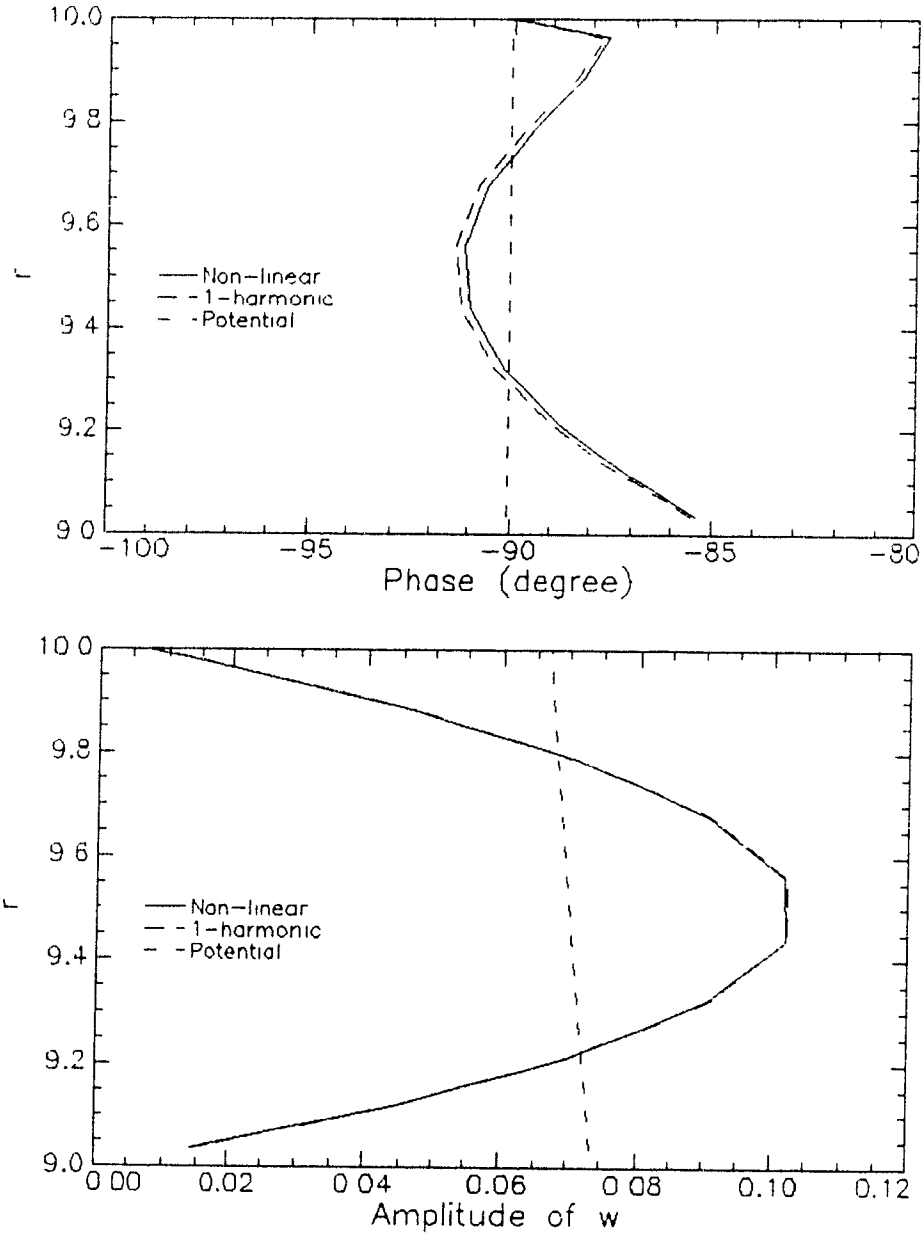

Figure 8.7: Radial profiles of w taken at $x = 30$, $\theta = 45°$, for $Re = 100$, $s = 5$: amplitude and phase of w are plotted.

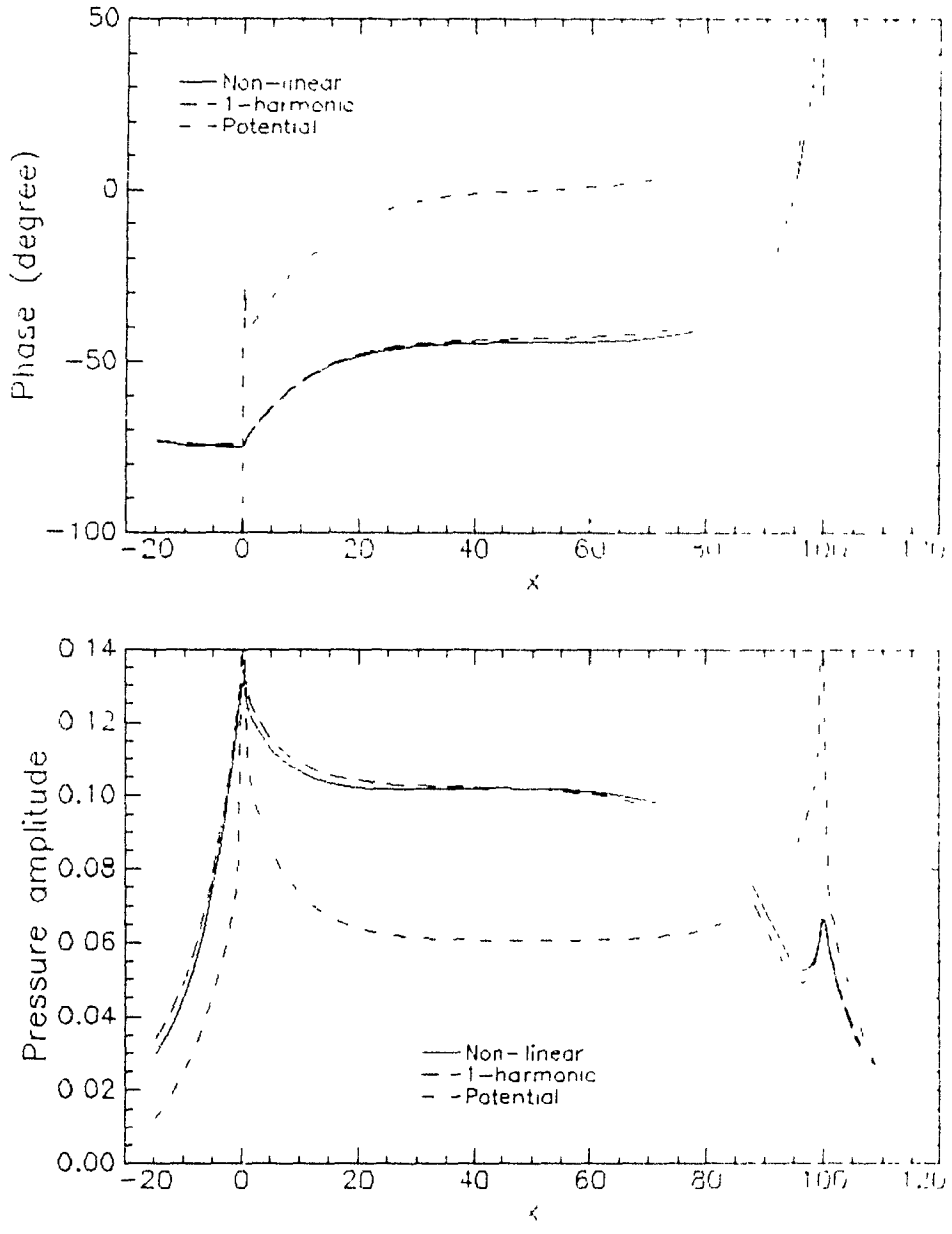

Figure 8.8: Axial variation in the amplitude and phase of pressure, taken at $t = 9.93$, $\theta = 7.5°$, for $Re = 250$, $s = 10$.

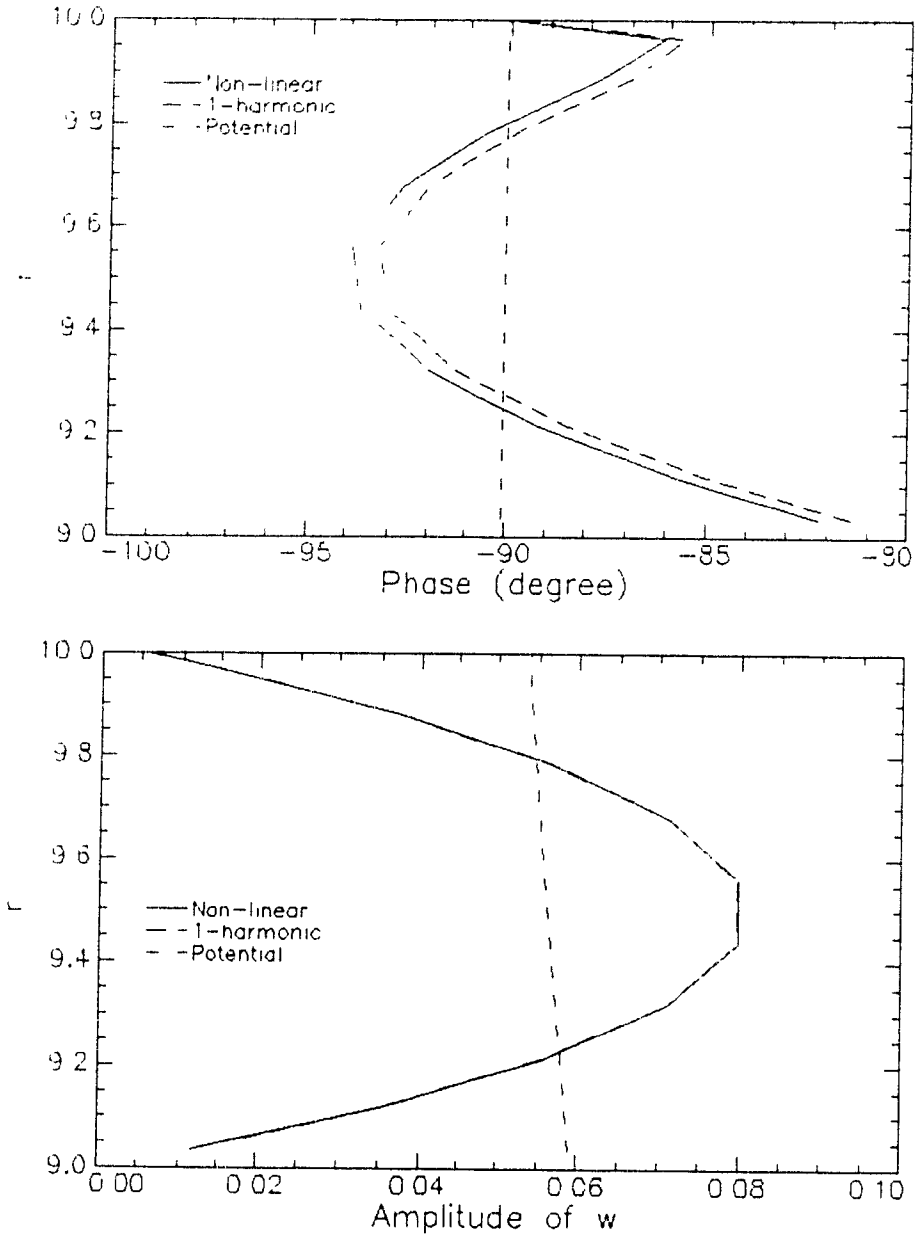

Figure 8.9: Radial profiles of w taken at $x = 50$, $\theta = 45°$, for $Re = 250$, $s = 10$; amplitude and phase of w are plotted.

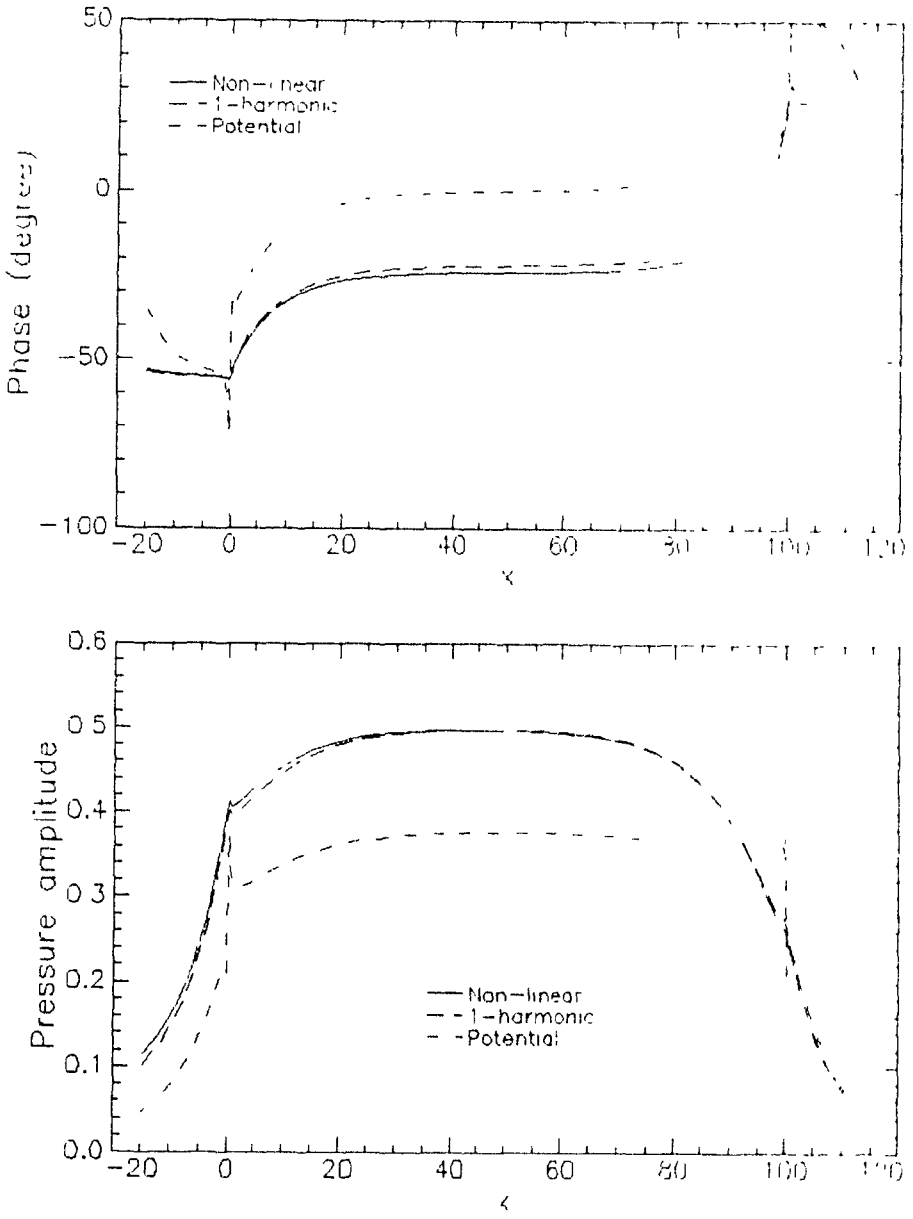

Figure 8.10: Axial variation in the amplitude and phase of pressure, taken at $r = 9.93$, $\theta = 7.5°$, for $Re = 250$, $s = 25$

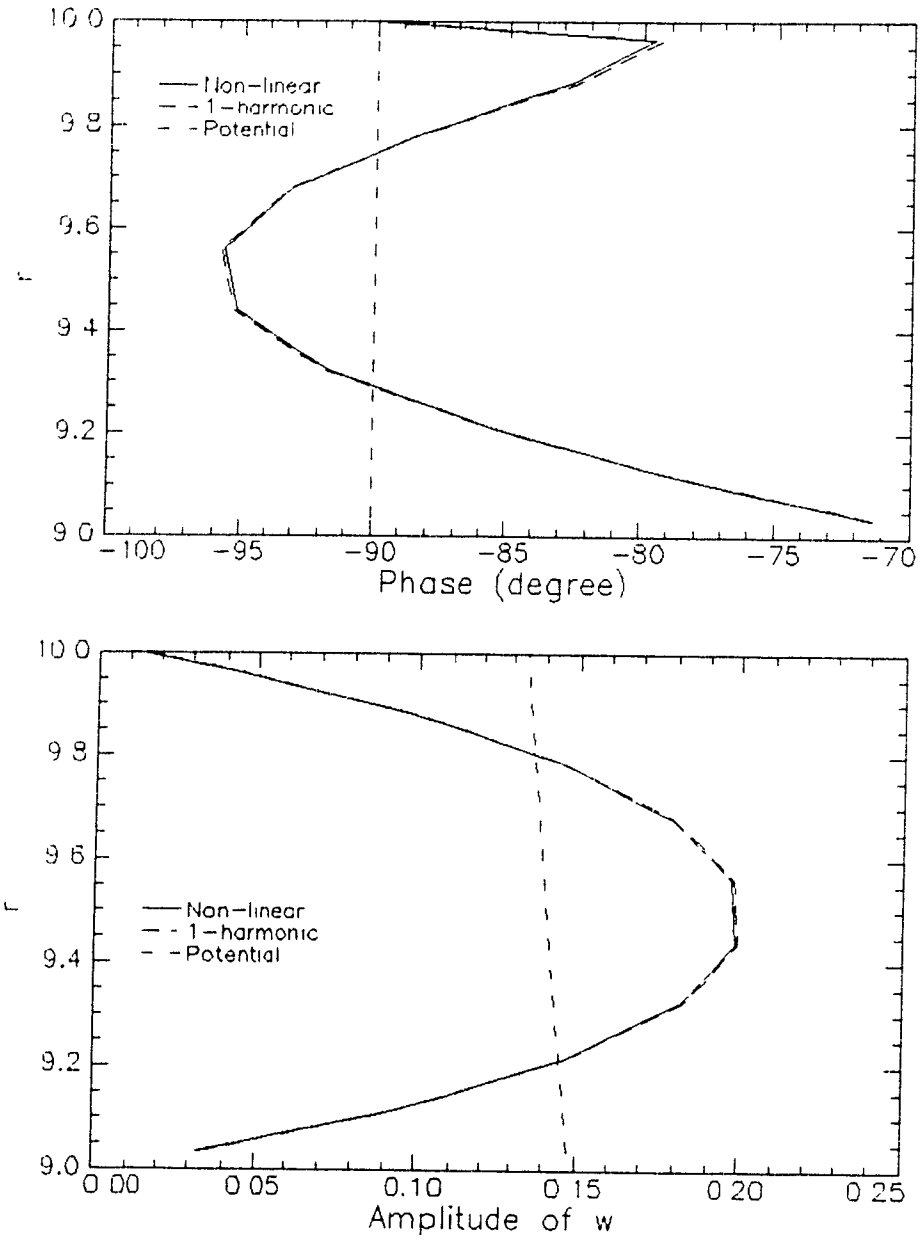

Figure 8.11: Radial profiles of w taken at $x = 50$, $\theta = 45°$, for $Re = 250$, $s = 25$: amplitude and phase of w are plotted.

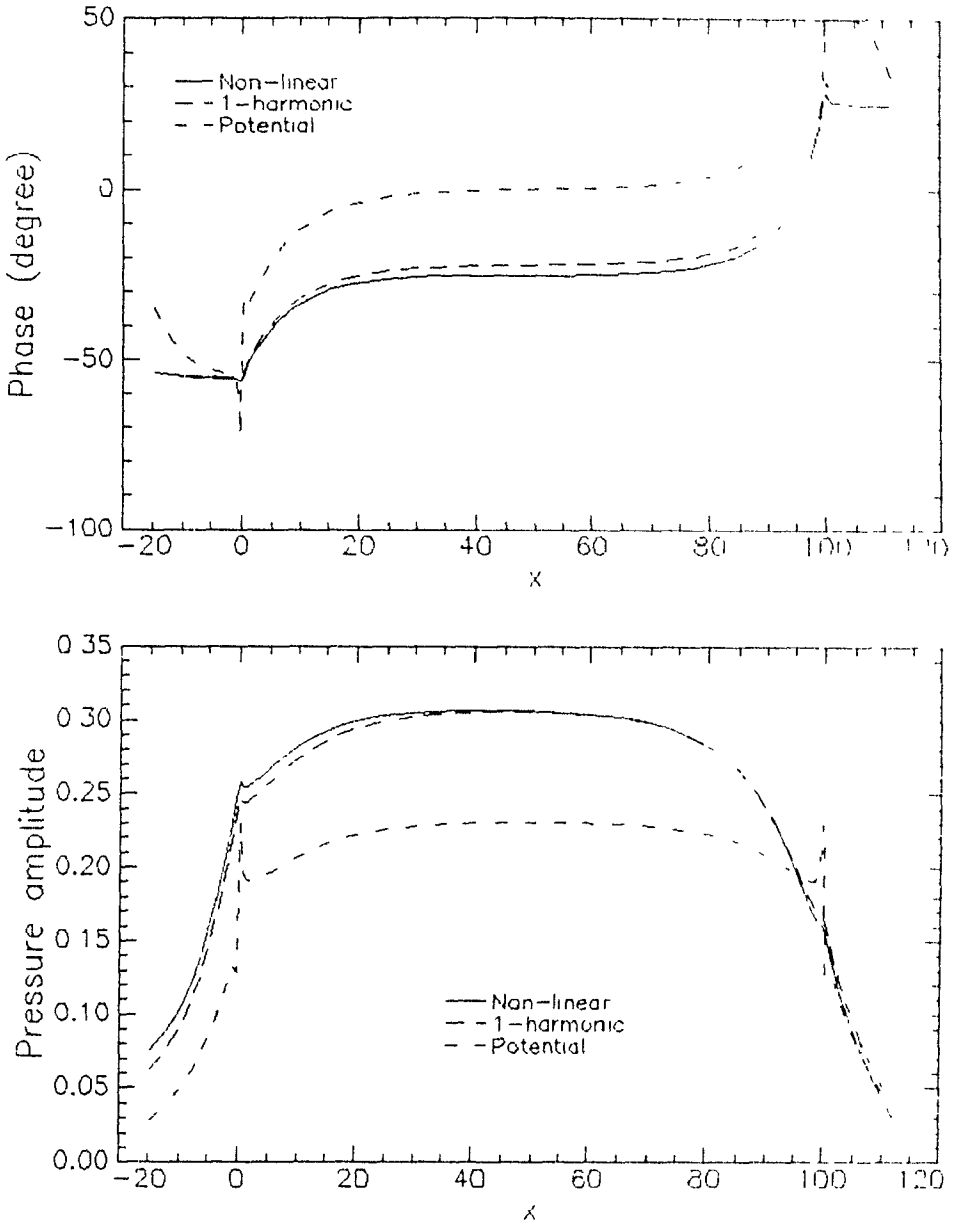

Figure 8.12: Axial variation in the amplitude and phase of pressure, taken at $r = 9.93$, $\theta = 52.5°$, for $Re = 250$, $s = 25$

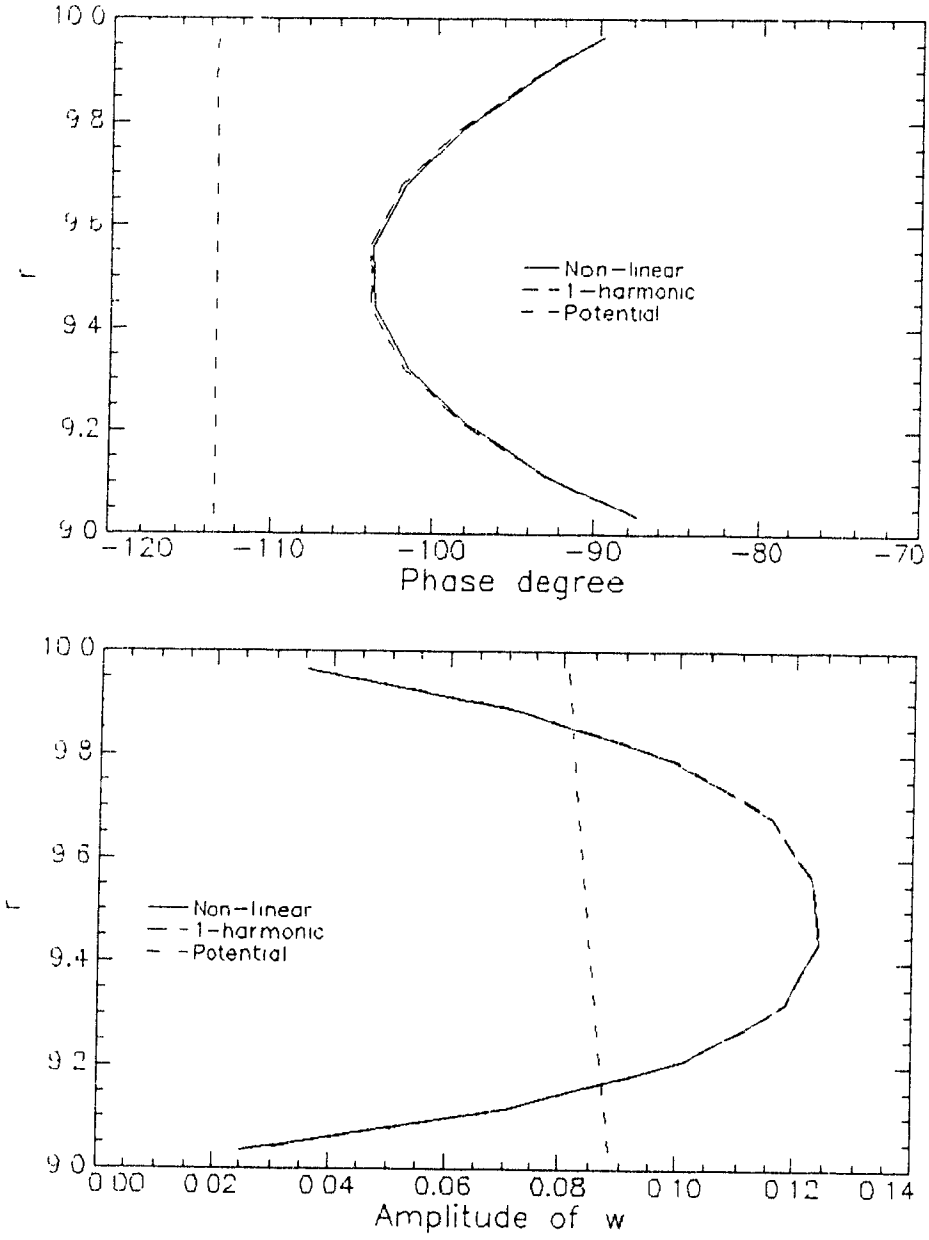

Figure 8.13: Radial profile of w taken at $x = 1$, $\theta = 45°$, for $Re = 250$, $s = 25$; amplitude and phase of w are plotted.

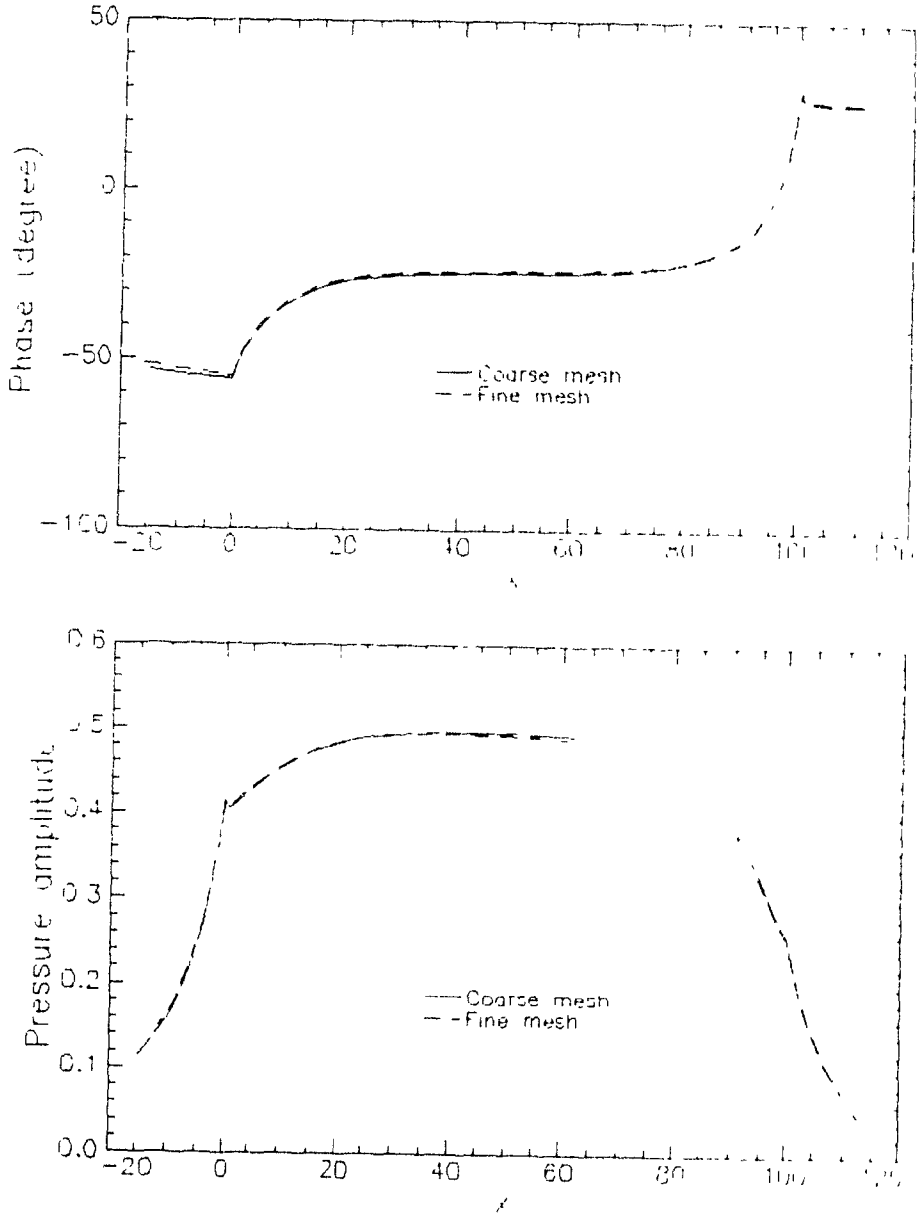

Figure 8.14: Comparison of coarse mesh and fine mesh results - axial variation of pressure taken at $r = 9.93$, $\theta = 7.5°$, for $Re = 250$, $s = 25$

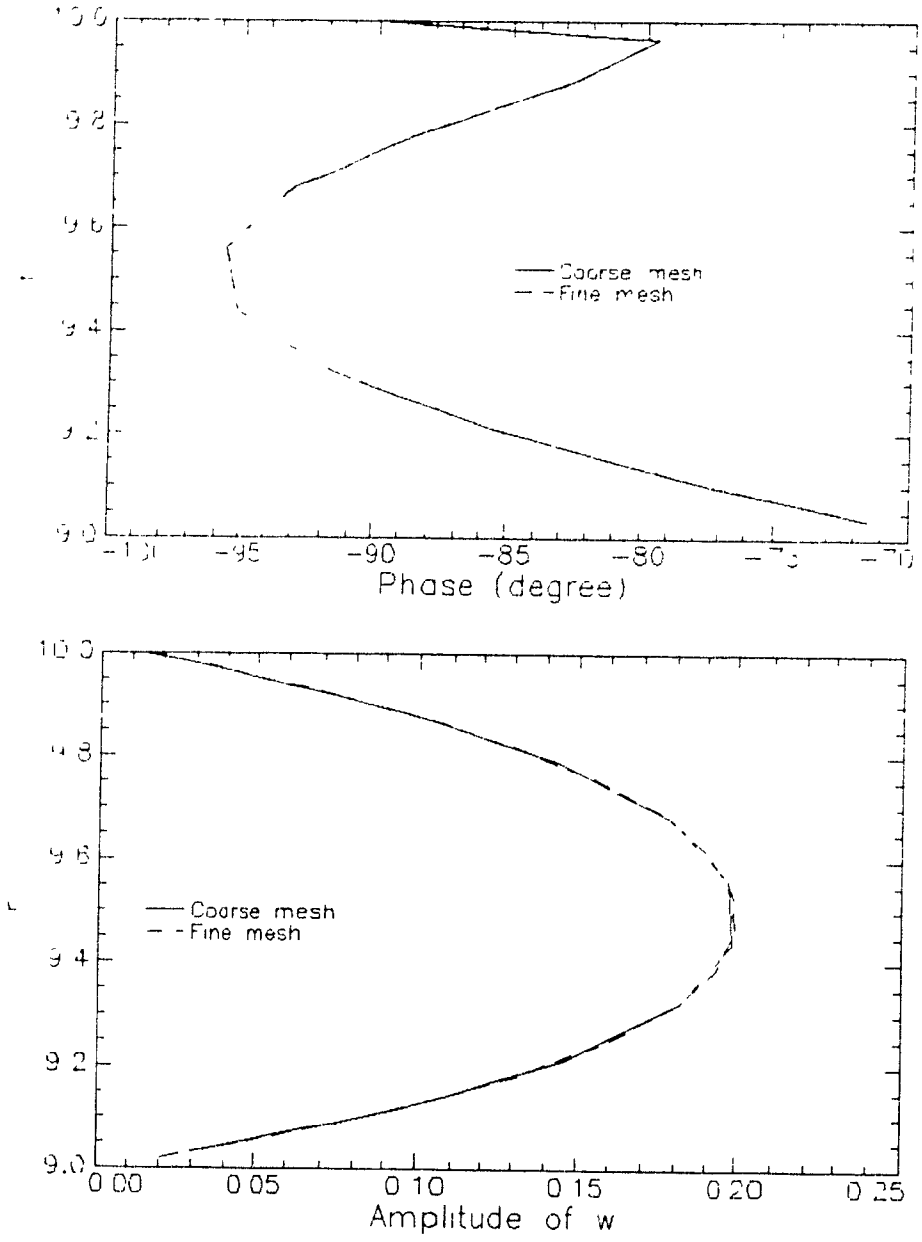

Figure 8.15. Comparison of coarse mesh and fine mesh results: radial profiles of w taken at $x = 50$, $\theta = 45°$, for $Re = 250$, $s = 25$.

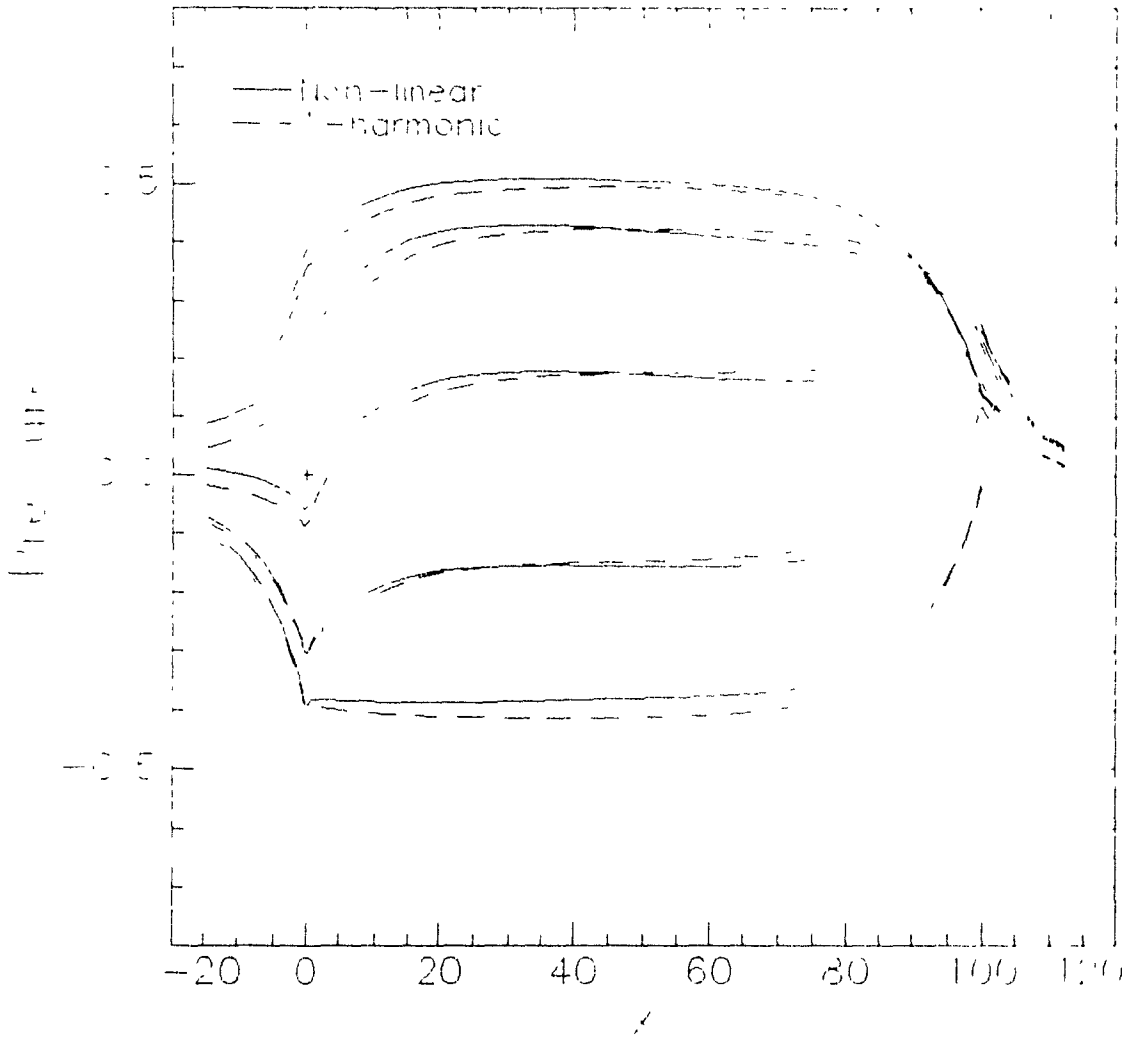

Figure 8.16: Axial profiles of pressure taken at $r = 9.93$, $\theta = 7.5°$, for $Re = 250$, $s = 25$. Five different instants within the harmonic cycle are represented

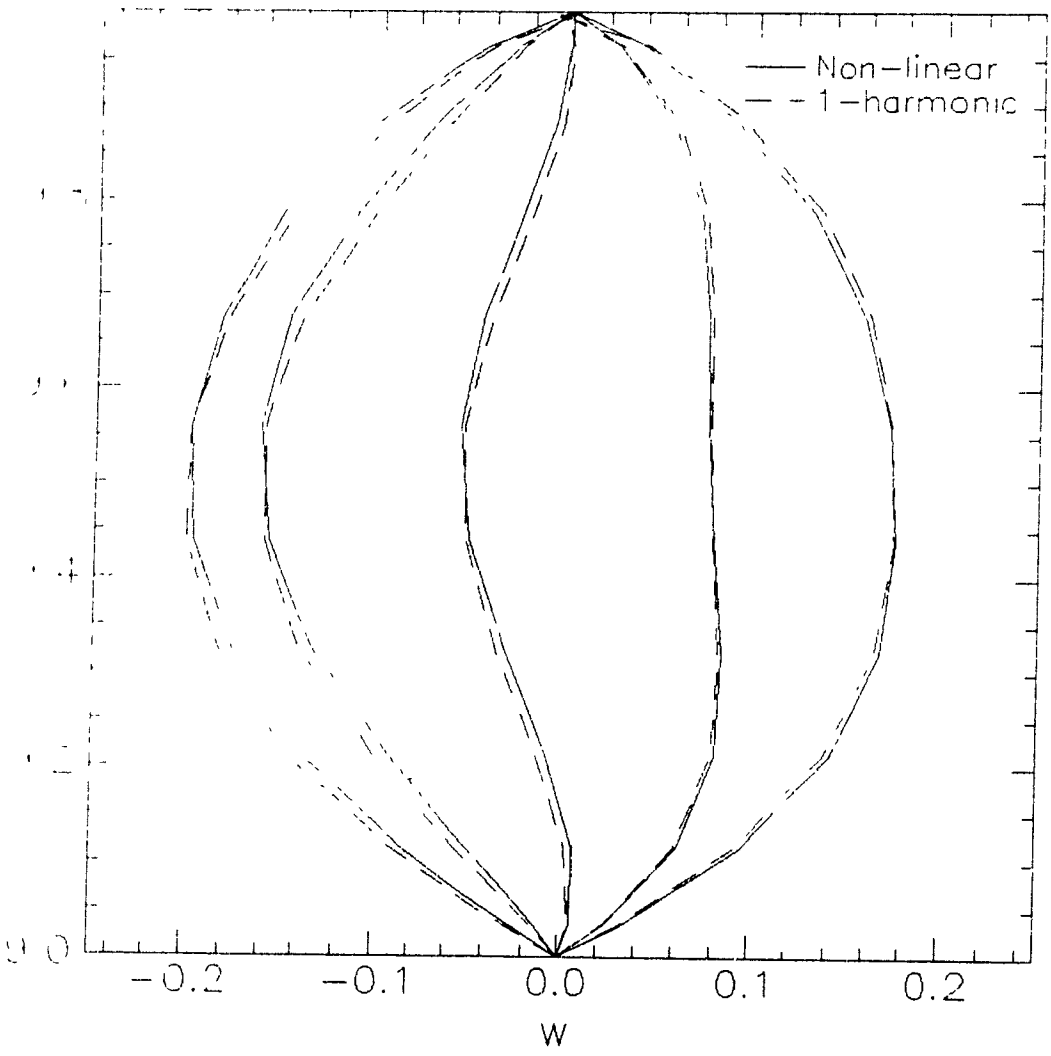

Figure 8.17: Radial profiles of w taken at $x = 50$, $\theta = 45°$, for $Re = 250$, $s = 25$. Five different instants within the harmonic cycle are represented.

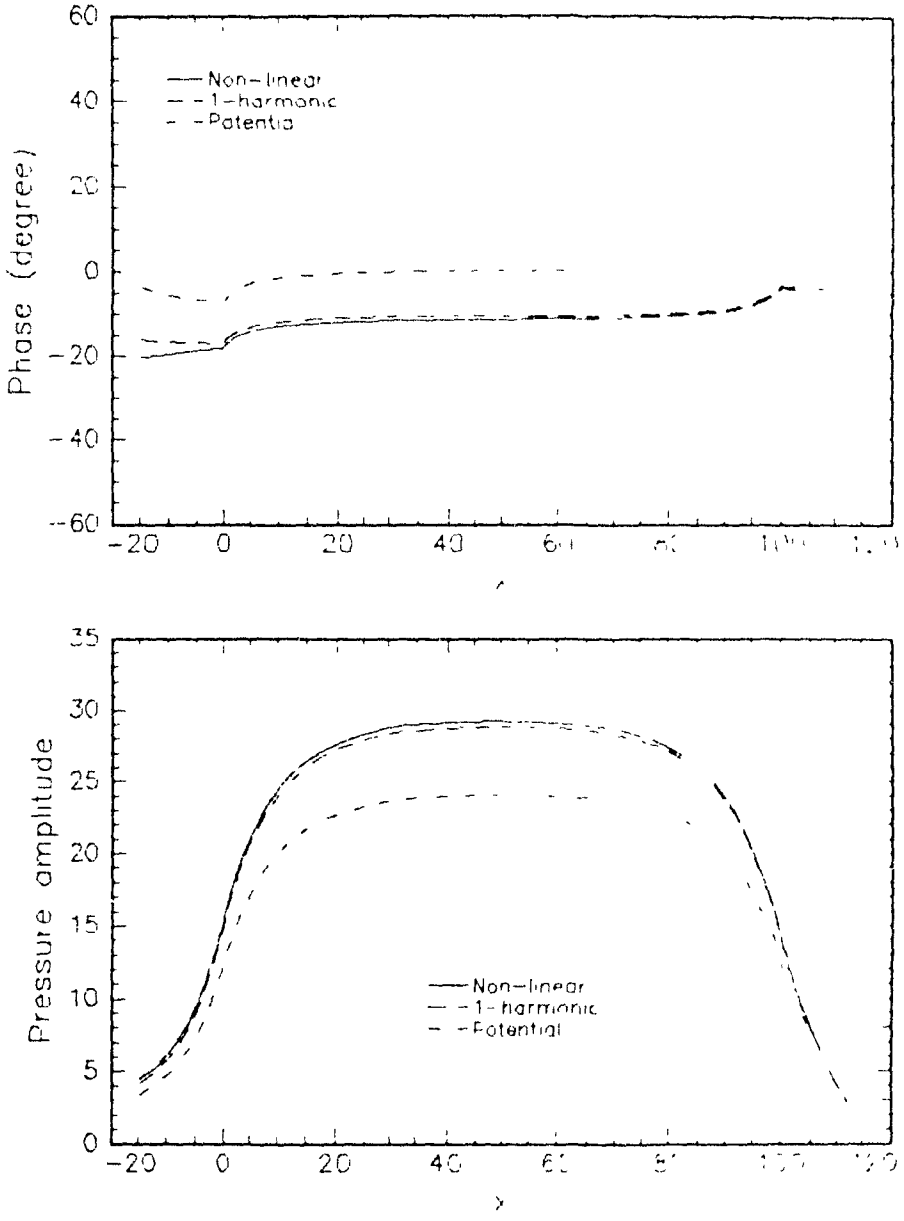

Figure 8.18: Axial variation in the amplitude and phase of pressure taken at $r = 9.93$, $\theta = 7.5°$, for $Re = 100$, $s = 80$

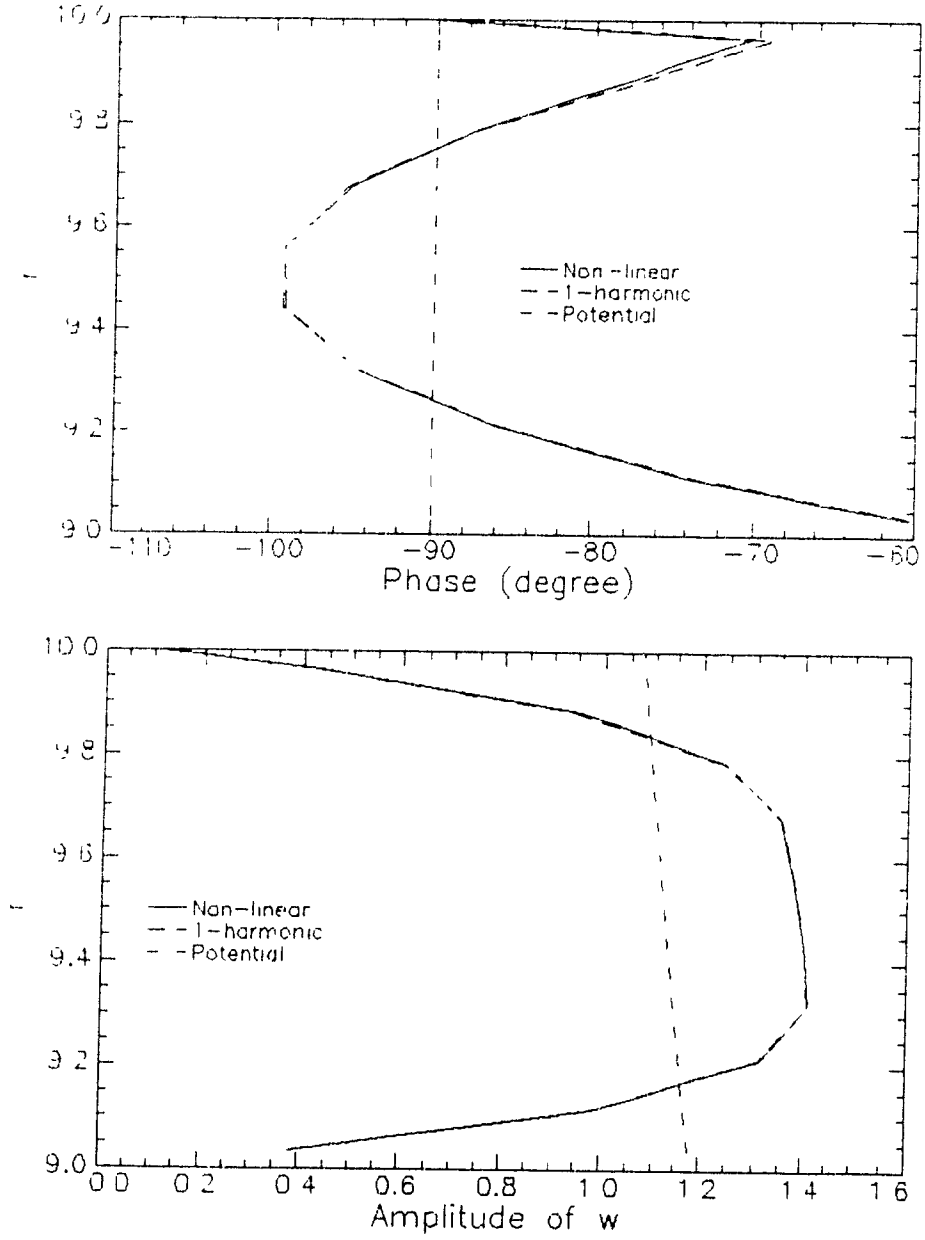

Figure 8.19: Radial profiles of w taken at $x = 50$, $\theta = 45°$, for $Re = 100$, $s = 80$; amplitude and phase of w are plotted.

n	k	rms(R_u)	rms(R_v)	rms(R_w)	rms(R_p)
2	62	0.2295E-04	0.9217E-04	0.9878E-04	0.9075E-04
3	46	0.3084E-04	0.9744E-04	0.9082E-04	0.8261E-04
4	43	0.2768E-04	0.9927E-04	0.8881E-04	0.8095E-04
5	40	0.2858E-04	0.9509E-04	0.8611E-04	0.8003E-04
6	40	0.3028E-04	0.9675E-04	0.9662E-04	0.9194E-04
7	40	0.2744E-04	0.9565E-04	0.9629E-04	0.9358E-04
8	38	0.2375E-04	0.9837E-04	0.9262E-04	0.9030E-04
9	36	0.1773E-04	0.9917E-04	0.8030E-04	0.7813E-04
10	35	0.1261E-04	0.9618E-04	0.5580E-04	0.5665E-04
11	35	0.1904E-04	0.9720E-04	0.4290E-04	0.4827E-04
12	37	0.2604E-04	0.9517E-04	0.5802E-04	0.6096E-04
13	39	0.2839E-04	0.9816E-04	0.7443E-04	0.7191E-04
14	41	0.2727E-04	0.9649E-04	0.8168E-04	0.7485E-04
15	41	0.2812E-04	0.9693E-04	0.9017E-04	0.8260E-04
16	40	0.2946E-04	0.9737E-04	0.9777E-04	0.9273E-04
17	39	0.2729E-04	0.9488E-04	0.9598E-04	0.9348E-04
18	37	0.2214E-04	0.9851E-04	0.8778E-04	0.8486E-04
19	37	0.1225E-04	0.9497E-04	0.6248E-04	0.5865E-04
20	37	0.1071E-04	0.9395E-04	0.3804E-04	0.3612E-04

Table 8.1: Number, k, of pseudo-time steps required to converge at time level t^n, and rms values of residuals at convergence. The computations were performed at $Re = 250$, $s = 25$, with the full non-linear three-dimensional Navier-Stokes equations.

n	k	rms(R_u)	rms(R_v)	rms(R_w)	rms(R_p)
2	57	0 2479E-04	0 9275E-04	0.9908E-04	0 8985E-04
3	41	0 3310E-04	0 9671E-04	0 8876E-04	0 7985E-04
4	40	0 2881E-04	0.9422E-04	0 8827E-04	0.7969E-04
5	35	0 3103E-04	0 9640E-04	0 8945E-04	0 8074E-04
6	36	0 3122E-04	0 9451E-04	0.9569E-04	0 8657E-04
7	35	0 2981E-04	0 9785E-04	0.9984E-04	0 9054E-04
8	34	0 2517E-04	0 9731E-04	0 9286E-04	0 8432E-04
9	32	0 1914E-04	0 9855E-04	0.7920E-04	0 7186E-04
10	31	0 1331E-04	0.9763E-04	0 5738E-04	0 5149E-04
11	31	0 1842E-04	0 9930E-04	0 4775E-04	0.4169E-04
12	33	0 2589E-04	0 9739E-04	0.6153E-04	0 5446E-04
13	35	0 2919E-04	0.9767E-04	0 7587E-04	0 6800E-04
14	36	0 3072E-04	0 9874E-04	0.8649E-04	0 7794E-04
15	36	0 3175E-04	0.9933E-04	0 9557E-04	0.8639E-04
16	36	0.2992E-04	0.9490E-04	0 9695E-04	0.8784E-04
17	34	0 2857E-04	0.9777E-04	0.9912E-04	0 8996E-04
18	33	0.2280E-04	0.9751E-04	0.8836E-04	0.8025E-04
19	32	0.1472E-04	0.9806E-04	0 6609E-04	0.5979E-04
20	32	0 1310E-04	0.9928E-04	0 4437E-04	0.3919E-04

Table 8 2: Number, k, of pseudo-time steps required to converge at time level t^n, and rms values of residuals at convergence. The computations were performed at $Re = 250$, $s = 25$, with the linearized three-dimensional Navier-Stokes equations.

n	k	rms(R_u)	rms(R_v)	rms(R_w)	rms(R_p)
2	207	0 1874E-04	0 8335E-04	0 9848E-04	0 5465E-01
3	174	0.2070E-04	0 8387E-04	0 9888E-01	0 5273E-01
4	146	0.2477E-04	0 8459E-04	0 9881E-01	0 5413E-01
5	154	0 2722E-04	0 8466E-04	0.9940E-04	0 5821E-01
6	159	0.2596E-04	0.8325E-04	0.9789E-04	0.6069E-01
7	159	0 2255E-04	0 8396E-04	0 9885E-01	0 6319E-01
8	156	0.2090E-04	0.8293E-04	0 9750E-04	0 6540E-01
9	147	0.2539E-04	0 8541E-04	0 9968E-01	0 6972E-01
10	131	0.3067E-04	0.8694E-04	0 9889E-04	0 7114E-01
11	100	0.2954E-04	0.9788E-04	0.6813E-04	0.5878E-01
12	109	0.3422E-04	0.9878E-04	0 9698E-01	0 6202E-01
13	139	0.2382E-04	0.8597E-04	0 9923E-04	0 5366E-01
14	151	0.2178E-04	0.8406E-04	0.9813E-04	0.5197E-01
15	157	0.2789E-04	0.8510E-04	0.9995E-04	0.5940E-04
16	160	0.2890E-04	0.8298E-04	0 9760E-04	0 6121E-04
17	158	0.2435E-04	0 8402E-04	0 9879E-04	0 5890E-04
18	152	0.2060E-04	0 8535E-04	0.9979E-04	0 5789E-04
19	141	0.2324E-04	0 8489E-04	0.9822E-04	0 6108E-04
20	117	0.2761E-04	0 9172E-04	0 9724E-04	0.6621E-04

Table 8.3: Number, k, of pseudo-time steps required to converge at time level t^n and rms values of residuals at convergence. The computations were performed at $Re = 100$, $s = 80$, with the full non-linear three-dimensional Navier-Stokes equations.

8.2 Annular Flow Geometry with Backstep

The second geometry for which numerical results were computed is obtained from Figure 8.1 by taking $h_d = 1$. The outer cylinder, of radius $r_o = 10$, in dimensionless form, is made up of three sections, as before, where the central section is oscillated while two fixed portions are situated upstream and downstream of it. The length of the central section is $l = 40$, whereas the fixed portions have lengths $l_u = l_d = 20$.

The fixed inner cylinder has radius $r_{i_u} = 9$ in its upstream section, and radius $r_{i_d} = 8$ in its downstream section. A sudden expansion, or backstep, situated at $x = 20$, delimits the transition between the two parts. The flow at the inlet has mean value U, or $U = 1$ in non-dimensional form, and the non-dimensional gap width upstream is equal to 1. The non-dimensional parameters which have been defined in the previous section are still valid in the present case, where H and U, which are, respectively, the annular gap width and mean flow velocity upstream, serve as characteristic length and velocity. The Reynolds number and Stokes number are thus given by

$$Re = \frac{2HU}{\nu}, \qquad S = \frac{\Omega H^2}{\nu}$$

The mesh on which the equations were solved has the following characteristics. First of all, its layout in the radial direction is like the one which is depicted in Figure 4.1, page 45. The minimum mesh spacing near the walls was $\Delta y = 0.1$, and 12 grid points spanned the radial direction in the downstream section (or 6 grid points upstream). As for the axial direction, the grid was also like that of Figure 4.1 in the vicinity of the step, and the minimum mesh spacing at the step was $\Delta x = 0.2$. Then, the grid was stretched moving from the step in either the upstream or downstream directions, to reach a maximum spacing of $\Delta x = 1.9$ at $x = 10$ and $x = 30$. As we approached either extremities of the oscillating portion

of the outer cylinder, the grid was again made finer to reach the minimum spacing of $\Delta x = 0.96$ at $x = 0$ and $r = 40$. Finally, grid stretching was increased moving toward the inlet or outlet of the fluid domain, to reach the maximum spacing of $\Delta x = 3.2$ at $x = -20$ and $x = 60$.

Figures 8.20 -8.25 give amplitude and phase results for the pressure, p, and circumferential velocity component, w, where the phase is with respect to the displacement of the oscillating outer cylinder. The pressure results are axial profiles plotted for $r = 9.94$ and $\theta = 7.5°$, whereas the results for w are radial profiles presented for $x = 23.3$ and $\theta = 90°$. Figures 8.20 and 8.21 are for $Re = 100$, $s = 5$ whereas Figures 8.22 -8.25 are for $Re = 250$, $s = 10$ and $s = 20$. Only the viscous solutions are plotted. It is seen that in all cases the agreement between the linearized theory and the full non-linear one is again very good. The pressure amplitude is seen to suddenly drop at the expansion, which is explained by the confinement which becomes larger.

Finally, Figure 8.26 plots axial profiles of pressure taken on the surface of the outer cylinder, as well as on the surface of the inner cylinder. The computations are for the linearized viscous solution at $Re = 250$, $s = 20$, and for $\theta = 7.5°$. We can conclude from Figure 8.26 that there is no radial variation in the pressure across the annular gap, as both its amplitude and phase are the same on the inner and outer cylinder walls. There is some small discrepancy only in the vicinity of the step.

The choices of artificial compressibility, δ, and pseudo-time step, $\Delta\tau$, for the computations of this section were made in the same manner as in the previous section. Thus, the values predicted for δ by (5.11) were corrected by a factor of 0.2, and a Courant number of 40 was chosen in (5.12) in order to set the pseudo-time step. Furthermore, the convergence characteristics were in all points similar to the results presented in Tables 8.1 and 8.2 in last section, namely the number of

pseudo-time steps required for convergence at each real time level was of the order of 40 to 50

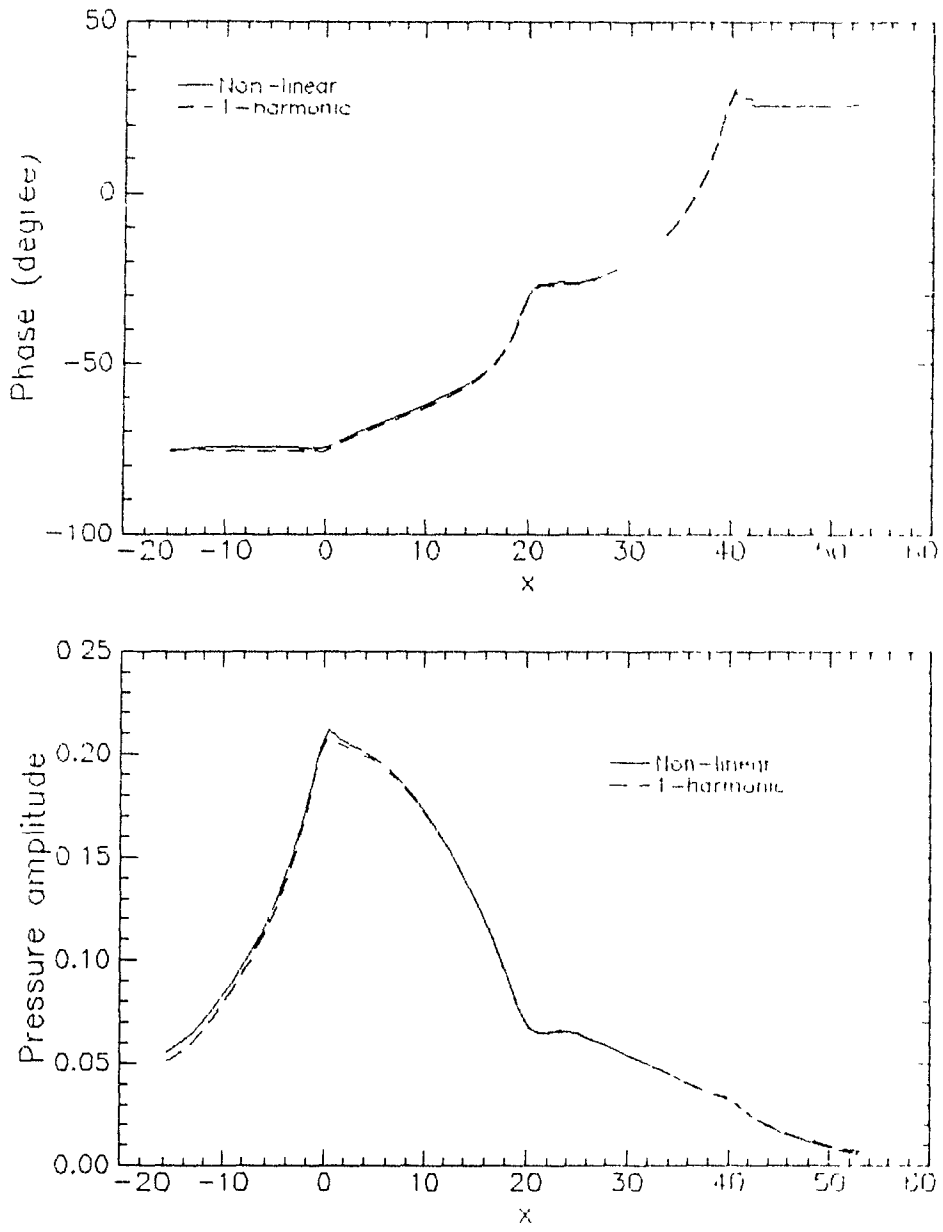

Figure 8.20: Axial variation of pressure taken at $r = 0.94$, $\theta = 7.5°$, for $Re = 100$, $s = 5$.

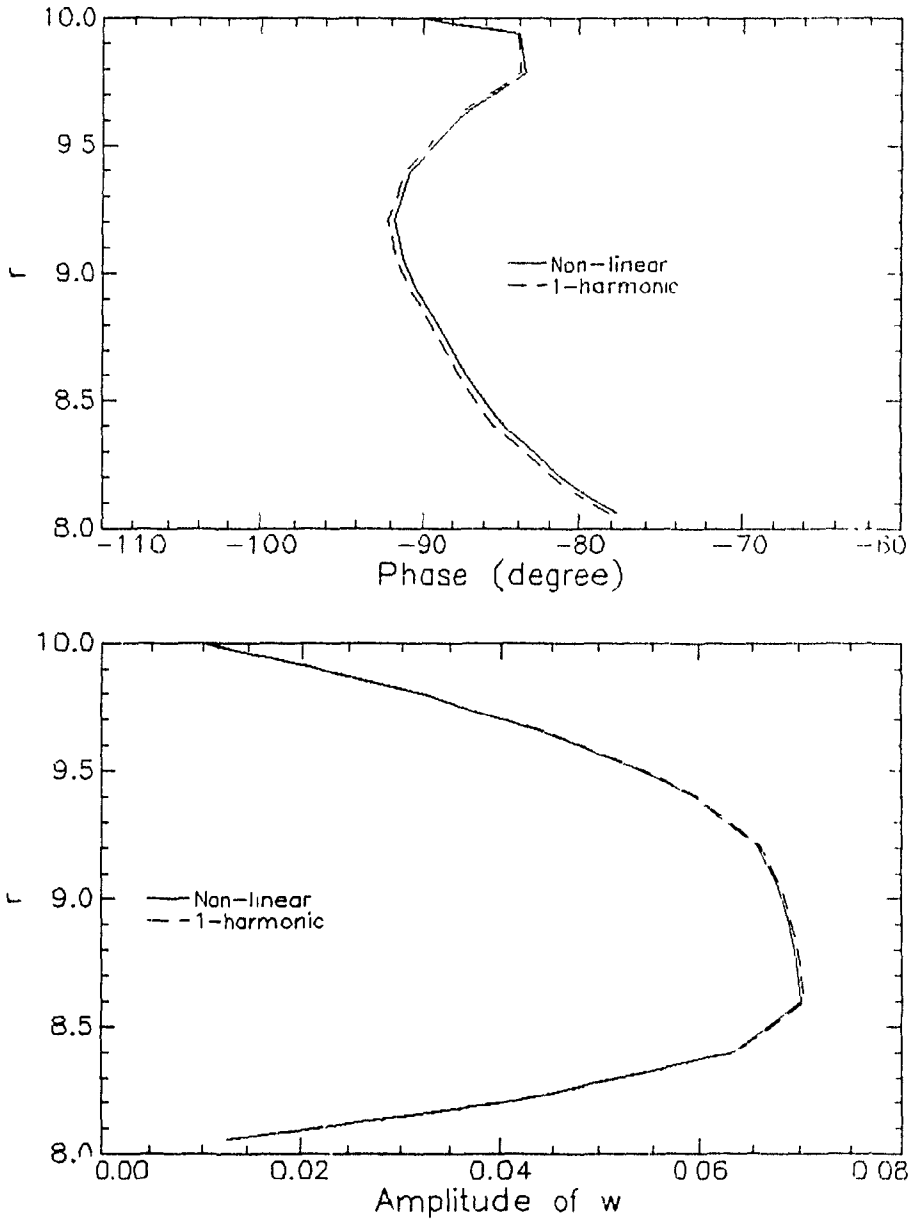

Figure 8.21: Radial profiles of w taken at $x = 23.3$, $\theta = 90°$, for $Re = 100$, $s = 5$.

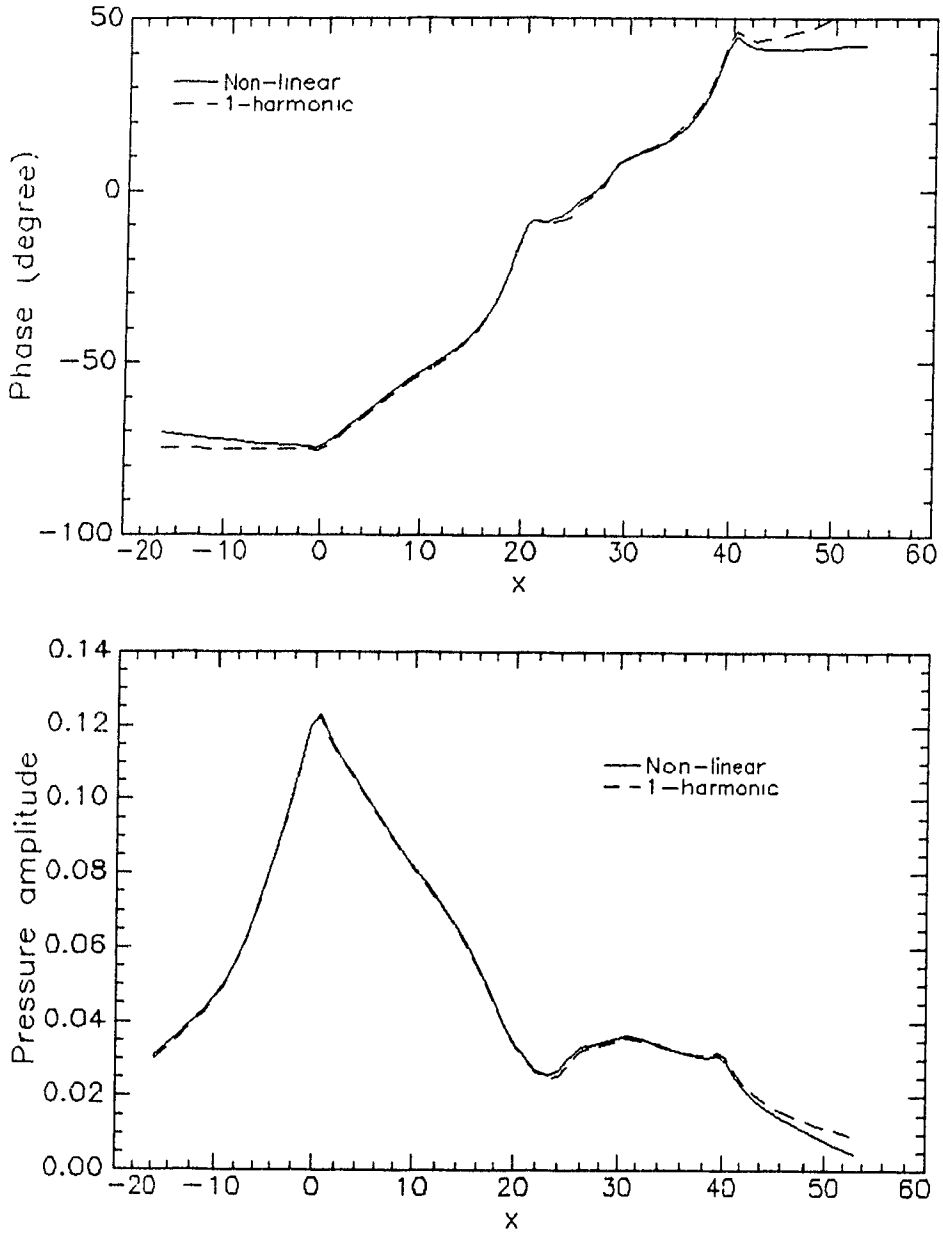

Figure 8.22: Axial variation of pressure taken at $r = 9.94$, $\theta = 7.5°$, for $Re = 250$, $s = 10$.

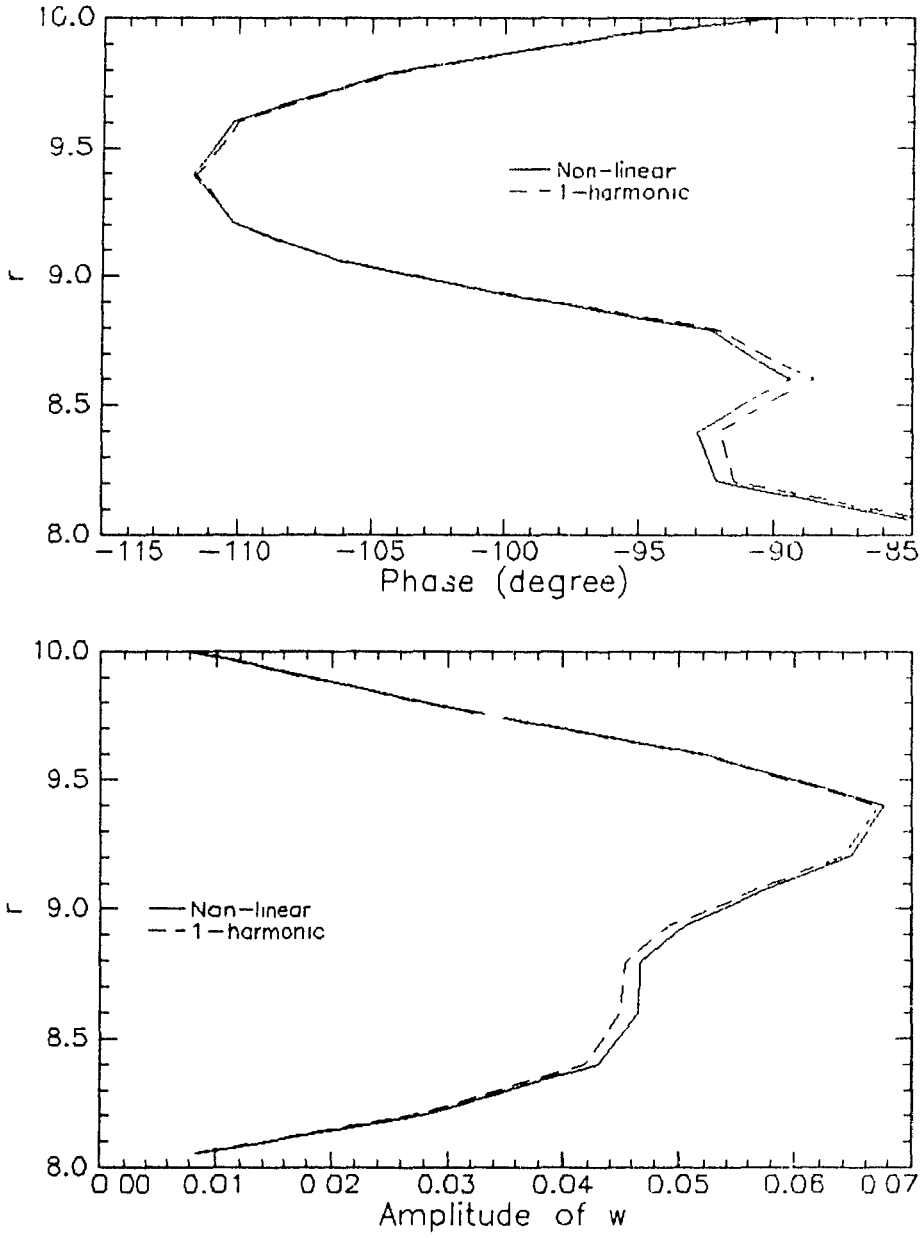

Figure 8.23: Radial profiles of w taken at $x = 23.3$, $\theta = 90°$, for $Re = 250$, $s = 10$.

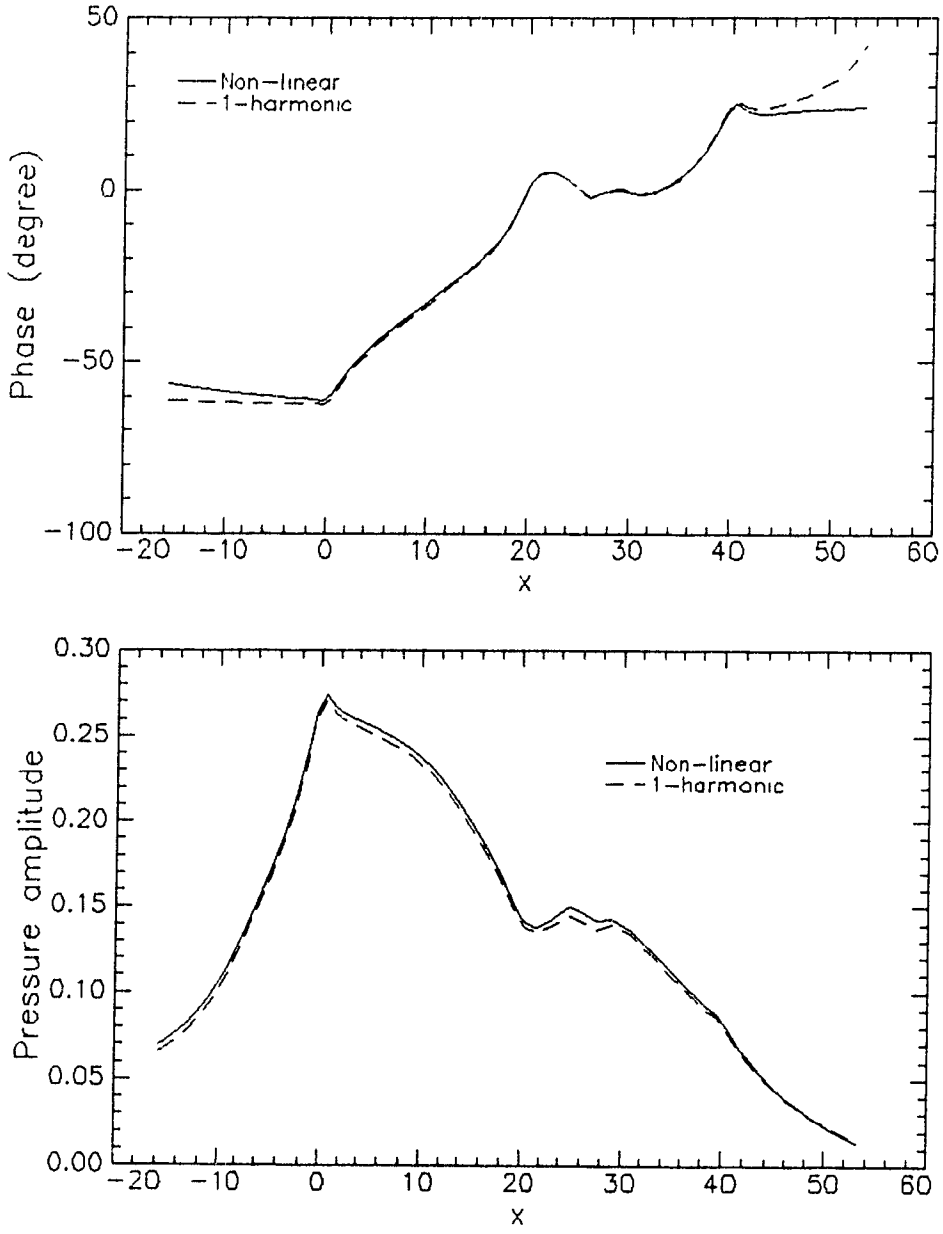

Figure 8.24: Axial variation of pressure taken at $r = 9.94$, $\theta = 7.5°$, for $Re = 250$, $s = 20$.

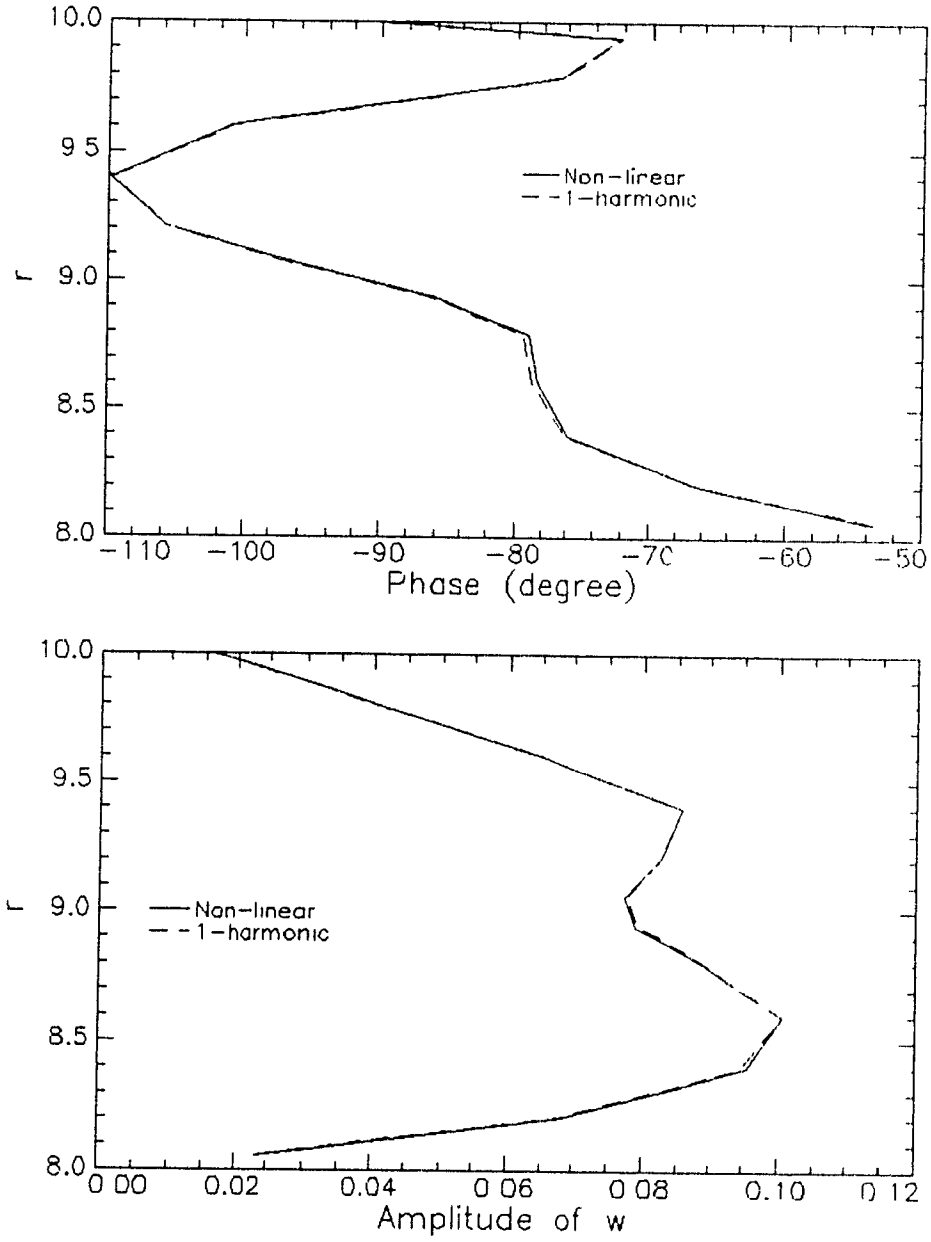

Figure 8.25: Radial profiles of w taken at $r = 23.3$, $\theta = 90°$, for $Re = 250$, $s = 20$

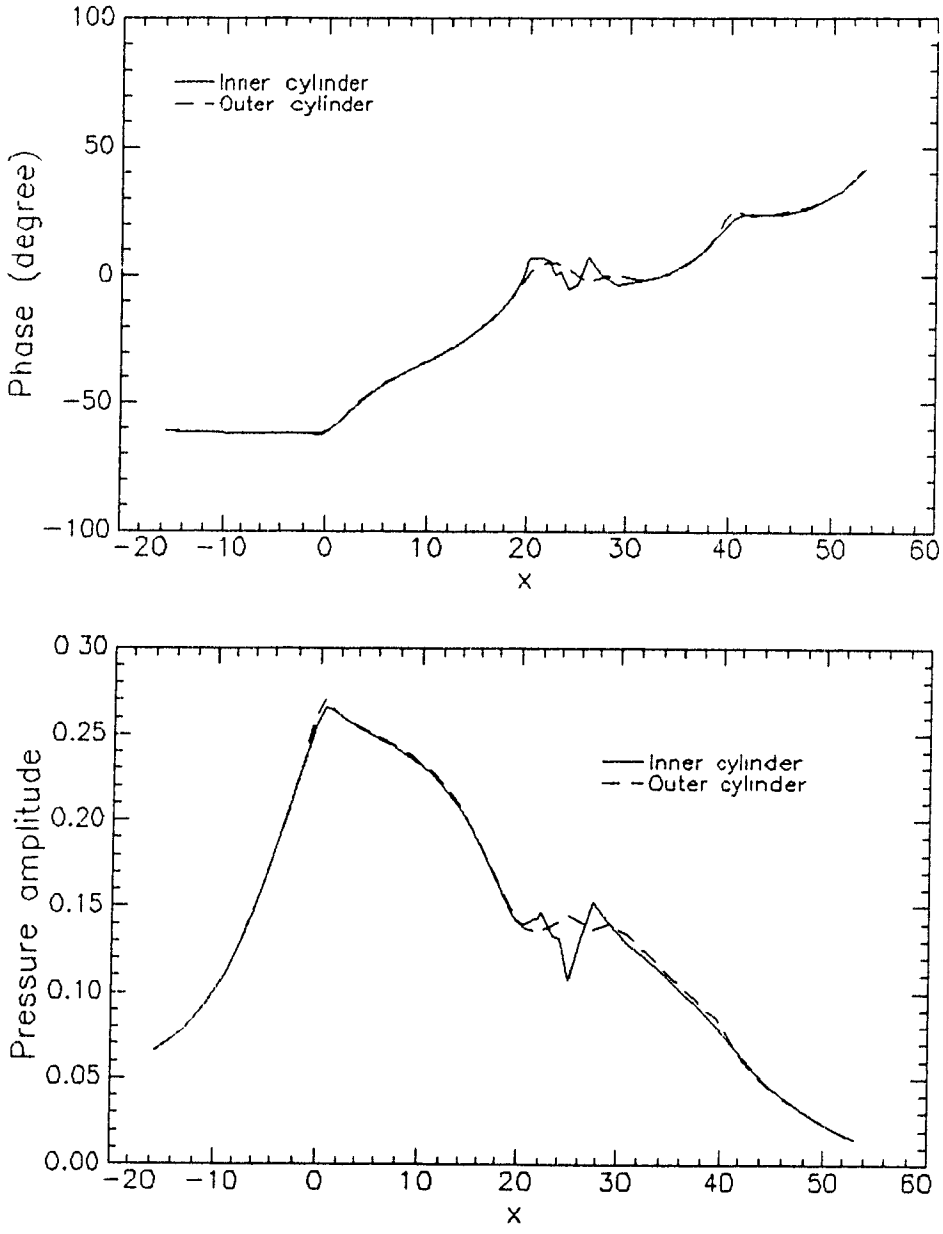

Figure 8.26: Axial variation of pressure taken on the surface of both the inner and outer cylinders, for $\theta = 7.5°$, $Re = 250$, $s = 20$.

Chapter 9

FLUID-STRUCTURE INTERACTION AND STABILITY ANALYSIS IN THE TIME DOMAIN

9.1 Introduction

In Chapters 3 to 8, a method for integrating the incompressible Navier-Stokes equations was developed and applied to the solution of various unsteady flow problems. Forced-vibration numerical computations were performed as the motion of structural boundaries which caused unsteadiness in the flow pattern was assumed to be a known, given function of time. Boundary motion was prescribed for all time, for example in the form of harmonic variation.

We have seen that the boundary condition required to solve the unsteady flow equations was the velocity of the walls bounding the fluid domain. In the

time-discretized form of the equations, the known wall velocity at an advanced level t^{n+1} is required and imposed as a boundary condition in order to obtain and advance the whole solution to t^{n+1}. The solution is known at all previous time levels t^k, $k \leq n$. The unsteady, time-dependent fluid force exerted on the structural walls was calculated for forced-vibration regimes, and consisted in the pressure and viscous shearing forces. We thus remark in this respect that the fluid force is a function of the velocity of the walls of the structure: given the wall velocity at an advanced time level, the fluid equations can be integrated up to that time level and then the fluid force can be calculated. (The fluid force, f^{n+1}, at time level t^{n+1} depends only on the values of $\mathbf{V}^{n+1}$ and p^{n+1}, not on values defined at previous time levels. However in order to integrate the fluid equations to advance to t^{n+1} and compute f^{n+1}, the evaluation of the time derivative $\partial \mathbf{V}/\partial t$ in the equations of motion requires that $\mathbf{V}^n$ and $\mathbf{V}^{n-1}$ be known, see Chapter 3.)

In this chapter, we now consider fluid-structure interaction problems whereby the motion of the structure is not imposed, and does not take place according to a pre-determined time sequence, but is rather allowed to evolve in accordance with the forces acting on it, and these are fluid forces. The latter are external forces determined as a function of the velocity of the structural walls, which results in the fluid-structure interaction.

The procedure that we adopt is thus the following one. Given a structure and fluid flow about it, we force the structure into a small displacement out of its equilibrium position, and then we release it. There are mechanical restoring and damping forces which will act so as to return the structure to its equilibrium position. However, as it undergoes displacement toward equilibrium, fluid forces come into play and may render the fluid-structure system unstable, or add more damping or stiffness to it. The time-evolution of the displacement of the structure allows us to assess whether the system is stable or unstable. It is obtained by

integrating the equation of motion of the structure under the combined mechanical and fluid forces, using in the present case a fourth-order Runge-Kutta scheme

9.2 Numerical Procedure

We consider a structure having one degree of freedom, $\bar{\epsilon}(t)$ which is its displacement, a function of time. It has mass M, mechanical damping and stiffness C and K, respectively, and is subjected to an external fluid force, $\bar{F}(\epsilon)$, which is a function of velocity, $\bar{\epsilon}(t)$. As usual barred quantities are dimensional, non-barred ones non-dimensional The equation of motion of the structure is thus

$$M\ddot{\bar{\epsilon}} + C\dot{\bar{\epsilon}} + K\bar{\epsilon} = \bar{F}(\bar{\epsilon}) \tag{9.1}$$

When appropriate characteristic length, H, of structure, and velocity, U, of fluid are chosen to non-dimensionalize (9.1), it can be put in the form

$$\ddot{\epsilon} \equiv \ddot{\epsilon}(\dot{\epsilon}, \epsilon) = -2\omega_n \xi \dot{\epsilon} - \omega_n^2 \epsilon + \sigma F(\epsilon) , \tag{9.2}$$

where the non-dimensional frequency, ω_n, reduced damping, ξ, and non-dimensional mass, σ, are defined as

$$\omega_n = \sqrt{\frac{K}{M}}\frac{H}{U} , \qquad \xi = \frac{C}{2\sqrt{KM}} , \qquad \sigma = \frac{\rho H^3}{M} , \tag{9.3}$$

with ρ being the fluid density. The non-dimensional fluid force is thus $F(\epsilon)$, and we remark in (9.2) that $\ddot{\epsilon}$ is a function of $\dot{\epsilon}$ and ϵ

Now, in order to integrate (9.2) we suppose that we are at time level t^n, where all the quantities necessary to describe the motion of the structure are known. These are its displacement, ϵ^n, velocity, $\dot{\epsilon}^n$, and acceleration, $\ddot{\epsilon}^n$, as well as the fluid forces acting on it, $F(\dot{\epsilon}^n) \equiv F^n$. We note that F^n is made a function of

the velocity of the structure, according to the remarks made in the introduction. In fact, all those quantities are known at the previous time levels, t^k, $k \leq n$, and now we want to advance to t^{n+1}.

$T_1 = t^n$	$X_1 = \epsilon^n$	$V_1 = \dot{\epsilon}^n$	$A_1 = \ddot{\epsilon}(X_1, V_1)$
$T_2 = t^n + \frac{\Delta t}{2}$	$X_2 = \epsilon^n + \frac{\Delta t}{2} V_1$	$V_2 = \dot{\epsilon}^n + \frac{\Delta t}{2} A_1$	$A_2 = \ddot{\epsilon}(X_2, V_2)$
$T_3 = t^n + \frac{\Delta t}{2}$	$X_3 = \epsilon^n + \frac{\Delta t}{2} V_2$	$V_3 = \dot{\epsilon}^n + \frac{\Delta t}{2} A_2$	$A_3 = \ddot{\epsilon}(X_3, V_3)$
$T_4 = t^n + \Delta t$	$X_4 = \epsilon^n + \Delta t V_3$	$V_4 = \dot{\epsilon}^n + \Delta t A_3$	$A_4 = \ddot{\epsilon}(X_4, V_4)$

Table 9.1: Runge-Kutta scheme applied to the integration of the equation of the structure

The Runge-Kutta scheme is then the 4-step procedure which is illustrated in Table 9.1 [35], where the quantities X_i, V_i, A_i, $i = 1, \ldots, 4$, are variables of displacement, velocity and acceleration, respectively. After they have been obtained by means of the process outlined in Table 9.1, we advance to time level t^{n+1} as follows:

$$\epsilon^{n+1} = \epsilon^n + \frac{\Delta t}{6}(V_1 + 2V_2 + 2V_3 + V_4) \tag{9.4}$$

$$\dot{\epsilon}^{n+1} = \dot{\epsilon}^n + \frac{\Delta t}{6}(A_1 + 2A_2 + 2A_3 + A_4) \tag{9.5}$$

$$F^{n+1} = F(\dot{\epsilon}^{n+1}) \tag{9.6}$$

$$\ddot{\epsilon}^{n+1} = -2\omega_n \xi \dot{\epsilon}^{n+1} - \omega_n^2 \epsilon^{n+1} + \sigma F^{n+1}, \tag{9.7}$$

We see that the first line in Table 9.1 is simply an initialization step in which the variables X_1, V_1, and A_1 are set to the known values ϵ^n, $\dot{\epsilon}^n$ and $\ddot{\epsilon}^n$, respectively.

The second step, line 2 in Table 9.1, projects the solution to an intermediate time level $t^{n+1/2}$, and in the second and third columns, X_2 and V_2 are easily determined. Ounce V_2 is obtained, the equations of fluid motion can be integrated up to that time level $t^{n+1/2}$, by imposing V_2 as boundary condition, and the fluid force at $t^{n+1/2}$ can be determined. This in turn allows for calculating A_2 by means of (9.2).

The third step in Table 9.1 proceeds in exactly the same manner as the second one, as is the case for the fourth step, except that in this fourth step the solution projects itself at time $T_4 = t^n + \Delta t$, not at $t^n + \Delta t/2$. Finally, after ϵ^{n+1} and $\dot{\epsilon}^{n+1}$ have been obtained from equations (9.4) and (9.5), the fluid force F^{n+1} can be computed by integrating the fluid equations up to time level t^{n+1}, after imposing $\dot{\epsilon}^{n+1}$ as boundary condition. Then ϵ^{n+1} is obtained by means of (9.7), and the procedure can be repeated to advance to another time level

Some additional precisions will now be given at this point. The time step, Δt, is chosen to be equal to a fraction of the natural period, $T_n = 2\pi/\omega_n$, of the system, such as

$$T_n = \frac{1}{N}\frac{2\pi}{\omega_n}\,, \tag{9.8}$$

where N is an integer which is of the order of 10 or more. Also, steps 2 and 3 in Table 9.1 require that the fluid equations be integrated up to the intermediate time level $t^{n+1/2} = t^n + \Delta t/2$. In that case, we don't use the time-differencing scheme (3.4), but instead the following one.

$$\frac{8\,\mathbf{V}^{n+1/2} - 9\,\mathbf{V}^n + \mathbf{V}^{n-1}}{3\,\Delta t} + \mathbf{G}^{n+1/2} = \mathbf{0}\,, \tag{9.9}$$

which is also a three-step, second order time-accurate scheme, written this time in terms of the velocity at time levels t^{n-1}, t^n and $t^{n+1/2}$, instead of the velocity at

time levels t^{n-1}, t^n and t^{n+1}. Equation (9.9) can be rewritten as

$$\mathbf{V}^{n+1/2} + \alpha\, \mathbf{G}^{n+1/2} = \mathbf{F}^n \,, \tag{9.10}$$

where

$$\alpha = \frac{3}{8}\,\Delta t \,, \quad \mathbf{F}^n = \frac{1}{8}\,(9\,\mathbf{V}^n - \mathbf{V}^{n-1}) \,.$$

When (9.10) is augmented with the continuity equation written at $t^{n+1/2}$, namely $\nabla \cdot \mathbf{V}^{n+1/2} = 0$, then a set of equations like (3.6) and (3.7) is obtained, which is solved in the same manner for the quantities $\mathbf{V}^{n+1/2}$ and $p^{n+1/2}$, instead of the quantities $\mathbf{V}^{n+1}$ and p^{n+1}. Thus, according to the notation of Chapter 3, in order to solve those equations we need to impose as boundary condition the known wall velocity $\mathbf{V}_w^{n+1/2}$, which is given in Table 9.1 by V_2 and V_3, in steps 2 and 3 respectively. Step 4 in Table 9.1, and the final updating of the solution, equation (9.7), which both project the solution at $t^n + \Delta t$, can use the time differencing scheme (3.4).

In order to provide initial conditions to start the whole numerical procedure, the following strategy has been adopted. At times t^1 and t^2, we set $\epsilon(t^1) = \epsilon(t^2) = \epsilon_o$, where ϵ_o is a small displacement of the structure, out of its equilibrium position. The other quantities, namely velocity, acceleration and fluid force, are all equal to zero. The structure is thus at rest for the first two time steps and the fluid flow about it will be the corresponding steady state flow pattern. Then the structure is let go of, and time integration is started. We remark that by imposing initial conditions for two initial time levels, the three-level schemes (3.4) and (9.9) can be used to integrate the fluid equations for t^n, $n > 2$. Also, in view of the small displacement which is imposed as a boundary condition to the structure, the steady mean flow which exists initially before releasing the structure is taken to be the same as that which exists in the equilibrium position of the structure, for $\epsilon = 0$.

9.3 Numerical Results

9.3.1 Fluid-structure interaction in 2D annular geometry

Here we treat the problem that was first discussed in Section 7.4, see Figure 7.1 page 108. The two cylinders are infinite in extent and of constant cross-section, having inner radius r_i and outer radius r_o. In their equilibrium position, they are concentric with each other and the outer cylinder has one degree of freedom in lateral displacement, as its axis always remains parallel with the axis of the fixed inner cylinder. We denote by $\epsilon(t)$ the displacement of the outer cylinder axis. We saw in chapter 7 that in this case the dynamics of the fluid motion in the annular space is independent of any axial flow which may be present there, and three methods of solution for the integration of the flow equations have been presented.

The outer cylinder, of mass m, is assumed to be restrained by a spring k and dashpot c, where lowercase letters indicate quantities defined per unit length. In that case the fluid force, f^n, per unit length at time level t^n is given by (7.49) when the one- or two-harmonic solutions are chosen, as described in Chapter 7, or by (7.48) when the full non-linear Navier-Stokes equations are resolved. The boundary conditions for the fluid solutions are given by (7.16) and (7.17) when the non-linear equations are used, and by (7.27) and (7.28) for the one- and two-harmonic solutions. In both cases, they are expressed in terms of the velocity of the outer cylinder axis, $\dot{\epsilon}$, which is consistent with the approach adopted in the previous section of this chapter.

To non-dimensionalize the equations we choose as characteristic length, H, the annular gap width, and as characteristic velocity, $\Omega_n H$, where Ω_n is the dimensional natural frequency of the in vacuo mass-spring system, defined by

$\Omega_n = \sqrt{k/m}$. The Reynolds number in the fluid equations is thus given by

$$Re = \frac{\Omega_n H^2}{\nu} , \tag{9.11}$$

where ν is the fluid kinematic viscosity. Now, we have seen in Section 7.4 that the fluid force on the oscillating outer cylinder as determined by either of the three methods of Sections 7.1, 7.2 or 7.3, is essentially the same for each of these methods. We elect to perform the numerical examples of this section, to be presented shortly, using the two-harmonic solution of Section 7.3. Given the choice of characteristic length and velocity that was made, the equation of motion of the outer cylinder becomes, cf. equation (9.2),

$$\ddot{\epsilon} = -2\xi\,\dot{\epsilon} - \epsilon + \sigma f(\dot{\epsilon}) , \tag{9.12}$$

where the non-dimensional frequency, ω_n, reduced damping, ξ, and non-dimensional mass, σ, are given by

$$\omega_n = \sqrt{\frac{k}{m}}\frac{H}{\Omega_n H} = 1 , \qquad \xi = \frac{c}{2\sqrt{km}} , \qquad \sigma = \frac{\rho H^2}{m} , \tag{9.13}$$

and where the fluid force per unit length, f, is given by (7.49). Now, in the computations the reduced damping, ξ, was taken equal to zero in order not to introduce mechanical damping, and hence in order to clearly identify the fluid damping.

As initial conditions, we took $\epsilon_o = 0.1$, in non-dimensional units (which corresponds to a small displacement amplitude), and we chose $\Delta t = 2\pi/19$. The geometry that we considered had non-dimensional outer cylinder radius $r_o = 10$. The unit of time chosen for the figures presented in this section, as well as in the next section, is the natural period, T_n, of the system, which is equal to $T_n = 2\pi/\omega_n$.

Figure 9.1(a) presents results for the time evolution of $\epsilon(t)$, the displacement of the outer cylinder, at three different Reynolds numbers. We see that at a very low Reynolds number, $Re = 2$, viscosity dominates the solution and the cylinder motion is highly damped as no oscillations are present, the cylinder is rapidly brought to its equilibrium position, $\epsilon = 0$. As the Reynolds number increases, $Re = 200$ and $Re = 20\,000$, oscillations appear, and the higher the Reynolds number the more the viscous solution approaches the potential flow solution. The latter has also been plotted in Figure 9.1(a); it has been obtained by means of linearized potential flow theory, which is outlined in Appendix D, and we see that there is no damping present in the potential solution, as expected

The value of σ in (9.12) has been selected under the following guidance. Linearized potential flow theory permits the determination of the added mass per unit length, σ_m, for the present geometry [38], which we write in dimensionless form as

$$\sigma_m = \frac{\rho H^2}{m_a} = \frac{1}{\pi r_o^2} \frac{b^2 - 1}{b^2 + 1}, \tag{9.14}$$

where m_a is the dimensional added mass and $b = r_o/r_i$. Actually, σ_m is inversely proportional to the added mass. We then have that the ratio

$$\frac{\sigma_m}{\sigma} = \frac{m}{m_a}, \tag{9.15}$$

is equal to the ratio of structural mass to fluid-added mass. The value of σ in (9.12) was then chosen to be equal to

$$\sigma = \frac{\sigma_m}{1.5}, \tag{9.16}$$

which corresponds to a structural mass which is 1.5 times larger than the fluid-added mass determined by potential flow theory

The curve depicting the potential flow results in Figure 9.1(a) has been computed by solving the equation of the structure (9.12), in which the fluid force f was determined by linearized potential flow theory. Potential flow theory can actually be used in the present case to test the accuracy of the fourth-order Runge-Kutta scheme used to integrate the equation of the vibrating cylinder, and can thus provide a reference for validating the procedure adopted for the fluid-structure interaction problems.

Indeed, it is easy to show for the problem at hand that the only fluid force present from the point of view of potential theory comes from the presence of the added mass, which is given analytically by (9.14). Hence the equation of the structure can be put in the following closed form,

$$\left(1 + \frac{\sigma}{\sigma_m}\right) \ddot{\epsilon}(t) + \epsilon(t) = 0 \,, \tag{9.17}$$

which has an analytic solution. This analytic solution is plotted in Figure 9.1(b), along with the solution obtained from the fluid-structure integration of (9.12), in which the fluid force, f, is determined by linearized potential flow theory. The ratio σ/σ_m is $1/1.5$ It is seen that the agreement is very good, which provides for validating the use of the Runge-Kutta method in fluid-structure interaction studies.

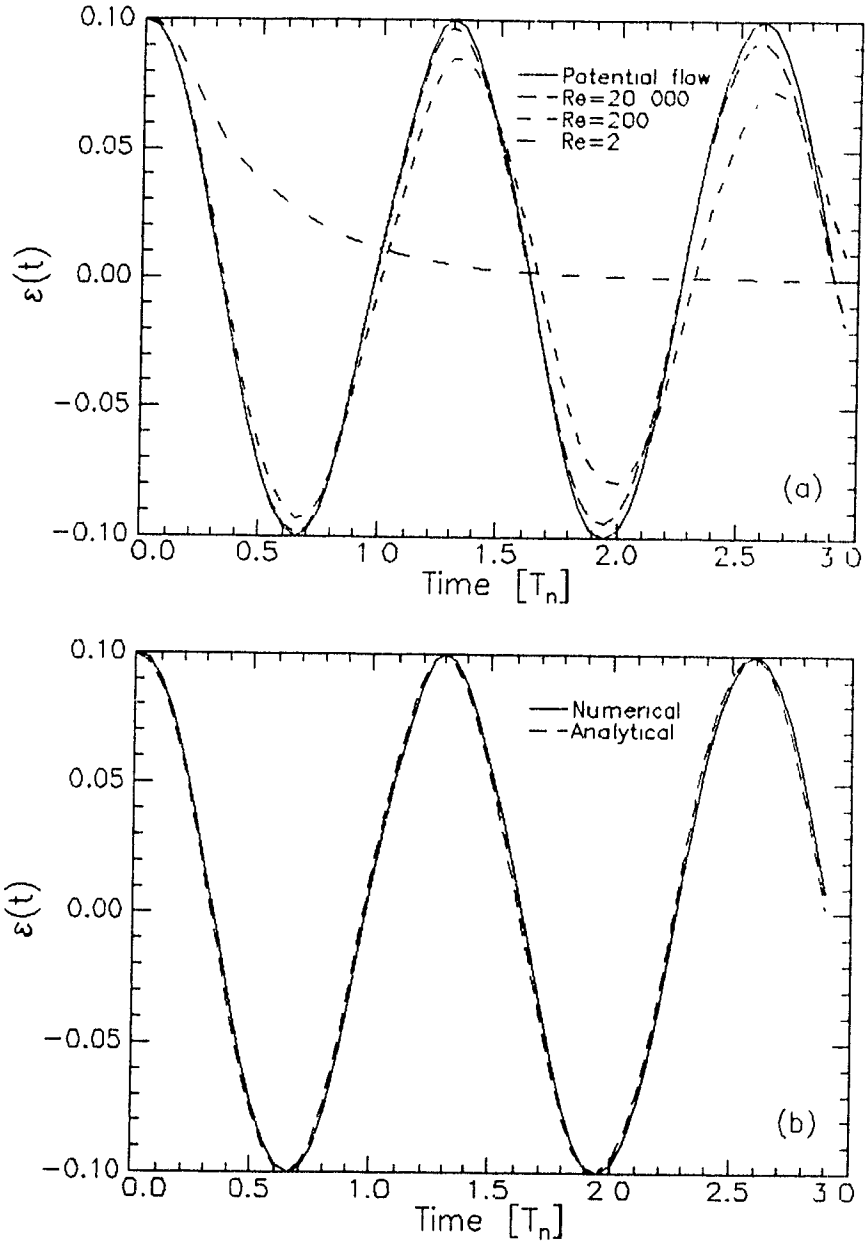

Figure 9.1: Time evolution of cylinder displacement. (a) Comparison of the potential flow solution with viscous flow solutions computed for three different Reynolds numbers; (b) comparison of numerical and analytical potential flow solutions.

9.3.2 Fluid-structure interaction in 3D annular geometry

The geometry that we now consider has been detailed in Section 8.1, see Figure 8.1 page 139. It is a uniform annular geometry made up of a fixed inner cylinder concentric with an outer tube the central portion of which is free to vibrate in lateral motion. Two fixed ends thus terminate the outer tube and the vibrating central portion, of mass M, is restrained by a spring K and dashpot C. As in Section 8.1, the equations are non-dimensionalized by chosing H, the annular gap width, to be the characteristic length, and the characteristic velocity is U, the mean flow velocity in the annular region. The equation of motion of the structure is thus (9.2), in which the non-dimensional frequency, ω_n, reduced damping, ξ, and non-dimensional mass, σ, are given by (9.3)

The fluid force per unit length at time t^n for that problem is still given by (7.49) when the linearized three-dimensional viscous solution presented in Section 6.4 is chosen, and the total force, $F^n = F(\epsilon^n)$, in (9.2) is found by integrating (7.49) over the vibrating portion of the outer tube. The Reynolds number appearing in the equations of fluid motion is given by (8.1).

If we consider potential flow theory, the equation of motion of the oscillating outer cylinder can be written in the form [37]

$$(1 + \sigma q_2)\ddot{\epsilon} + (2\omega_n \xi + \sigma q_1)\dot{\epsilon} + (\omega_n^2 + \sigma q_0)\epsilon = 0 \,, \tag{9.18}$$

where q_2, q_1 and q_0 are the non-dimensional added mass, added damping and added stiffness, respectively. They are given by

$$q_2 = \frac{M_a}{\rho H^3} \,, \qquad q_1 = \frac{C_a}{M}\frac{H}{U} \,, \qquad q_0 = \frac{K_a}{M}\frac{H^2}{U^2} \,, \tag{9.19}$$

where M_a, C_a and K_a are the dimensional added mass, added damping and added stiffness. Preliminary computations have permitted to determine the following

values for those parameters: $q_2 = 270\,750$, $q_1 = 0$, $q_0 = -320$. The possibility of an instability of the system by divergence is indicated by the presence of a negative added stiffness. In that case, it can be shown that divergence occurs when

$$\omega_n^2 < \sigma\,|q_0| \ , \tag{9.20}$$

which, it is to be stressed, is valid according to the potential flow assumption. We remark that viscous flow computations might result in an actual added mass which is slightly larger than 270 750 [36], especially at low vibration frequency (low Stokes number); furthermore, the viscous solution will most likely introduce positive damping and may also modify the added stiffness as compared to the potential flow value.

Figure 9.2 presents time evolution solutions for the displacement of the vibrating outer cylinder, where the viscous flow results have been computed using the linearized one-harmonic solution of Section 6.4. Linearized potential flow results are also included. Since we have $\sigma q_2 = M_a/M$, the value of σ in (9.2) was chosen in such a way as to have a structural mass which is 1.5 times larger than the fluid-added mass determined by potential flow theory, namely $\sigma = 1/(1.5 \times q_2)$. The computations of Figure 9.2 are for a Reynolds number Re of 250, and different values of ω_n were chosen, namely $\omega_n = 0.1$ in Figure 9.2(a) and $\omega_n = 1$ in Figure 9.2(b). For an annular geometry of given dimensions, as well as for a given mass, M, of the oscillating cylinder, this corresponds to a system in which the spring stiffness K is changed so as to correspondingly modify ω_n. We see from Figure 9.2 that for a stiff system, $\omega_n = 1$, the viscous solution is not as highly damped as for a system which has less rigidity, $\omega_n = 0.1$. In both cases, the potential solution has no attenuation in the amplitude of the displacement, as expected.

Now, in Figure 9 3 smaller values of ω_n were chosen, namely $\omega_n = 0.03$ in Figure 9.3(a), and $\omega_n = 0.01$ in Figure 9 3(b); the Reynolds number was also $Re = 250$. The critical value of ω_n for divergence is 0.028, as predicted by (9.20), and it is seen that both the potential and viscous solutions in Figure 9.3(a) do not diverge, as $\omega_n = 0\ 03 > 0.028$. However, in Figure 9.3(b) divergence occurs for both solutions, where we have $\omega_n = 0.01 < 0\ 028$ Potential flow has thus provided a good estimate for the onset of instability, which is determined more precisely by the viscous flow computations as the latter represent more realistically the fluid flow behavior

To refine the predictions, computations were also performed at $\omega_n = 0.02$, for $Re = 250$, and the results are presented in Figure 9.4. It is seen that, as expected, divergence occurs in the potential flow results, whereas the viscous flow calculations exhibit a rather erratic behavior, probably indicative of the transition to instability.

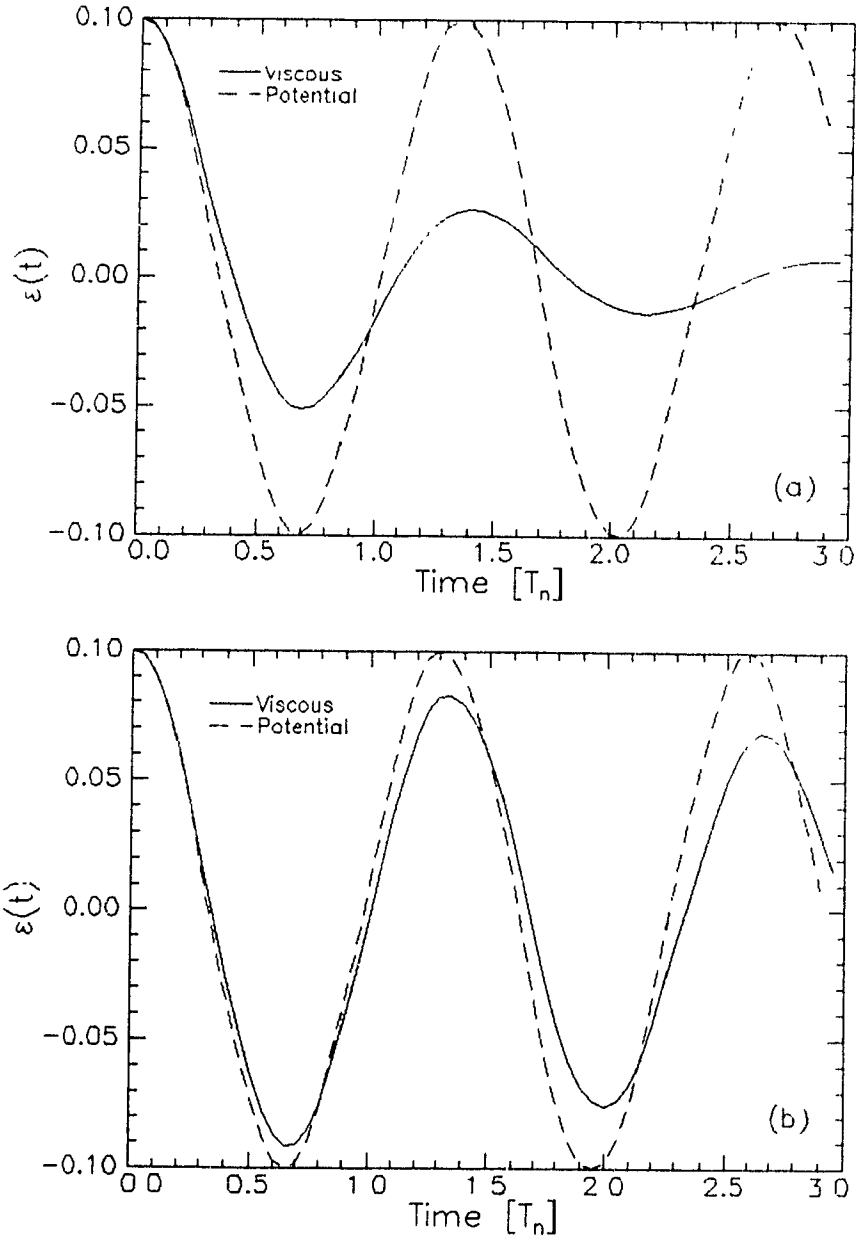

Figure 9.2: Comparison between potential and viscous flow solutions for the displacement of the oscillating cylinder. (a) $\omega_n = 0.1$, (b) $\omega_n = 1$.

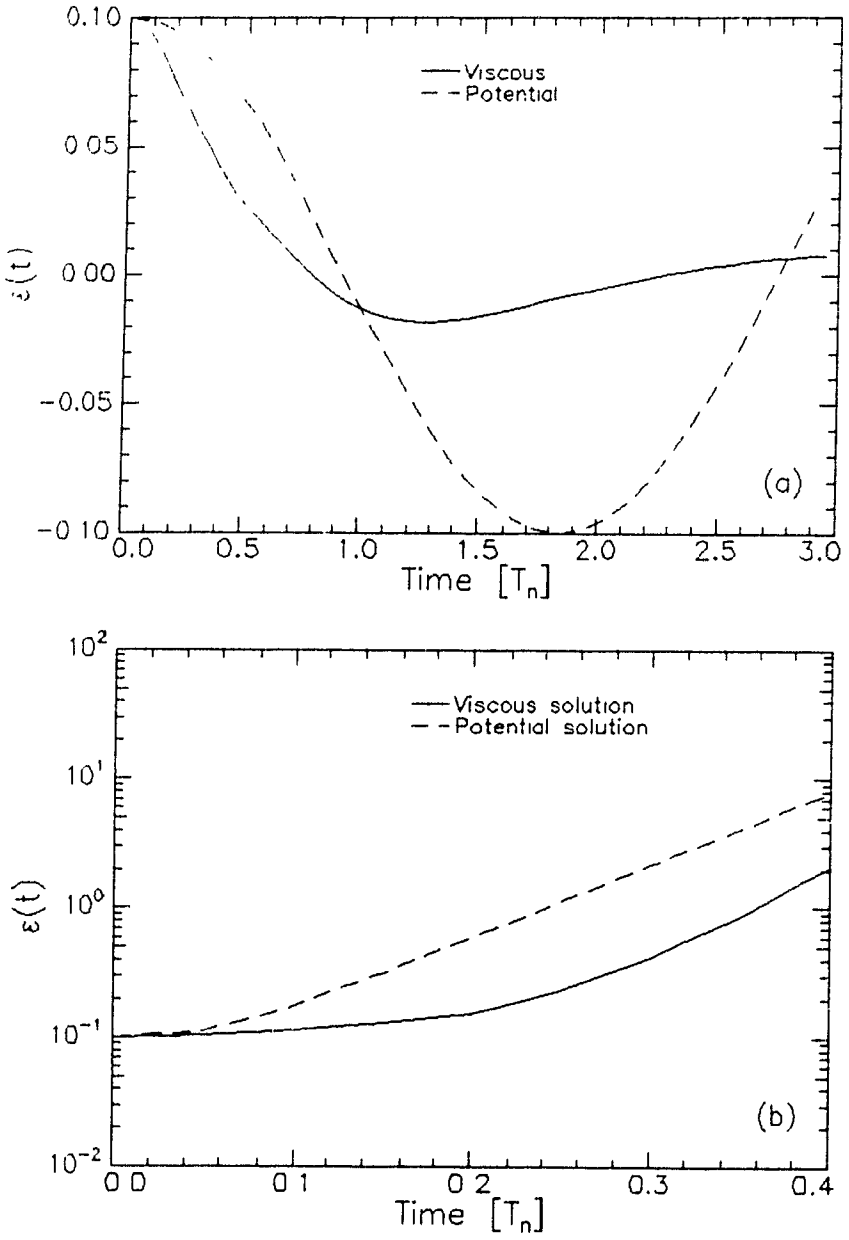

Figure 9.3: Comparison between potential and viscous flow solutions for the displacement of the oscillating cylinder. (a) $\omega_n = 0.03$. (b) $\omega_n = 0.01$.

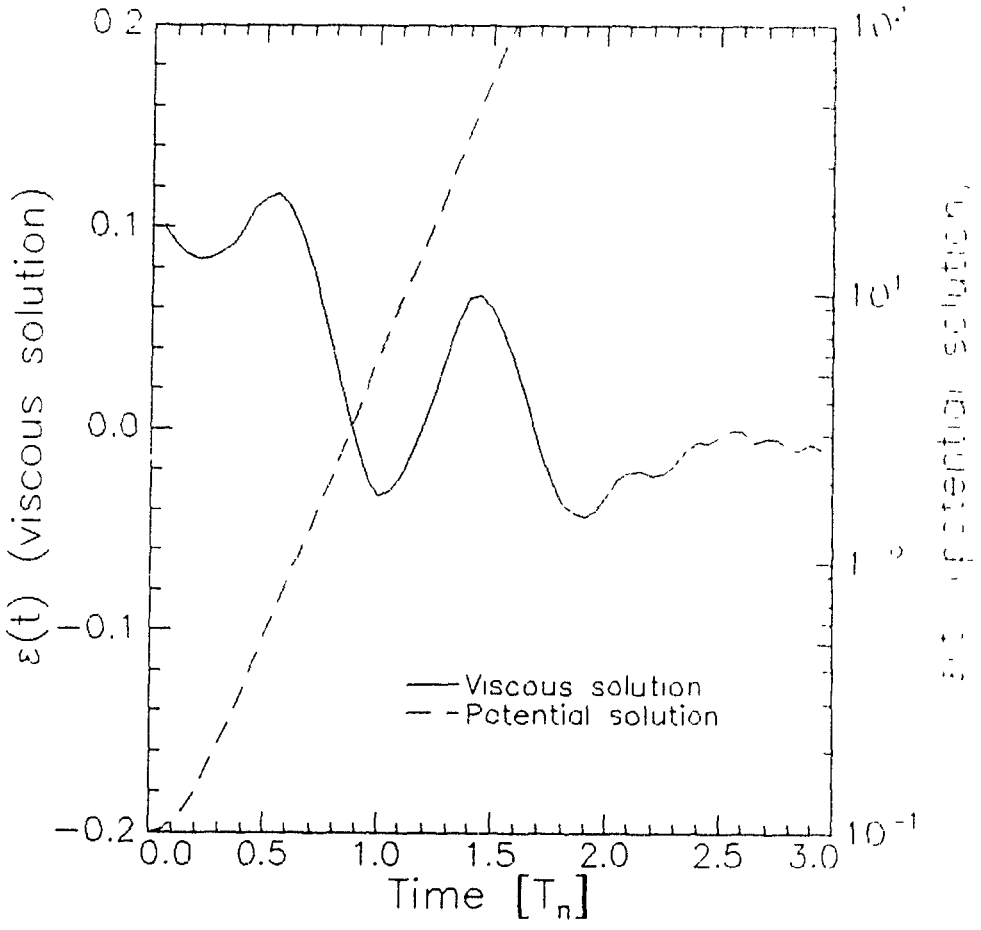

Figure 9.4: Comparison between potential and viscous flow solutions for the displacement of the oscillating cylinder and for $\omega_n = 0.02$

9.4 Discussion

The method expounded in this chapter for the study of fluid-coupled structural systems makes possible the use of numerical methods designed to solve flow problems in such a way as to predict the structural stability of complicated fluid-structure systems.

The reader might not have failed to notice that we have been careful in always selecting a structural mass which was larger than the fluid-added mass. The reason is that when the fluid-added mass becomes larger than the structural mass, the method as set up in this chapter fails. The solution diverges immediately and the displacement of the structure rapidly tends toward infinity. Some ways to circumvent that problem have been devised [39, 40], but more study may be necessary before a solution is established on a sound theoretical and physical basis. At this point, we will advance a few reasons to explain the occurence of the problem, which should provide some guidance toward its solution.

First of all, we note that like any other scheme devised to integrate ordinary differential equations, the Runge-Kutta scheme is meant to perform the following task. We have a function, $\epsilon(t)$, which obeys the differential equation

$$\dot{\epsilon}(t) = g(t, \epsilon) \ , \tag{9.21}$$

and we want to solve (9.21) to obtain the time evolution of $\epsilon(t)$. The important fact about $g(t, \epsilon)$ is that it is precisely a function of t and ϵ, and not also of $\dot{\epsilon}$. Numerical schemes like fourth-order Runge-Kutta are derived under those assumptions on $g(t, \epsilon)$.

In fluid-structure interaction problems the fluid force is a function of the displacement, velocity and acceleration of the structure, and this results in the appearance of added stiffness, added damping and added mass. In equation (9.2),

we have indicated that the fluid force is a function of the velocity, which it is, from the point of view of the numerical method and for imposing boundary conditions to solve the flow problem. In that respect, the equation of the structure was integrated very successfully in the previous sections, at least for the ratios of fluid-added mass to structural mass chosen.

However, in the solving of the fluid equations, a time derivative of the velocity vector is evaluated numerically, and this actually translates into an acceleration term which reflects the added mass effect. The fluid force thus has a "hidden" acceleration-dependent component, and since the solution of the second-order ordinary differential equation of the structure is done by writing it down in terms of two first-order equations, a scheme devised to solve a fluid-structure interaction problem might have to be derived by considering from the outset the equation

$$\epsilon(t) = g(t, \epsilon, \epsilon) \ , \tag{9.22}$$

where $g(t, \epsilon, \epsilon)$ is also a function of ϵ. Nevertheless, it is of interest to notice that the present scheme proves very accurate in solving the fluid-structure equations, as long as the fluid-added mass remains smaller than the structural mass. This has been made clear in the previous sections.

The tackling of the problem by means of a scheme based on (9.22) might prove to be simply impossible from a theoretical point of view. Other approaches might be needed to solve problems in which large added mass is present, for example investigation of schemes adapted from the sub-structuring method used in the finite element analysis of large structures [38] might prove successful. Finally, it is to be remarked that the failing of the method as the added mass becomes larger than the structural mass maybe reflects the impossibility of the mechanical system to oscillate in this case.

Chapter 10

CONCLUSIONS

This Thesis developed three novel aspects in annular-flow-induced vibrations. These are the development of methods to (1) compute the unsteady turbulent forces acting on a cylinder vibrating in uniform turbulent flow, (2) perform the accurate time-integration of the Navier-Stokes equations for viscous incompressible laminar flow, and (3) perform the fluid-structure stability analysis of a system in the time domain.

The first part, Chapter 2, introduced the subject by treating uniform configurations subjected to turbulent flow. The turbulent contribution to the unsteady fluid forces was determined by a method which consisted in the superposition of the fluctuating small-scale quantities present in turbulent flow upon a potential flow, instead of a "viscous" one.

Potential flow is used to determine an unsteady pressure contribution, induced by the oscillation of the cylinder, as well as the perturbations in the velocity field induced by these oscillations. Then, the wall shear stress associated with the mean turbulent flow is calculated, which, in the present study, was done using results specific to narrow-channel flow. The unteady turbulent pressure is deter-

mined by projecting the wall shear stress associated with the mean turbulent flow in the direction of the instantaneous mean velocity vector in the annulus, which includes the potential velocity perturbation The unsteady fluid forces on the oscillating cylinder is then the superposition of the unsteady potential pressure and the turbulent one The theoretical results were compared with experiments and the agreement was shown to be good

Then, the computation of unsteady laminar flows was considered and the method developed to accomplish the time-accurate integration of the incompressible Navier-Stokes equations was presented A semi-discretization of the momentum equation using a three-point-backward implicit time-differencing scheme is introduced, which is shown to rectify the problems encountered when a Crank-Nicolson scheme is used instead. After the semi-discretization, artificial "pseudo-time" derivative terms are added to the equations, including artificial compressibility in the continuity equation, and the solution is advanced from one real (physical) time level to the next by integrating in pseudo-time until steady state is reached The equations are cast in delta-form after differencing the pseudo-time derivatives using an Euler scheme The procedure uses the existing time-marching methods to complete the solution, in particular the Approximate Factorization and Alternating Direction Implicit techniques are implemented in the present work Finite differences written on stretched staggered grids provide for differencing the spatial differential operators appearing in the equations

Numerical examples performed on various geometries have shown that the performance of the method is consistently good The method was first validated by considering steady and unsteady flow problems, namely steady flow inside a square cavity with a moving lid and over a backward-facing step, and unsteady flow between oscillating parallel plates and inside a square cavity with an oscillating lid.

The method has proven to have a very high computational efficiency, combined with good accuracy. For example, the test example devoted to the two-dimensional flow over a backward-facing step took a little more than one hour to run on a PC (equiped with an Alacron i860 co-computer board), compared with the same problem treated by Gartling on a similar grid which took one hour per iteration on a Cray XMP.

The method was then applied to unsteady annular flow problems, both for two- and three-dimensional geometries.

A hybrid finite difference/Fourier expansion procedure has been developed in order to obtain the flow solutions with an even better computing efficiency; typically three-dimensional problems were solved with computational times comparable with two-dimensional problems (a three-dimensional mesh indeed reduces to a two-dimensional one). The performance of the method was established by integrating the three-dimensional full non-linear Navier-Stokes equations, as well as the equations obtained from the hybrid finite difference/Fourier expansion method, in geometries with uniform cross-section or with annular backstep where the outer cylinder was oscillating.

Finally, the hybrid finite difference/Fourier expansion method has been used in conjunction with a method for integrating the equations determining the dynamical behavior of an annular flow system, and this allowed to perform the fluid-structure stability analysis of this system; to the author's best knowledge, this has been the first attempt to perform the simultaneous integration of the Navier-Stokes equations for the unsteady fluid flow and the equations of motion of the structure. A fourth-order Runge-Kutta scheme was employed to integrate the equation of the structure under the combined action of mechanical forces (composed of a restraining spring and dashpot) and fluid forces, the latter being determined from the time-integration of the Navier-Stokes equations. This study has been rendered

possible because of the efficient hybrid finite difference/Fourier expansion method, and the temporal evolution of the motion of the structure thus obtained allowed for assessing the stability of the structure.

Bibliography

[1] M. P. Païdoussis 1980. Flow-induced vibrations in nuclear reactors and heat exchangers: Practical experiences and state of knowledge. In *Practical Experiences with Flow-Induced Vibration* (eds E. Naudascher and D. Rockwell), pp. 1-81, Berlin: Springer-Verlag.

[2] M. P Païdoussis 1987. Flow-induced instabilities of cylindrical structures. *Applied Mechanics Reviews* **40**, 163-175

[3] D. E. Hobson 1984. Instabilities of the AGR fuel assembly during on-load refuelling. In *Proceedings of the ASME Symposium on Flow-Induced Vibrations* (eds M. P. Paidoussis and M. K. Au-Yang), Vol. 4, pp. 25-40.

[4] D. E. Hobson 1982. Fluid-elastic instabilities caused by flow in an annulus. In Proceedings *Third Keswick International Conference*, pp. 440-463.

[5] D. Mateescu and M. P. Païdoussis 1985. The unsteady potential in an axially variable annulus and its effect on the dynamics of the rigid centre-body. *Journal of Fluids Engineering* **107**, 421-427.

[6] D. Mateescu and M. P. Païdoussis 1985. Unsteady viscous effects on the annular-flow-induced instabilities of a rigid cylindrical body in a narrow duct. *Journal of Fluids and Structures* **1**, 197-215.

[7] D. Mateescu, M. P. Païdoussis and F. Bélanger 1989. A theoretical model compared with experiments for the unsteady pressure on a cylinder oscillating in turbulent annular flow. *Journal of Sound and Vibration* **135**, 487-498

[8] D. Mateescu, M. P. Païdoussis and F. Bélanger 1989. The unsteady pressure on a cylinder oscillating in annular flow — a theoretical model compared with experiments. In *Flow-Induced Vibration* (eds M.K Au-Yang et al), pp 85-92. ASME: New-york.

[9] D. Mateescu, M. P. Païdoussis and F. Bélanger 1988 Unsteady pressure measurements on an oscillating cylinder in annular flow. *Journal of Fluids and Structures* **2**, 615-628.

[10] D. Mateescu, M. P. Païdoussis and F. Bélanger 1988. Experiments on the unsteady annular flow around an oscillating cylinder. AIAA Paper 88-2031, in Proceedings of the *AIAA 15th Aerodynamic Testing Conference*, San Diego, Cal., pp. 282-292.

[11] A. J. Chorin 1967. A numerical method for solving incompressible viscous flow problems. *Journal of Computational Physics* **2**, 12-26.

[12] F. H. Harlow and J. E. Welch 1965. Numerical computation of time-dependent viscous incompressible flow of fluid with free surface *Physics of Fluids* **8**, 2182- 2189

[13] A. J. Chorin 1968. Numerical solution of the Navier-Stokes equations *Mathematics of Computation*, **22**, 745-762.

[14] R. Temam 1969. Sur l'approximation de la solution des équations de Navier-Stokes par la méthode des pas fractionnaires. *Archive for Rational Mechanics and Analysis* **33**, 377-385

[15] N. N. Yanenko 1971. *The Method of Fractional Steps*, New York: Springer Verlag.

[16] W Y. Soh and J. W. Goodrich 1988. Unsteady solution of incompressible Navier-Stokes equations. *Journal of Computational Physics* **79**, 113-134.

[17] W. Y. Soh 1987. Time-marching solution of incompressible Navier-Stokes equations for internal flows. *Journal of Computational Physics* **70**, 232-252.

[18] D. Mateescu, M. P. Païdoussis and F. Bélanger 1991. Computational Solutions based on a finite difference formulation for unsteady internal flows. *29th Aerospace Sciences Meeting*, Reno, Nevada; AIAA Paper 91-0724.

[19] M. P. Païdoussis, D. Mateescu and W.-G. Sim 1990. Dynamics and stability of a flexible cylinder in a narrow coaxial cylindrical duct subjected to annular flow. *Journal of Applied Mechanics* **57**, pp. 232-240.

[20] F. Bélanger 1987. Experiments on the unsteady pressure generated by oscillation of a cylinder in a duct with annular flow. *Master's thesis*, McGill University, Montreal.

[21] H. Schlichting 1979. *Boundary layer theory.* New York: McGraw-Hill, seventh edition.

[22] D. A Anderson, J. C. Tannehill and R. H. Pletcher 1984. *Computational Fluid Mechanics and Heat Transfer.* New York: McGraw Hill.

[23] Ch. Hirsch 1988. *Numerical Computation of Internal and External Flow*, Vol. 1. New York. John Wiley & Sons.

[24] R. M. Beam and R. F. Warming 1978. An implicit factored scheme for the compressible Navier-Stokes equations. *AIAA Journal* **16**, 393-402.

[25] M. Vinokur 1983. On one-dimensional sretching functions foı finite-difference calculations. *Journal of Computatıonel Physıcs* **50**, 216-234

[26] J. F. Thompson, Z. U. A. Warsi and C. W. Mastin 1985 *Numerical Grid Generation: Foundations and Applications*. New York: North-Holland Elsevier.

[27] T. H. Pulliam and J. L. Steger 1980. Implicit finite-difference simulations of three-dimensional compressible flow *AIAA Journal* **18**, pp. 159-167

[28] D.K. Gartling 1990. A test problem for outflow boundary conditions Flow over a backward-facing step. *International Journal for Numerical Methods in Fluids* **11**, 953-967.

[29] C. Benocci, P. Bellomi and V. Michelassi 1987 Comparison of Cartesian and curvilinear grids for incompressible flow around steps. *Numerical Methods in Laminar and Turbulent Flows*, Vol **5**, Part 1, pp 584-594, Eds C Taylor, W.G. Habashi and M.M Hafez, *Pineridge Press, Swansea, U.K.*

[30] J. W Cooley, P. A. W. Lewis and P. D. Welch 1969. The Finite Fourier Transform. *IEEE Transactions on Audio and Electroacoustics*, pp 77-85

[31] Z.U.A. Warsi 1981. Conservation form of the Navier-Stokes equations in general nonsteady coordinates. *AIAA Journal* **19**, 240-242

[32] P.D. Thomas and C.K. Lombard 1979 Geometric conservation law and its application to flow computations on moving grids. *AIAA Journal* **17**, 1030-1037.

[33] C. Temperton 1975. Algorithms for the solution of cyclic tridiagonal systems *Journal of Computational Physics* **19**, 317-323.

[34] J. N. Reddy and R. M. Rasmussen 1984. *Advanced engineering analysis.* McGraw-Hill.

[35] W. T Thomson 1981. *Theory of vibration with applications*, Second Edition. Prentice-Hall, Inc., Englewood Cliffs, N.J.

[36] F. Axisa 1990. Effets dissipatifs linéaires d'un fluide en absence d'écoulement permanent. *Notes de cours au DEA*, CEN Saclay, France.

[37] F Bélanger and E. de Langre 1990. Forces fluide-elastiques associées à une structure vibrant dans un écoulement potentiel. *Rapport DMT/90.397*, Commissariat à l'Energie Atomique français.

[38] R.-J. Gibert 1988. *Vibrations des structures*, Éditions Eyrolles, Paris.

[39] H. Esmonde, J. A. Fitzpatrick, H. J. Rice and F. Axisa 1990. Analysis of non-linear squeeze film dynamics – Part I: Physical theory and modelling. *ASME PVP Conference* , Nashville.

[40] H. Esmonde, J A Fitzpatrick, H. J. Rice and F. Axisa 1990. Analysis of non-linear squeeze film dynamics – Part II: Experimental measurement and model verification. *ASME PVP Conference*, Nashville.

[41] E Kreyszig 1964. *Differential geometry.* University of Toronto Press.

Appendix A

Discretization of 3D Linearized Solution

The staggered mesh used to discretize equations (6.41–6.52) is shown in Figure A.1. It is a two-dimensional grid spanning the axial and radial directions, z and r, and it is generally stretched in both directions either to concentrate points near solid walls or in regions of strong discontinuity in flow domain geometry, such as in the vicinity of a step, see Figure 4.1, page 45. The velocity components $\hat{u}_{i,j}$ and $\hat{v}_{i,j}$ are defined at the grid points (x_i^u, r_j^u) and (x_i^v, r_j^v), respectively, whereas the pressure $\hat{p}_{i,j}$ is defined at the grid point (x_i^v, r_j^u); in this work we have elected to define $\hat{w}_{i,j}$ at the same point as $\hat{p}_{i,j}$, namely at (x_i^v, r_j^u), which we will see is convenient for the present method. Then, the axial, radial and circumferential momentum equations and the continuity one are differenced about the points where $\hat{u}_{i,j}$, $\hat{v}_{i,j}$, $\hat{w}_{i,j}$ and $\hat{p}_{i,j}$ are defined, respectively. Subscripts 0 or 1 have been omitted. Equations (6.56–6.59) are thus discretized on the staggered grid as follows, where we have dropped the superscript ν to simplify the notation. First the term $(G_u)_{i(i,j)}$ is

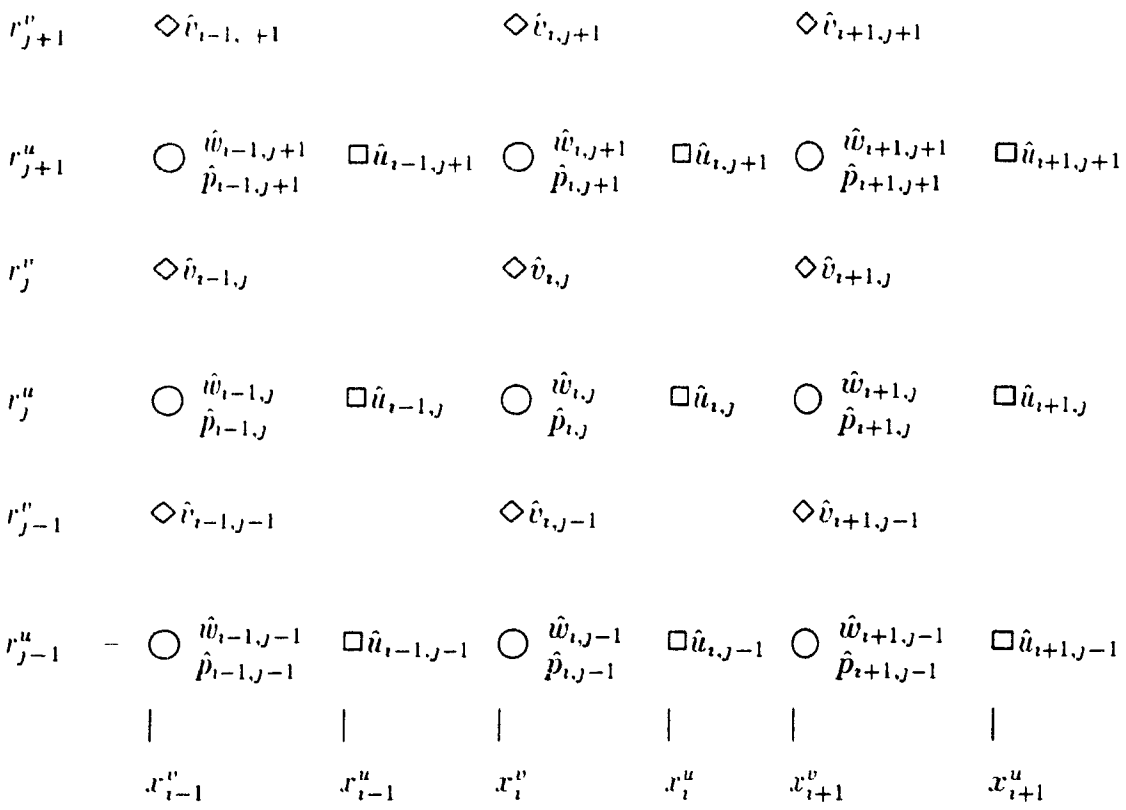

Figure A.1: Schematic representation of the staggered grid used in the spatial discretization of the three-dimensional linearized equations.

$$
\begin{aligned}
(\hat{G}_u)_{1(i,j)} \;=\; & \frac{1}{\Delta x^u_i}\Bigg[2\left(\hat{u}^{x+}_{0u}\,\hat{u}^{x+}_{1u} - \hat{u}^{x-}_{0u}\,\hat{u}^{x-}_{1u}\right) \\
& + \hat{p}_{1(i+1,j)} - \hat{p}_{1(i,j)} - \frac{1}{Re}\left\{\frac{\hat{u}_{1(i+1,j)} - \hat{u}_{1(i,j)}}{\Delta x^v_{i+1}} - \frac{\hat{u}_{1(i,j)} - \hat{u}_{1(i-1,j)}}{\Delta x^v_i}\right\}\Bigg] \\
& + \frac{1}{r^u_j\,\Delta r^u_j}\Bigg[r^v_j\left(\hat{v}^{r+}_{0u}\,\hat{u}^{r+}_{1u} + \hat{v}^{r+}_{1u}\,\hat{u}^{r+}_{0u}\right) - r^v_{j-1}\left(\hat{v}^{r-}_{0u}\,\hat{u}^{r-}_{1u} + \hat{v}^{r-}_{1u}\,\hat{u}^{r-}_{0u}\right) \\
& - \frac{1}{Re}\left\{\frac{r^v_j}{\Delta r^v_j}\left(\hat{u}_{1(i,j+1)} - \hat{u}_{1(i,j)}\right) - \frac{r^v_{j-1}}{\Delta r^v_{j-1}}\left(\hat{u}_{1(i,j)} - \hat{u}_{1(i,j-1)}\right)\right\}\Bigg] \\
& - \frac{\hat{w}_{1u}\,\hat{u}_{0(i,j)}}{r^u_j} + \frac{1}{Re\,(r^u_j)^2}\,\hat{u}_{1(i,j)}\,,
\end{aligned}
\tag{A.1}
$$

where the interpolates are defined, omitting subscripts 0 or 1, as

$$\hat{u}_u^{x+} = \frac{\nabla x_{i+1}^u \, \hat{u}_{i,j} + \nabla x_{i+1}^v \, \hat{u}_{i+1,j}}{\Delta x_{i+1}^v} \quad , \qquad \hat{u}_u^{x-} = \frac{\nabla x_i^u \, \hat{u}_{i-1,j} + \nabla x_i^v \, \hat{u}_{i,j}}{\Delta x_i^v}$$

$$\hat{u}_u^{r+} = \frac{\nabla r_{j+1}^u \, \hat{u}_{i,j} + \nabla r_j^v \, \hat{u}_{i,j+1}}{\Delta r_j^v} \quad , \qquad \hat{u}_u^{r-} = \frac{\nabla r_j^u \, \hat{u}_{i,j-1} + \nabla r_{j-1}^v \, \hat{u}_{i,j}}{\Delta r_{j-1}^v}$$

$$\hat{v}_u^{r+} = \frac{\nabla x_{i+1}^v \, \hat{v}_{i,j} + \nabla x_i^u \, \hat{v}_{i+1,j}}{\Delta x_i^u} \quad , \qquad \hat{v}_u^{r-} = \frac{\nabla x_{i+1}^v \, \hat{v}_{i,j-1} + \nabla r_i^u \, \hat{v}_{i+1,j-1}}{\Delta x_i^u}$$

$$\hat{w}_u = \frac{\nabla x_{i+1}^v \, \hat{w}_{i,j} + \nabla x_i^u \, \hat{w}_{i+1,j}}{\Delta x_i^u} \, .$$

The term $(\hat{G}_v)_{1(i,j)}$ is then given by

$$\begin{aligned}
(\hat{G}_v)_{1(i,j)} \;=\; & \frac{1}{\Delta x_i^v} \left[\hat{u}_{0v}^{x+} \, \hat{v}_{1v}^{x+} - \hat{u}_{0v}^{x-} \, \hat{v}_{1v}^{x-} + \hat{u}_{1v}^{x+} \, \hat{v}_{0v}^{x+} - \hat{u}_{1v}^{x-} \, \hat{v}_{0v}^{x-} \right. \\
& \left. - \frac{1}{Re} \left\{ \frac{\hat{v}_{1(i+1,j)} - \hat{v}_{1(i,j)}}{\Delta x_i^u} - \frac{\hat{v}_{1(i,j)} - \hat{v}_{1(i-1,j)}}{\Delta x_{i-1}^u} \right\} \right] \\
& + \frac{1}{r_j^v \, \Delta r_j^v} \left[2 \left(r_{j+1}^u \, \hat{v}_{0v}^{r+} \, \hat{v}_{1v}^{r+} - r_j^u \, \hat{v}_{0v}^{r-} \, \hat{v}_{1v}^{r-} \right) \right. \\
& \left. - \frac{1}{Re} \left\{ \frac{r_{j+1}^u}{\Delta r_{j+1}^u} \left(\hat{v}_{1(i,j+1)} - \hat{v}_{1(i,j)} \right) - \frac{r_j^u}{\Delta r_j^u} \left(\hat{v}_{1(i,j)} - \hat{v}_{1(i,j-1)} \right) \right\} \right] \\
& - \frac{\hat{w}_{1v} \, \hat{v}_{0(i,j)}}{r_j^v} + \frac{\hat{p}_{1(i,j+1)} - \hat{p}_{1(i,j)}}{\Delta r_j^v} + \frac{2}{Re \, (r_j^v)^2} \left(\hat{v}_{1(i,j)} - \hat{w}_{1v} \right) \, . \qquad \text{(A 2)}
\end{aligned}$$

in which the interpolates are obtained as

$$\hat{v}_v^{x+} = \frac{\nabla x_{i+1}^v \, \hat{v}_{i,j} + \nabla x_i^u \, \hat{v}_{i+1,j}}{\Delta x_i^u} \quad , \qquad \hat{v}_v^{x-} = \frac{\nabla x_i^v \, \hat{v}_{i-1,j} + \nabla x_{i-1}^u \, \hat{v}_{i,j}}{\Delta x_{i-1}^u}$$

$$\hat{v}_v^{r+} = \frac{\nabla r_{j+1}^v \, \hat{v}_{i,j} + \nabla r_{j+1}^u \, \hat{v}_{i,j+1}}{\Delta r_{j+1}^u} \quad , \qquad \hat{v}_v^{r-} = \frac{\nabla r_j^v \, \hat{v}_{i,j-1} + \nabla r_j^u \, \hat{v}_{i,j}}{\Delta r_j^u}$$

$$\hat{u}_v^{x+} = \frac{\nabla r_{j+1}^u \, \hat{u}_{i,j} + \nabla r_j^v \, \hat{u}_{i,j+1}}{\Delta r_j^v} \quad , \qquad \hat{u}_v^{x-} = \frac{\nabla r_{j+1}^u \, \hat{u}_{i-1,j} + \nabla r_j^v \, \hat{v}_{i-1,j+1}}{\Delta r_j^v}$$

$$\hat{w}_v = \frac{\nabla r_{j+1}^u \, \hat{w}_{i,j} + \nabla r_j^v \, \hat{w}_{i,j+1}}{\Delta r_j^v} \, ,$$

whereas $(\hat{G}_w)_{1(i,j)}$ is computed by the following formula:

$$\begin{aligned}
(\hat{G}_w)_{1(i,j)} &= \frac{1}{\Delta x_i^v} \left[\hat{u}_{0(i,j)} \, \hat{w}_{1w}^{x+} - \hat{u}_{0(i-1,j)} \, \hat{w}_{1w}^{x-} \right. \\
&- \left. \frac{1}{Re} \left(\frac{\hat{w}_{1(i+1,j)} - \hat{w}_{1(i,j)}}{\Delta x_i^u} - \frac{\hat{w}_{1(i,j)} - \hat{w}_{1(i-1,j)}}{\Delta x_{i-1}^u} \right) \right] \\
&+ \frac{1}{r_j^u \, \Delta r_j^u} \left[r_j^v \, \hat{v}_{0(i,j)} \, \hat{w}_{1w}^{r+} - r_{j-1}^v \, \hat{v}_{0(i,j-1)} \, \hat{w}_{1w}^{r-} \right. \\
&- \left. \frac{1}{Re} \left\{ \frac{r_j^v}{\Delta r_j^v} \left(\hat{w}_{1(i,j+1)} - \hat{w}_{1(i,j)} \right) - \frac{r_{j-1}^v}{\Delta r_{j-1}^v} \left(\hat{w}_{1(i,j)} - \hat{w}_{1(i,j-1)} \right) \right\} \right] \\
&+ \frac{\hat{v}_{0w} \, \hat{w}_{1(i,j)} + \hat{p}_{1(i,j)}}{r_j^u} + \frac{2}{Re \, (r_j^u)^2} \left(\hat{w}_{1(i,j)} - \hat{v}_{1w} \right) \, . \qquad \text{(A.3)}
\end{aligned}$$

with the interpolates being given by

$$\begin{aligned}
\hat{w}_w^{x+} &= \frac{\nabla x_{i+1}^v \, \hat{w}_{i,j} + \nabla x_i^u \, \hat{w}_{i+1,j}}{\Delta x_i^u} \, , \qquad \hat{w}_w^{x-} = \frac{\nabla x_i^v \, \hat{w}_{i-1,j} + \nabla x_{i-1}^u \, \hat{w}_{i,j}}{\Delta x_{i-1}^u} \\
\hat{w}_w^{r+} &= \frac{\nabla r_{j+1}^u \, \hat{w}_{i,j} + \nabla r_j^v \, \hat{w}_{i,j+1}}{\Delta r_j^v} \, , \qquad \hat{w}_w^{r-} = \frac{\nabla r_j^u \, \hat{w}_{i,j-1} + \nabla r_{j-1}^v \, \hat{w}_{i,j}}{\Delta r_{j-1}^v} \\
\hat{v}_w &= \frac{\nabla r_j^v \, \hat{v}_{i,j-1} + \nabla r_j^u \, \hat{v}_{i,j}}{\Delta r_j^u} \, .
\end{aligned}$$

Finally, we obtain for $(\nabla \cdot \hat{\mathbf{V}})_{1(i,j)}$

$$(\nabla \cdot \hat{\mathbf{V}})_{1(i,j)} = \frac{\hat{u}_{1(i,j)} - \hat{u}_{1(i-1,j)}}{\Delta x_i^v} + \frac{r_j^v \, \hat{v}_{1(i,j)} - r_{j-1}^v \, \hat{v}_{1(i,j-1)}}{r_j^u \, \Delta r_j^u} - \frac{\hat{w}_{1(i,j)}}{r_j^u} \, . \qquad \text{(A.4)}$$

As in Chapter 4 for Cartesian coordinates, Δ and ∇ denote the central and backward difference operators applied to the grid point coordinates. They are defined by

$$\Delta x_i^u = x_{i+1}^v - x_i^v \,, \qquad \Delta x_i^v = x_i^u - x_{i-1}^u \,,$$
$$\Delta r_j^u = r_j^v - r_{j-1}^v \,, \qquad \Delta r_j^v = r_{j+1}^u - r_j^u \,,$$
$$\nabla x_i^u = x_i^u - x_i^v \,, \qquad \nabla x_i^v = x_i^v - x_{i-1}^u \,,$$
$$\nabla r_j^u = r_j^u - r_{j-1}^v \,, \qquad \nabla r_j^v = r_j^v - r_j^u \,.$$

As also was the case in Cartesian coordinates, the evaluation of the viscous derivative terms $(1/r)(\partial/\partial r)(r\,\partial\hat{u}_1/\partial r)$ and $(1/r)(\partial/\partial r)(r\,\partial\hat{w}_1/\partial r)$ near the outer or inner cylinder wall requires special treatment. Referring to Figure A.2, it is done as follows near the inner cylinder wall,

$$\frac{\partial}{r\,\partial r}\left(r\,\frac{\partial\hat{u}_1}{\partial r}\right)_{r=r_2^u} = \frac{1}{r_2^u\,\Delta r_2^u}\left[r_2^v\left(\frac{\hat{u}_{1(i,3)}-\hat{u}_{1(i,2)}}{\Delta r_2^v}\right) - r_1^v\left(\frac{\frac{8}{3}\,\hat{u}_{1(i,w)}-3\,\hat{u}_{1(i,2)}+\frac{1}{3}\,\hat{u}_{1(i,3)}}{\frac{8}{3}\,r_1^v-3\,r_2^u+\frac{1}{3}\,r_3^u}\right)\right] ,$$

$$\frac{\partial}{r\,\partial r}\left(r\,\frac{\partial\hat{w}_1}{\partial r}\right)_{r=r_2^u} = \frac{1}{r_2^u\,\Delta r_2^u}\left[r_2^v\left(\frac{\hat{w}_{1(i,3)}-\hat{w}_{1(i,2)}}{\Delta r_2^v}\right) - r_1^v\left(\frac{\frac{8}{3}\,\hat{w}_{1(i,w)}-3\,\hat{w}_{1(i,2)}+\frac{1}{3}\,w_{1(i,3)}}{\frac{8}{3}\,r_1^v-3\,r_2^u+\frac{1}{3}\,r_3^u}\right)\right] ,$$

where $\hat{u}_{1(i,w)}$ and $\hat{w}_{1(i,w)}$ are the wall velocity boundary conditions. Similar expressions apply for the evaluation of the derivatives near the outer cylinder wall, or near a vertical wall in a plane of constant x such as in a region of discontinuity in the annular space.

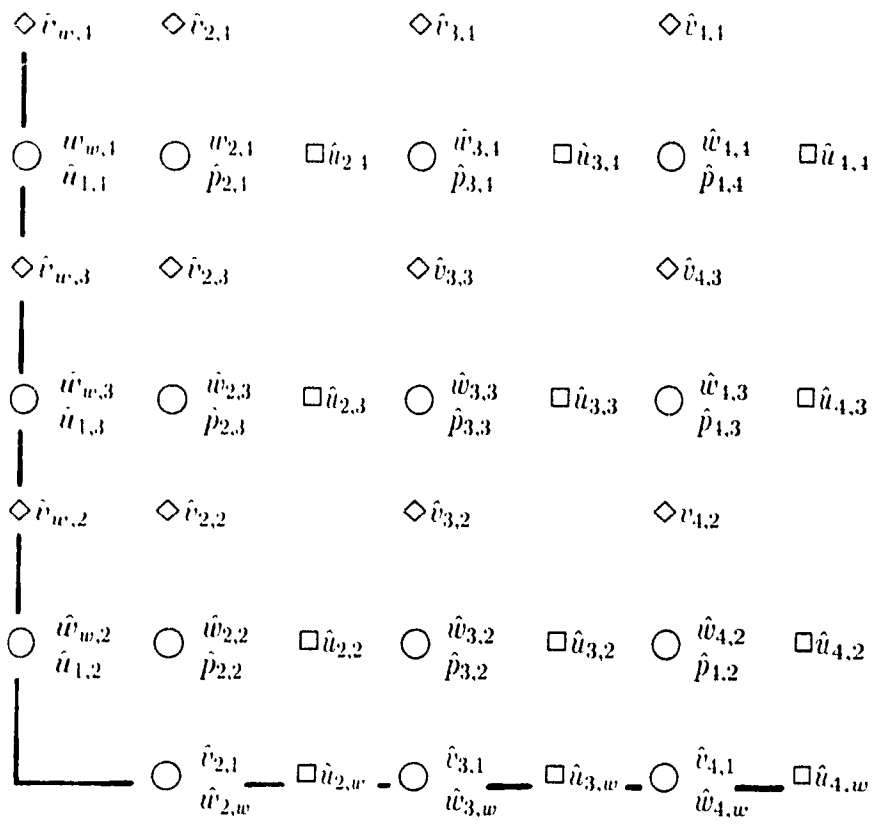

Figure A 2. Evaluation of viscous derivatives near solid walls, where $\hat{u}_{i,w}$, $\hat{v}_{w,j}$, $\hat{w}_{i,w}$ and $\hat{w}_{w,j}$ have been defined.

Now, the solution of (6.41–6.52) proceeds as follows, after introducing difference expressions like those of equations (A.1–A.4) in the left-hand sides of (6.41-6.52). In the x-sweep, $\widetilde{\Delta\hat{v}}_1$ and $\widetilde{\Delta\hat{w}}_1$ are obtained from equations (6.42) and (6.43), respectively, and $\widetilde{\Delta\hat{u}}_1$ is obtained from (6.41) after eliminating $\widetilde{\Delta\hat{p}}_1$ with the aid of (6.44). Scalar tridiagonal systems of equations have to be inverted as is shown in Chapter 4. A similar procedure applies in the r-sweep, equations (6.45-6.48).

When it comes to solving the θ-sweep equations (6.49-6.52), we see first that it can be done without inverting systems of equations as no derivatives appear

in the left-hand sides of equations (6.49-6.52); this is a benefit of the Galerkin procedure. So after $\Delta\hat{u}_1$ and $\Delta\hat{v}_1$ have been obtained algebraically from (6.49) and (6.50), the expression from (6.52) for $\Delta\hat{p}_1$ is substituted in (6.51) which is then solved for $\Delta\hat{w}_1$. It is to be realized that this last step is made easy when $(\hat{w}_1)_{i,j}$ and $(\hat{p}_1)_{i,j}$ are defined at the same location in the staggered grid, which we have elected to do in the present work.

Appendix B

Discretization of 2D Nonlinear Solution

The staggered mesh used to discretize (7.1–7.9) is shown in Figure B.1. The grid has uniform spacing $\Delta\theta$ in the circumferential direction θ and is stretched in the radial direction r in order to concentrate more points near the cylinder walls. The velocity components $v_{j,k}$ and $w_{j,k}$ are defined at the grid points (r_j^v, θ_k^v) and (r_j^w, θ_k^w), whereas the pressure $p_{j,k}$ is defined at the point (r_j^w, θ_k^v). Moreover, the r- and θ-momentum and continuity equations are differenced about the points where $v_{j,k}$, $w_{j,k}$ and $p_{j,k}$ are defined, respectively. Equations (7.1–7.9) are thus discretized on the staggered grid in the form:

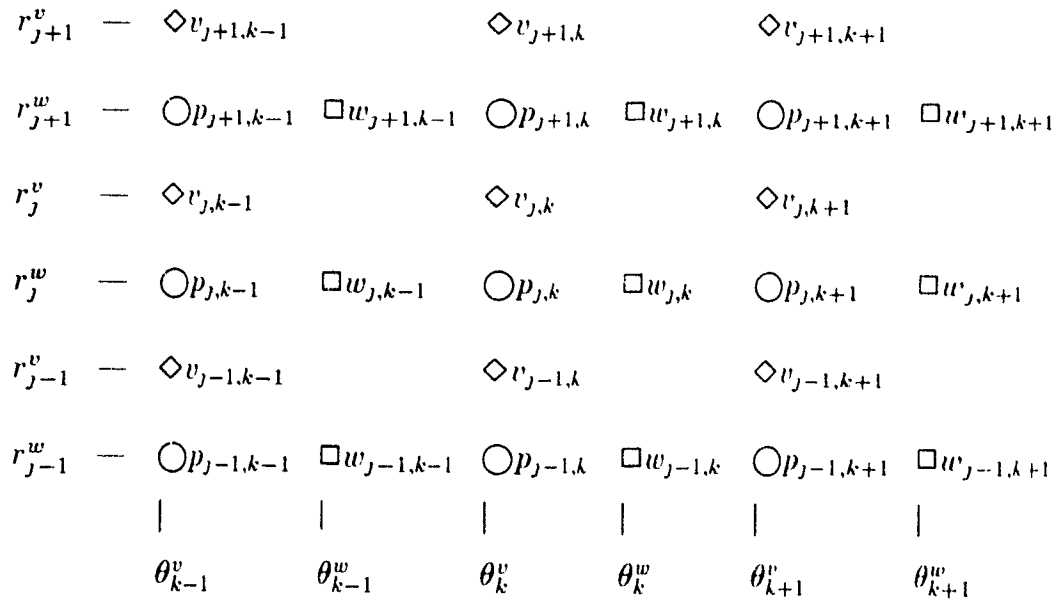

Figure B.1: Schematic representation of the staggered grid used to discretize the two-dimensional non-linear unsteady annular flow equations.

$$
\begin{aligned}
(G_v)_{j,k} \;=\; & \frac{1}{r^v_j\,\Delta r^v_j}\left[r^w_{j+1}\,(v^{r+}_v)^2 - r^w_j\,(v^{r-}_v)^2 \right. \\
& \left. - \frac{1}{Re}\left\{ \frac{r^w_{j+1}}{\Delta r^w_{j+1}}\,(v_{j+1,k} - v_{j,k}) - \frac{r^w_j}{\Delta r^w_j}\,(v_{j,k} - v_{j-1,k}) \right\} \right] \\
& + \frac{p_{j+1,k} - p_{j,k}}{\Delta r^v_j} + \frac{1}{r^v_j}\left[\frac{w^{\theta+}_v\, v^{\theta+}_v - w^{\theta-}_v\, v^{\theta-}_v}{\Delta\theta} - (w_v)^2 \right] \\
& - \frac{1}{Re\,(r^v_j)^2}\left[\frac{v_{j,k+1} + v_{j,k-1} - 2\,v_{j,k}}{(\Delta\theta)^2} - 2\,\frac{w^{\theta+}_v - w^{\theta-}_v}{\Delta\theta} - v_{j,k} \right] \qquad \text{(B.1)}
\end{aligned}
$$

$$
\begin{aligned}
(G_w)_{j,k} &= \frac{1}{r_j^w\,\Delta r_j^w}\left[r_j^v\, v_w^{r+} w_w^{r+} - r_{j-1}^v\, v_w^{r-} w_w^{r-}\right.\\
&- \left.\frac{1}{Re}\left\{\frac{r_j^v}{\Delta r_j^v}\,(w_{j+1,k}-w_{j,k}) - \frac{r_{j-1}^v}{\Delta r_{j-1}^v}\,(w_{j,k}-w_{j-1,k})\right\}\right]\\
&+ \frac{1}{r_j^w}\left[\frac{(w_w^{\theta+})^2-(w_w^{\theta-})^2+p_{j,k+1}-p_{j,k}}{\Delta\theta} + v_w\, w_{j,k}\right]\\
&- \frac{1}{Re\,(r_j^w)^2}\left[\frac{w_{j,k+1}+w_{j,k-1}-2\,w_{j,k}}{(\Delta\theta)^2} + 2\,\frac{v_w^{\theta+}-v_w^{\theta-}}{\Delta\theta} - w_{j,k}\right] \qquad \text{(B.2)}
\end{aligned}
$$

$$
(\nabla\cdot\mathbf{V})_{j,k} = \frac{r_j^v\, v_{j,k} - r_{j-1}^v\, v_{j-1,k}}{r_j^w\,\Delta r_j^w} + \frac{w_{j,k}-w_{j,k-1}}{r_j^w\,\Delta\theta}\,. \qquad \text{(B.3)}
$$

The linear interpolates of the velocity components on the staggered mesh are defined by

$$
v_v^{r+} = \frac{\nabla r_{j+1}^v\, v_{j,k} + \nabla r_{j+1}^w\, v_{j+1,k}}{\Delta r_{j+1}^w}\,, \qquad v_v^{r-} = \frac{\nabla r_j^v\, v_{j-1,k} + \nabla r_j^w\, v_{j,k}}{\Delta r_j^w}
$$

$$
v_v^{\theta+} = \frac{v_{j,k}+v_{j,k+1}}{2}\,, \qquad v_v^{\theta-} = \frac{v_{j,k}+v_{j,k-1}}{2}
$$

$$
v_w^{r+} = \frac{v_{j,k}+v_{j,k+1}}{2}\,, \qquad v_w^{r-} = \frac{v_{j-1,k}+v_{j-1,k+1}}{2}
$$

$$
v_w^{\theta+} = \frac{\nabla r_j^v\, v_{j-1,k+1} + \nabla r_j^w\, v_{j,k+1}}{\Delta r_j^w}\,, \qquad v_w^{\theta-} = \frac{\nabla r_j^v\, v_{j-1,k} + \nabla r_j^w\, v_{j,k}}{\Delta r_j^w}
$$

$$
w_v^{\theta+} = \frac{\nabla r_{j+1}^w\, w_{j,k} + \nabla r_j^v\, w_{j+1,k}}{\Delta r_j^v}\,, \qquad w_v^{\theta-} = \frac{\nabla r_{j+1}^w\, w_{j,k-1} + \nabla r_j^v\, w_{j+1,k-1}}{\Delta r_j^v}
$$

$$
w_w^{r+} = \frac{\nabla r_{j+1}^w\, w_{j,k} + \nabla r_j^v\, w_{j+1,k}}{\Delta r_j^v}\,, \qquad w_w^{r-} = \frac{\nabla r_j^w\, w_{j-1,k} + \nabla r_{j-1}^v\, w_{j,k}}{\Delta r_{j-1}^v}
$$

$$w_w^{\theta+} = \frac{w_{j,k+1} + w_{j,k}}{2} \quad , \qquad w_w^{\theta-} = \frac{w_{j,k} + w_{j,k-1}}{2}$$

$$v_w = \frac{1}{2}\left[\frac{\nabla r_j^v}{\Delta r_j^w}\left(v_{j-1,k} + v_{j-1,k+1}\right) + \frac{\nabla r_j^w}{\Delta r_j^w}\left(v_{j,k} + v_{j,k+1}\right)\right]$$

$$w_v = \frac{1}{2}\left[\frac{\nabla r_j^v}{\Delta r_j^v}\left(w_{j+1,k} + w_{j+1,k-1}\right) + \frac{\nabla r_{j+1}^w}{\Delta r_j^v}\left(w_{j,k} + w_{j,k-1}\right)\right]$$

As in Chapter 4 for Cartesian coordinates, Δ and ∇ denote the central and backward difference operators applied to the grid point coordinates. They are defined as

$$\begin{aligned} \Delta r_j^w &= r_j^v - r_{j-1}^v \,, & \Delta r_j^v &= r_{j+1}^w - r_j^w \,, \\ \nabla r_j^w &= r_j^w - r_{j-1}^v \,, & \nabla r_j^v &= r_j^v - r_j^w \,. \end{aligned} \tag{B.4}$$

As also was the case in Cartesian coordinates, the evaluation of the viscous derivative term $(1/r)(\partial/\partial r)(r\,\partial w/\partial r)$ near the the outer or inner cylinder wall requires special treatment. Referring to Figure B.2 it is done as follows, near the inner cylinder wall,

$$\begin{aligned} \frac{\partial}{r\,\partial r}\left(r\frac{\partial w}{\partial r}\right)_{r=r_2^w} &= \frac{1}{r_2^w\,\Delta r_2^w}\left[r_2^v\left(\frac{w_{3,k} - w_{2,k}}{\Delta r_2^v}\right)\right. \\ &\quad - \left. r_1^v\left(\frac{\frac{8}{3}\,w_{w,k} - 3\,w_{2,k} + \frac{1}{3}\,w_{3,k}}{\frac{8}{3}\,r_1^v - 3\,r_2^w + \frac{1}{3}\,r_3^w}\right)\right] \,, \end{aligned}$$

where $w_{w,k}$ is the wall velocity boundary condition which is given in terms of (7.16) and (7.17).

We note that in view of the symmetry of the domain and flow variables with respect to the plane of oscillation, the mesh is set up in the circumferential direction only between $\theta = 0$ and $\theta = \pi$ Symmetry boundary conditions apply

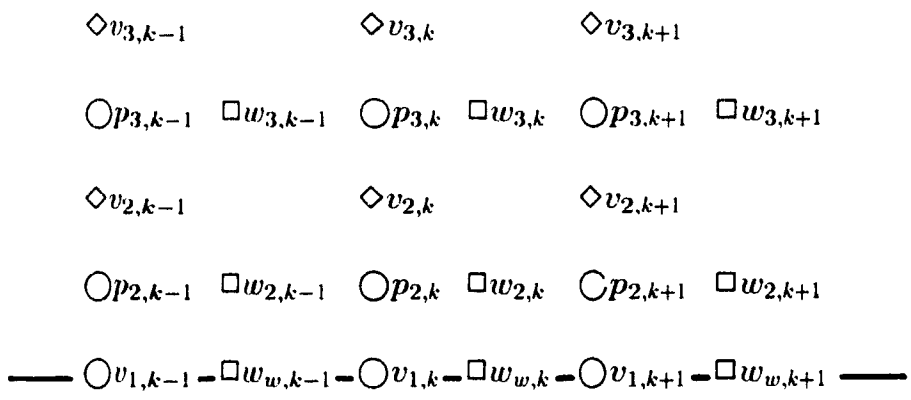

Figure B.2: Evaluation of viscous derivatives near the inner cylinder wall, where the quantity $w_{w,k}$ has been defined.

at $\theta = 0$ and $\theta = \pi$, namely, looking at Figure B.3, we have at $\theta = 0$ that $v_{j,2} = v_{j,3}$, $w_{j,1} = -w_{j,3}$ and $p_{j,2} = p_{j,3}$. Similar conditions apply at $\theta = \pi$.

The method of solution is then the following one. Difference expressions similar to (B.1–B.3) replace the differential operators in (7.1–7.6) and the expressions for the interpolates of the variables $\overline{\Delta v}$, $\overline{\Delta w}$, Δv and Δw are substituted therein. Equation (7.2) is then solved for $\overline{\Delta w}$ by inverting a scalar tridiagonal system of equations, and the pressure is eliminated from (7.1) with the aid of (7.3) to obtain $\overline{\Delta v}$ from (7.1), and then $\overline{\Delta p}$ from (7.3). A similar procedure applies in the θ-sweep for equations (7.4–7.6).

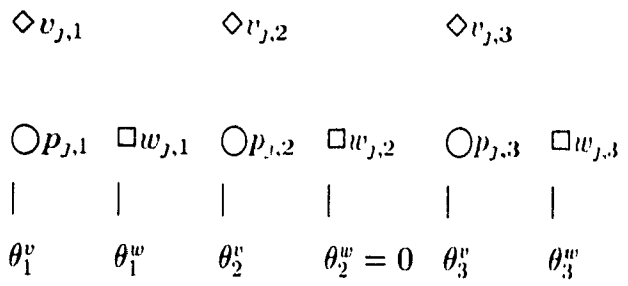

Figure B.3: Diagram showing the symmetry boundary conditions applied at $\theta = 0$

Appendix C

Discretization of 3D Nonlinear Solution

The staggered mesh used to solve the full non-linear three-dimensional Navier-Stokes equations (6.9–6.20) is a combination of the meshes shown in Figures A.1 and B.1. Indeed, the mesh is exactly like that depicted in Figure A.1 for the axial and radial directions, in which the velocity component $w_{i,j}$ is eliminated and we omit the hat symbol $\hat{}$ on the quantities; a third index, k, is added to the flow quantities u, v and p, denoting the circumferential direction. The mesh is also like that shown in Figure B.1 for the radial and circumferential directions, in which the index i is added to the flow quantities v, w and p to denote the axial direction. The three-dimensional mesh can thus be constructed by orthogonally joining the meshes of Figures A.1 and B.1, in which the points where $v_{i,j,k}$ and $p_{i,j,k}$ are defined are put in common.

The velocity component $u_{i,j,k}$ is defined at the grid point $(x_i^u, r_j^u, \theta_k^u)$, $v_{i,j,k}$ is defined at $(x_i^v, r_j^v, \theta_k^v)$, $w_{i,j,k}$ at $(x_i^v, r_j^u, \theta_k^w)$, and the pressure $p_{i,j,k}$ is defined at the grid point $(x_i^v, r_j^u, \theta_k^v)$. Moreover, the axial, radial and circumferential mo-

mentum equations and the continuity one are differenced about the points where $u_{i,j,k}$, $v_{i,j,k}$, $w_{i,j,k}$ and $p_{i,j,k}$ are defined, respectively. Equations (6.1 6.4) are thus discretized on the staggered grid as follows, where we have first for $G_u(u, v, w, p)$,

$$
\begin{aligned}
(G_u)_{i,j,k} &= \frac{1}{\Delta x_i^u}\left[u_u^{x+}\, u_u^{x+} - u_u^{x-}\, u_u^{x-} \right. \\
&+ \left. p_{i+1,j,k} - p_{i,j,k} - \frac{1}{Re}\left\{ \frac{u_{i+1,j,k} - u_{i,j,k}}{\Delta x_{i+1}^v} - \frac{u_{i,j,k} - u_{i-1,j,k}}{\Delta x_i^v} \right\} \right] \\
&+ \frac{1}{r_j^u\, \Delta r_j^u}\left[r_j^v v_u^{r+}\, u_u^{r+} - r_{j-1}^v v_u^{r-}\, u_u^{r-} \right. \\
&- \left. \frac{1}{Re}\left\{ \frac{r_j^v}{\Delta r_j^v}\left(u_{i,j+1,k} - u_{i,j,k}\right) - \frac{r_{j-1}^v}{\Delta r_{j-1}^v}\left(u_{i,j,k} - u_{i,j-1,k}\right) \right\} \right] \qquad \text{(C.1)} \\
&+ \frac{w_u^{\theta+}\, u_u^{\theta+} - w_u^{\theta-}\, u_u^{\theta-}}{r_j^u \Delta\theta} - \frac{u_{i,j,k+1} + u_{i,j,k-1} - 2\, u_{i,j,k}}{Re\,(r_j^u)^2 (\Delta\theta)^2}
\end{aligned}
$$

where the interpolates are defined by

$$
u_u^{x+} = \frac{\nabla x_{i+1}^u\, u_{i,j,k} + \nabla x_{i+1}^v\, u_{i+1,j,k}}{\Delta x_{i+1}^v} \quad , \qquad u_u^{x-} = \frac{\nabla x_i^u\, u_{i-1,j,k} + \nabla x_i^v\, u_{i,j,k}}{\Delta x_i^v}
$$

$$
u_u^{r+} = \frac{\nabla r_{j+1}^u\, u_{i,j,k} + \nabla r_j^v\, u_{i,j+1,k}}{\Delta r_j^v} \quad , \qquad u_u^{r-} = \frac{\nabla r_j^u\, u_{i,j-1,k} + \nabla r_{j-1}^v\, u_{i,j,k}}{\Delta r_{j-1}^v}
$$

$$
u_u^{\theta+} = \frac{1}{2}\left(u_{i,j,k+1} + u_{i,j,k}\right) \quad , \qquad u_u^{\theta-} = \frac{1}{2}\left(u_{i,j,k} + u_{i,j,k-1}\right)
$$

$$
v_u^{r+} = \frac{\nabla x_{i+1}^v\, v_{i,j,k} + \nabla x_i^u\, v_{i+1,j,k}}{\Delta x_i^u} \quad , \qquad v_u^{r-} = \frac{\nabla x_{i+1}^v\, v_{i,j-1,k} + \nabla x_i^u\, v_{i+1,j-1,k}}{\Delta x_i^u}
$$

$$
w_u^{\theta+} = \frac{\nabla x_i^u\, w_{i+1,j,k} + \nabla x_{i+1}^v\, w_{i,j,k}}{\Delta x_i^u} \quad , \qquad w_u^{\theta-} = \frac{\nabla x_i^u\, w_{i+1,j,k-1} + \nabla x_{i+1}^v\, w_{i,j,k-1}}{\Delta x_i^u}
$$

The term $G_v(u, v, w, p)$ is then given by

$$
\begin{aligned}
(G_v)_{i,j,k} \;=\; & \frac{1}{\Delta x_i^v}\left[u_v^{x+}\, v_v^{x+} - u_v^{x-}\, v_v^{x-} \right. \\
& \left. - \frac{1}{Re}\left\{ \frac{v_{i+1,j,k} - v_{i,j,k}}{\Delta x_i^u} - \frac{v_{i,j,k} - v_{i-1,j,k}}{\Delta x_{i-1}^u} \right\} \right] \\
& + \frac{1}{r_j^v\, \Delta r_j^v}\left[r_{j+1}^u\, (v_v^{r+})^2 - r_j^u\, (v_v^{r-})^2 \right. \\
& \left. - \frac{1}{Re}\left\{ \frac{r_{j+1}^u}{\Delta r_{j+1}^u}\,(v_{i,j+1,k} - v_{i,j,k}) - \frac{r_j^u}{\Delta r_j^u}\,(v_{i,j,k} - v_{i,j-1,k}) \right\} \right] \\
& + \frac{p_{i,j+1,k} - p_{i,j,k}}{\Delta r_j^v} + \frac{1}{r_j^v}\left[\frac{w_v^{\theta+}\, v_v^{\theta+} - w_v^{\theta-}\, v_v^{\theta-}}{\Delta\theta} - (w_v)^2 \right] \qquad \text{(C.2)} \\
& - \frac{1}{Re\,(r_j^v)^2}\left[\frac{v_{i,j,k+1} + v_{i,j,k-1} - 2\,v_{i,j,k}}{(\Delta\theta)^2} - 2\,\frac{w_v^{\theta+} - w_v^{\theta-}}{\Delta\theta} - v_{i,j,k} \right]
\end{aligned}
$$

in which the interpolates are obtained as

$$
v_v^{x+} = \frac{\nabla x_{i+1}^v\; v_{i,j,k} + \nabla x_i^u\; v_{i+1,j,k}}{\Delta x_i^u} \quad , \qquad v_v^{x-} = \frac{\nabla x_i^v\; v_{i-1,j,k} + \nabla x_{i-1}^u\; v_{i,j,k}}{\Delta x_{i-1}^u}
$$

$$
v_v^{r+} = \frac{\nabla r_{j+1}^v\; v_{i,j,k} + \nabla r_{j+1}^u\; v_{i,j+1,k}}{\Delta r_{j+1}^u} \quad , \qquad v_v^{r-} = \frac{\nabla r_j^v\; v_{i,j-1,k} + \nabla r_j^u\; v_{i,j,k}}{\Delta r_j^u}
$$

$$
v_v^{\theta+} = \frac{v_{i,j,k} + v_{i,j,k+1}}{2} \quad , \qquad v_v^{\theta-} = \frac{v_{i,j,k} + v_{i,j,k-1}}{2}
$$

$$
u_v^{x+} = \frac{\nabla r_{j+1}^u\; u_{i,j,k} + \nabla r_j^v\; u_{i,j+1,k}}{\Delta r_j^v} \quad , \qquad u_v^{x-} = \frac{\nabla r_{j+1}^u\; u_{i-1,j,k} + \nabla r_j^v\; u_{i-1,j+1,k}}{\Delta r_j^v}
$$

$$
w_v^{\theta+} = \frac{\nabla r_{j+1}^u\; w_{i,j,k} + \nabla r_j^v\; w_{i,j+1,k}}{\Delta r_j^v} \quad , \qquad w_v^{\theta-} = \frac{\nabla r_{j+1}^u\; w_{i,j,k-1} + \nabla r_j^v\; w_{i,j+1,k-1}}{\Delta r_j^v}
$$

$$w_v = \frac{1}{2}\left[\frac{\nabla r_j^v}{\Delta r_j^v}\left(w_{i,j+1,k} + w_{i,j+1,k-1}\right) + \frac{\nabla r_{j+1}^u}{\Delta r_j^v}\left(w_{i,j,k} + w_{i,j,k-1}\right)\right] ,$$

whereas $G_w(u, v, w, p)$ is computed by the following formula:

$$\begin{aligned}
(G_w)_{i,j,k} &= \frac{1}{\Delta x_i^v}\left[u_w^{x+}\, w_w^{x+} - u_w^{x-}\, w_w^{x-}\right. \\
&- \left.\frac{1}{Re}\left(\frac{w_{i+1,j,k} - w_{i,j,k}}{\Delta x_i^u} - \frac{w_{i,j,k} - w_{i-1,j,k}}{\Delta x_{i-1}^u}\right)\right] \\
&+ \frac{1}{r_j^u\, \Delta r_j^u}\left[r_j^v\, v_w^{r+} w_w^{r+} - r_{j-1}^v\, v_w^{r-} w_w^{r-}\right. \\
&- \left.\frac{1}{Re}\left\{\frac{r_j^v}{\Delta r_j^v}\left(w_{i,j+1,k} - w_{i,j,k}\right) - \frac{r_{j-1}^v}{\Delta r_{j-1}^v}\left(w_{i,j,k} - w_{i,j-1,k}\right)\right\}\right] \\
&+ \frac{1}{r_j^u}\left[\frac{(w_w^{\theta+})^2 - (w_w^{\theta-})^2 + p_{i,j,k+1} - p_{i,j,k}}{\Delta\theta} + v_w\, w_{i,j,k}\right] \qquad (C\text{-}3) \\
&- \frac{1}{Re\,(r_j^u)^2}\left[\frac{w_{i,j,k+1} + w_{i,j,k-1} - 2\, w_{i,j,k}}{(\Delta\theta)^2} + 2\,\frac{v_w^{\theta+} - v_w^{\theta-}}{\Delta\theta} - w_{i,j,k}\right] .
\end{aligned}$$

with the interpolates being given by

$$w_w^{x+} = \frac{\nabla x_{i+1}^v\, w_{i,j,k} + \nabla x_i^u\, w_{i+1,j,k}}{\Delta x_i^u} , \qquad w_w^{x-} = \frac{\nabla x_i^v\, w_{i-1,j,k} + \nabla x_{i-1}^u\, w_{i,j,k}}{\Delta x_{i-1}^u}$$

$$w_w^{r+} = \frac{\nabla r_{j+1}^u\, w_{i,j,k} + \nabla r_j^v\, w_{i,j+1,k}}{\Delta r_j^v} , \qquad w_w^{r-} = \frac{\nabla r_j^u\, w_{i,j-1,k} + \nabla r_{j-1}^v\, w_{i,j,k}}{\Delta r_{j-1}^v}$$

$$w_w^{\theta+} = \frac{w_{i,j,k+1} + w_{i,j,k}}{2} , \qquad w_w^{\theta-} = \frac{w_{i,j,k} + w_{i,j,k-1}}{2}$$

$$v_w^{r+} = \frac{v_{i,j,k} + v_{i,j,k+1}}{2} , \qquad v_w^{r-} = \frac{v_{i,j-1,k} + v_{i,j-1,k+1}}{2}$$

$$v_w^{\theta+} = \frac{\nabla r_j^u\, v_{i,j,k+1} + \nabla r_j^u\, v_{i,j-1,k+1}}{\Delta r_j^u} , \qquad v_w^{\theta-} = \frac{\nabla r_j^u\, v_{i,j,k} + \nabla r_j^v\, v_{i,j-1,k}}{\Delta r_j^u}$$

$$u_w^{x+} = \frac{u_{i,j,k} + u_{i,j,k+1}}{2} \quad , \qquad u_w^{x-} = \frac{u_{i-1,j,k} + u_{i-1,j,k+1}}{2}$$

$$v_w \;=\; \frac{1}{2}\left[\frac{\nabla r_j^v}{\Delta r_j^u}\left(v_{i,j,k} + v_{i,j,k+1}\right) + \frac{\nabla r_j^u}{\Delta r_j^u}\left(v_{i,j-1,k} + v_{i,j-1,k+1}\right)\right]$$

Finally, we obtain for $\nabla \cdot \mathbf{V}$

$$(\nabla \cdot \mathbf{V})_{i,j,k} = \frac{u_{i,j,k} - u_{i-1,j,k}}{\Delta x_i^v} + \frac{r_j^v\, v_{i,j,k} - r_{j-1}^v\, v_{i,j-1,k}}{r_j^u\, \Delta r_j^u} + \frac{w_{i,j,k} - w_{i,j,k-1}}{r_j^u\, \Delta\theta} \,. \qquad \text{(C.4)}$$

As in Chapter 4 for Cartesian coordinates, Δ and ∇ denote the central and backward difference operators applied to the grid point coordinates. They are defined by

$$\Delta x_i^u = x_{i+1}^v - x_i^v \,, \qquad \Delta x_i^v = x_i^u - x_{i-1}^u \,,$$
$$\Delta r_j^u = r_j^v - r_{j-1}^v \,, \qquad \Delta r_j^v = r_{j+1}^u - r_j^u \,,$$
$$\nabla x_i^u = x_i^u - x_i^v \,, \qquad \nabla x_i^v = x_i^v - x_{i-1}^u \,,$$
$$\nabla r_j^u = r_j^u - r_{j-1}^v \,, \qquad \nabla r_j^v = r_j^v - r_j^u \,.$$

Also, the evaluation of the viscous derivative terms $(1/r)(\partial/\partial r)(r\,\partial u/\partial r)$ and $(1/r)(\partial/\partial r)(r\,\partial w/\partial r)$ near the outer or inner cylinder wall has to be done as was demonstrated in Chapter 4 and the previous two appendices.

Now, the solution of (6.9–6.20) proceeds as follows, after introducing difference expressions like those of equations (C.1–C.4) in the left-hand sides of (6.9–6.20). In the x-sweep, $\widetilde{\Delta v}$ and $\widetilde{\Delta w}$ are obtained from equations (6.10) and (6.11), respectively, and $\widetilde{\Delta u}$ is obtained from (6.9) after eliminating $\widetilde{\Delta p}$ with the aid of (6.12). Scalar tridiagonal systems of equations have to be inverted as is shown in Chapter 4. A similar procedure applies in the r- and θ-sweeps, equations (6.13-6.20).

Appendix D

Linearized Potential Flow Theory

This Appendix is a brief outline of linearized potential flow theory applied to the computation of unsteady flows. More details are provided in Refs [37, 38]

We consider a fluid domain delimited by walls, with inlet and outlet flow portions, and there is a steady mean flow with preferred direction in the fluid domain. Small oscillations of the walls bounding the fluid domain cause unsteadiness in the flow pattern, and small perturbations in the flow parameters are introduced by the wall vibration.

The fluid under consideration is incompressible, inviscid and irrotational, and the condition of irrotationality allows us to express the velocity vector, $\mathbf{U}$, in terms of the gradient of a flow potential Φ:

$$\mathbf{U} = \nabla\Phi \,. \tag{D 1}$$

The equation of conservation of mass becomes

$$\nabla \cdot \mathbf{U} = \nabla^2\Phi = 0 \,, \tag{D.2}$$

and is valid for both steady and unsteady flows. Denoting by $\mathbf{x}$, the vibrational

displacement of a wall and by $\dot{\mathbf{x}}_s$ its velocity, the Laplace equation (D.2) for Φ is solved under the boundary condition that the normal velocity components of both fluid and wall are equal, at the wall, which is written

$$\mathbf{U}' \cdot \mathbf{n}' = \left.\frac{\partial \Phi}{\partial n}\right|_{\text{wall}} = \dot{\mathbf{x}}_s \cdot \mathbf{n}' \,. \tag{D.3}$$

The unit normal to the wall surface is denoted by $\mathbf{n}$ and a primed quantity is evaluated on the instantaneous, deformed position of the vibrating wall.

Since the fluid is inviscid, only pressure forces act on the vibrating structure, and the pressure must then be expressed in terms of the potential Φ. To that end, we consider the momentum equation for an inviscid fluid, which is Euler's equation of motion,

$$\frac{\partial \mathbf{U}}{\partial t} + \mathbf{U} \cdot \nabla \mathbf{U} + \nabla \left(\frac{\Pi}{\rho} \right) = 0 \,,$$

where Π is the pressure and ρ the fluid density. Upon substituting in that equation the expression for $\mathbf{U}$ from (D.1), we obtain, after using the condition of irrotationality, the Bernouilli-Lagrange equation,

$$\frac{\partial \Phi}{\partial t} + \frac{\nabla \Phi \cdot \nabla \Phi}{2} + \frac{\Pi}{\rho} = 0 \,. \tag{D.4}$$

In linearized potential flow theory we express the pressure and velocity vector as

$$\mathbf{U} = \mathbf{V} + \mathbf{v} \,, \quad \Pi = P + p \,, \tag{D.5}$$

where $\mathbf{V}$ is the steady, mean component of flow and $\mathbf{v}$ is the wall-induced perturbation superimposed on it, we have $|\mathbf{v}| \ll |\mathbf{V}|$. Similarly, P is the pressure associated with the steady mean flow and p is the unsteady pressure associated with the wall vibration. The flow potential Φ is correspondingly decomposed into the steady component ϕ_s, and the time-dependent component ϕ,

$$\Phi = \phi_s + \phi \,, \qquad \text{where we have} \quad \nabla\phi_s = \mathbf{V}, \quad \nabla\phi = \mathbf{v} \,, \tag{D.6}$$

and both ϕ_s and ϕ have to satisfy Laplace's equation:

$$\nabla^2\phi_s = 0 \,, \qquad \nabla^2\phi = 0 \,. \tag{D.7}$$

The solution is linearized with respect to the steady mean flow $\mathbf{V}$, by substituting (D.5) and (D.6) into (D.4) to obtain the expression for the unsteady pressure p:

$$p = -\rho\left(\frac{\partial\phi}{\partial t} + \mathbf{V}\cdot\nabla\phi\right) \,. \tag{D.8}$$

The boundary conditions associated with the Laplace equation (D.7) for ϕ are obtained by expressing (D.3) with respect to the undeformed, equilibrium position of the wall in its non-vibrating state, where the quantities are denoted without primes. The resulting linearized expression is

$$\mathbf{v}\cdot\mathbf{n} = \dot{\mathbf{x}}_s\cdot\mathbf{n} - \mathbf{V}\cdot(\mathbf{n}' - \mathbf{n}) - (\mathbf{V}' - \mathbf{V})\cdot\mathbf{n} \,.$$

which can be expressed in terms of the normal displacement of the wall surface, $x_{sn} = \mathbf{x}_s\cdot\mathbf{n}$, and the normal wall velocity, $\dot{x}_{sn} = \mathbf{v}_s\cdot\mathbf{n}$:

$$\mathbf{v}\cdot\mathbf{n} \equiv \frac{\partial\phi}{\partial n} = \dot{x}_{sn} + \mathbf{V}\cdot\nabla_w x_{sn} + x_{sn}\left(\nabla_w\cdot\mathbf{V}\right) \,. \tag{D.9}$$

In equation (D.9), ∇_w is the nabla operator taken in the surface of the wall,

$$\nabla_w = \mathbf{e}_1\frac{\partial}{\partial X_1} + \mathbf{e}_2\frac{\partial}{\partial X_2} \,,$$

where X_1 and X_2 are local coordinates on the surface which are aligned with the principal curvature directions (Refs [38, 41]), and $\mathbf{e}_1$ and $\mathbf{e}_2$ are the unit vectors in those directions.

Now, in the problems treated in Chapters 8 and 9, the wall vibration consisted in the oscillation of the outer cylinder, and we denoted by $\epsilon(t)$ the displacement of the cylinder axis. Hence we may write

$$\mathbf{x}_s = \epsilon(t)\mathbf{i} \,, \tag{D.10}$$

for the outer cylinder wall displacement, where $\mathbf{i}$ is a unit vector in the plane of vibration. In order to obtain an expression for the unsteady pressure p, we first decompose the non-steady flow potential ϕ into two parts,

$$\phi = \dot{\epsilon}(t)\phi^{(1)} + \epsilon(t)\phi^{(2)} \,. \tag{D.11}$$

By inserting (D 11) into (D.7), we note that both $\phi^{(1)}$ and $\phi^{(2)}$ also satisfy Laplace's equation, and furthermore they are solved under the boundary conditions

$$\begin{aligned} \frac{\partial \phi^{(1)}}{\partial n} &= \mathbf{i}\cdot\mathbf{n} \,, \\ \frac{\partial \phi^{(2)}}{\partial n} &= (\mathbf{i}\cdot\mathbf{n})(\nabla_w \cdot \mathbf{V}) + \mathbf{V}\cdot\nabla_w(\mathbf{i}\cdot\mathbf{n}) \,, \end{aligned}$$

which are obtained by substituting (D.10) and (D.11) into (D.9). The unsteady pressure p comes from inserting (D.11) into (D.8):

$$p = -\rho\left[\ddot{\epsilon}(t)\phi^{(1)} + \dot{\epsilon}(t)\left\{\phi^{(2)} + \mathbf{V}\cdot\nabla\phi^{(1)}\right\} + \epsilon(t)\mathbf{V}\cdot\nabla\phi^{(2)}\right] \,.$$

It is seen that the unsteady pressure, p, is proportional to the acceleration, $\ddot{\epsilon}$, the velocity, $\dot{\epsilon}$, and the displacement, ϵ, of the cylinder axis, and this gives rise to the added mass, added damping and added stiffness, respectively.

Appendix E

Program Listings

This Appendix presents the listings of two programs which are typical of the programs used to obtain the results presented in this Thesis.

The first program was used to resolve the non-linear three-dimensional Navier-Stokes equations in the geometry which is described in Section 8.1, namely the uniform annular gap geometry in which the outer cylinder executes transverse oscillations over its central portion.

The second program listing relates to the fluid-structure interaction problem treated in Section 9.3.1, in which the geometry is the two-dimensional annular configuration described in Chapter 7; the fluid forces in that case are determined by means of the two-harmonic solution developed in Section 7.3.

SOLUTION OF
THREE-DIMENSIONAL NAVIER-STOKES EQUATIONS
IN UNIFORM ANNULAR GAP GEOMETRY

```
C  This is a listing of the program which resolves the
C  unsteady Navier-Stokes equations for a three-dimensional
C  uniform annular flow geometry, such as is treated in
C  Section 8.1.

      PROGRAM NS3D
      PARAMETER (NXC=100,NYC=20,NZC=25)
      CHARACTER*20 MESH, FILOUT, FILIN

C  ******************************
C  Dimensioning of the variables
C  ******************************

C    U is the axial velocity component
C    V is the radial velocity component
C    W is the circumferential velocity component
C    P is the pressure

C  DU, DV, DW and DP are the delta-increments in the above
C                    variables during the pseudo-time
C                    integration

C   FU is the non-homogeneous forcing term involving U
C   FV is the non-homogeneous forcing term involving V
C   FW is the non-homogeneous forcing term involving W


       DIMENSION U(NXC,NYC,NZC), V(NXC,NYC,NZC),
      &          W(NXC,NYC,NZC), P(NXC,NYC,NZC)

       DIMENSION DU(NXC,NYC,NZC), DV(NXC,NYC,NZC),
      &          DW(NXC,NYC,NZC), DP(NXC,NYC,NZC)

       DIMENSION FU(NXC,NYC,NZC), FV(NXC,NYC,NZC),
      &          FW(NXC,NYC,NZC)

C  -------------------------------------------------------

C  YRU and YRV are the radial coordinates of the grid points

C  XKU, XKV, YNU, YNV  are the metric term derivatives, also
C                      defined as the delta's of the grid
C                      point coordinates in Section 4.2

C  DXU, DXV, DYU, DYV  are the nabla's of the grid point
C                      coordinates defined in Section 4.2

       DIMENSION YRU(NYC), YRV(NYC),
      &          XKU(NXC), XKV(NXC), YNU(NYC), YNV(NYC),
      &          DXU(NXC), DXV(NXC), DYU(NYC), DYV(NYC)
```

```
C-----------------------------------------------------

C  The quantities which are dimensioned next involve the
C  metric derivatives. They are defined below.

      DIMENSION CYU(NYC), CYV(NYC), RYU(NYC), RYV(NYC),
     &          TYU(NYC), TYV(NYC), AYU(NYC), AYV(NYC),
     &          AXU(NXC), AXV(NXC)

C  -----------------------------------------------------

C  B, D, A and RHS are used in the solution of the tridiagonal
C                  systems of equations
C  RESIDU and RES2 contain convergence parameters, i.e. the
C                  maximum and rms residuals, respectively

C  RP contains residuals of the continuity equation

C  WALL contains the displacement of the cylinder axis. It is
C       zero on the fixed extremities of the outer pipe.

C  COSZ contains the cosine values of the angles at the grid
C       points where u, v and p are defined
C  SINZ contains the sine values of the angles at the grid
C       points where w are defined

      DIMENSION B(NXC), D(NXC), A(NXC), RHS(NXC), RP(NYC),
     &          RESIDU(4), RES2(4),
     &          WALL(NXC), SINZ(NZC), COSZ(NZC)

C  ************************
C  Initialization of data
C  ************************

C  IDT is the counter for the real time integration

      DATA IDT/2/
      PI = ACOS(-1.0)

      DO 1 I=1,NXC
        WALL(I) = 0.0
      DO 2 J=1,NYC
      DO 3 K=1,NZC
        U(I,J,K) = 0.0
        V(I,J,K) = 0.0
        W(I,J,K) = 0.0
        P(I,J,K) = 0.0
        DU(I,J,K) = 0.0
        DV(I,J,K) = 0.0
        DW(I,J,K) = 0.0
3       DP(I,J,K) = 0.0
```

```
2     CONTINUE
1     CONTINUE

C  FILIN is the file containing the initial conditions
C       for the unsteady flow solution; it is a direct-access
C        file
C  FILOUT is the file containing the unsteady flow solution
C         over one full harmonic cycle, in which each record
C         contains the flow solution at one time step; it is
C         a direct-access file
C  MESH is a file containing the mesh parameters such as the
C       grid point coordinates and the nabla's and delta's of
C        the grid point coordinates, defined in the Thesis,
C        Section 4.2.

        FILIN  = NAX3D.250
        FILOUT = NS3D.C1
        MESH   = UP3DMO.1

C  RE is the Reynolds number
C  S  is the Stokes number
C  OMEGA is the angular frequency of oscillation
C  FREQ is the frequency of oscillation

        RE = 250.
        S = 25.
         OMEGA = 2.0*S/RE
         FREQ = OMEGA/(2.0*PI)

C  NDT is the number of time steps per harmonic cycle
C  EPS is the amplitude of displacement of the
C      cyclinder axis
C  NZ-3 represents the number of grid points in the
C       circumferential direction
C  TOLTAU is the tolerance for the iteration in pseudo-time

        NDT = 19
        EPS = 0.1
        NZ = 15
        TOLTAU = 1.E-4

C ********************************************************
C  The mesh parameters are loaded into program memory,
C  including the grid point coordinates and the delta's and
C  nabla's defined in Section 4.2
C ********************************************************

C  NX is the number of grid points in the axial direction
C  NY is the number of grid points in the radial direction
C  NMS is the index at the axial location of the upstream
C      extremity of the oscillating cyclinder
```

```
C  NME is the index at the axial location of the downstream
C       extremity of the oscillating cyclinder

       OPEN(2,FILE=MESH)
         READ(2,'(4I5,F15.7)') NX, NY, NMS, NME
         READ(2,'(I5,4F15.7)')
      &        (II,XKU(I),XKV(I),DXU(I),DXV(I),I=1,NX)
         READ(2,*)
         READ(2,'(I5,4F15.7)')
      &        (JJ,YNU(J),YNV(J),DYU(J),DYV(J),J=1,NY)
         READ(2,*)
         READ(2,'(I5,2F15.7)') (JJ,YRU(J),YRV(J),J=1,NY)
       CLOSE(2)

        NX1=NX-1
        NX2=NX-2
        NY1=NY-1
        NY2=NY-2
        NZ1=NZ-1
        NZ2=NZ-2

C  Note that YRV(1) and YRV(NY1) are the radial coordinates of
C  the inner and outer cylinders, respectively. Also, the
C  indices I, J and K will be for the axial, radial and
C  circumferential directions. We thus have the inflow at
C  I=1, the outflow at I=NX, and θ=0 corresponds with
C  W(I,J,2), whereas θ=π is with W(I,J,NZ1)

C  DZ is the mesh spacing in the circumferential direction

       DZ = PI/REAL(NZ-3)
     DZDZ = DZ*DZ

C  Calculation of the cosine values of the angles at the
C  grid points where u, v and p are defined
C  Calculation of the sine values of the angles at the
C  grid points where w is defined

       DO 70 K=1,NZ
        COSZ(K) = COS( (REAL(K)-2.5)*DZ )
70      SINZ(K) = SIN( (REAL(K)-2.0)*DZ )

C  ************************************************************
C  Calculation of real-time step size and artificial
C  compressibility and pseudo-time step size
C  ************************************************************

C  DTREAL is the real-time step size Δt
C  UMOY is the representative mean flow speed
C  DELTA is the artificial compressibility δ. The typical mesh
C        spacing was taken to be the minimum spacing at the
```

```
C        wall
C  DTAU is the pseudo-time step size Δτ

       DTREAL = 1.0/(FREQ*REAL(NDT))

      UMOY = 0.8
       DELTA = 0.2 / (DTREAL*UMOY**2)

      UMOY = UMOY * DTREAL
       DTAU = 40.0 * YNU(2)/(UMOY+SQRT(UMOY**2+DTREAL/DELTA))

C  The Reynolds number appearing in the equations is scaled
C  (Chapter 8) and different parameters are defined

       RE = RE / 2.0
       DTAC = DTAU/DELTA
       DTACE = DTAU*RE/DELTA
       RNU = 1.0 / RE

C  ************************************************************
C  The initial conditions are loaded into program memory and
C  the values are given to the velocity components and
C  pressure
C  ************************************************************

       OPEN(2,FILE=FILIN,ACCESS='DIRECT',RECL=2*4*NY2*NX)
         READ(2,REC=1) ((U(I,J,1), P(I,J,1), J=2,NY1),I=1,NX)
       CLOSE(2)

       DO 621 K=2,NZ
       DO 620 J=2,NY1
       DO 610 I=1,NX
         U(I,J,K) = U(I,J,1)
610      P(I,J,K) = P(I,J,1)
620    CONTINUE
621    CONTINUE

C  The output file FILOUT is initialized for the first
C  two time steps

      OPEN(2,FILE=FILOUT,ACCESS='DIRECT',RECL=4*4*NX2*NY2*NZ2)

       DO 11 IREC=1,2
        WRITE(2,REC=IREC)  (((U(I,J,K),0.0,0.0,P(I,J,K),
     &                          I=2,NX1),J=2,NY1),K=2,NZ1)
11     CONTINUE

C -------------------------------------------------------------
C  The value of ALPHA is set and different parameters are
C  defined
```

```
      ALPHA = 2.0*DTREAL/3.0
      DTAL  = DTAU*ALPHA
      ALDL  = ALPHA*DELTA
      ALDLDZ  = ALDL*DZ

C  ---------------------------------------------------------
C  Initialization of the vectors containing the metric terms
C  and of the parameters used for the evaluation
C  of the viscous derivatives and undifferentiated terms

       DO 59 J=1,NY1
         CYU(J) = DTAL/(YRU(J)*YNU(J))
         CYV(J) = DTAL/(YRV(J)*YNV(J))
         RYU(J) = YRU(J)/(RE*YNU(J))
         RYV(J) = YRV(J)/(RE*YNV(J))
         TYU(J) = DTAL/(RE*YRU(J)**2)
         TYV(J) = DTAL/(RE*YRV(J)**2)
         AYU(J) = DTAL/YRU(J)
59       AYV(J) = DTAL/YRV(J)
       DO 57 I=1,NX
         AXU(I) = DTAL/XKU(I)
57       AXV(I) = DTAL/XKV(I)

C ************************************************************
C  Beginning of the main loop which is the integration in real
C  time; each trip through the loop advances the solution to
C  the next time level
C ************************************************************


C     -------------
999   IDT = IDT + 1
C     -------------

C  The values of the flow quantities at time level t^n-1 are
C  fetched from file FILOUT (modulo NDT) and then FU, FV and
C  FW are calculated

     IREC = MOD(IDT-3,NDT) + 1
      READ(2,REC=IREC) (((FU(I,J,K), FV(I,J,K), FW(I,J,K),
     &                   RES2(1),I=2,NX1),J=2,NY1),K=2,NZ1)

     DO 20 I=2,NX1
      DO 30 J=2,NY1
       DO 29 K=2,NZ1
        FU(I,J,K) = ( 4.0*U(I,J,K) - FU(I,J,K) ) /3.0
        FV(I,J,K) = ( 4.0*V(I,J,K) - FV(I,J,K) ) /3.0
29      FW(I,J,K) = ( 4.0*W(I,J,K) - FW(I,J,K) ) /3.0
30    CONTINUE
20   CONTINUE
```

```
C ... ********************************************
C ... Beginning of the integration in pseudo-time
C ... ********************************************

C  The procedure adopted here is that for one given momentum
C  equation the radial, circumferential and axial sweeps are
C  done in succession, before to solve for the next momentum
C  equation; the momentum equations are solved in that order:
C  (1) radial, (2) circumferential and (3) axial.

C  VOT is the velocity at time level t^n+1 of the cylinder
C      axis
C  ITER is the pseudo-time counter

      VOT =  OMEGA*EPS*SIN(2.0*PI*REAL(IDT-2)/REAL(NDT))

      ITER = 0
998   ITER = ITER + 1

C  Setting of the boundary conditions at the solid walls, and
C  at the staggered grid points near the walls. The latter is
C  an artifice which allows to use the grid points outside the
C  actual physical domain to compute in exactly the same way
C  the viscous derivatives which are close or far from the
C  wall. For example, in view of the value given to W(I,NY,K)
C  below, one can verify that W(I,NY,K) - W(I,NY-1,K) gives
C  the expression for the one-sided evaluation of the viscous
C  derivatives at the solid walls, as discussed in
C  Section 4.2.

      DO 450 I=1,NX
       DO 445 K=1,NZ
         U(I,1,K) = -2.0*U(I,2,K) + U(I,3,K)/3.0
         U(I,NY,K) = - 2.0*U(I,NY1,K) + U(I,NY2,K)/3.0
         W(I,1,K) = -2.0*W(I,2,K) + W(I,3,K)/3.0
445      W(I,NY,K) = - 2.0*W(I,NY1,K) + W(I,NY2,K)/3.0
450   CONTINUE

       DO 8 I=NMS,NME
         WALL(I) =  VOT
       DO 10 K=1,NZ
         V(I,NY1,K) =  VOT*COSZ(K)
10       W(I,NY,K)  = - 8.0/3.0*VOT*SINZ(K) - 2.0*W(I,NY1,K)
     &                + W(I,NY2,K)/3.0
8      CONTINUE

      DO 888 I=1,4
       RESIDU(I) = 0.0
888    RES2(I) = 0.0
```

```
C     ****************************************
C     Solving of the radial momentum equation
C     ****************************************

C     ------------------------
C ... Radial sweep for V(I,J,K)
C     ------------------------

      DO 1010 I=2,NX1
      DO 1011 K=3,NZ1

C  Computation of the continuity equation residual, RP,
C  as well as the maximum and rms residual values, RESIDU(4)
C  and RES2(4).

       DO 1032 J=2,NY1
      RP(J) = ( - AXV(I)*(U(I,J,K)-U(I-1,J,K))
     1        - CYU(J)*(YRV(J)*V(I,J,K)
     2                 -YRV(J-1)*V(I J-1,K)) )/ALDL
     3        - AYU(J)/ALDLDZ*(W(I,J,K)-W(I,J,K-1))
       IF(ABS(RP(J)).GT.RESIDU(4)) RESIDU(4)=ABS(RP(J))
      RES2(4) = RES2(4) + RP(J)*RP(J)
1032  CONTINUE

      DO 1020 J=2,NY2

C  Evaluation of the velocity interpolates

        VXP = (1.0-DXV(I+1))*V(I+1,J,K) + DXV(I+1)*V(I,J,K)
        VXM = (1.0-DXV(I))*V(I,J,K) + DXV(I)*V(I-1,J,K)
        VYP = (1.0-DYV(J+1))*V(I,J+1,K) + DYV(J+1)*V(I,J,K)
        VYM = (1.0-DYV(J))*V(I,J,K) + DYV(J)*V(I,J-1,K)
        VZP = 0.5*(V(I,J,K)+V(I,J,K+1))
        VZM = 0.5*(V(I,J,K)+V(I,J,K-1))
        UXP = (1.0-DYU(J+1))*U(I,J+1,K) + DYU(J+1)*U(I,J,K)
        UXM = (1.0-DYU(J+1))*U(I-1,J+1,K) +
     &        DYU(J+1)*U(I-1,J,K)

        WZP = (1.0-DYU(J+1))*W(I,J+1,K) + DYU(J+1)*W(I,J,K)
        WZM = (1.0-DYU(J+1))*W(I,J+1,K-1) +
     &        DYU(J+1)*W(I,J,K-1)
        WV  = 0.5*( (1.0-DYU(J+1))*(W(I,J+1,K-1)+W(I,J+1,K))
     &        + DYU(J+1)*(W(I,J,K-1)+W(I,J,K)) )

      CR = YRU(J+1)*VYP
      CL = YRU(J)*VYM

C  Setting up of the tridiagonal system of equations

      B(J) = CYV(J)*(-CL*DYV(J)-RYU(J)) -
     &       DTAC*CYU(J)*YRV(J-1)/YNV(J)
```

```
        D(J) = 1.0 + DTAU + TYV(J) +
     &         CYV(J)*(CR*DYV(J+1)+CL*(DYV(J)-1.0)
     &    +RYU(J)+RYU(J+1))  + DTACE*RYV(J)*(CYU(J)+CYU(J+1))
        A(J) = CYV(J)*(-CR*(DYV(J+1)-1.0)-RYU(J+1))
     &            - DTAC*CYU(J+1)*YRV(J+1)/YNV(J)

C  Computation of the radial momentum equation
C  residual RHV (=RHS)

        RHS(J) =  DTAU*(FV(I,J,K)-V(I,J,K))
     1 - AXV(I)*( UXP*VXP-UXM*VXM
     2      -  ( (V(I+1,J,K)-V(I,J,K))/XKU(I)
     3         - (V(I,J,K)-V(I-1,J,K))/XKU(I-1) ) / RE )
     4 - CYV(J)*( YRU(J+1)*VYP*VYP - YRU(J)*VYM*VYM
     5 - (RYU(J+1)*(V(I,J+1,K)-V(I,J,K))
     6   -RYU(J)*(V(I,J,K)-V(I,J-1,K))) )
     7 - AYV(J)*( (WZP*VZP-WZM*VZM)/DZ - WV*WV )
     8 - DTAL/YNV(J)*(P(I,J+1,K)-P(I,J,K))
     9 + TYV(J)*( (V(I,J,K+1)+V(I,J,K-1)-2.0*V(I,J,K))/DZDZ
     0      - 2.0*(WZP-WZM)/DZ - V(I,J,K) )

C  Computation of maximum and rms residuals

        IF(ABS(RHS(J)).GT.RESIDU(2)) RESIDU(2) = ABS(RHS(J))
        RES2(2) = RES2(2) + RHS(J)*RHS(J)
        RHS(J) = RHS(J) - DTAL/YNV(J)*(RP(J+1)-RP(J))

1020  CONTINUE

C  Solving of the tridiagonal system of equations

       CALL SY(2,NY2,B,D,A,RHS)

C  Computation of DV and DP

         DO 1040 J=2,NY2
1040   DV(I,J,K) = RHS(J)
         DO 1060 J=2,NY1
1060   DP(I,J,K) = RP(J)
     & - CYU(J)/ALDL*(YRV(J)*DV(I,J,K)-YRV(J-1)*DV(I,J-1,K))

1011  CONTINUE
1010  CONTINUE

C  Use is made of the symmetry boundary condition at θ=0

       DO 1012 I=2,NX1
       DO 1013 J=2,NY1
1013     DP(I,J,2) = DP(I,J,3)
1012   CONTINUE
```

```
C     ---------------------------------
C ... Circumferential sweep for V(I,J,K)
C     ---------------------------------

      DO 3000 J=2,NY2
        DUM = AYV(J)/(2.0*DZ)
        COD = TYV(J)/DZDZ
      DO 3019 I=2,NX1

      DO 3020 K=3,NZ1
       WZP = (1.0-DYU(J+1))*W(I,J+1,K) + DYU(J+1)*W(I,J,K)
       WZM = (1.0-DYU(J+1))*W(I,J+1,K-1) + DYU(J+1)*W(I,J,K-1)
       CL = DUM*WZM
       CR = DUM*WZP

       B(K) = - CL - COD
       D(K) = 1.0 + CR - CL  + 2.0*COD
       A(K) = CR - COD
3020   RHS(K) = DV(I,J,K)

C  Setting of the symmetry boundary condition on the
C  implicit left-hand side

       D(3) = D(3) + B(3)
       D(NZ1) = D(NZ1) + A(NZ1)

C  Solving of the tridiagonal system of equations

       CALL SY(3,NZ1,B,D,A,RHS)

      DO 3040 K=3,NZ1
3040   DV(I,J,K) = RHS(K)

3019  CONTINUE
3000  CONTINUE

C     ------------------------
C ... Axial sweep for V(I,J,K)
C     ------------------------

      DO 1210 J=2,NY2
      DO 1209 K=3,NZ1

      DO 1250 I=2,NX1
       UXP = (1.0-DYU(J+1))*U(I,J+1,K) + DYU(J+1)*U(I,J,K)
       UXM = (1.0-DYU(J+1))*U(I-1,J+1,K) + DYU(J+1)*U(I-1,J,K)
        VL = RNU/XKU(I-1)
        VR = RNU/XKU(I)
        CL = UXM*DXV(I)
        CR = UXP*DXV(I+1)
       B(I) = AXV(I)*(-CL-VL)
```

```
        D(I) = 1.0 + AXV(I)*(CR+CL-UXM+VL+VR)
        A(I) = AXV(I)*(-CR+UXP-VR)
1250    RHS(I) = DV(I,J,K)

C  Setting of the outflow boundary condition on the implicit
C  left-hand side

       D(NX1)= D(NX1) + (1.0+XKU(NX1)/XKU(NX2))*A(NX1)
       B(NX1)= B(NX1) - XKU(NX1)/XKU(NX2)*A(NX1)

C  Solving of the tridiagonal system of equations

       CALL SY(2,NX1,B,D,A,RHS)

       DO 1260 I=2,NX1
        DV(I,J,K) = RHS(I)
1260   CONTINUE

1209   CONTINUE
1210   CONTINUE

C  updating of the solution for V(I,J,K), extrapolation of
C  the velocity component at the outlet and setting of the
C  symmetry boundary condition at θ=0 and θ=π.

       DO 1300 J=2,NY2
       DO 1299 K=3,NZ1
       DO 1310 I=2,NX1
1310    V(I,J,K) = V(I,J,K) + DV(I,J,K)
        V(NX,J,K) = (1.0+XKU(NX1)/XKU(NX2))*V(NX1,J,K)
     &              - XKU(NX1)/XKU(NX2)*V(NX2,J,K)
1299   CONTINUE
1300   CONTINUE

       DO 1321 I=2,NX1
       DO 1322 J=2,NY2
        V(I,J,2) = V(I,J,3)
1322    V(I,J,NZ) = V(I,J,NZ1)
1321   CONTINUE

C      ************************************************
C      Solving of the circumferential momentum equation
C      ************************************************

C      -------------------------
C ...  Radial sweep for W(I,J,K)
C      -------------------------

       DO 3010 I=2,NX1
       DO 3009 K=3,NZ2
```

```
      DO 3120 J=2,NY1

       WXP = (1.0-DXV(I+1))*W(I+1,J,K) + DXV(I+1)*W(I,J,K)
       WXM = (1.0-DXV(I))*W(I,J,K) + DXV(I)*W(I-1,J,K)
       WYP = (1.0-DYU(J+1))*W(I,J+1,K) + DYU(J+1)*W(I,J,K)
       WYM = (1.0-DYU(J))*W(I,J,K) + DYU(J)*W(I,J-1,K)
       WZP = 0.5*(W(I,J,K+1)+W(I,J,K))
       WZM = 0.5*(W(I,J,K)+W(I,J,K-1))

       UXP = 0.5*(U(I,J,K+1)+U(I,J,K))
       UXM = 0.5*(U(I-1,J,K+1)+U(I-1,J,K))

       VYP = 0.5*(V(I,J,K)+V(I,J,K+1))
       VYM = 0.5*(V(I,J-1,K)+V(I,J-1,K+1))
       VZP = (1.0-DYV(J))*V(I,J,K+1) + DYV(J)*V(I,J-1,K+1)
       VZM = (1.0-DYV(J))*V(I,J,K) + DYV(J)*V(I,J-1,K)
       VW = 0.5*( (1.0-DYV(J))*(V(I,J,K)+V(I,J,K+1)) +
     &          DYV(J)*(V(I,J-1,K)+V(I,J-1,K+1)) )

      CL = YRV(J-1)*VYM
      CR = YRV(J)*VYP

       B(J) = CYU(J)*( -CL*DYU(J) - RYV(J-1) )
       D(J) = 1.0 + AYU(J)*VW + TYU(J)
     & + CYU(J)* (CR*DYU(J+1) + CL*(DYU(J)-1.0)
     & + RYV(J-1) + RYV(J) )
       A(J) = CYU(J)*( -CR*(DYU(J+1)-1.0) - RYV(J) )

       RHS(J) =  DTAU*( - W(I,J,K) + FW(I,J,K) )
     1 - AXV(I)*( UXP*WXP - UXM*WXM
     2       - ( (W(I+1,J,K)-W(I,J,K))/XKU(I)
     3         - (W(I,J,K)-W(I-1,J,K))/XKU(I-1) ) /RE )
     4 - CYU(J)*( CR*WYP - CL*WYM
     5         - ( RYV(J)*(W(I,J+1,K)-W(I,J,K))
     6           - RYV(J-1)*(W(I,J,K)-W(I,J-1,K)) ) )
     7    - AYU(J)*( (WZP*WZP - WZM*WZM
     8               + P(I,J,K+1)-P(I,J,K)) / DZ
     9                                  + VW*W(I,J,K) )
     0 + TYU(J)*( (W(I,J,K+1)+W(I,J,K-1)-2.0*W(I,J,K))/DZDZ
     1       + 2.0*(VZP-VZM)/DZ - W(I,J,K) )

3120  CONTINUE

C  Modification of the implicit left-hand side according to
C  the implicit evaluation of the viscous derivatives near the
C  solid walls (inner and outer cylinders)

      D(2) = D(2) + 2.0*CYU(2)*RYV(1)
      A(2) = A(2) - CYU(2)*RYV(1)/3.0
      B(NY1) = B(NY1) - CYU(NY1)*RYV(NY1)/3.0
      D(NY1) = D(NY1) + CYU(NY1)*(2.0*RYV(NY1) - CR*DYU(NY))
```

```
C  Fine-tuning in the evaluation of the circumferential
C  momentum equation residual at the oscillating cylinder
C  wall

        RHS(NY1) = RHS(NY1)
     &           - CYU(NY1)*CR*(-WALL(I)*SINZ(K) - WYP)


       DO 1100 J=2,NY1
        IF(ABS(RHS(J)).GT.RESIDU(3)) RESIDU(3) = ABS(RHS(J))
        RES2(3) = RES2(3) + RHS(J)*RHS(J)
1100   CONTINUE

       CALL SY(2,NY1,B,D,A,RHS)
       DO 3050 J=2,NY1
3050    DW(I,J,K) = RHS(J)

3009   CONTINUE
3010   CONTINUE

C      ----------------------------------
C ...  Circumferential sweep for W(I,J,K)
C      ----------------------------------

       DO 4000 J=2,NY1
        DUM = AYU(J)/(2.0*DZ)
        COD = TYU(J)/DZDZ
        DUM2 = 4.0*DUM*DUM/ALDL
       DO 3999 I=2,NX1

       DO 4020 K=3,NZ2
        WZP = 0.5*(W(I,J,K+1)+W(I,J,K))
        WZM = 0.5*(W(I,J,K)+W(I,J,K-1))
        CL = DUM*WZM
        CR = DUM*WZP

        B(K) = - CL - COD - DUM2
        D(K) = 1.0 + DTAU + CR - CL + 2.0*(COD+DUM2)
        A(K) = CR - COD - DUM2

4020    RHS(K) = DW(I,J,K) - AYU(J)/DZ*(DP(I,J,K+1)-DP(I,J,K))

        CALL SY(3,NZ2,B,D,A,RHS)
        DO 4040 K=3,NZ2
4040   DW(I,J,K) = RHS(K)

       DO 3220 K=3,NZ1
3220    DP(I,J,K) = DP(I,J,K) -
     &         AYU(J)/ALDLDZ*(DW(I,J,K)-DW(I,J,K-1))

3999   CONTINUE
```

```
4000  CONTINUE

C     ------------------------
C ... Axial sweep for W(I,J,K)
C     ------------------------

      DO 3410 J=2,NY1
      DO 3409 K=3,NZ2

      DO 3450 I=2,NX1
       UXP = 0.5*(U(I,J,K+1)+U(I,J,K))
       UXM = 0.5*(U(I-1,J,K+1)+U(I-1,J,K))

       VL = RNU/XKU(I-1)
       VR = RNU/XKU(I)
       CL = UXM*DXV(I)
       CR = UXP*DXV(I+1)

       B(I) = AXV(I)*(-CL-VL)
       D(I) = 1.0 + AXV(I)*(CR+CL-UXM+VL+VR)
       A(I) = AXV(I)*(-CR+UXP-VR)
3450   RHS(I) = DW(I,J,K)

        D(NX1)= D(NX1) + (1.0+XKU(NX1)/XKU(NX2))*A(NX1)
        B(NX1)= B(NX1) - XKU(NX1)/XKU(NX2)*A(NX1)

      CALL SY(2,NX1,B,D,A,RHS)

      DO 3460 I=2,NX1
       DW(I,J,K) = RHS(I)
3460  CONTINUE

3409  CONTINUE
3410  CONTINUE

      DO 3310 J=2,NY1
      DO 3300 K=3,NZ2
      DO 3299 I=2,NX1
3299    W(I,J,K) = W(I,J,K) + DW(I,J,K)
        W(NX,J,K) = (1.0+XKU(NX1)/XKU(NX2))*W(NX1,J,K)
     &              - XKU(NX1)/XKU(NX2)*W(NX2,J,K)
3300  CONTINUE
3310  CONTINUE

      DO 3321 I=2,NX1
      DO 3322 J=2,NY1
       W(I,J,1) = - W(I,J,3)
3322   W(I,J,NZ) = - W(I,J,NZ2)
3321  CONTINUE

C     ****************************************
```

```
C     Solving of the axial momentum equation
C     **************************************

C     -------------------------
C ... Radial sweep for U(I,J,K)
C     -------------------------

      DO 2010 I=2,NX1
      DO 2009 K=3,NZ1

      DO 2020 J=2,NY1
       UXP = (1.0-DXU(I+1))*U(I+1,J,K) + DXU(I+1)*U(I,J,K)
       UXM = (1.0-DXU(I))*U(I,J,K) + DXU(I)*U(I-1,J,K)
       UYP = (1.0-DYU(J+1))*U(I,J+1,K) + DYU(J+1)*U(I,J,K)
       UYM = (1.0-DYU(J))*U(I,J,K) + DYU(J)*U(I,J-1,K)
       UZP = 0.5*(U(I,J,K)+U(I,J,K+1))
       UZM = 0.5*(U(I,J,K)+U(I,J,K-1))

       VYP = (1.0-DXV(I+1))*V(I+1,J,K) + DXV(I+1)*V(I,J,K)
       VYM = (1.0-DXV(I+1))*V(I+1,J-1,K) + DXV(I+1)*V(I,J-1,K)
       WZP = (1.0-DXV(I+1))*W(I+1,J,K) + DXV(I+1)*W(I,J,K)
       WZM = (1.0-DXV(I+1))*W(I+1,J,K-1) + DXV(I+1)*W(I,J,K-1)

       CR = YRV(J)*VYP
       CL = YRV(J-1)*VYM

       B(J) = CYU(J)*(-CL*DYU(J)-RYV(J-1))
       D(J) = 1.0 +
     &  CYU(J)*(CR*DYU(J+1)+CL*(DYU(J)-1.0)+RYV(J)+RYV(J-1))
       A(J) = CYU(J)*(-CR*(DYU(J+1)-1.0)-RYV(J))

       RHS(J) =  DTAU*(FU(I,J,K)-U(I,J,K))
     1 - AXU(I)*( UXP*UXP - UXM*UXM + P(I+1,J,K)-P(I,J,K)
     2       - RNU*( (U(I+1,J,K)-U(I,J,K))/XKV(I+1)
     3          - (U(I,J,K)-U(I-1,J,K))/XKV(I) ) )
     4 - CYU(J)*( YRV(J)*VYP*UYP - YRV(J-1)*VYM*UYM
     5 - (RYV(J)*(U(I,J+1,K)-U(I,J,K))
     6   -RYV(J-1)*(U(I,J,K)-U(I,J-1,K))) )
     7 - AYU(J)*(WZP*UZP - WZM*UZM) / DZ
     8 + TYU(J)*(U(I,J,K+1)+U(I,J,K-1)-2.0*U(I,J,K)) / DZDZ

2020  CONTINUE

       A(2) = A(2) - CYU(2)*RYV(1)/3.0
       D(2) = D(2) + 2.0*CYU(2)*RYV(1)
       B(NY1) = B(NY1) - CYU(NY1)*RYV(NY1)/3.0
       D(NY1) = D(NY1) + 2.0*CYU(NY1)*RYV(NY1)
       RHS(NY1) = RHS(NY1) + CYU(NY1)*YRV(NY1)*VYP*UYP
      DO 2222 J=2,NY1
       IF(ABS(RHS(J)).GT.RESIDU(1)) RESIDU(1) = ABS(RHS(J))
2222   RES2(1) = RES2(1) + RHS(J)*RHS(J)
```

```
      CALL SY(2,NY1,B,D,A,RHS)
      DO 2050 J=2,NY1
2050   DU(I,J,K) = RHS(J)

2009  CONTINUE
2010  CONTINUE

C     ----------------------------------
C ... Circumferential sweep for U(I,J,K)
C     ----------------------------------

      DO 2600 J=2,NY1
       DUM = AYU(J)/(2.0*DZ)
       COD = TYU(J)/DZDZ
      DO 2619 I=2,NX1

      DO 2620 K=3,NZ1
       WZP = (1.0-DXV(I+1))*W(I+1,J,K) + DXV(I+1)*W(I,J,K)
       WZM = (1.0-DXV(I+1))*W(I+1,J,K-1) + DXV(I+1)*W(I,J,K-1)
       CL = DUM*WZM
       CR = DUM*WZP

       B(K) = - CL - COD
       D(K) = 1.0 + CR - CL  + 2.0*COD
       A(K) = CR - COD
2620   RHS(K) = DU(I,J,K)

       D(3) = D(3) + B(3)
       D(NZ1) = D(NZ1) + A(NZ1)
       CALL SY(3,NZ1,B,D,A,RHS)

      DO 2640 K=3,NZ1
2640   DU(I,J,K) = RHS(K)

2619  CONTINUE
2600  CONTINUE

C     ------------------------
C ... Axial sweep for U(I,J,K)
C     ------------------------

      DO 2410 J=2,NY1
      DO 2409 K=3,NZ1

      DO 2450 I=2,NX1
       UXP = (1.0-DXU(I+1))*U(I+1,J,K) + DXU(I+1)*U(I,J,K)
       UXM = (1.0-DXU(I))*U(I,J,K) + DXU(I)*U(I-1,J,K)
       VL = RNU/XKV(I)
       VR = RNU/XKV(I+1)
       CL = UXM*DXU(I)
       CR = UXP*DXU(I+1)
```

```
        AR = AXV(I+1)/ALDL
        AL = AXV(I)/ALDL

        B(I) = AXU(I)*(-2.0*CL-AL-VL)
        D(I) = 1.0 + DTAU +
     &    AXU(I)*(2.0*(CR+CL-UXM)+AL+AR+VL+VR)
        A(I) = AXU(I)*(-2.0*(CR-UXP)-AR-VR)
2450    RHS(I) = DU(I,J,K) - AXU(I)*(DP(I+1,J,K)-DP(I,J,K))

       CALL SY(2,NX1,B,D,A,RHS)

       DO 2460 I=2,NX1
2460    DU(I,J,K) = RHS(I)

       DO 2470 I=2,NX1
2470    DP(I,J,K) = DP(I,J,K) -
     &              AXV(I)/ALDL*(DU(I,J,K)-DU(I-1,J,K))

2409   CONTINUE
2410   CONTINUE


       DO 5300 J=2,NY1
       DO 5299 K=3,NZ1
       DO 5310 I=2,NX1
        U(I,J,K) = U(I,J,K) + DU(I,J,K)
5310    P(I,J,K) = P(I,J,K) + DP(I,J,K)
        U(NX,J,K) = (1.0+XKV(NX)/XKV(NX1))*U(NX1,J,K)
     &              - XKV(NX)/XKV(NX1)*U(NX2,J,K)
5299   CONTINUE
5300   CONTINUE


       DO 5321 I=2,NX1
       DO 5322 J=2,NY1
        U(I,J,2) = U(I,J,3)
        P(I,J,2) = P(I,J,3)
        U(I,J,NZ) = U(I,J,NZ1)
5322    P(I,J,NZ) = P(I,J,NZ1)
5321   CONTINUE

C  ---------------------------------------
C  The residual calculations are fine-tuned
C  ---------------------------------------

       DO 5025 I=1,3
      RES2(I) = SQRT(RES2(I)/(NX1*NY1*NZ1))/DTAL
5025  RESIDU(I) = RESIDU(I)/DTAL
       RES2(4) = SQRT(RES2(4)/(NX1*NY1*NZ1))/DTAC
       RESIDU(4) = RESIDU(4)/DTAC
```

```
C  Test for convergence

        DO 433 I=1,4
       IF(RES2(I).GT.TOLTAU) GOTO 998
433     CONTINUE

C  ************************
C  END OF PSEUDO-TIME LOOP
C  ************************

C  The flow variables obtained for that time step are
C  stored in FILOUT

      IREC = MOD(IDT-1,NDT) + 1
         WRITE(2,REC=IREC) (((U(I,J,K), V(I,J,K), W(I,J,K),
      &                  P(I,J,K),I=2,NX1),J=2,NY1),K=2,NZ1)


C  Test to see if the time integration has been done
C  for five harmonic cycles

       IF(IDT.LT.5*NDT+1) GOTO 999

       CLOSE(2)

       END

C  The next subroutine solves tridiagonal systems of equations

C ... ***********************************
      SUBROUTINE SY(IL,IU,BB,DD,AA,CC)
C ... ***********************************

      DIMENSION AA(*), BB(*), CC(*), DD(*)

      LP = IL+1
      DO 10 I=LP,IU
      R = BB(I)/DD(I-1)
      DD(I) = DD(I)-R*AA(I-1)
10    CC(I) = CC(I)-R*CC(I-1)

      CC(IU) = CC(IU)/DD(IU)
      DO 20 I=LP,IU
      J = IU-I+IL
20    CC(J) = (CC(J)-AA(J)*CC(J+1))/DD(J)
      RETURN
      END
```

SOLUTION OF
FLUID-STRUCTURE INTERACTION PROBLEM
IN TWO-DIMENSIONAL ANNULAR GEOMETRY

```
C  This program performs the integration of the equation
C  of motion of a structure under the combined action of
C  mechanical and fluid forces. The structure is the two-
C  dimensional geometry treated in Chapter 7 and in Chapter 9,
C  Section 9.3.1. The viscous flow results of Section 9.3.1
C  were ontained with this program. The fluid forces are
C  determined by the two-harmonic solution described in
C  Section 7.3, which requires a one-dimensional mesh spanning
C  the radial direction.

C  The main program represents the fourth-order Runge-Kutta
C  scheme used for the integration of the equation of the
C  structure. The suboutine MOHT2 is used to compute the fluid
C  forces.

C     **************
      PROGRAM MOHTWO
C     **************

      PARAMETER (NYC=40)

C  TIME stores the time at each time step
C  X, V and A are the displacement, velocity and acceleration
C             of the structure at each time step

C  YRU and YRV are the grid point radial coordinates
C  YNU and YNV are the delta's of the grid point coordinates
C  DYU and DYV are the nabla's of the grid point coordinates

C  MESH is the file containing the mesh parameters

      DIMENSION TIME(1000), X(1000), V(1000), A(1000)
      DIMENSION YNU(NYC), YNV(NYC), DYU(NYC), DYV(NYC)
      DIMENSION YRU(NYC), YRV(NYC)

      CHARACTER*20 MESH

      COMMON NY, YNU, YNV, DYU, DYV, YRU, YRV, RE, DTREAL,
     &          DELTA, DTAU, TOLTAU, ITMAX


C     ***************************
C     Initialization of the data
C     ***************************

      DATA TIME,X,V,A/4000*0.0/
      PI = ACOS(-1.0)

C  RATIOM is the ratio of structural mass to fluid-added mass
C  RE is the Reynolds number
```

```
C  NDT is the number on time steps per natural period of the
C      in vacuo mass-spring system. The Runge-Kutta
C      integration is performed during NNDT*NDT time steps.
C  TOLTAU is the tolerance for the pseudo-time integration
C         when calculating the fluid force
C  RKSI is the mechanical damping, set to zero
C  EPS is the initial displacement of the outer cyclinder axis


      MESH = UPENO.1
      RATIOM = 1.5
      RE = 200.
      NDT = 19
      NNDT = 3
      TOLTAU = 1.e-4

      RKSI = 0.0
      EPS = 0.1


C   ************************************************************

C  The mesh parameters are loaded into program memory; they
C  are passed to the subroutine MOHT2 using a COMMON block.
C  The value of the real-time step size Δt is determined, as
C  well as the values of σ, of the pseudo-time step size Δτ
C  and the artificial compressibility δ.

C  NY is the number of grid points in the radial direction
C  DTREAL is the real time step size Δt
C  SIGMA is the value of σ in equation (9.2)
C  DELTA is the artificial compressibility δ
C  DTAU is the pseudo-time step size Δτ

      OPEN(2,FILE=MESH)
        READ(2,'(I5)') NY
        READ(2,'(I5,4F15.7)')
     &       (JJ,YNU(J),YNV(J),DYU(J),DYV(J),J=1,NY)
        READ(2,*)
        READ(2,'(I5,2F15.7)') (JJ,YRU(J),YRV(J),J=1,NY)
      CLOSE(2)

      DTREAL = 2.0*PI / REAL(NDT)

         SMAJ = (YRV(NY-1)/YRV(1)) ** 2
        SMAJ = (SMAJ-1.)/((SMAJ+1)*PI*YRV(NY-1)**2)
       SIGMA = SMAJ/RATIOM

       DELTA = 0.0001 * 1.0/(DTREAL*EPS**2)
       DTAU = EPS*DTREAL
       DTAU = 1500.0 *
```

```
     &   YNU(2)/(DTAU + SQRT(DTAU**2+DTREAL/DELTA))

C     ************************************************
C     Beginning of the Runge-Kutta integration scheme
C     ************************************************

C  FLUIDE is the fluid force returned from the
C         subroutine MOHT2. The parameters
C         passed to MOHT2 in order to calculate FLUIDE
C         are described below.

      FLUIDE = 0.0

C  The initial conditions are set

      X(1) = EPS
      X(2) = EPS

C  Start of the Runge-Kutta loop

      DO 10 IDT=3, NNDT*NDT

C  Second step illustrated in Table 9.1 of Thesis

        X2 = X(IDT-1) + DTREAL/2.0 * V(IDT-1)
        V2 = V(IDT-1) + DTREAL/2.0 * A(IDT-1)
        CALL MOHT2(V2, FLUIDE, .FALSE., IDT)
        A2 =  - 2.0*RKSI*V2 - X2 + SIGMA*FLUIDE

C  Third step illustrated in Table 9.1 of Thesis

        X3 = X(IDT-1) + DTREAL/2.0 * V2
        V3 = V(IDT-1) + DTREAL/2.0 * A2
        CALL MOHT2(V3, FLUIDE, .FALSE., IDT)
        A3 =  - 2.0*RKSI*V3 - X3 + SIGMA*FLUIDE

C  Fourth step illustrated in Table 9.1 of Thesis

        X4 = X(IDT-1) + DTREAL * V3
        V4 = V(IDT-1) + DTREAL * A3
        CALL MOHT2(V4, FLUIDE, .TRUE., IDT)
        A4 =  - 2.0*RKSI*V4 - X4 + SIGMA*FLUIDE

C  Updating of variables as per equations (9.4-9.7)

        X(IDT) = X(IDT-1)
     &    + DTREAL/6.0*(V(IDT-1) + 2.0*V2 + 2.0*V3 + V4)
        V(IDT) = V(IDT-1)
     &    + DTREAL/6.0*(A(IDT-1) + 2.0*A2 + 2.0*A3 + A4)
        CALL MOHT2(V(IDT), FLUIDE, .TRUE., IDT)
        A(IDT) =  - 2.0*RKSI*V(IDT) - X(IDT) + SIGMA*FLUIDE
```

```
10    WRITE(*,'(I5,E15.4)') IDT, X(IDT)/EPS


      STOP
      END


C ... ****************************************
      SUBROUTINE MOHT2(VOT, FLUIDE, DTUN, IDT)
C ... ****************************************

C  The subroutine MOHT2 computes the fluid forces on the
C  oscillating outer cylinder.

C  VOT is the velocity of the cylinder axis at the advanced
C      time level for which the solution is sought
C  FLUIDE is the fluid force at the advanced time level
C  DTUN is a logical variable. When it is true, the solution
C       is projected to time level t^n + Δt, else to t^n + Δt/2.
C  IDT is the time counter

      PARAMETER (NYC=40)

C  FILOUT is a direct-access file which stores the solution,
C         i.e. velocity components and pressure, for three
C        consecutive real-time levels: the latest three time
C         levels during the time integration. Each record
C         represents the solution at one time level
C  INIT is a logical variable which is used to detect the
C       first time MOHT2 is called in order to initialize
C       variables

      CHARACTER FILOUT*20
      LOGICAL DTUN, INIT

C  The following variables have been defined above

      DIMENSION YNU(NYC), YNV(NYC), DYU(NYC), DYV(NYC),
     &          YRU(NYC), YRV(NYC)

C  The next variables are defined below and contain the
C  grid point coordinates and their delta's; they are used to
C  evaluate the equation residuals

      DIMENSION CYU(NYC), CYV(NYC), RYU(NYC), RYV(NYC)
      DIMENSION TYU(NYC), TYV(NYC), AYU(NYC), AYV(NYC)

C  V1 is the first circumferential harmonic of the
C     radial velocity component
C  V2 is the second circumferential harmonic of the
C     radial velocity component
```

```
C  W1 is the first circumferential harmonic of the
C     circumferential velocity component
C  W2 is the second circumferential harmonic of the
C     circumferential velocity component
C  P1 is the first circumferential harmonic of the pressure
C  P2 is the second circumferential harmonic of the pressure

C  DV, DW and DP are the increments in the variables during
C                the pseudo-time integration
C  RP contains residuals of the continuity equation

      DIMENSION V1(NYC), V2(NYC), DV(NYC)
      DIMENSION W1(NYC), W2(NYC), DW(NYC)
      DIMENSION P1(NYC), P2(NYC), DP(NYC), RP(NYC)

C  FV1 is the non-homogeneous forcing term containing V1
C  FV2 is the non-homogeneous forcing term containing V2
C  FW1 is the non-homogeneous forcing term containing W1
C  FW2 is the non-homogeneous forcing term containing W2

      DIMENSION FV1(NYC), FV2(NYC), FW1(NYC), FW2(NYC)

C  B, D and A are used in the solution of the tridiagonal
C             systems of equations
C  RES2 and RESI contain the rms and maximum residuals of the
C                equations, respectively

      DIMENSION B(NYC), D(NYC), A(NYC), RHS(NYC)
      DIMENSION RES2(6), RESI(6)

      COMMON NY, YNU, YNV, DYU, DYV, YRU, YRV, RE, DTREAL,
     &          DELTA, DTAU, TOLTAU, ITMAX

      DATA V1,V2,DV,W1,W2,DW,P1,P2,DP/360*0.0/
      DATA FILOUT/'CYCLE'/, INIT/.FALSE./
      SAVE
      PI = ACOS(-1.0)

C  ************************************************************

C  If it is the first time the subroutine is called, then
C  the following variables are initialized

C     ------------------
      IF(.NOT.INIT) THEN
C     ------------------

      INIT = .TRUE.

      NY1=NY-1
      NY2=NY-2
```

```
      DTAC = DTAU/DELTA
      DTACE = DTAU*RE/DELTA

        IWFL = 4*6*NY2

C  FILOUT is initialized to zero for three time levels

      OPEN(2,FILE=FILOUT,ACCESS='DIRECT',RECL=IWFL)
        DO 1466 IREC=1,3
1466      WRITE(2,REC=IREC) (0.0,0.0,0.0,0.0,0.0,0.0,J=2,NY1)
      CLOSE(2)

       ENDIF

C  ****************************************
C  Computation of the non-homogeneous terms
C  ****************************************

C  The solutions at the time levels t^n and t^n-1 are first
C  obtained from the file FILOUT

       OPEN(2,FILE=FILOUT,ACCESS='DIRECT',RECL=IWFL)
          IREC = MOD(IDT-2+3, 3) + 1
          READ(2,REC=IREC)
     &       (V1(J),V2(J),W1(J),W2(J),P1(J),P2(J),J=2,NY1)
          IREC = MOD(IDT-3+3, 3) + 1
          READ(2,REC=IREC) (FV1(J),FV2(J),
     &       FW1(J),FW2(J), GDP,GDP,J=2,NY1)
       CLOSE(2)

C  ---------------------------------------------------

C  If DTUN is true, then the solution is projected
C                   to t^n+1 (t^n + Δt)

       IF(DTUN) THEN

         ALPHA = 2.0*DTREAL/3.0

         DO 30 J=2,NY1
           FV1(J) = ( 4.0*V1(J) - FV1(J) ) / 3.0
           FV2(J) = ( 4.0*V2(J) - FV2(J) ) / 3.0
           FW1(J) = ( 4.0*W1(J) - FW1(J) ) / 3.0
30         FW2(J) = ( 4.0*W2(J) - FW2(J) ) / 3.0

C  ---------------------------------------------------

C  Else, DTUN is false and the solution is projected
C              to t^n+1/2 (t^n + Δt/2)

       ELSE
```

```
            ALPHA = 3.0*DTREAL/8.0

            DO 31 J=2,NY1
              FV1(J) = ( 9.0*V1(J) - FV1(J) ) / 8.0
              FV2(J) = ( 9.0*V2(J) - FV2(J) ) / 8.0
              FW1(J) = ( 9.0*W1(J) - FW1(J) ) / 8.0
31            FW2(J) = ( 9.0*W2(J) - FW2(J) ) / 8.0

          ENDIF

C     ***************************************************************

C     The values of the parameters used in the calculation of the
C     equations are set

          DTAL = DTAU*ALPHA
          ALDL = ALPHA*DELTA

          DO 59 J=1,NY1
            CYU(J) = DTAL/(YRU(J)*YNU(J))
            CYV(J) = DTAL/(YRV(J)*YNV(J))
            RYU(J) = YRU(J)/(RE*YNU(J))
            RYV(J) = YRV(J)/(RE*YNV(J))
            TYU(J) = DTAL/(RE*YRU(J)**2)
            TYV(J) = DTAL/(RE*YRV(J)**2)
            AYU(J) = DTAL/YRU(J)
59          AYV(J) = DTAL/YRV(J)

C     The boundary conditions are calculated

C     WALL1 is the boundary condition on the first harmonic of
C           the circumferential velocity component

           WALL1 = VOT/2.0
           V1(NY1) = VOT/2.0

C ... ****************************************
C ... Beginning of the iteration in pseudo-time
C ... ****************************************

C     As was the case for the previous program listed in this
C     Appendix, the radial and circumferential sweeps are done
C     in succession for one given momentum equation, before to
C     consider the next momentum equation.

C     Here we have a total of six equations: three equations
C     describing the first-circumferential harmonic variables,
C     V1, W1 and P1, which are, respectively, the radial and
C     circumferential momentum and the continuity equations; the
C     other three equations are their counterparts for the second
C     harmonic variables, V2, W2 and P2.
```

```
      ITER = 0
998   ITER = ITER + 1

      DO 14 I=1,6
        RES2(I) = 0.0
14      RESI(I) = 0.0

C     ****************************************************
C ... Solving of the radial momentum equation for V1(J)
C     ****************************************************

C     -------------------
C     Radial sweep for V1
C     -------------------

C  Computation of the residuals of the continuity equation
C  for the first circumferential harmonic

      DO 1032 J=2,NY1
       RP(J) = - CYU(J)/ALDL*(YRV(J)*V1(J)-YRV(J-1)*V1(J-1))
     &         + AYU(J)/ALDL*W1(J)
        IF(ABS(RP(J)).GT.RESI(5)) RESI(5)=ABS(RP(J))
        RES2(5) = RES2(5) + RP(J)*RP(J)
1032  CONTINUE

      DO 1020 J=2,NY2

C  Computation of the velocity interpolates

       V2YP = (1.0-DYV(J+1))*V2(J+1) + DYV(J+1)*V2(J)
       V2YM = (1.0-DYV(J))*V2(J) + DYV(J)*V2(J-1)
       V1YP = (1.0-DYV(J+1))*V1(J+1) + DYV(J+1)*V1(J)
       V1YM = (1.0-DYV(J))*V1(J) + DYV(J)*V1(J-1)
       W1V = (1.0-DYU(J+1))*W1(J+1) + DYU(J+1)*W1(J)
       W2V = (1.0-DYU(J+1))*W2(J+1) + DYU(J+1)*W2(J)

C  Setting up of the implicit left-hand side of the
C  tridiagonal system of equations

       B(J) = CYV(J)* (-2.0*YRU(J)*V2YM*DYV(J) - RYU(J))
     &                - DTAC*CYU(J)*YRV(J-1)/YNV(J)
       D(J) = 1.0 + DTAU + TYV(J)
     1  + CYV(J)*( 2.0*(YRU(J+1)*V2YP*DYV(J+1)
     2               + YRU(J)*V2YM*(DYV(J)-1.0))
     3           + RYU(J+1) + RYU(J) )
     4        + DTACE*RYV(J)*(CYU(J)+CYU(J+1))
       A(J) = CYV(J)*( -2.0*YRU(J+1)*V2YP*(DYV(J+1)-1.0)
     &   - RYU(J+1) ) - DTAC*CYU(J+1)*YRV(J+1)/YNV(J)

C  Computation of the residuals for V1
```

```
        RHS(J) = DTAU*(-V1(J)+FV1(J))  - 2.0*TYV(J)*(V1(J)-W1V)
     1    - CYV(J)*( 2.0*(YRU(J+1)*V2YP*V1YP-YRU(J)*V2YM*V1YM)
     2      - ( RYU(J+1)*(V1(J+1)-V1(J))
     3        - RYU(J)*(V1(J)-V1(J-1)) ) )
     4      - AYV(J)*( W1V*V2(J) - W2V*V1(J) - 2.0*W1V*W2V )
     5        - DTAL/YNV(J)*(P1(J+1)-P1(J))

        IF(ABS(RHS(J)).GT.RESI(1)) RESI(1) = ABS(RHS(J))
       RES2(1) = RES2(1) + RHS(J)*RHS(J)
        RHS(J) = RHS(J) - DTAL/YNV(J)*(RP(J+1)-RP(J))
1020  CONTINUE

C  Solving of the tridiagonal system of equations

      CALL SY(2,NY2,B,D,A,RHS)

C  Computation of DV and DP

       DO 1040 J=2,NY2
1040     DV(J) = RHS(J)
       DO 1060 J=2,NY1
1060     DP(J) = RP(J)
     &         -CYU(J)/ALDL*(YRV(J)*DV(J)-YRV(J-1)*DV(J-1))

C  ---------------------------
C  Circumferential sweep for V1
C  ---------------------------

      DO 1080 J=2,NY2
        W2V = (1.0-DYU(J+1))*W2(J+1) + DYU(J+1)*W2(J)
        DV(J) = DV(J)/( 1.0 - AYV(J)*W2V + TYV(J) )
1080  CONTINUE


C     ****************************************************
C ... Solving of the circumferential momentum equation
C     for W1(J)
C     ****************************************************

C  Setting of the boundary conditions near the solid walls.
C  The program listing starting on page E-3 explains the
C  reasons behind that procedure

       W1(NY) = 8.0/3.0*WALL1 - 2.0*W1(NY1) + W1(NY2)/3.0
       W1(1) = - 2.0*W1(2) + W1(3)/3.0

C  ------------------
C  Radial sweep for W1
C  ------------------

      DO 3020 J=2,NY1
```

```
          W1YP = (1.0-DYU(J+1))*W1(J+1) + DYU(J+1)*W1(J)
          W1YM = (1.0-DYU(J))*W1(J) + DYU(J)*W1(J-1)
          W2YP = (1.0-DYU(J+1))*W2(J+1) + DYU(J+1)*W2(J)
          W2YM = (1.0-DYU(J))*W2(J) + DYU(J)*W2(J-1)
          V1W = (1.0-DYV(J))*V1(J) + DYV(J)*V1(J-1)
          V2W = (1.0-DYV(J))*V2(J) + DYV(J)*V2(J-1)

          B(J) = CYU(J)*( YRV(J-1)*V2(J-1)*DYU(J) - RYV(J-1) )
          D(J) = 1.0 + TYU(J) - AYU(J)*V2W
        1  + CYU(J)*( -YRV(J)*V2(J)*DYU(J+1)
        2             - YRV(J-1)*V2(J-1)*(DYU(J)-1.0)
        3          + RYV(J-1) + RYV(J) )
          A(J) = CYU(J)*( YRV(J)*V2(J)*(DYU(J+1)-1.0) - RYV(J) )

          RHS(J) = DTAU*(-W1(J)+FW1(J)) - 2.0*TYU(J)*(W1(J)-V1W)
        1    - CYU(J)*( YRV(J)*( V1(J)*W2YP - V2(J)*W1YP )
        2           - YRV(J-1)*( V1(J-1)*W2YM - V2(J-1)*W1YM )
        3         - ( RYV(J)*(W1(J+1)-W1(J))
        4            -RYV(J-1)*(W1(J)-W1(J-1)) ) )
        5    - AYU(J)*( 2.0*W1(J)*W2(J)
        6               + V1W*W2(J) - V2W*W1(J) + P1(J) )
3020  CONTINUE

C  The implicit left-hand side of the equations is corrected
C  in order to take into account the evaluation of the viscous
C  derivatives near the solid walls

          D(2) = D(2) + 2.0*CYU(2)*RYV(1)
          A(2) = A(2) - CYU(2)*RYV(1)/3.0
          B(NY1) = B(NY1) - CYU(NY1)*RYV(NY1)/3.0
          D(NY1) = D(NY1) + 2.0*CYU(NY1)*RYV(NY1)

C  The evaluation of the residual at the oscillating cylinder
C  wall is corrected and the maximum and rms residuals are
C  calculated

          RHS(NY1) = RHS(NY1) + CYU(NY1)*YRV(NY1)*V1(NY1)*W2YP

        DO 3100 J=2,NY1
          IF(ABS(RHS(J)).GT.RESI(3)) RESI(3) = ABS(RHS(J))
          RES2(3) = RES2(3) + RHS(J)*RHS(J)
3100  CONTINUE

        CALL SY(2,NY1,B,D,A,RHS)

        DO 3050 J=2,NY1
3050      DW(J) = RHS(J)

C  ----------------------------
C  Circumferential sweep for W1
C  ----------------------------
```

```
      DO 3200 J=2,NY1
        DW(J) = (DW(J) - AYU(J)*DP(J)) /
     1          ( 1 + DTAU + TYU(J)
     2     + AYU(J)*(2.0*W2(J)+AYU(J)/ALDL) )
3200  CONTINUE

      DO 3220 J=2,NY1
        DP(J) = DP(J) + AYU(J)/ALDL*DW(J)
3220  CONTINUE

C  ---------------------------------------
C  Updating of the first-haromnic variables
C  ---------------------------------------

      DO 5000 J=2,NY1
       V1(J) = V1(J) + DV(J)
       W1(J) = W1(J) + DW(J)
5000   P1(J) = P1(J) + DP(J)


C     ****************************************************
C ... Solving of the radial momentum equation for V2(J)
C     ****************************************************

C  -------------------
C  Radial sweep for V2
C  -------------------

C  Computation of the residuals of the continuity equation
C  for the second circumferential harmonic

      DO 6032 J=2,NY1
        RP(J) = - CYU(J)/ALDL*(YRV(J)*V2(J)-YRV(J-1)*V2(J-1))
     &          + 2.0*AYU(J)/ALDL*W2(J)
        IF(ABS(RP(J)).GT.RESI(6)) RESI(6)=ABS(RP(J))
          RES2(6) = RES2(6) + RP(J)*RP(J)
6032  CONTINUE

      DO 6020 J=2,NY2
       V1YP = (1.0-DYV(J+1))*V1(J+1) + DYV(J+1)*V1(J)
       V1YM = (1.0-DYV(J))*V1(J) + DYV(J)*V1(J-1)
       W1V = (1.0-DYU(J+1))*W1(J+1) + DYU(J+1)*W1(J)
       W2V = (1.0-DYU(J+1))*W2(J+1) + DYU(J+1)*W2(J)

       B(J) = - CYV(J)*RYU(J) - DTAC*CYU(J)*YRV(J-1)/YNV(J)
       D(J) = 1.0 + DTAU + TYV(J) + CYV(J)*(RYU(J)+RYU(J+1))
     &            + DTACE*RYV(J)*(CYU(J)+CYU(J+1))
       A(J) = - CYV(J)*RYU(J+1)
     &        - DTAC*CYU(J+1)*YRV(J+1)/YNV(J)
       RHS(J) = DTAU*(-V2(J)+FV2(J))
     1    - TYV(J)*(5.0*V2(J) - 4.0*W2V)
```

```
     2     - CYV(J)*( YRU(J+1)*V1YP*V1YP - YRU(J)*V1YM*V1YM
     3     - ( RYU(J+1)*(V2(J+1)-V2(J))
     4       - RYU(J)*(V2(J)-V2(J-1)) ) )
     5     - AYV(J)*W1V*(-2.0*V1(J)+W1V)
     6     - DTAL/YNV(J)*(P2(J+1)-P2(J))

          IF(ABS(RHS(J)).GT.RESI(2)) RESI(2) = ABS(RHS(J))
          RES2(2) = RES2(2) + RHS(J)*RHS(J)
        RHS(J) = RHS(J) - DTAL/YNV(J)*(RP(J+1)-RP(J))
6020  CONTINUE

      CALL SY(2,NY2,B,D,A,RHS)

       DO 6040 J=2,NY2
6040     DV(J) = RHS(J)
       DO 6060 J=2,NY1
6060     DP(J) = RP(J)
     &        -CYU(J)/ALDL*(YRV(J)*DV(J)-YRV(J-1)*DV(J-1))

C  ----------------------------
C  Circumferential sweep for V2
C  ----------------------------

      DO 6080 J=2,NY2
        DV(J) = DV(J)/( 1.0 + 4.0*TYV(J) )
6080  CONTINUE


C     ****************************************************
C ... Solving of the circumferential momentum equation
C     for W2(J)
C     ****************************************************

C  -------------------
C  Radial sweep for W2
C  -------------------

       W2(NY) = - 2.0*W2(NY1) + W2(NY2)/3.0
       W2(1) = - 2.0*W2(2) + W2(3)/3.0

      DO 7020 J=2,NY1
        W1YP = (1.0-DYU(J+1))*W1(J+1) + DYU(J+1)*W1(J)
        W1YM = (1.0-DYU(J))*W1(J) + DYU(J)*W1(J-1)
        V1W = (1.0-DYV(J))*V1(J) + DYV(J)*V1(J-1)
        V2W = (1.0-DYV(J))*V2(J) + DYV(J)*V2(J-1)
         CR = CYU(J)*RYV(J)
         CL = CYU(J)*RYV(J-1)

       B(J) = - CL
       D(J) = 1.0 + TYU(J) + CL + CR
       A(J) = - CR
```

```
          RHS(J) = DTAU*(-W2(J)+FW2(J))
         1     - TYU(J)*(5.0*W2(J)-4.0*V2W)
         2     - CYU(J)*( YRV(J)*V1(J)*W1YP - YRV(J-1)*V1(J-1)*W1YM
         3           - ( RYV(J)*(W2(J+1)-W2(J))
         4             - RYV(J-1)*(W2(J)-W2(J-1)) ) )
         5     - AYU(J)*( W1(J)*(-2.0*W1(J)+V1W) + 2.0*P2(J) )
 7020   CONTINUE

          D(2) = D(2) + 2.0*CYU(2)*RYV(1)
          A(2) = A(2) - CYU(2)*RYV(1)/3.0
          B(NY1) = B(NY1) - CYU(NY1)*RYV(NY1)/3.0
          D(NY1) = D(NY1) + 2.0*CYU(NY1)*RYV(NY1)

          RHS(NY1) = RHS(NY1)
        &      CYU(NY1)*YRV(NY1)*V1(NY1)*(WALL1-W1YP)

         DO 7100 J=2,NY1
           IF(ABS(RHS(J)).GT.RESI(4)) RESI(4) = ABS(RHS(J))
           RES2(4) = RES2(4) + RHS(J)*RHS(J)
 7100   CONTINUE

         CALL SY(2,NY1,B,D,A,RHS)

         DO 7050 J=2,NY1
 7050    DW(J) = RHS(J)

 C  ----------------------------
 C  Circumferential sweep for W2
 C  ----------------------------

         DO 7200 J=2,NY1
          DW(J) = (DW(J) - 2.0*AYU(J)*DP(J)) /
        &   ( 1 + DTAU + 4.0*( TYU(J) + AYU(J)*AYU(J)/ALDL ) )
 7200   CONTINUE

         DO 7220 J=2,NY1
          DP(J) = DP(J) + 2.0*AYU(J)/ALDL*DW(J)
 7220   CONTINUE

 C  ------------------------------------
 C  UPDATING OF SECOND-HARMONIC VARIABLES
 C  ------------------------------------

         DO 7300 J=2.NY1
          V2(J) = V2(J) + DV(J)
          W2(J) = W2(J) + DW(J)
 7300     P2(J) = P2(J) + DP(J)


 C  The calculations of the residuals are fine-tuned
```

```
      DO 15 I=1,4
        RESI(I) = RESI(I)/DTAL
15      RES2(I) = SQRT(RES2(I)/NY2)/DTAL
      DO 16 I=5,6
        RESI(I) = RESI(I)/DTAC
16      RES2(I) = SQRT(RES2(I)/NY2)/DTAC

C   ************************************
C   test for convergence in pseudo-time
C   ------------------------------------

       DO 17 I=1,6
         IF(RES2(I).GT.TOLTAU) GOTO 998
17     CONTINUE
C   ************************************

C  After convergence in pseudo-time, the variables are stored
C  in the file FILOUT

       OPEN(2,FILE=FILOUT,ACCESS='DIRECT',RECL=IWFL)
         IREC = MOD(IDT-1+3,3) + 1
         WRITE(2,REC=IREC) (V1(J),V2(J),W1(J),W2(J),
      &                     P1(J),P2(J),J=2,NY1)
       CLOSE(2)


C   ************************************************************
C   Computation of the fluid force FLUIDE
C   ------------------------------------

        GRV = 3.0*V1(NY1) - 4.0*V1(NY2) + V1(NY-3)
       GRV = GRV/(3.0*YNU(NY1)-YNU(NY2))
        GRW = 8.0/3.0*WALL1 - 3.0*W1(NY1) + W1(NY2)/3.0
       GRW = GRW/(8.0/3.0*DYV(NY1)*YNU(NY1)-YNV(NY2)/3.0)
       FLUIDE = P1(NY1) - (2.0*GRV+GRW)/RE
       FLUIDE = 2.0*PI*YRV(NY1) * FLUIDE
C   ************************************************************

       RETURN
       END

C  The next subroutine solves tridiagonal systems of equations

C      **********************************
       SUBROUTINE SY(IL,IU,BB,DD,AA,CC)
C      **********************************

       DIMENSION AA(*), BB(*), CC(*), DD(*)

       LP = IL+1
       DO 10 I=LP,IU
```

```
      R = BB(I)/DD(I-1)
      DD(I) = DD(I)-R*AA(I-1)
10    CC(I) = CC(I)-R*CC(I-1)

      CC(IU) = CC(IU)/DD(IU)
      DO 20 I=LP,IU
      J = IU-I+IL
20    CC(J) = (CC(J)-AA(J)*CC(J+1))/DD(J)
      RETURN
      END
```